

AD-A181 816

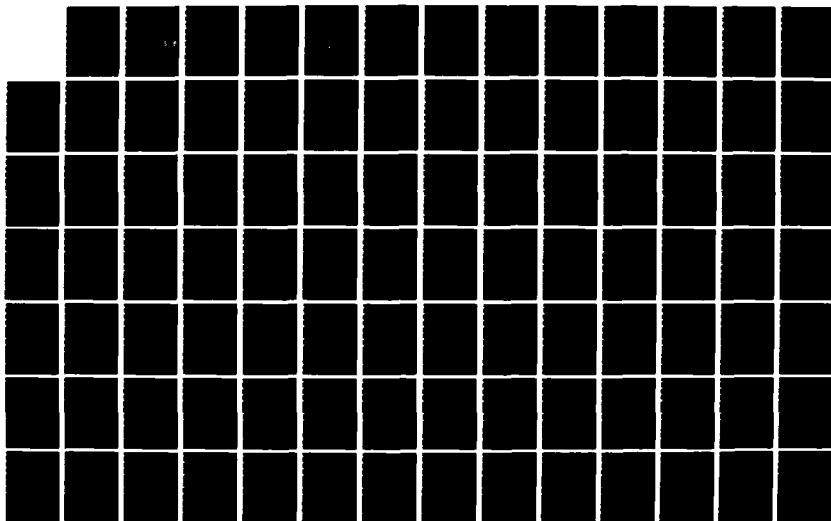
CHARACTERIZATION OF INFRARED PROPERTIES OF LAYERED  
SEMICONDUCTORS(U) CALIFORNIA UNIV LOS ANGELES DEPT OF  
PHYSICS R BRAUNSTEIN 20 FEB 87 AFOSR-TR-87-8721  
AFOSR-83-8169

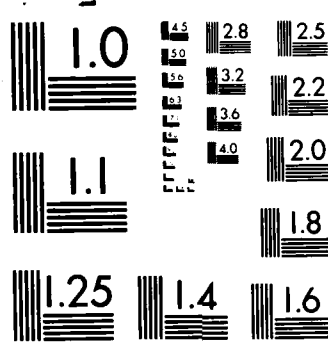
1/2

UNCLASSIFIED

F/G 28/12

NL





AD-A181 016

DTIC FILE COPY

(2)

SECURITY CLASSIFICATION OF THIS PAGE (When Data Entered)

REPORT DOCUMENTATION PAGE		READ INSTRUCTIONS BEFORE COMPLETING FORM
1. REPORT NUMBER <b>APOSR-TR- 87-0481</b>	2. GOVT ACCESSION NO.	3. RECIPIENT'S CATALOG NUMBER
4. TITLE (and Subtitle)  Characterization Of Infrared Properties of Layered Semiconductors		5. TYPE OF REPORT & PERIOD COVERED Final Scientific Report 4/1/83 - 2/29/87
		6. PERFORMING ORG. REPORT NUMBER
7. AUTHOR(s) Rubin Braunstein		8. CONTRACT OR GRANT NUMBER(s) AFOSR 83-0169
9. PERFORMING ORGANIZATION NAME AND ADDRESS Department of Physics University of California, Los Angeles, CA. 90024		10. PROGRAM ELEMENT, PROJECT, TASK AREA & WORK UNIT NUMBERS 61102F 2306/B1
11. CONTROLLING OFFICE NAME AND ADDRESS Air Force Office of Scientific Research/Bldg 410 Bolling Air Force Base, D.C., 20332 NE		12. REPORT DATE 2/20/87
		13. NUMBER OF PAGES 160
14. MONITORING AGENCY NAME & ADDRESS (if different from Controlling Office)  Same as 11		15. SECURITY CLASS. (of this report)
		15a. DECLASSIFICATION/DOWNGRADING SCHEDULE
16. DISTRIBUTION STATEMENT (of this Report)  Approved for public release; distribution unlimited.		
17. DISTRIBUTION STATEMENT (of the abstract entered in Block 20, if different from Report)  S D		
18. SUPPLEMENTARY NOTES		
19. KEY WORDS (Continue on reverse side if necessary and identify by block number) Infrared Wavelength Modulation, Photo-Mixing, Drift Velocity, Photo-Induced Transients, Deep Levels, Oxide Growth, Raman Scattering, Lifetime, <span style="float: right;">←</span>		
20. ABSTRACT (Continue on reverse side if necessary and identify by block number) The technique of infrared wavelength modulation absorption, photo-induced transient-spectroscopy, Raman scattering, and photo-mixing were developed for non-destructive characterization of layered semi- conductors. Infrared wavelength modulation on semi-insulating GaAs reveals two resonant type (continued on back of page.)		

DD FORM 1 JAN 73 1473

SECURITY CLASSIFICATION OF THIS PAGE (When Data Entered)

cont'd → peaks with fine structures near 0.37 and 0.40 eV as well as plateaus and thresholds at higher energies. The absorption at 0.37 eV is interpreted as due to the intra-center transition between levels of an accidental iron impurity. The absorption band near 0.40 eV can be annealed out by heat treatment and is characterized as belonging to a structural multi-level defect complex. Photo-induced-transient- spectroscopy technique also reveals an annealable level at 0.42 eV. Crystalline Arsenic was observed to grow on the surface of GaAs during exposure to continuous-wave laser radiation. A study of the time development of the Arsenic growth as revealed by Raman backscattering indicated that a surface diffusion process was responsible for limiting the growth process. Temperature measurements were performed from which the diffusion barrier energies were obtained for various GaAs samples. From these results the diffusion process was shown to depend on the Fermi level of the sample. A technique was developed to measure drift velocities in the hot-carrier small distance regimes in semiconductors. Extensive measurements were performed on GaAs, HgCdTe, and Si as a function of electric and temperature with contacts of the order of microns. Electric field dependent drift velocities and minority carrier lifetimes were determined as a function of temperature.

(Keyman's)



**AFOSR-TR- 87-0721**

**Characterization of Infrared Properties  
of Layered Semiconductors**

**Contract: AFOSR 83-0169**

**Final Scientific Report  
for Period: 4/1/83 - 2/29/87**

**SUBMITTED TO:**

Approved for public release;  
distribution unlimited. ✓

**Air Force Office of Scientific Research  
Bolling Air Force Base, D.C. 20332**

**PREPARED BY:**

**Rubin Braunstein  
Department of Physics  
University of California at Los Angeles**

**AIR FORCE OFFICE OF SCIENTIFIC RESEARCH (AFSC)  
NOTICE OF TRANSMITTAL TO DTIC  
This technical report has been reviewed and is  
approved for public release IAW AFR 190-12.  
Distribution is unlimited.  
MATTHEW J. KERPER  
Chief, Technical Information Division**

## TABLE OF CONTENTS

### I. Objectives of Program

### II. Summary of Accomplishments

- a. Deep Level Derivative Spectroscopy.
- b. Photo-Induced-Transient-Spectroscopy of Semi-Insulating (LEC) GaAs.
- c. Raman Backscattering
- d. Photo-mixing Determination of Hot-Carrier Drift Velocities
- e. Collaborative Work on HgCdTe.

### III. Summary and Conclusion

### IV. Participating Scientific Personnel

### V. Publications Included

### VI. Appendix



Accession For	
NTIS CRA&I	<input checked="checked" type="checkbox"/>
DTIC TAB	<input type="checkbox"/>
Unannounced	<input type="checkbox"/>
Justification	
By	
Distribution/	
Availability Codes	
Dist	Avail and/or Special
A-1	

## I. OBJECTIVES OF PROGRAM

The broad objectives of this program were to extend our understanding of the electrical properties of layered semiconductors employed for low noise amplification, generation and detection of high frequency radiation in large scale integrated circuit technologies. The present research program developed and exploited nondestructive techniques to analyze imperfections in layered semiconductors utilizing optical coupled with electrical measurements, requiring no special processing, and can be used on substrates and epitaxial layers to map crystal quality and electrical characteristics. The techniques of infrared wavelength modulation, photo-induced-transient-spectroscopy, Raman scattering, and photo-mixing were employed; the combination of these enable a determination of impurity concentration, structural defects, recombination rates, and transport properties by optical means.

## II. SUMMARY OF ACCOMPLISHMENTS

### *A. Deep Level Derivative Spectroscopy*

An infrared wavelength modulated spectrometer system was developed which is capable of measuring changes in the absorption or reflection of one part in  $10^5$  in the spectral region from 0.2—20  $\mu\text{m}$ . The system consists of a modified grating monochromator. The modulation of the wavelength is accomplished by oscillating an output diagonal mirror and thus is equally applicable for any wavelength in the spectral range of the microchromator and the amplitude of wavelength modulation can be continuously varied up to  $\Delta\lambda/\lambda \cdot 10^{-2}$ . The wavelength modulation technique yields essentially the energy derivatives of the absorption coefficient. To obtain the absolute value of the absorption coefficient, one numerically integrates the observed derivative spectra and the constant of integration is supplied by a direct loss measurement in the same apparatus at a fixed wavelength where the absorption can be measured with good precision.

We have demonstrated that the infrared wavelength modulation system can detect impurity concentrations at levels of  $10^{12}$ - $10^{14}/\text{cm}^3$  in semiconductors; previously, it had only been only

possible to study such concentrations by junction techniques, and consequently it was not possible to observe absorption thresholds and excited states of deep impurities.

A detailed study of the derivative absorption of GaAs:Cr was completed. The extensive fine structure observed for the first time out of a previously observed smooth absorption background by conventional absorption techniques was correlated with a proposed energy scheme for ( $\text{Cr}^{+4}$ - $\text{Cr}^{+3}$ ) ions in GaAs. This work indicates that a comparable number of Cr ions are at tetragonal and trigonal sites. This work has been published; a reprint of this publication is included in the Appendix of this report.

The versatility of this system was further demonstrated by a study of the band structure of metal alloys reported in a series of papers included as reprints in the Appendix.

A study of bulk and surface absorption in a range of materials employed this system. The results of the study of deep levels in semi-insulating GaAs, surface layers on Si, GaAs, and HgCdTe, oxygen complexes in floating zone silicon and the determination of strain ion due to implanted layers was presented in various publications, reprints of which are included in the Appendix.

The results of the above studies demonstrate that the wavelength modulation system we have developed is a unique tool for studying low level absorption in materials. The sensitivity of the method as well as the unambiguous line shapes obtained allow one to identify excited states as well as ground states of defects in semiconductors, as opposed to electrical methods such as the variety of DLTS techniques, which are essentially thermal methods and merely determine ground states. At present there is a tendency to utilize FTIR techniques to arrive at material characterization standards for impurity concentrations in semiconductors for the microelectronics industry. This approach depends upon the multiplexing advantage of interferometry if one desires to examine a broad spectral range. However, when one has a narrow spectral range to identify energy levels, the multiplexing advantage of interferometry vanishes and infrared wavelength modulation will have a greater sensitivity.

***B. Photo-Induced-Transient-Spectroscopy of Semi-Insulating (LEC) GaAs.***

A computer-controlled photo-induced-transient-spectrometer (P.I.T.S.) was constructed and employed for the study of the electrical manifestations of deep levels in semi-insulating GaAs. A detailed study was completed of the levels in LEC GaAs in sections of the same samples that were employed for our wavelength modulation measurements so as to obtain a possible correlation between optical absorption and the P.I.T.S. measurements. Measurements were performed on samples which received a variety of heat treatment.

A rich spectrum of deep levels were observed in samples not subjected to any heat treatment after they were initially grown. However, there was significant differences between the as-grown samples and the same samples which received heat treatment. Levels at 0.52, 0.42 and 0.36 eV in as-grown samples readily annealed; there seems to be a correlation between there P.I.T.S. results and similar levels observed in our wavelength modulation measurements which were identified as structural defects. However, an exact correlation by these different methods must take into account the fact that the P.I.T.S. results yield information on the thermal emission rates from a level to a band, whereas the optical absorption measurement yields information regarding intra-center as well as transitions to bands before thermal relaxation.

This work has been submitted for publication to The Journal of Physics and Chemistry of Solids, a preprint of which has been included in the Appendix. A complete exposition of this work is contained in a thesis by M. Burd entitled: "A Study of Deep Levels in Semi-Insulating Layers of Liquid-Encapsulated-Czochralski-Grown Gallium Arsenide by Photo-Induced-Transient-Spectroscopy."

Further study of the observed levels which readily anneal out and reappear upon thermal quenching is worthy of future study in GaAs and other III-IV and II-VI compounds; the proclivity of these material to contain annealable defects can be exploited for device fabrication.

### *C. Raman Backscattering*

Raman backscattering was employed as a non-destructive technique for the study of surface treatment, strain due to passivation layers, and changes in the space-charge layer near the surface. By observing the changes in the width and position of the LO phonon in the depletion layer, inhomogeneous strain associated with lattice defects can be inferred. From the shift of the high frequency coupled  $L^+$  mode in the bulk beyond the depletion layer it was possible to observe increases or decreases in the charge carrier concentration near the surface depending on the surface treatment.

The growth of an oxide in a III-V compound surface is a topic of current research with both technological and fundamental interest. Some insight into the kinetics of the oxidation of GaAs was obtained by studying the time dependence of the growth of crystalline arsenic during the oxidation of GaAs as monitored by Raman backscattering. It was found that a surface diffusion process rather than bulk diffusion, as was formerly thought, is operative for the production of elemental arsenic. An enhancement of the growth of crystalline arsenic was observed due to 5145 Å illumination. These measurements have shown that the surface diffusion barrier energies and sticking coefficients involved in arsenic grain growth are determined by the charge states of the grain, which in turn is determined by the Fermi level of the GaAs substrate.

This work has been completed and has been submitted for publication in The Journal of Physical Chemistry of Solids. A preprint of this work entitled "Arsenic Growth on the Gallium Arsenide Surface During Oxidation" is included in the Appendix. A more complete exposition of this work is contained in a thesis by R. Martin entitled: "Raman Scattering from Subsurface Regions of Semiconductors."

The above work indicates that Raman scattering is an excellent technique for monitoring the surface condition of semiconductors. The use of this technique for studying nucleation processes during interface growth is worthy of continued study.

#### ***D. Photo-Mixing Determination of Hot-Carrier Drift Velocities***

A technique of photo-mixing was developed to measure drift velocities in the hot-carrier small distance regimes in semiconductors. The method consists of mixing two microchromatic optical frequencies to generate a microwave difference frequency ( $\omega$ ) whose power is independent of ( $\tau$ ) [the minority carrier lifetime] and is proportional to the drift mobility squared if  $\omega\tau \gg 1$ . If  $\omega\tau \sim 1$  or  $\omega\tau \ll 1$  the output power depends on the lifetime. By measuring the microwave power, the dark current, and the photo-current as a function of electric field, the field dependence of the drift velocity and lifetime as a function of temperature can be determined. Measurements were made on GaAs, HgCdTe, and Si with contact separations of the order of microns. Extensive measurements were made on the field and temperature dependence of the carrier lifetimes in GaAs which gave some insight into the little known extrinsic recombination centers in GaAs. Abstracts of this work were given at the International Conference on the Physics of Semiconductors, Stockholm, talks at Wright Patterson Airforce Base, the Aerojet ElectroSystems at Azusa, and the March 1987 Meeting of the American Physical Society; Publications of this work are in preparation.

The technique of photo-mixing is proving to be a useful technique to measure transport properties in the small channel regime. Measurements up to the present were performed on micron channels; the sensitivity of the technique will allow measurements in sub-micron structures in the ballistic and velocity overshoot regimes.

#### ***E. Collaborative Work on HgCdTe.***

Although the dominant effort in this program was directed toward GaAs some collaborative work was conducted with groups involved in the characterization of HgCdTe. Reprints of the resulting publications are included in the Appendix.

### III. SUMMARY AND CONCLUSION

The techniques of infrared wavelength modulation, photo-induced-transient spectroscopy, Raman Scattering, and photo-mixing form a combination of nondestructive techniques to determine deep levels, surface properties, and transport processes in a wide class of semiconductors. The above nondestructive analytical techniques enable a rapid assessment of the initial characteristics of the semiconductor as well as changes that may occur during device processing and can ultimately be used on the production line.



#### IV. PARTICIPATING SCIENTIFIC PERSONNEL

R. Braunstein	Principal investigator
M. Burd	Ph.D. granted Thesis: "A Study of Deep Levels in Layered Liquid Encapsulated-Czochralski Grown Gallium Arsenide"
M. Estemadi	Ph.D. granted Thesis: "Wavelength Modulation Spectroscopy of Deep Levels in Semi-Insulating GaAs"
R. Martin	Ph.D. granted Thesis: "Raman Scattering from Subsurface Regions of Semiconductors"
A. Melo	Post Doctral
B. Dorfman	Post Doctral, Participating but supported by NIH Fellowship
P. Yang	Ph.D. candidate
M. Argavani	Ph.D. candidate
M. Abdelouhab	Ph.D. candidate

## V. PUBLICATIONS INCLUDED WITH REPORT

- 1) R. Braunstein, R. K. Kim, D. Matthews, and M. Braunstein: "Derivative Absorption Spectroscopy of GaAs:Cr," *Physica* 117B and 118B, 163 (1983).
- 2) M. Burd, R. Stearns, and R. Braunstein: "De-Correlation Technique for Separation of Drude Parameters from Wavelength Modulation Spectroscopy Data," *Phys. Stat. Sol. (b)* 117, 101-107 (1983).
- 3) R. Stearns, J. Steele, and R. Braunstein: "Fully Electronic Servocircuitry for Wavelength-Modulation Spectroscopy," *Rev. Sci. Instr.* 54(8), 984-988 (1983).
- 4) R. Stearns, R. Braunstein, and L. Muldower: "Wavelength Modulation Spectra of  $\alpha$ -Ag<sub>0.7</sub>Zn<sub>0.3</sub> Near the Optical Absorption Edge," *Phys. Stat. Sol.(b)* 131, 659 (1983).
- 5) R. K. Kim and R. Braunstein: "Infrared Wavelength Modulation Spectroscopy of Some Optical Material," *Appl. Optics* 23(8), 1166 (1984).
- 6) C.E. Jones, K. James, J. Merz, R. Braunstein, M. Burd, and M. Eetemadi: "States of Point Defects in HgCdTe," *J. Vac. Sci. Technol. A* 3(1) 131 (1985).
- 7) R. Stearns, R. Braunstein, and L. Muldower: "Wavelength-Modulated Spectra of the Optical Properties of  $\beta'$ -Cu<sub>x</sub>Zn<sub>1-x</sub> from 1.5 to 5.1 eV," *Phys. Stat. Sol.(b)* 130, 595 (1985).
- 8) R. Stearns, R. Braunstein, and L. Muldower: "Optical Properties of  $\beta^1$ -AuZn by Wavelength-Modulated Derivative Spectroscopy," *Phys. Stat. Sol(b)* 129 735 (1985).
- 9) R. Braunstein, S.M. Eetemadi, and R.K. Kim: "Deep Level Derivative Spectroscopy of Semiconductors by Wavelength Modulation Techniques," SPIE vol. 524-Spectroscopic Characterization Techniques for Semiconductor Technology II(1985), published by the Society of Photo-Optical Instrumentation Engineers, Box 10, Bellingham, WA 98227-0010, USA.
- 10) S.M. Eetemadi and R. Braunstein: "Reexamination of the Wavelength Modulation Photoresponse Spectroscopies," *J. Appl. Phys.* 58 (10) 3856 (1985).
- 11) S.M. Eetamadi and R. Braunstein: "Wavelength Modulation Absorption Spectroscopy of Deep Levels in Semi-Insulating GaAs," *J. Appl. Phys.* 58 (6) (1985).
- 12) C.E.Jones, M.E.Boyd, W.H.Konkel, S.Perkowitz, and R.Braunstein: "Noncontact Electrical Characterization of epitaxial HgCdTe," *J.Vac.Sci.Technol. A* 4,2056(1986).
- 13) R.Martin and R. Braunstein: "Arsenic Growth on the Gallium Arsenide Surface During Oxidation," preprint - submitted to *J. Phys. Chem. Solids*
- 14) M.R.Burd and R.Braunstein: "Deep Levels in Semi-Insulating, Liquid-Encapsulated-Czochralski Grown GaAs," preprint - submitted to *J. Phys. Chem. Solids*.

**VL APPENDIX**

DERIVATIVE ABSORPTION SPECTROSCOPY OF GaAs:Cr

R. Braunstein<sup>(a)</sup>, R.K. Kim<sup>(a)</sup>, D. Matthews<sup>(b)</sup>, and M. Braunstein<sup>(b)</sup>

(a.) Physics Department, University of California, Los Angeles, U.S.A. 90024

(b.) Hughes Research Laboratories, Malibu, Calif., U.S.A. 90265

Infrared wavelength modulation measurements at 300K in the spectral range 0.5-1.4 eV on semi-insulating n and p-type Cr doped GaAs have revealed extensive fine structure with variations in absorption coefficient  $\Delta K \sim 10^{-1} - 10^{-2} \text{ cm}^{-1}$  out of a relatively smoothly varying background absorption of  $1-2 \text{ cm}^{-1}$ . These results can be interpreted in terms of transitions from  $(\text{Cr}^{3+} - \text{Cr}^{2+})$  to the valence and conduction bands and excited states.

1. INTRODUCTION - EXPERIMENTAL PROCEDURES

Although the deep levels of Cr in GaAs have been extensively studied by luminescence, absorption, photoconductivity and junction techniques, there are still questions concerning the possible energy level schemes of this important deep impurity. In general, excited states are not observed by the above techniques and absorption thresholds are not easily observed. We have developed an infrared wavelength modulated spectrometer that is capable of detecting changes in absorption of a part in  $10^5$  out of a relatively smoothly varying background in the spectral range 0.05-5.0 eV. Consequently, our detection limit for concentrations of deep levels is  $10^{12}-10^{14}/\text{cm}^3$  which was previously only possible by DLTS techniques. It has been possible to observe absorption thresholds and excited states in highly transparent solids<sup>(1)</sup>. In the present work, we report the results of a study of semi-insulating GaAs:Cr compensated with n and p-type impurities. Structures have been resolved in previously reported smoothly varying absorption bands which we interpret in terms of the level of Cr at various lattice sites. The infrared wavelength modulation system used in our work has been previously described<sup>(1)</sup>.

2. RESULTS

Figures 1 and 2 show the integrated derivative wavelength data of semi-insulating GaAs:Cr at 300K with varying degrees of shallow donor and acceptor compensations. The constants of integration were supplied by direct absorption measurements. Although data was taken in the spectral range 0.5-1.5 eV, for purposes of the present discussion, we shall discuss the data for the 0.5-1.2 eV region since the vast literature on GaAs:Cr has considered this regime. The region above 1.2 eV shows structures which can be associated with transitions from the  $\text{Cr}^{2+}$  ground state to the X and L conduction bands as well as EL2 structures. The scale of the absorption should be noted; in general the best previous absorption data have a precision of  $\Delta K \sim 0.1 \text{ cm}^{-1}$ <sup>(2)</sup>. The present work reveals structures at levels of  $\Delta K \sim 10^{-2} \text{ cm}^{-1}$  in samples of the order of 1mm thick.

The samples were all semi-insulating and contained  $\sim 10^{16}/\text{cm}^3$  Cr and were grown by horizontal Bridgman techniques. The samples in Figure 1 were highly compensated while those in Figure 2a and 2b were slightly more p and n-type respectively. Although quantitative measurements of shallow donor or acceptor compensation are difficult for such high resistivity samples, qualitative differences in n and p-type were measured by the changes in the characteristics of the space-charge limited I-V curves under illumination and in the dark.

The general features of the data exhibit clusters of lines in the 0.5-0.7, 0.8-0.95 and the 0.95-1.05 eV regions with extensive fine structure in every region, but with more pronounced structures in the 0.8-0.93 eV range. Previous conventional absorption measurements have shown a no-phonon line in the 0.82 region<sup>(2)</sup> and a broad continuum peaking at 0.9 eV for n-type material. In the 0.5-0.72 eV region, previous absorption measurements showed no fine structures but a smoothly varying free carrier absorption. A number of luminescence bands have been observed in GaAs:Cr in the range 0.57-0.81 eV, but their interpretation has been difficult<sup>(3)</sup>.

The relative magnitudes and the fine details vary from sample to sample as seen in Figures 1 and 2, but the envelopes of the dominant structures tend to vary in a systematic fashion with a degree of compensation. Samples in Figure 1 show essentially the same features but the sample in Figure 1b exhibits finer structure at 0.9-0.9 eV while the bands in the 0.5-0.72 eV have somewhat the same relative intensities. These samples were from the same crystal, but different parts of a single wafer. The samples in Figure 2a and 2b were more heavily doped p and n-type respectively than the samples in Figure 1. It should be noted that the relative intensities of the 0.5-0.72 eV bands change in Figures 2a and 2b with the 0.67 band enhanced in the n-type sample while the 0.58 eV band is enhanced in the p-type sample and the general level of absorption has increased over that of Figure 1. In addition, in the p-type sample, the cluster of lines between 0.8 eV

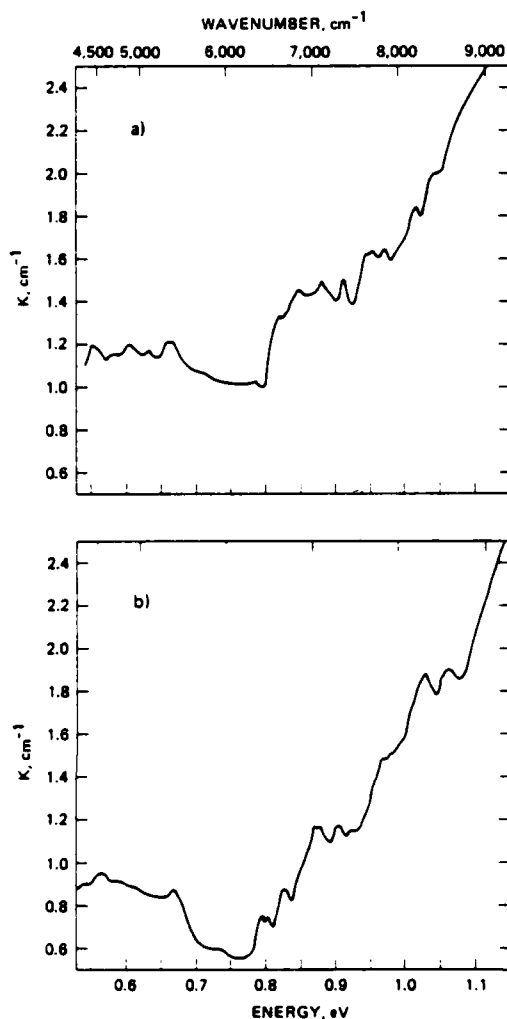


Figure 1. a) and b) Semi-insulating GaAs:Cr

and 0.9 eV have suppressed while the fine structure is maintained in the n-type sample.

## 1. DISCUSSION

The explanation of some of the varied structures and their variation with the degree of free carrier compensation can be explained in terms of transitions between  $(Cr^{3+} - Cr^{2+})$  states in a tetragonal environment and the conduction and valence bands and excited states. Figure 3 shows a level scheme of a  $3D$  state of  $Cr^{2+}$  placed within the energy gap of GaAs (4). We shall see that the explanation of the bands in the 0.6-0.72 eV region cannot be explained by this level scheme but is consistent with  $Cr^{2+}$  being in a  $T_d$  symmetry site.

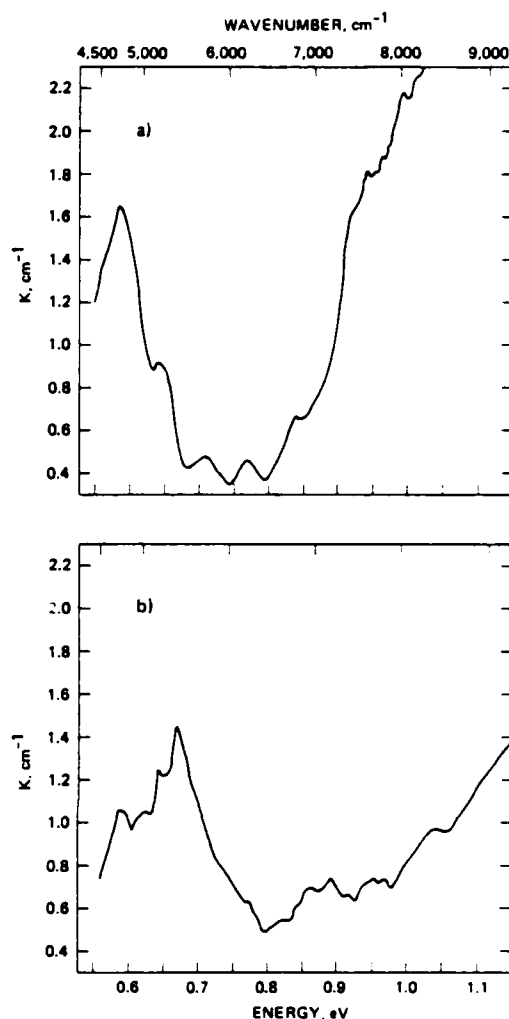


Figure 2. a) p-type, b) n-type GaAs:Cr

The data in the 0.8-1.05 eV region shows two main thresholds roughly around 0.8 eV and the other around 0.93 eV with fine structure in each band with the 0.8 eV threshold enhanced in the more n-type samples. We can attribute the 0.8 eV transition from the  $Cr^{2+}$  ground state to a resonant state in the conduction band:  $5B_2(5T_2) \rightarrow 5A_1(5E)$ ,  $P_1$  in Figure 1 (4). The second threshold can be ascribed to the transition from the valence band to the  $Cr^{2+}$  level  $Cr^{2+}(5T_2)$ , i.e.  $P_2$  and  $P_3$ . The  $5T_2$  state can be split by a tetragonal Jahn-Teller distortion into a  $5B_2$  and  $5E$  level. The ground state can be further split by spin-orbit coupling, however these are not shown because of the scale of the resolution of our experiments. The structure seen in the

0.93 - 1.05 eV region can be associated with valence band to  $\text{Cr}^{3+}$ ,  $P_2$  and  $P_3$ , transitions. Various estimates have been made of the magnitude of the Jahn-Teller distortion for  $\text{Cr}^{3+}$  and these have varied from  $175 \text{ cm}^{-1}$  to  $700 \text{ cm}^{-1}$  (2). If we take the peak at 0.95 eV and the shoulder at 1.04 eV as due to the transitions from the valence band to  ${}^5B_1({}^5T_2)$ ,  $P_2$ , and  ${}^5E({}^5T_2)$ ,  $P_3$ , respectively the Jahn-Teller distortion  $E_{JT} = 300 \text{ cm}^{-1}$ . The transition  ${}^5B_1 \rightarrow {}^5E$  has not been seen in absorption in GaAs:Cr despite extensive studies which merely reveal free carrier absorption in this region.

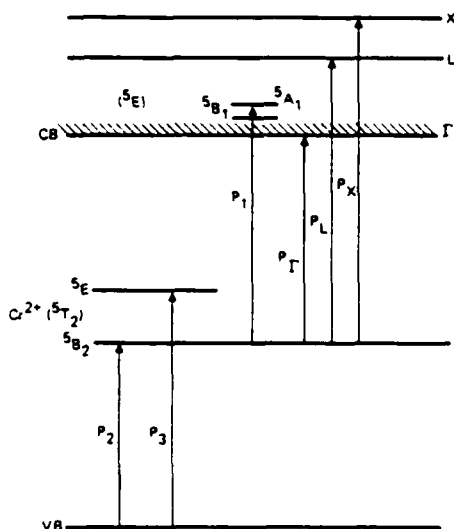


Figure 1. Energy levels of  $\text{Cr}^{3+}$ - $\text{Cr}^{2+}$  ions in GaAs.

Although all our absorption measurements show extensive structure in the 0.8-0.93 eV - more so in n-type samples, most previous measurements show a broad peak around 0.9 eV. Recently (2) an absorption band at 0.91 eV and a no-phonon line have been resolved and have been interpreted as the interval transition  ${}^5B_1({}^5T_2) \rightarrow {}^5A_1({}^5E)$  of  $\text{Cr}^{3+}$ . It is of interest to note that the fine structure around 0.8 eV in Figure 1 maybe due to these no-phonon lines, although our measurements were performed at 300K while the above work was at 4K. Luminescence experiments have shown a band at 0.61 eV and a no-phonon line at 0.639 eV (5). These lines have commonly been considered to be an internal  ${}^5E \rightarrow {}^5T_2$  transition of  $\text{Cr}^{3+}$ , however, it has been argued that the ground splitting of the 0.83 - 0.9 eV line is inconsistent with EPR measurements (2).

The luminescence bands in GaAs:Cr at 0.57, 0.61, 0.64, 0.68 eV have been difficult to interpret; it has been suggested that the 0.57 and 0.61 eV bands are due to the transition from a  $\text{Cr}^{3+}$  to the valence band and from the conduction band to a  $\text{Cr}^{3+}$  (6). The 0.62 eV band is always present in n-type material while in semi-insulating or p-type GaAs:Cr the 0.57 eV is more intense, while accompanied by the 0.3 eV band and thus can be attributed to the  $\text{Cr}^{3+}$  state. Arguments have recently been advanced that dispute that the 0.839 eV and the no-phonon line is being related to a single Cr acceptor center in a tetragonal Ga site (3). It has been proposed that the 0.839 eV band and the 0.574-0.535 eV lines are due to Cr at a  $C_{3v}$  symmetry site induced by coupling of a chromium atom at an interstitial or on a Ga site to a first neighbor impurity (2). For a trigonal field,  $C_{3v}$ , this work shows that there is a reordering of the Cr levels different from the tetragonal site shown in Figure 1. For interstitial chromium at a trigonal  $C_{3v}$  site coupled to an acceptor, the ordering of the orbital levels are  ${}^5E$ ,  ${}^5A_1$ , and  ${}^5B_1$  from lower to upper, while for a substitutional chromium at  $C_{3v}$  symmetry site coupled to a donor the ordering from lower to upper is  ${}^5E$ ,  ${}^5A_1$ ,  ${}^5B_1$ . The 0.574 eV and its associated emission are interpreted as transitions from the ground state to the valence band.

It is strongly suggestive that the absorption bands observed in the present work are related to the luminescence bands in this spectral region. It should be noted that for the samples in Figures 1a and 2b, which have a slightly higher doping, the level of absorption is greater for these bands than in the more compensated samples of Figures 1a and 1b. In the p-type sample of Figure 2a, the 0.585 eV line is enhanced over the 0.641 eV line, while for the n-type sample the 0.671 eV line is enhanced over the 0.59, 0.62 and 0.64 eV lines. Thus it seems that these absorption bands can be the complements of the luminescence bands. The complexity of this structure is evident and if they are due to  $C_{3v}$  trigonal symmetry due to coupling with Cr to donor or acceptor complexes, the subtle changes are due to degree of compensation and consequent position of the Fermi level in these four semi-insulating samples. The level of absorption in the 0.5 - 0.72 eV and 0.85 - 1.05 eV regions would indicate that about a comparable number of Cr atoms are at tetragonal and trigonal sites.

#### Acknowledgement

We would like to thank C.F. Krumm, R.E. Lee and S. Kamath for fruitful discussions. The M.D.A. work was supported by AFOSR - 78-1065, ARS-DAA620-91-K-0164 and California - MICRO.

## References

- (1) Braunstein, R., Kim, R.K., and Braunstein, M., NBS Special Publication 568, U.S. Government Printing Office.
- (2) Clerjaued, B., Hennel, A.M., and Martinez, G., Solid State Comm. 33 (1980) 983-985.
- (3) Picoli, G., Deveaue, B., and Galland, D., Le Journal De Physique T42, No. T (1980) 133-145.
- (4) Leyral, P., Litty, F., Loublichni, S., Mouailhot, A., and Guillot, S., Solid State Comm. 38 (1981) 333-336.
- (5) Lightowlers, E.C., and Penchina, C.M., J. Phys. C: Solid State Phys. 11 (1978) L405.
- (6) Deveaue, B., Hennel, A.M., Suzukiewicz, Picoli, G., Martinez, G., Revue Phys. Appl 15 (1980) 671.

phys. stat. sol. (b) 117, 101 (1983)

Subject classification: 13.1 and 20.1; 21.1; 21.6

Department of Physics, University of California, Los Angeles<sup>1)</sup>

## De-Correlation Technique for Separation of Drude Parameters from Wavelength Modulation Spectroscopy Data<sup>2)</sup>

By

M. BURD, R. STEARNS<sup>3)</sup>, and R. BRAUNSTEIN

Separation of bound- and free-electron contributions to the dielectric function is necessary for an accurate analysis of interband transitions. A technique for doing this separation which does not require low energy data is presented. The technique makes use of the fact that the functions which describe the contributions of each part are sufficiently uncorrelated, allowing the construction of a correlation function which uses the Drude effective mass and Drude relaxation time as adjustable parameters. The technique is shown to properly separate a test function and to yield reasonable results from experimental data.

Une analyse rigoureuse des transitions entre bandes nécessite une séparation entre les contributions des électrons libres et celles des électrons liés. Nous présentons ici une technique pour effectuer une telle séparation qui n'exige pas de données à basse énergie. La technique en question utilise le fait que les fonctions décrivant les deux types de contributions sont suffisamment non corrélées. Cela permet de construire une fonction de corrélation en faisant de la masse effective de Drude et du temps de relaxation de Drude des paramètres ajustables. Nous montrons que cette technique sépare proprement une fonction test et fournit des résultats raisonnables à partir de données expérimentales.

### 1. Introduction

The dielectric function,  $\epsilon(\omega)$ , contains important information about the optical properties of solids. It is defined as the response of a crystal to an electromagnetic field,

$$D(\omega) = \epsilon(\omega) E(\omega). \quad (1)$$

The dielectric function is sensitive to the electronic band structure of the material, and the determination of the dielectric function by optical spectroscopy is an important tool for investigating the overall band structure.

The broad bands found in solid state spectroscopy are convolutions of a number of contributions which emerge when derivatives of the reflectance are taken. A number of modulation techniques are available, which include temperature [1, 2], electric field [3, 4], pressure or uniaxial stress [5, 6] modulation. Wavelength modulation is employed in these studies because of the unambiguous lineshapes which emerge [7 to 11]. Transitions are strongest at points where the lower and upper bands are parallel, i.e., at frequencies which satisfy

$$\nabla_k[E_c(k) - E_v(k)] = 0, \quad (2)$$

where  $E_c$  and  $E_v$  are the energies of the upper and lower bands, respectively. At these critical points in  $k$ -space, which are the van Hove singularities [12], the joint density

<sup>1)</sup> Los Angeles, California 90024, USA.

<sup>2)</sup> Work supported in part by U.S. Army Research Office, Durham, North Carolina, and by the Air Force Office of Scientific Research.

<sup>3)</sup> Current address: TRW Technology Research Center, El Segundo, CA 90245, USA.



of states is singular. These critical points dominate the interband structure of the reflectivity spectrum. With the proper experimental feedback, band-to-band energy differences can be calculated with an accuracy of 0.1 eV. Energy band calculations are usually adjusted to fit the results of optical determinations of interband transition energies.

It is necessary to find the real and imaginary parts of the dielectric function,  $\epsilon_1$  and  $\epsilon_2$ , and their derivatives to examine the interband structure of the material under study. However, the dielectric function may not be directly available from experimental measurements. In some experiments, the reflectivity,  $R(\omega)$ , is obtained by integrating the data from wavelength modulation spectroscopy; the real and imaginary parts of the dielectric function are subsequently calculated by a Kramers-Kronig analysis [13]. When the material being studied is a metal or metal alloy, however, another step is needed. The dielectric function is the sum of two parts, a contribution due to interband structure and a contribution due to intraband transitions of the electrons at the Fermi level in the partially filled conduction bands. In order to separate the interband and intraband transitions, low-energy data are required which sometimes are not readily available.

We report a new technique for separating these contributions. For continuity of presentation, Section 2 of this paper will review the classical formalism which is used to describe the intraband contribution. Section 3 will deal with the interband structure, and Section 4 will present the new method of separation.

## 2. Classical Drude Theory

The classical Drude theory of the electronic properties of solids is due mainly to Lorentz [14] and Drude [15]. The Lorentz model assumes that an electron bound to the nucleus of an atom may be dealt with in much the same way as a small mass bound to a large mass by a spring. A classical damped oscillator model yields the Lorentz dielectric function

$$\epsilon = 1 + \frac{4\pi N e^2}{m} \frac{1}{(\omega_0^2 - \omega^2) - i\Gamma\omega}, \quad (3)$$

where  $\Gamma$  is a viscous damping coefficient,  $N$  the electron density, and  $m\omega_0^2 r$  is a Hooke's law force. The Drude model for metals is derived from the Lorentz model: the conduction electrons in a metal are not bound to a nucleus so the restoring force is set equal to zero.

When  $\omega_0$  is set to zero in (3) and real and imaginary parts are taken, we have

$$\epsilon_1 = 1 - \frac{\omega_p^2 \tau^2}{1 + \omega^2 \tau^2}, \quad (4a)$$

$$\epsilon_2 = \frac{\omega_p^2 \tau^3}{\omega(1 + \omega^2 \tau^2)}, \quad (4b)$$

where  $\omega_p = (4\pi N e^2/m)^{1/2}$  is the free-electron plasma frequency, and  $\tau = 1/\Gamma$  is a relaxation due to the ordinary scattering responsible for electrical resistivity.

The Drude model provides a good fit for the optical properties of metals at energies below those of any interband transition. The experimentally derived dielectric function may be fitted to equations (4a) and (4b) where  $m$  is now replaced by an effective mass,  $m^*$ , and  $m^*$  and  $\tau$  are used as adjustable curve-fitting parameters. Once this is done, the Drude dielectric function may be subtracted from the total dielectric function throughout the spectrum to yield the interband contribution.

One would expect that at energies where the photon energy is greater than the width of the actual bands in a solid, the Drude model could not be used. However, it should be remembered that the Drude model is simply a classical approximation and that the values found for  $m^*$  and  $\tau$  are measures of the fitness of that approximation at the Fermi level.

### 3. Interband Transitions

Points in  $k$ -space for which (2) applies are van Hove singularities. These critical points form the dominant contribution to the interband part of the dielectric function. There are four types of critical points which are labelled as  $M_s$  critical points, with  $s = 0, 1, 2, 3$  for the number of negative values of the effective masses associated with the band curvatures at these points. The lineshapes of the four types of critical points determined by the joint density of states,  $J_{cv}$ , without broadening are summarized in Table 1.

Table 1  
 $J_{cv}$  for critical points

critical point	$J_{cv}$	
	$E < \hbar\omega_g$	$E > \hbar\omega_g$
$M_0$	0	$C_0(E - \hbar\omega_g)^{1/2}$
$M_1$	$C_1 - C_2'(\hbar\omega_g - E)^{1/2}$	$C_1$
$M_2$	$C_2$	$C_2 - C_2'(E - \hbar\omega_g)^{1/2}$
$M_3$	$C_3(\hbar\omega_g - E)^{1/2}$	0

The effects of phonon broadening may be included in the dielectric function by introducing a phenomenological broadening parameter,  $\eta$ . A dielectric function which includes broadening near an  $M_0$  critical point can be defined by [16, 17]

$$\epsilon - 1 \sim (\omega + i\eta)^{-2} [2\omega_g^{1/2} + (\omega_g - \omega - i\eta)^{1/2} + (\omega_g + \omega + i\eta)^{1/2}]. \quad (5)$$

When derivative spectroscopy is being done, the derivatives of  $\epsilon$  need to be considered. If the broadening parameter,  $\eta$ , is small ( $\omega \ll \omega_g$ ), the main contribution to the derivative of (5) is due to the  $(\omega_g - \omega - i\eta)^{1/2}$  term. This term is singular in the limit  $\eta \rightarrow 0$  while the other terms are well behaved. Using an  $M_0$  critical point as an example, and defining a reduced frequency  $W = (\omega - \omega_g)/\eta$ , we obtained [18, 19]

$$\begin{aligned} \frac{d\epsilon_1}{d\omega} &\sim \text{Re} \left[ \frac{1}{2} (\omega + i\eta)^{-2} (\omega_g - \omega - i\eta)^{-1/2} \right] \\ &= \frac{1}{2} \eta^{-1/2} [W^2 + 1]^{-1/2} [(W^2 + 1)^{1/2} - W]^{1/2} \\ &= \frac{1}{2} \eta^{-1/2} F(-W), \end{aligned} \quad (6a)$$

$$\begin{aligned} \frac{d\epsilon_2}{d\omega} &\sim \text{Im} \left[ \frac{1}{2} (\omega + i\eta)^{-2} (\omega_g - \omega - i\eta)^{-1/2} \right] \\ &= \frac{1}{2} \eta^{-1/2} [W^2 + 1]^{-1/2} [(W^2 + 1)^{1/2} + W]^{1/2} \\ &= \frac{1}{2} \eta^{-1/2} F(W). \end{aligned} \quad (6b)$$

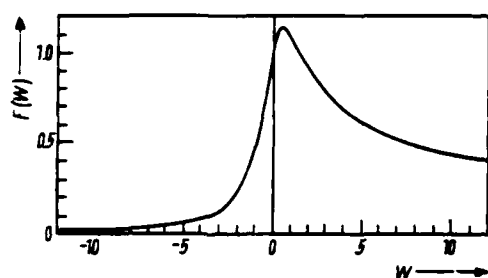


Fig. 1. Universal function derived by Batz [18]. The function  $F(W) = (W^2 + 1)^{-1/2} \times [(W^2 + 1)^{1/2} + W]^{1/2}$ , where  $W$  is a normalized frequency.  $\eta^{-1/2}F(W)$  becomes  $(\omega - \omega_g)^{1/2}$  in the limit  $\eta \rightarrow 0$ .  $W = (\omega - \omega_g)/\eta$

The universal function  $F(W)$  was derived by Batz [18] and is illustrated in Fig. 1. It is found that the derivative spectra around other types of critical points can also be expressed in terms of this function. The results are summarized in Table 2. The function  $\eta^{-1/2} F(W)$  goes to  $(\omega - \omega_g)^{-1/2}$  in the limit  $\eta \rightarrow 0$ , as expected.

Table 2

Derivatives of critical points with broadening included in terms of  $F(W)$

critical point	$2\eta^{1/2} \frac{d\epsilon_1}{d\omega}$	$2\eta^{1/2} \frac{d\epsilon_2}{d\omega}$
$M_0$	$F(-W)$	$F(W)$
$M_1$	$-F(W)$	$F(-W)$
$M_2$	$-F(-W)$	$-F(W)$
$M_3$	$F(W)$	$-F(-W)$

#### 4. Separation of Bound- and Free-Electron Contributions

When experimental data exist for energies less than any interband transition, the Drude forms in (4a) and (4b) may be fit to these low-energy data in order to determine  $m^*$  and  $\tau$ . The spectral range of our wavelength-modulated spectrometer is 1.5 to 5.1 eV. Since many metals and metal alloys have significant interband structure down to the lowest energies of this spectral region, the above method cannot be used. However, when the derivatives of (4a) and (4b) are compared to (6a) and (6b), it is noted that the Drude dielectric function and the interband term at the critical points are sufficiently uncorrelated to justify the method used here to separate them.

The method of separation is the use of  $m^*$  and  $\tau$  as adjustable parameters in writing a trial Drude function, subtract the Drude function from the total dielectric function obtaining a difference function, and calculate the correlation of the Drude and difference functions. The de-correlation function may be written [20] as

$$C_j(m^*, \tau) = \frac{(\text{cov}[B_j, A_j - B_j])^2}{V[B_j] V[A_j - B_j]}, \quad (7a)$$

where

$$\text{cov}[B_j, A_j - B_j] = \frac{1}{N} \sum_i (B_{ij} - \bar{B}_j) [(A_{ij} - B_{ij}) - (\bar{A}_j - \bar{B}_j)], \quad (7b)$$

$$V[B_j] = \frac{1}{N} \sum_i (B_{ij} - \bar{B}_j)^2. \quad (7c)$$

The function  $A$  is the derivative of the experimental dielectric function, and  $B$  is the derivative of the trial Drude function. The sums are over data points,  $N$ , the subscript  $j = 1$  or  $2$  for the real or imaginary parts, and the bars indicate averages over all points.  $\text{cov}(B_j, A_j - B_j)$  is the covariance of  $B_j$  and  $A_j - B_j$ .  $V[B_j]$  is the variance of  $B_j$ .

A computer program has been written which, for a given  $\tau$ , finds the value of  $m^*$  which best minimizes (7a) [19]. This produces two curves  $m^*(\tau)$ , one for  $j = 1$  and another for  $j = 2$ . Then these two curves are plotted together; their intersection gives the physical values of  $m^*$  and  $\tau$ . These are the correct values of the Drude parameters since they are the ones which simultaneously minimize the de-correlation function for both the real and imaginary part. In each de-correlation function alone there is only one independent variable, which has been chosen to be  $\tau$ . When  $\tau$  is fixed, there will always be some value of  $m^*$  which best minimizes  $C_i(m^*, \tau)$ . When values of  $m^*$  and  $\tau$  are found which minimize both  $C_1$  and  $C_2$ , we have confidence that we have found the correct physical values. Once  $m^*$  and  $\tau$  are determined the Drude part of  $\epsilon$  is subtracted leaving the interband part.

To test the method, a trial function was formed. It was the sum of Drude and interband contributions in the range from 1.5 to 5.1 eV. The Drude term was given an effective mass of 1.4 electron rest masses and a relaxation time of  $1.2 \times 10^{-14}$  s. These values are within the normal range found in typical metals. The interband part had an  $M_0$  critical point at 2.5 eV and an  $M_2$  critical point at 4.0 eV. The two parts were cal-

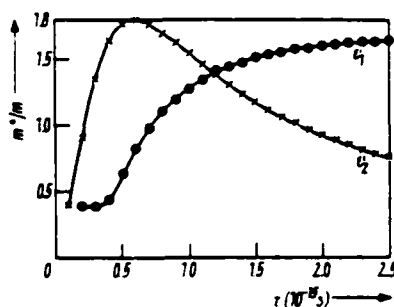


Fig. 2

Fig. 2. Results of de-correlation functions for the test functions described in the text. A function,  $m^*(\tau)$ , is generated for each de-correlation function,  $C_1$  and  $C_2$ .  $m^*(\tau)$  is the value of the effective mass which best minimizes  $C_1$  or  $C_2$  for a given value of the relaxation time,  $\tau$ . One curve is generated by using  $\epsilon_1$  in (7a) to (7c) and the other curve is from  $\epsilon_2$ . The point where the curves cross represents the correct physical value of  $m^*$  and  $\tau$ . Test function:  $m^*/m = 1.39$ ,  $\tau = 1.19 \times 10^{-14}$  s

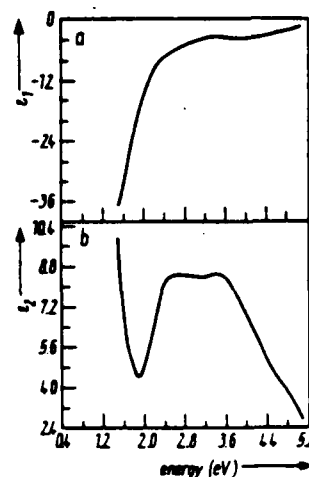


Fig. 3

Fig. 3. Dielectric function of  $\beta'$ -AuZn which was used to test the de-correlation technique. a) Real part,  $\epsilon_1$ ; b) imaginary part,  $\epsilon_2$ . The derivatives of these were used to find the Drude parameters

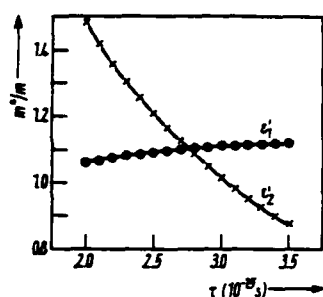


Fig. 4

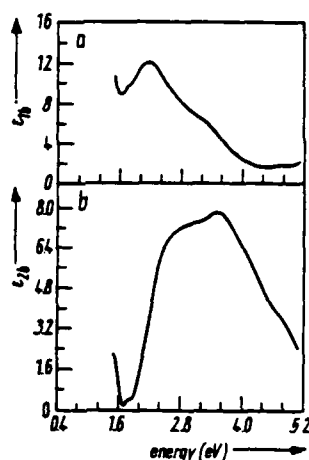


Fig. 5

Fig. 4. Results of the de-correlation functions for  $\beta'$ -AuZn. The point where the curves cross is at  $m^*/m = 1.10$  electron masses and  $\tau = 2.76 \times 10^{-13}$  s.

Fig. 5. Interband contribution to the dielectric function of  $\beta'$ -AuZn. The Drude parameters found in Fig. 4 were used in (4a) and (4b), which was then subtracted from the experimental dielectric function of Fig. 3.

culated using (4a) and (4b) and Table 2. The curves for the solution of the test function are shown in Fig. 2. The values found at the intersection of the curves were  $m^* = 1.39$  electron masses and  $\tau = 1.19 \times 10^{-13}$  s.

Fig. 3 shows  $\epsilon_1$  and  $\epsilon_2$  for  $\beta'$ -AuZn obtained by integrating wavelength modulation data. The graph of the correlation minima is given in Fig. 4. The values at the intersection of the curves are  $m^* = 1.10$  electron masses and  $\tau = 2.76 \times 10^{-13}$  s. The value for  $m^*$  is slightly lower than previously reported [21]. Fig. 5 shows the bound parts of  $\epsilon_1$  and  $\epsilon_2$  ( $\epsilon_{1b}$  and  $\epsilon_{2b}$ ) after the Drude terms are subtracted.

This separation technique has two shortcomings. The first is that the Drude relaxation time is not actually a constant over the entire spectrum. The value obtained is assumed to be an average value over the spectral range. However, this problem also occurs when extrapolations from low-energy data are used. The advantage in this calculation is that here the values are from the visible-ultraviolet part of the spectrum which is actually under study. Secondly, there is a small  $\omega^{-2}$ -contribution to the bound parts of the dielectric function. However, if the linewidths of the interband transitions are small compared to the transition energies, these terms may be neglected [18, 22]. Such terms may cause a small error in the Drude parameters, but will not cause any change in the general lineshapes of the interband contributions to the dielectric function, which are the important results for band structure determinations.

### References

- [1] B. BATZ, Solid State Commun. 4, 241 (1965).
- [2] C. N. BERGLUND, J. appl. Phys. 37, 3019 (1966).
- [3] B. O. SERAPHIN and R. B. HESS, Phys. Rev. Letters 14, 138 (1965).
- [4] M. CARDONA, K. L. SHARLEE, and F. H. POLLACK, Phys. Rev. 154, 696 (1967).

- [5] W. E. ENGELIS, H. FRITZSCHE, M. GARFINKEL, and J. J. TEIMANN, *Phys. Rev. Letters* 14, 1069 (1965).
- [6] G. W. GOBELI and E. O. KANE, *Phys. Rev. Letters* 15, 142 (1965).
- [7] I. BALSLEV, *Phys. Rev.* 143, 636 (1965).
- [8] G. BONFIGLIOLI and P. BROVETTO, *Appl. Optics* 3, 1417 (1964).
- [9] R. E. DREWS, *Bull. Amer. Phys. Soc.* 12, 384 (1967).
- [10] M. WELKOWSKY and R. BRAUNSTEIN, *Rev. sci. Instrum.* 43, 399 (1972).
- [11] M. WELKOWSKY, Ph. D. Thesis, Univ. California, Los Angeles 1971.
- [12] L. VAN HOVE, *Phys. Rev.* 89, 1189 (1953).
- [13] J. MATHEWS and R. L. WALKER, *Mathematical Methods of Physics*, W. A. Benjamin, Inc., New York 1970.
- [14] H. A. LORENTZ, *The Theory of Electrons*, Dover Publ., Inc., New York 1952.
- [15] P. K. L. DRUDE, *Theory of Optics*, Dover, Publ., Inc., New York 1959.
- [16] B. BATZ, *Solid State Commun.* 5, 985 (1967).
- [17] O. H. F. VREEHEN, *Phys. Rev.* 145, 675 (1966).
- [18] B. BATZ, Ph. D. Thesis, Univ. Libre de Bruxelles, 1967.
- [19] R. STRAENS, Ph. D. Thesis, Univ. California, Los Angeles 1982.
- [20] K. A. BROWNLEE, *Statistical Theory and Methodology in Science and Engineering*, John Wiley & Sons, New York 1960.
- [21] J. P. JAN and S. S. VISHNUBHATLA, *Canad. J. Phys.* 45, 2505 (1967).
- [22] M. CARDONA, *Modulation Spectroscopy*, Academic Press, New York 1969.

(Received December 8, 1982)

# Fully electronic servocircuitry for wavelength-modulation spectroscopy

R. Stearns,<sup>a)</sup> J. Steele,<sup>b)</sup> and R. Braunstein

*Department of Physics, University of California, Los Angeles, California 90024*

(Received 3 February 1983; accepted for publication 20 April 1983)

Electronic circuits have been developed to replace the mechanical servos and lock-in amplifiers customarily used in a wavelength-modulated derivative spectrometer. The result is a faster response and wider range of gain while maintaining a constant photomultiplier-tube voltage.

PACS numbers: 84.30.Wp, 06.70.Td

## INTRODUCTION

The identification of Van Hove Singularities<sup>1</sup> in optical absorption or reflection spectra can be difficult, since singularities are usually superimposed on a broad structureless background. In the case of metals, this background is the Drude intraband spectrum, and interband singularities can be small compared to this background. This problem is especially acute in the case of three dimensions as Van Hove singularities do not produce infinite peaks, but only changes in the slope of the optical properties. Broadening mechanisms reduce the optical structure in all cases.

The optical structure associated with critical points can be greatly enhanced by the use of derivative, or modulation, spectroscopic methods. The dielectric function near a three-dimensional critical point may be written as<sup>1-4</sup>

$$\epsilon(\omega) = b(\omega - \omega_s)^{1/2} + \text{constant}, \quad (1)$$

$\hbar\omega$  is the photon energy and  $\hbar\omega_s$  is the transition energy at the critical point. The constant in Eq. (1) represents the background contribution, which may be larger than the singular part. Thus, observation of the critical structure may be lost in the background. Therefore, it would be most advantageous to measure, not  $\epsilon$  directly, but the derivative of  $\epsilon$  with respect to some parameter  $x$ . Since the background does not vary rapidly, it would essentially be eliminated from the spectrum. This leads to

$$\frac{d\epsilon}{dx} = \frac{b}{2}(\omega - \omega_s)^{-1/2} \frac{d(\omega - \omega_s)}{dx} + \frac{db}{dx}(\omega - \omega_s)^{1/2}. \quad (2)$$

The first term in Eq. (2) diverges at the critical point  $\omega = \omega_s$  and is, therefore, easily detectable in a derivative spectrum. The second term in Eq. (2) is generally negligible near  $\omega = \omega_s$  since  $b$  can vary slowly. There are two obvious possibilities for the differentiation parameter  $x$ . The first is the energy of the incident radiation  $\hbar\omega$  and the second is the critical point transition energy  $\hbar\omega_s$ .

Techniques which modulate the energy critical point transition avoid experimental complications which will be found in frequency (wavelength) modulation experiments, but have the analytical problem of ambiguous interpretation of line shapes. Possible parameters which modulate the energy gap include hydrostatic pressure and uniaxial stress,<sup>5,6</sup> electric field,<sup>7,8</sup> and temperature<sup>9,10</sup> modulation. The ambiguity of these methods can be seen when Eq. (2) is reduced to

$$\frac{d\epsilon}{dx} \propto (\omega - \omega_s)^{-1/2} \frac{d\omega_s}{dx}. \quad (3)$$

Detailed analysis of the lineshapes of Van Hove singularities is not possible unless one already has knowledge of the contribution from  $d\omega_s/dx$ . Thus, the theory of internal modulation experiments depends not only on the theory of the optical properties, but also on the effect of the perturbation parameter  $x$  on those optical properties.

When a frequency-modulated light beam<sup>11-14</sup> is used, Eq. (2) reduces to

$$\frac{d\epsilon}{d\omega} = \frac{b}{2}(\omega - \omega_s)^{-1/2}. \quad (4)$$

Thus, there are no theoretical ambiguities in the interpretation of data. If the dependence of the frequency of the modulated beam is

$$\omega = \omega_0 + (\Delta\omega) \cos \Omega t, \quad (5)$$

where  $\Delta\omega$  is the depth of modulation and  $\Omega$  is the modulation frequency, then we have

$$\epsilon = \epsilon(\omega_0) + \Delta\epsilon \cos \Omega t. \quad (6)$$

If  $\Delta\epsilon$  is measured, the derivative of the dielectric function may be found from

$$\frac{d\epsilon}{d\omega} = \lim_{\Delta\omega \rightarrow 0} \frac{\Delta\epsilon}{\Delta\omega}. \quad (7)$$

However,  $\Delta\epsilon$  is generally not measured directly. Instead, the modulation of the reflectivity  $\Delta R$  or the transmission  $\Delta T$  is measured. Great accuracy and sensitivity can be achieved in the measurement of  $\Delta R$  or  $\Delta T$  by means of phase sensitive detection with a lock-in amplifier.

A double-beam, single-detector optical system with its associated electronics for obtaining wavelength-modulated derivative spectra was previously reported.<sup>14</sup> This system eliminated problems due to background derivative structure caused by source, detectors, optics, and atmospheric absorption. We now report electronic circuitry which has been designed to replace the system of mechanical servos and lock-in amplifiers which is normally used.<sup>14</sup> This new system has the advantage of faster response times and wider ranges of gains while maintaining a constant voltage to the photomultiplier tube.

## I. WAVELENGTH MODULATION

Wavelength-modulation derivative spectroscopy has experimental difficulties, which may be overcome, compared to other types of modulation as may be seen in the following.

In conventional reflection measurements, the total sig-

nal  $I$  reflected from the sample is

$$I(\lambda) = R(\lambda) I_0(\lambda), \quad (8)$$

where  $R$  is the reflectivity and  $I_0$  is the signal incident on the sample. The wavelength derivative of Eq. (8), which is denoted by prime, is

$$I' = R'I_0 + RI'_0. \quad (9)$$

The second term in Eq. (9) is what causes the difficulty in wavelength modulation experiments with respect to other modulation techniques. In other methods, where only sample is modulated, this term is zero. However, when the wavelength is modulated, this term contains the derivative of the incident beam, which includes wavelength-dependent information about the light source, optical path, atmospheric absorption, and detector response.  $RI'_0$  is, more often than not, on the same order as  $R'I_0$  and, as is the case of a light source with sharp line structure, may be orders of magnitude larger than  $R'I_0$ . A means of subtracting this contribution to the total derivative signal is essential if meaningful wavelength modulation data are to be obtained.

If Eq. (9) is divided by Eq. (8) and the terms are rearranged, we get

$$\frac{R'}{R} = \frac{I'}{I} - \frac{I'_0}{I_0}. \quad (10)$$

This is the quantity which we wish to extract from the experiment. We choose to keep the signal level in each term equal, so that the subtraction may be easily done electronically. Rearranging Eq. (10), we now have

$$\frac{R'}{R} = \frac{1}{I} (I' - kI'_0), \quad (11)$$

where  $k = I/I_0$ . A qualitative description of how  $R'/R$  is determined will be given first, and then the new electronic system will be described.

The double-beam optical system is shown in Fig. 1. The signal from a Perkin-Elmer 99G monochromator<sup>15</sup> is modulated at 217 Hz by a vibrating mirror.<sup>14,16</sup> The signal reflected from the sample when the chopping mirror, which rotates at 13 Hz, does not block the beam will be called the sample channel. The signal reflected from the chopping mirror during the other half cycle will be called the background

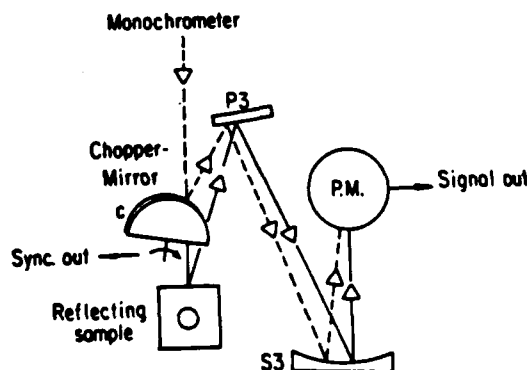


FIG. 1. Double-beam signal detector optical system. Light from the Perkin-Elmer 99G monochromator is modulated at 217 Hz. The chopper C rotates at 13 Hz.

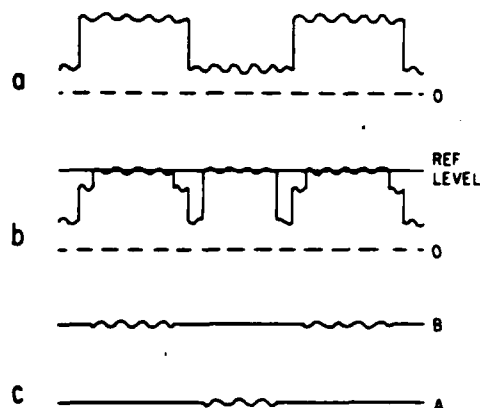


FIG. 2. Wavelength-modulation waveforms: (a) Chopper cycle of the raw signal from the photomultiplier. The higher level is the background channel; the lower level is the sample channel. (b) The raw signals have been gated and servoed to a predetermined reference level. (c) The servoed and gated signals have been separated into their own output channels and ac coupled to eliminate the 13-Hz component.

channel. Figure 2 shows how we would like to process the signal. Figure 2(a) is the raw signal from the photomultiplier tube. The higher level is  $I_0$  and the lower level is  $I$ , because the aluminum chopping mirror will be more reflective than the sample. In Fig. 2(b) we have gated a portion of each channel and amplified it to a reference level, which will be kept constant. Thus we have brought the signal channel to a constant level which is our new level for  $I$  and also made  $I_0$  equal to  $I$ . The constant  $k$  in Eq. (11) now represents the fact that different gains are needed in the sample and background channels to bring them to the reference level. The 217-Hz components in the sample and reference channels are now proportional to  $kI'_0$  and  $I'$  and are shown by signals B and A, respectively, in Fig. 2(c). We can now run these to a differential lock-in amplifier, and the difference between the two signals will now be proportional to  $I' - kI'_0$ .

This new electronic circuit is designed to make the source to output gain at the 13-Hz chopping frequency the same for both the sample and background channels. The differential derivative and logical circuits are shown in Figs. 3 and 4, respectively. The current output of the photomultiplier

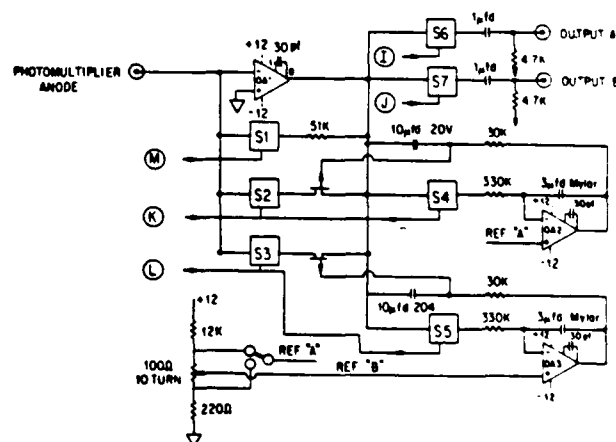


FIG. 3. Differential derivative circuitry. Signals K, L, and M are from the logic circuit (Fig. 4).





one-half of the rotation time of the mirror, 38.5 ms. It is used to determine which channel, sample or background, is being gated at any particular time. When one-shot B ends its period it starts one-shot C. One-shot C starts one-shot D and is also used to center the sample and background periods in their respective time windows. This sequence then provides the delay signal for timing the starts of the gates. One-shot D sets flip flop F, which controls the feedback network sampling time, that is, the width of the gates. D also starts one-shot E. The starting of one-shot E sets flip flop G, which is used to start the gate time of the output circuits.

When the signal from flip flop F is added to signals B and B inverse, signals K and L are formed. These are the actual gating signals which control the active feedback networks. The signal from flip flop G, when added to B and B inverse, forms signals I and J, which control the output switches. Signal M controls the impedance of the amplifier during the transition of the chopper between sample and background. It is the complement of F from the same flip flop.

All of the logic was implemented in CMOS, using CD4047's for the one shots and 74C74's for the flip flops. NAND gates are 74C00's and inverters are 74C04's.

The output signals are sent to a PAR Model 124 A Lock-In Amplifier with a PAR Model 116 Differential Preamplifier.<sup>19</sup> The sample and background signals are differentially amplified, with the 124A in the high dynamic range with a  $Q$  of 1.

The differential derivative circuit was constructed with conventional point-to-point wiring in a double NIM module. All power is obtained from the NIM bin. For convenience in checking and calibrating the unit, a 217-Hz reference oscillator was constructed in the same module.

## II. SYSTEM SENSITIVITY

The critical test of the system is its ability to eliminate signals which are due to sharp structure in the source. Figure 6 shows the structure from the line at 4193 Å in the spectrum

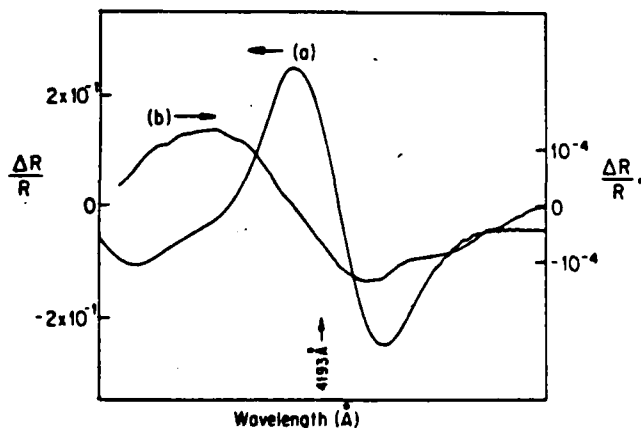


FIG. 6. Comparison of balanced (b) and unbalanced (a) scans of the Xe line at 4193 Å. Note the scale changes between the two curves. The wavelength scale extends 100 Å on either side of the 4193 Å line.

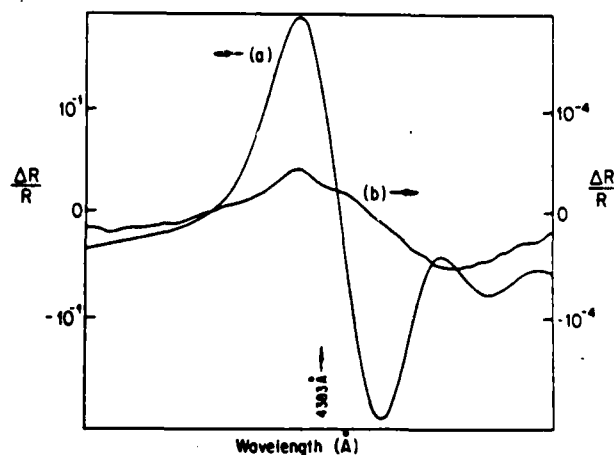


FIG. 7. Comparison of balanced (b) and unbalanced (a) scans of the Xe line at 4383 Å. Note the scale change between the two curves. The wavelength scale extends to approximately 100 Å on either side of the 4383 Å line.

of a 150-W Hanovia Xenon arc lamp which is the source for the violet and ultraviolet regions. The figure shows the results for both the modulated signal (a) which has not been processed by the differential derivative circuitry and also the signal (b) when this spectra line has been balanced by the system. Note that the balancing by the system reduces the signal by three orders of magnitude. The signal level of the balanced line of Fig. 6 represents a maximum sensitivity of  $\Delta R/R = 1.3 \times 10^{-4}$ ; this is the worst case result. In practice, sensitivities of better than  $10^{-4}$  and down to  $10^{-5}$  are routinely obtained in regions of the spectrum without sharp lines in the source. Figure 7 shows the structure at 4383 Å in the same source spectrum. Here the improvement is much better than three orders of magnitude with the best  $\Delta R/R$  being  $9 \times 10^{-5}$ .

## ACKNOWLEDGMENTS

The authors would like to extend their thanks to Ed Carmody of the UCLA Physics Department Electronics Shop for his valuable assistance in the building and maintenance of the differential derivative circuitry system.

Work supported in part by the U.S. Army Research Office—DAAG-29-K-0164; the Air Force Office of Scientific Research—78-3665; and the California-MICRO Program.

<sup>19</sup> Current address: TRW Technology Research Center, El Segundo, CA 90245.

<sup>20</sup> Current address: Litton Industries, Woodland Hills, CA 91304.

<sup>1</sup> L. Van Hove, *Phys. Rev.* **89**, 1189 (1953).

<sup>2</sup> M. Carodona, *Modulation Spectroscopy* (Academic, New York, 1969).

<sup>3</sup> B. Batz, Ph.D. thesis, Université Libre de Bruxelles, 1967.

<sup>4</sup> F. Wooten, *Optical Properties of Solids* (Academic, New York, 1972).

<sup>5</sup> W. E. Engeles, H. Fritzache, M. Garfinkel, and J. J. Tiemann, *Phys. Rev. Lett.* **14**, 1069 (1965).

<sup>6</sup> G. W. Gobeli and E. O. Kane, *Phys. Rev. Lett.* **15**, 142 (1965).

<sup>7</sup> B. O. Seraphin and R. B. Hess, *Phys. Rev. Lett.* **14**, 138 (1965).

<sup>8</sup> M. Cardona, K. L. Shaklee, and F. H. Pollak, *Phys. Rev.* **154**, 696 (1967).

<sup>9</sup>B. Batz, Solid State Commun. 4, 241 (1965).

<sup>10</sup>C. N. Berglund, J. Appl. Phys. 37, 301 (1966).

<sup>11</sup>I. Bahalev, Phys. Rev. 143, 636 (1966).

<sup>12</sup>G. Bonfiglioli and P. Brovetti, Appl. Opt. 3, 1417 (1964).

<sup>13</sup>R. E. Drewa, Bull. Am. Phys. Soc. 12, 384 (1967).

<sup>14</sup>M. Welkowsky and R. Braunstein, Rev. Sci. Instrum. 43, 399 (1972).

<sup>15</sup>Perkin-Elmer Corp., Costa Mesa, CA 92626.

<sup>16</sup>M. Welkowsky, Ph.D. thesis, University of California at Los Angeles, 1971.

<sup>17</sup>National Semiconductor Ltd., Plattsburgh, NY 12901.

<sup>18</sup>RCA Electronic Components, Harrison, NJ 07029.

<sup>19</sup>EG & G Princeton Applied Research, Princeton, NJ 08540.

phys. stat. sol. (b) 181, 659 (1983)

Subject classification: 13.1 and 20.1; 21.1; 21.6

Department of Physics, University of California, Los Angeles<sup>1)</sup>Wavelength Modulated Spectra of  $\alpha$ -Ag<sub>0.7</sub>Zn<sub>0.3</sub> near the Optical Absorption Edge <sup>2)</sup>

By

R. STEARNS<sup>3)</sup>, R. BRAUNSTEIN, and L. MULDAWER<sup>4)</sup>

Dedicated to Prof. Dr. Dr. h. c. Dr. E. h. P. GÖBLICH on the occasion of his 80th birthday

The optical properties of  $\alpha$ -phase Ag<sub>0.7</sub>Zn<sub>0.3</sub> are determined near the optical absorption edge. This alloy composition dampens the sharp Ag-plasma resonance. The band shifts which are observed are in qualitative agreement with calculations which are performed for the similar alloy,  $\alpha$ -Cu<sub>0.7</sub>Zn<sub>0.3</sub>.

Die optischen Eigenschaften der  $\alpha$ -Phase von Ag<sub>0.7</sub>Zn<sub>0.3</sub> werden in der Nähe der optischen Absorptionakante bestimmt. Diese Legierungszusammensetzung dämpft die scharfe Ag-Plasma-Resonanz. Die beobachteten Bandverschiebungen sind in qualitativer Übereinstimmung mit Berechnungen, die für die ähnliche Legierung  $\alpha$ -Cu<sub>0.7</sub>Zn<sub>0.3</sub> durchgeführt wurden.

## 1. Introduction

An outstanding feature of the optical properties of Ag is the sharp onset of interband transitions near 4.0 eV in the near ultraviolet, a feature which is very near the plasma resonance. This interband absorption edge is due to the overlap of contributions from d-band to Fermi level transitions and Fermi level to conduction band transitions, both in the L (111) direction in the Brillouin zone [1 to 3]. Optical results tend to support this interpretation [4 to 8], although it has been questioned by Christensen [9].

Near the absorption edge, the optical spectrum of Ag should be sensitive to alloying. Since the transitions which are involved in the absorption edge involve free electrons at either the initial or final state, alloying with Zn should shift the Fermi surface enough to

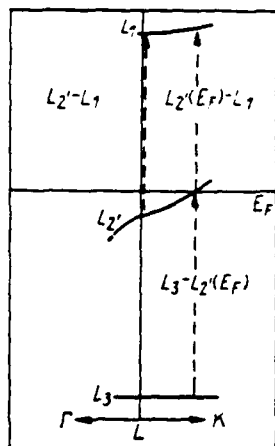


Fig. 1. Energy bands near the L point in pure Ag [6]

<sup>1)</sup> Los Angeles, California 90024, USA.<sup>2)</sup> Work supported in part by the U.S. Army Research Office, Durham, North Carolina, and by the Air Force Office of Scientific Research.<sup>3)</sup> Current address: Newport Corporation, Fountain Valley, CA 92708, USA.<sup>4)</sup> Permanent address: Temple University, Philadelphia, PA 19122, USA.

separate the two transitions. In noble metals, the  $L_1$  (s-like) level is more sensitive to the crystalline potential than the  $L_2$  (p-like) or the  $L_3$  (d-like) levels [6]. (These levels are illustrated in Fig. 1.) Therefore, perturbation of the potential by alloying should result in a separation of the two transitions. The experimental results presented here do show a separation of the transition energies. As expected, the separation appears to be due to a downward shift of the  $L_1$  level with respect to the Fermi level.

## 2. Sample Preparation

Precisely weighed amounts of 0.9999 pure Ag and 0.99999 pure Zn were sealed in quartz tubes at a pressure of less than  $10^{-4}$  mm Hg. They were melted and thoroughly mixed by being shaken in the liquid states 5000 times and then quenched to room temperature in a water bath to form a homogeneous ingot. This ingot was, in turn, homogenized by heating to 650 °C for 24 hours and then cooling slowly. After cutting and polishing, the sample was given another 24 hour anneal, this time at 225 °C, and then again slow cooled. This was to relieve cold work acquired in the polishing process.

Leavings from the cutting process were assayed for Ag content by the U.S. Mint, which confirmed that the final composition was within 0.1% of  $\text{Ag}_{0.7}\text{Zn}_{0.3}$ .

## 3. Experimental Method

Wavelength-modulated spectroscopy [10, 11] was used because of the unambiguous lineshapes obtained by this technique and the resulting ease of interpretation of these lineshapes. The theory of wavelength-modulation spectroscopy is well detailed elsewhere [12, 13]. The theory of lineshapes near a three-dimensional critical point was given by Batz [14, 15]. It is sufficient here to give the theoretical lineshapes for the sake of reference. All three dimensional critical point lineshapes may be expressed

Table 1

Derivative of critical points with broadening included in terms of  $F(W)$   
 $F(W) = (W^2 + 1)^{1/2} + W^{1/2} / (W^2 + 1)^{1/2}$ ,  $W = (\omega - \omega_g)/\eta$

critical point	$2\eta^{1/2} \frac{d\epsilon_1}{d\omega}$	$2\eta^{1/2} \frac{d\epsilon_2}{d\omega}$
$M_0$	$F(-W)$	$F(W)$
$M_1$	$-F(W)$	$F(-W)$
$M_2$	$-F(-W)$	$-F(W)$
$M_3$	$F(W)$	$-F(-W)$

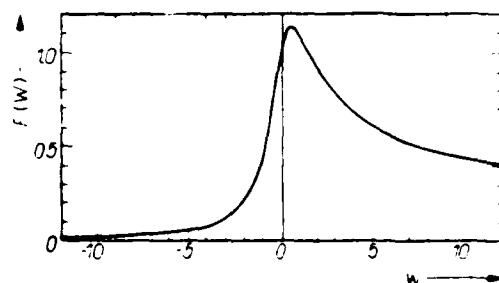


Fig. 2. Universal function,  $F(W)$ , derived by Batz [14, 15] for lineshapes near critical points as seen in wavelength modulation spectroscopy.  $F(W) = [W^2 - 1]^{-1/2} \times [(W^2 + 1)^{1/2} + W]^{1/2}$ , where  $W$  is the reduced frequency  $\omega - \omega_g/\eta$ .  $\hbar\omega_g$  is the interband energy (a the critical point and  $\eta$  is a phenomenological broadening parameter

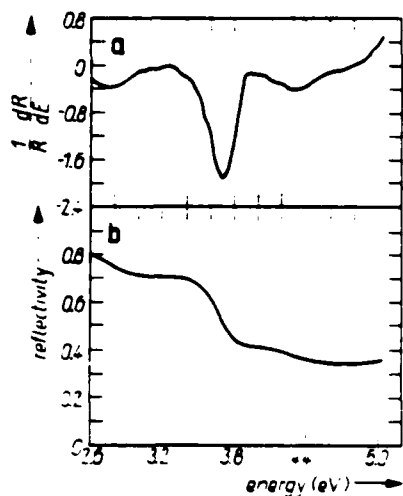


Fig. 3. a) Wavelength-modulated logarithmic derivative of the reflectivity of  $\alpha\text{-Ag}_{0.7}\text{Zn}_{0.3}$ . b) Reflectivity of  $\alpha\text{-Ag}_{0.7}\text{Zn}_{0.3}$ , found by integrating the data from Fig. 3a

in terms of a single function,  $F(W)$ , which is reproduced in Fig. 2. The behavior of critical points in terms of  $F(W)$  is listed in Table 1. Derivative data with a spacing of 0.02 eV between data points were taken between 2.60 and 5.10 eV.

#### 4. Experimental Results

The wavelength-modulated logarithmic derivative spectrum of the reflectivity, which is the direct result of the experiment, is displayed in Fig. 3a. This is integrated to give the reflectivity of the sample, as shown in Fig. 3b. In order to perform a Kramers-

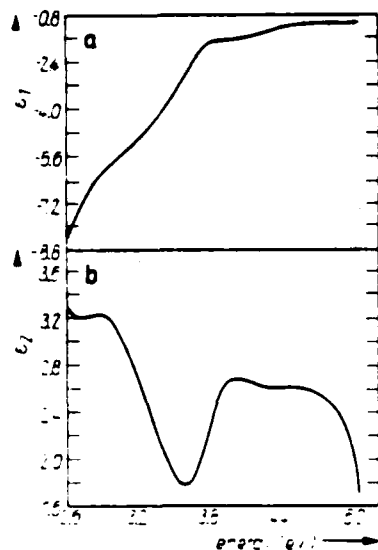


Fig. 4

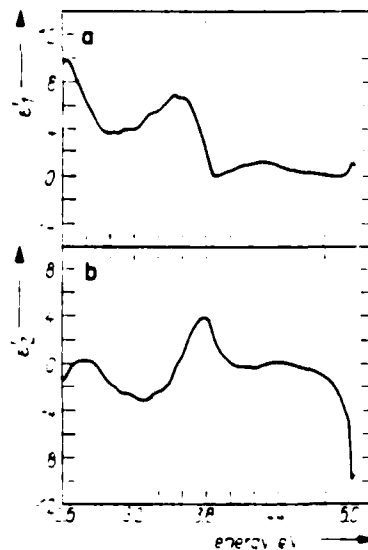
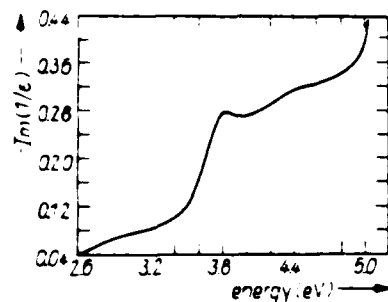


Fig. 5

Fig. 4. Dielectric function of  $\alpha\text{-Ag}_{0.7}\text{Zn}_{0.3}$  determined by a Kramers-Kronig analysis of the reflectivity data. a) Real part,  $\epsilon_1$ ; b) imaginary part,  $\epsilon_2$

Fig. 5. Derivative with respect to energy of the dielectric function of  $\alpha\text{-Ag}_{0.7}\text{Zn}_{0.3}$ . a) Real part,  $\epsilon_1'$ ; b) imaginary part,  $\epsilon_2'$

Fig. 6. Energy loss function of  $x\text{-Ag}_{0.7}\text{Zn}_{0.3}$ 

Kronig analysis of the data and separate the real and imaginary parts of the dielectric function, extrapolations over all energy must be done. For the infrared region, a Hagen-Rubens extrapolation to a reflectivity of 100% at zero energy was used [16]. For the ultraviolet extrapolation, modified silver data [17] were used. Using this, the real and imaginary parts of the dielectric function,  $\epsilon_1$  and  $\epsilon_2$ , are calculated. These are given in Fig. 4a and b. The dielectric function is then differentiated to give  $\epsilon_1'$  and  $\epsilon_2'$  (Fig. 5).

The important point to note concerning the data is that the plasma resonance which dominates the experimental spectrum of Ag [17] is greatly damped in this alloy, as may be seen from the fact that  $\epsilon_1$  does not go through zero at any point in the experimental energy range, and from the strongly damped peak in the energy loss function at 3.85 eV (Fig. 6). The  $\epsilon_1$  shown in Fig. 4 is in excellent agreement with that of previous results [5]. Note also that the principal dip in the reflectivity is at a considerably lower energy than in pure Ag. This occurs between about 3.6 and 3.8 eV in the alloy, compared with a minimum of about 3.85 eV in pure Ag.

### 5. Free-Electron Effects

The free and bound parts of the dielectric function have been separated by a de-convolution method which has been described elsewhere [18, 19]. The Drude effective mass was found to be 1.23 free electron masses and the Drude relaxation time was found to be  $1.87 \times 10^{-14}$  second. These results compare well with the values found for Ag. Previous results for the effective mass of silver are  $m^*/m = 1.03$  [1] and 0.97 [20]. The relaxation time in Ag was found to be  $1.6 \times 10^{-14}$  s at 3 eV [17].

We thus see that the Drude part of the dielectric function predicts some flattening of the bands at the Fermi level. Although alloying will be seen to have a considerable damping effect on the interband properties of Ag, the long relaxation time found here indicates that the behavior of free electrons is not significantly changed. We may conclude that this amount of alloying has only small consequences for those electronic properties described by the Drude theory.

### 6. Interband Transitions

Once the Drude effective mass and relaxation time are known, they may be used to subtract the intraband contributions to the dielectric function from the total experimental function. The resulting real and imaginary parts of the bound-electron contribution to the dielectric function are shown in Fig. 7. Their derivatives are given in Fig. 8. It is these derivatives of the bound part of the dielectric function which are used to assign interband transitions.

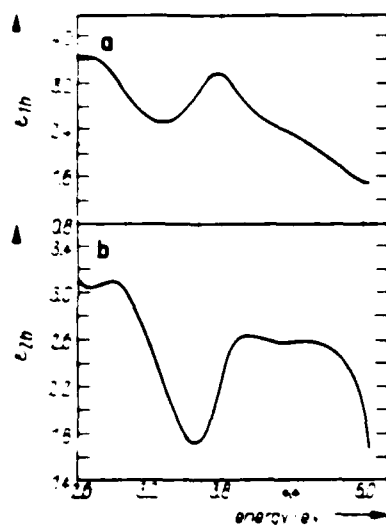


Fig. 7

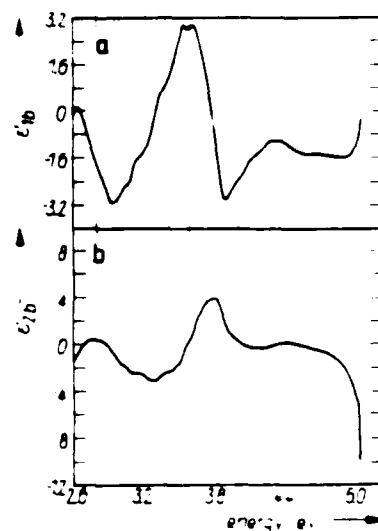


Fig. 8

Fig. 7. Bound part of dielectric function  $\alpha$ -Ag<sub>0.7</sub>Zn<sub>0.3</sub> determined by subtracting the Drude contribution from the data of Fig. 5. a) Real part,  $\epsilon_{1b}$ ; b) imaginary part,  $\epsilon_{2b}$ .

Fig. 8. Derivative with respect to energy of the bound part of the dielectric function of  $\alpha$ -Ag<sub>0.7</sub>Zn<sub>0.3</sub>. a) Real part,  $\epsilon_{1b}'$ ; b) imaginary part,  $\epsilon_{2b}'$ . With reference to the energy bands in Fig. 1, the following transitions are identified:  $L_2(E_F) \rightarrow L_1$  (3.55 eV),  $L_2 \rightarrow L_1$  (3.83 eV),  $L_3 \rightarrow L_2(E_F)$  (4.37 eV).

It is interesting to compare  $\epsilon_{2b}$  of Fig. 7 with the  $\epsilon_2$  results shown in Fig. 9e of [5]. The earlier work shows maxima in  $\epsilon_2$  at 3.1 and 4.9 eV with a minimum at 4.1 eV. The current work has a maximum at 2.8 eV, a minimum at 3.6 eV, and maxima at 4.0 eV, which are resolved here where they were not previously. We thus see that the features found in this study are at lower energies than in [5].

The current literature does not firmly fix the exact value of the Ag interband transitions of interest in this study. While the energy gap for the  $L_2 \rightarrow L_1$  transitions ranges from 3.8 eV [7] to 4.1 eV [5], the values quoted for the  $L_3 \rightarrow L_2(E_F)$  transition range from 4.1 eV [7] to 4.4 eV [5]. Clearly, there is enough discrepancy in the experimental values for these energies that it will be difficult to accurately assess the effects of alloying on them.

No band structure calculation has been reported for  $\alpha$ -Ag<sub>0.7</sub>Zn<sub>0.3</sub> but calculations do exist for  $\alpha$ -Cu<sub>0.7</sub>Zn<sub>0.3</sub> [21, 22]. In the work of Bansil et al. [22], predictions are made for the shifts in the interband transitions of interest due to alloying. The  $L_3 \rightarrow L_2(E_F)$  transition is predicted to move upward by about 0.3 eV and the  $L_2 \rightarrow L_1$  transition is to move downward in energy by 0.1 to 0.8 eV depending on the amount of lattice dilation due to alloying.

Since both transitions would be at saddle points in the Brillouin zone, a dip in  $\epsilon_{1b}$  would be expected near the critical point for each of them [14, 15]. The minimum in  $\epsilon_{1b}$  at 3.88 eV is the expected structure due to  $L_2 \rightarrow L_1$ . The associated structure in  $\epsilon_{2b}$  is the peak at 3.78 eV. This places the critical point at 3.83 eV, coinciding with the peak in the energy loss function. The peak in  $\epsilon_{1b}$  at 3.55 eV is due to the onset of transitions at  $L_2(E_F) \rightarrow L_1$ . We may then conclude that the  $L_2$  critical point lies 0.28 eV below the Fermi level.



Ehrenreich and Philipp [17] assigned the mean  $\epsilon_2$  Ag peak at 4.4 eV to the direct transition from the d-band to the Fermi surface  $L_3 \rightarrow L_2(E_F)$ . The  $L_2$  band is filled at the critical point, so the actual critical point transition structure for the  $L_3 \rightarrow L_2$  transition will not be seen. A break in the derivatives of  $\epsilon_2$  should be seen at the energy where transitions to the Fermi level begin to occur. The  $L_3 \rightarrow L_2(E_F)$  transition will produce a downward break in  $\epsilon_{1b}$  with an associated break in  $\epsilon_{2b}$  at the same energy, which is the energy of the onset of interband transitions. Such breaks are seen at 4.37 eV in Fig. 8. Thus, our data show that there is very little shift of the transition in the  $x\text{-Ag}_0\text{:Zn}_{0.3}$  alloy. This places the  $L_3 \rightarrow L_2$  critical point gap at 4.09 eV when the results from the data for the  $L_2 \rightarrow L_1$  transition are used.

## 7. Discussion

The results of this study indicate that the effects of alloying in the  $\text{Ag}_0\text{:Zn}_{0.3}$  are actually fairly small. The shifts in the interband transitions must be on the lower end of those predicted for the  $x\text{-Cu}_0\text{:Zn}_{0.3}$  system by Bansil et al. [22]. If the  $L_3 \rightarrow L_2(E_F)$  transition with an energy of 4.37 eV has been shifted by  $-0.3$  eV, as might be expected from the  $x\text{-Cu}_0\text{:Zn}_{0.3}$  study, then this transition should have an onset at about 4.1 eV in pure Ag. This value is just within the range of experimental values which have been quoted. However, there is also good evidence that this transition is essentially unshifted from that in pure Ag [5, 17].

The actual shift in  $x\text{-Cu}_0\text{:Zn}_{0.3}$  for the  $L_2 \rightarrow L_1$  transition is about  $-0.2$  eV [23, 24]. Using this value would place the  $L_2 \rightarrow L_1$  transition in pure Ag at 4.0 eV which is about the middle of the experimental values for this transition. Previous work which shows that  $L_3 \rightarrow L_2(E_F)$  is unshifted closely agrees with this assignment for  $L_2 \rightarrow L_1$  in pure Ag [5, 17].

The following may be cited as the important results of this study:

- (i) In this alloy composition,  $\epsilon_1$  is dampened such that the main Ag plasma resonance is greatly reduced.
- (ii) The Drude effective mass predicts a slight flattening of the bands. The fact that the energy difference  $L_3 \rightarrow L_2(E_F)$  is 0.28 eV is not any help in confirming the flattening since values for this difference for Ag are reported to lie between 0.2 and 0.3 eV.
- (iii) The fact that the Drude relaxation time for this alloy is approximately the same for pure Ag indicates that this amount of alloying has not greatly affected the mean free path of conduction electrons.
- (iv) The shifts found in the interband transitions between pure Ag and the alloy indicate that the transition usually more sensitive to perturbation of the crystal potential ( $L_2 \rightarrow L_1$ ) has a shift of about  $-0.2$  eV, while the less sensitive transition ( $L_3 \rightarrow L_2$ ) may be essentially unshifted. This indicates that, at least in this portion of the Brillouin zone, the rigid-band model may be used to describe the interband transitions of this alloy, with only a shift of the s-like ( $L_1$ ) band.

## References

- [1] D. BEAGLEHOLE, Proc. Phys. Soc. London, **85**, 1007 (1965); **87**, 461 (1966).
- [2] F. M. MUELLER and J. C. PHILLIPS, Phys. Rev. **157**, 600 (1967).
- [3] R. M. MORGAN and D. W. LYNCH, Phys. Rev. **182**, 719 (1969).
- [4] R. M. MORGAN and D. W. LYNCH, Phys. Rev. **172**, 628 (1968).
- [5] E. L. GREEN and L. MULDOWER, Phys. Rev. **B2**, 330 (1970).
- [6] H. G. LILJEVALL and A. G. MATHEWSON, J. Phys. C, **3**, 341 (1970).
- [7] P. O. NILSSON and B. SANDELL, Solid State Commun. **8**, 721 (1970).
- [8] B. F. SCHMIDT and D. W. LYNCH, Phys. Rev. **B3**, 4015 (1971).

- [9] N. E. CHRISTENSEN, *phys. stat. sol. (b)* **54**, 551 (1972).
- [10] M. WELKOWSKY and R. BRAUNSTEIN, *Rev. Sci. Instrum.* **43**, 399 (1972).
- [11] R. STEARNS, J. STEELE, and R. BRAUNSTEIN, *Rev. sci. Instrum.* **54**, 984 (1983).
- [12] M. CARDONA, *Modulation Spectroscopy*, Academic Press, 1969.
- [13] M. WELKOWSKY, Ph. D. Thesis, University of California at Los Angeles, 1971.
- [14] B. BATZ, Ph. D. Thesis, Univ. Libre de Bruxelles, 1967.
- [15] B. BATZ, *Solid State Commun.* **4**, 241 (1965).
- [16] N. F. MOTT and H. JONES, *The Theory of the Properties of Metals and Alloys*, Dover Publ., Inc., New York 1951.
- [17] H. EHRENREICH and J. R. PHILLIPP, *Phys. Rev.* **128**, 1622 (1962).
- [18] M. BURD, R. STEARNS, and R. BRAUNSTEIN, *phys. stat. sol. (b)* **117**, 101 (1983).
- [19] R. STEARNS, Ph. D. Thesis, University of California at Los Angeles, 1982.
- [20] L. G. SCHULTZ, *Suppl. Phil. Mag.* **6**, 102 (1957).
- [21] H. AMAR and K. JOHNSON, in: *Optical Properties and Electronic Structure of Metals and Alloys*, Ed. F. ABLES, North Holland Publ. Co., 1966 (p. 586).
- [22] A. BANSIL, H. EHRENREICH, L. SCHWARTZ, and R. E. WATSON, *Phys. Rev. B* **9**, 445 (1974).
- [23] M. A. BIONDI and J. A. RAYNE, *Phys. Rev.* **115**, 1522 (1959).
- [24] G. P. PELLIS and H. MONTGOMERY, *J. Phys. C* **3**, 5330 (1970).

(Received July 3, 1985)

# Infrared wavelength modulation spectroscopy of some optical materials

Ryu K. Kim and Rubin Braunstein

Infrared wavelength modulation techniques were developed and used to investigate the low-level absorption of some optical materials such as alkali halides and alkaline earth fluorides. The results reveal rich absorption structures which enable an identification of some of the surface and bulk impurities of these materials. These impurities are principal sources of optical absorption which limit the expected transparency of these materials in the spectral region studied (2.5–12  $\mu\text{m}$ ).

## 1. Introduction

The development of high-power laser sources has generated considerable interest in the study of very weak absorption processes difficult to detect by conventional spectroscopic methods because of the need for low absorption laser components. In recent years, extensive theoretical and experimental investigations have been conducted in an effort to determine the frequency and temperature dependence of the absorption coefficient of a number of alkali halides and alkaline earth fluorides to identify the principal mechanisms responsible for intrinsic and extrinsic absorption processes. The very low values expected of the absorption coefficient characteristic of multiphonon infrared absorption have spurred the development of various specialized measurement techniques and/or refinements of existing ones.<sup>1</sup>

The majority of the investigations have focused on ionic solids, especially alkali halide crystals. The latter are attractive for theoretical analysis because of their relative simplicity and the wealth of knowledge already available about many of their fundamental properties. Experimentally, alkali halides again represent relatively well-investigated materials in terms of fundamental properties as well as growth, preparation, and purification.

Deutsch<sup>2</sup> showed that the exponential dependence of absorption coefficient  $K(\omega)$  for multiphonon processes follows the empirical law

$$K(\omega) = A_0 \exp(-A\omega), \quad (1)$$

where  $A_0$  and  $A$  are material dependent parameters for a wide class of materials which includes alkali halides, alkaline earth fluorides, oxides, and semiconductors. Sparks and Sham<sup>3</sup> developed a theory for the exponential dependence of  $K(\omega)$ . Duthler<sup>4</sup> estimated the absorption coefficients for some alkali halides in the regions of interest, particularly at the wavelength of the  $\text{CO}_2$  laser line (10.6  $\mu\text{m}$ ), by assuming a Lorentzian line shape of impurities peaked at the appropriate wavelengths. The extrapolation of exponential dependence of the absorption coefficient to the spectral region of interest as laser window materials in the 2.5–12- $\mu\text{m}$  region predicts the absorption coefficient to be as low as  $\sim 10^{-7} \text{ cm}^{-1}$ , but in practice the absorption coefficients are always higher than the predicted values, sometimes by 2 orders of magnitude and varying from sample to sample, indicating the presence of extrinsic absorption due to impurities.

To improve the ability to measure the very small values of the absorption coefficient in very high-purity materials, a laser calorimeter has been employed.<sup>5</sup> In this method, an incident laser beam is passed through the sample, and the temperature rise produced by absorption of the radiation is measured. By this method, values of  $K(\omega)$  in the range of  $10^{-4}$  or  $10^{-5} \text{ cm}^{-1}$  have been measured.<sup>6</sup> The major disadvantage of the laser calorimetry approach is that one can measure  $K(\omega)$  only at those discrete frequencies at which laser radiation is available. To identify the mechanisms which limit the ultimate transparency of solids, knowledge of variations of the absorption coefficient as a function of frequencies and temperature at very low level is required.

We have developed an infrared wavelength modulation technique which has a sensitivity as low as  $\sim 10^{-5} \text{ cm}^{-1}$  in the spectral region between 2.5 and 12  $\mu\text{m}$  and have studied intrinsic and extrinsic absorption processes in alkali halides and alkaline earth fluorides.

The authors are with University of California, Physics Department, Los Angeles, California 90024.

Received 26 September 1983.

0003-6935/84/081166-12\$02.00/0.

© 1984 Optical Society of America.

## II. Experimental System

### A. Experimental Background

Derivative optical spectroscopy as a powerful technique for enhancing weak structure immersed in a relatively smooth background spectrum is well known. Several different modulation schemes were introduced in optical derivative spectroscopy.<sup>7</sup> In most cases, the optical spectrum of the sample is modulated by an external ac perturbation such as electric field,<sup>8</sup> pressure,<sup>9</sup> temperature,<sup>10</sup> and light intensity<sup>11</sup> on the sample. The modulation spectrum so obtained depends intimately on how the property of the sample is affected by the external perturbation, and such knowledge is often limited.

As opposed to other modulation schemes, wavelength modulation allows one to obtain a derivative spectrum by modulating the wavelength of light incident upon a sample without any external ac perturbation to the sample. The main difficulty of the wavelength modulation scheme is the elimination of the background derivative spectra due to light source, detector, optics, and atmospheric absorption. To normalize the background, various servo systems have been employed,<sup>7,12,13</sup> but these are difficult to employ with photoconductive detectors with varying dark current. We developed a wavelength modulation system which eliminates the background problem numerically.

Almost always the wavelength modulation technique has been applied in the ultraviolet and visible spectral regions.<sup>12-14</sup> We have extended the spectral range of the wavelength modulation technique into the infrared; for absorption measurements in the spectral region of this study, 2-12  $\mu\text{m}$ , the system has a sensitivity of  $\Delta I/I \sim 10^{-5}$ , where  $\Delta I$  is the fluctuation of signal in the derivative channel.

### B. Theory of Wavelength Modulation

In a conventional transmission measurement, the total signal  $S$  transmitted by the sample is

$$S(\lambda) = T(\lambda)I_0(\lambda), \quad (2)$$

where  $T$  is the sample transmission, and  $I_0$  is the background signal, which consists of the incident light source, optics, atmospheric absorption, and detector response.

When the wavelength is swept sinusoidally across the exit slit of the monochromator at a frequency  $\Omega$ , that is,

$$\lambda(t) = \lambda_0 + \Delta\lambda \cos(\Omega t), \quad (3)$$

where  $\lambda_0$  is a fixed wavelength around which the sinusoidal sweeping of the wavelength is performed, and  $\Delta\lambda$  is the amplitude of the sweep, the output of the monochromator becomes a function of time, that is,

$$S(\lambda_0, t) = T[\lambda_0 + \Delta\lambda \cos(\Omega t)]I_0[\lambda_0 + \Delta\lambda \cos(\Omega t)]. \quad (4)$$

Expansion of Eq. (4) in a Taylor series in powers of  $\Delta\lambda \cos(\Omega t)$  and using the trigonometric identities and collecting terms, we can show that, for small  $\Delta\lambda$ , retaining the terms up to linear in  $\Delta\lambda$ ,

$$S(\lambda_0, t) = S^{dc}(\lambda_0) + S^{ac}(\lambda_0) \cos(\Omega t), \quad (5)$$

where

$$S^{dc}(\lambda_0) = T_0(\lambda_0)I_0(\lambda_0), \quad (6)$$

$$S^{ac}(\lambda_0) = \Delta\lambda(T'I_0 + TI'_0). \quad (7)$$

Standard lock-in amplifiers measure the ac component of the signal at the reference frequency. Therefore, what is measured at the reference frequency of a lock-in amplifier, which is  $\Omega$  in our case, is the ac component of  $S(\lambda_0, t)$  at  $\Omega$ . Here we note that  $S^{ac}$  contains terms of the form  $T'I_0$  and  $TI'_0$ , that is, a term which is proportional to the first derivative of background as shown in Eq. (7).

In practice, the elimination of the derivative signal of the background is a crucial problem in wavelength modulation. This problem will be discussed in Sec. II.C. As expected, the derivative signal is proportional to the depth of modulation  $\Delta\lambda$ . The correction terms can be minimized by using the smallest possible  $\Delta\lambda$ . A convenient test for the distortion of the first derivative due to the correction terms is to measure the change in the magnitude of the signal as a function of  $\Delta\lambda$  if a linear relationship is desired. For further discussion of the theory, we refer the reader to the literature<sup>12</sup> and references therein.

### C. General Considerations

In a transmission measurement, the signal  $I(\lambda)$  transmitted through the sample is given by

$$I(\lambda) = I_0(\lambda) \exp[-K(\lambda)d], \quad (8)$$

where  $I_0(\lambda)$  is the background signal which consists of the incident light source, optics, atmospheric absorption, and detector response.  $K(\lambda)$  and  $d$  are absorption coefficients as a function of wavelength and sample thickness, respectively.

The differentiation of Eq. (8) with respect to the wavelength gives, after a little rearrangement of terms,

$$\frac{dK(\lambda)}{d\lambda} = \frac{1}{d} \left[ \frac{1}{I_0} \frac{dI_0(\lambda)}{d\lambda} - \frac{1}{I(\lambda)} \frac{dI(\lambda)}{d\lambda} \right], \quad (9)$$

or, in terms of energy,

$$\frac{dK}{dE} = \frac{1}{d} \left[ \frac{1}{I_0(E)} \frac{dI_0(E)}{dE} - \frac{1}{I(E)} \frac{dI(E)}{dE} \right]. \quad (10)$$

As indicated in the theory of wavelength modulation, the measured quantity by a lock-in amplifier for the derivative signal at the preset reference frequency is of the form  $\alpha(dI/dE)$ , where  $\alpha$  is a constant. But as shown in Eq. (7), the derivative signal contains the derivative of the background as well as the derivative of the transmitted intensity. To eliminate the derivative of the background, we use the sample-in and sample-out technique, which is described in a later section.

With the sample-in setting, the derivative signal is, from Eq. (7), for small  $\Delta\lambda$

$$S^{ac} \approx \Delta\lambda(T'I_0 + TI'_0), \quad (11)$$

or

$$\frac{S^{ac}}{I} = \frac{S^{ac}}{TI_0} = \Delta\lambda \left( \frac{T'}{T} + \frac{I'_0}{I_0} \right). \quad (12)$$

With the sample-out setting, the derivative signal of the background is

$$S_b^x \approx \Delta \lambda J_0 \quad (13)$$

or

$$\frac{S_b^x}{I_0} = \Delta \lambda \frac{I_0'}{I_0} \quad (14)$$

The subscripts *s* and *b* of  $S^x$  refer to the sample and background, respectively.

The difference of  $S_s^x/I$  and  $S_b^x/I_0$  will give the derivative of the transmitted intensity solely by the sample in principle. But in practice we encounter some difficulties; defocusing of the light beam at sample-in setting by the sample, for example. This defocusing effect by the sample, in conjunction with the nonuniformity of the active area of the photodetector surface, obscures the zero crossing of the derivative signal.

We overcome this difficulty by a number method. That is, with the measured quantities with sample-in and sample-out settings, we form the expression

$$\phi(E) = \alpha \frac{1}{I_0(E)} \frac{dI_0(E)}{dE} - \beta \frac{1}{I(E)} \frac{dI(E)}{dE} \quad (15)$$

where  $\alpha$  and  $\beta$  are multiplicative constants independent of energy. Here we note that the first term in Eq. (15) is solely due to the background, while the second term is due to the sample in addition to the background.

To convert Eq. (15) into the form of Eq. (10), we write Eq. (15) as

$$\phi(x, E) = \alpha \left[ \frac{1}{I_0(E)} \frac{dI_0(E)}{dE} - \frac{\beta}{\alpha} \times \frac{1}{I(E)} \frac{dI(E)}{dE} \right] \quad (16)$$

and determine the ratio of proportionality constants  $\gamma = \alpha/\beta$  in such a way that  $\phi(x, E)$  and

$$\alpha \frac{1}{I_0(E)} \frac{dI_0(E)}{dE}$$

are not correlated for  $\gamma = x$ . For this particular value of  $\gamma$ ,

$$\phi(E) = \alpha d \frac{dK}{dE} \quad (17)$$

This procedure is performed by a computer using a decorrelation algorithm.<sup>15</sup> Consider quantities  $a_i$ ,  $b_i$ , and

$$c_i = a_i + \gamma b_i \quad (18)$$

Here,  $a_i$  is a quantity due to sample alone,  $b_i$  is a quantity due to background alone, and  $c_i$  is a quantity due to sample and background together. If we relate these quantities to our study,  $b_i$  and  $c_i$  are measured quantities, that is, signal with sample-out setting and signal with sample-in setting, respectively. And  $a_i$  is the quantity to be obtained by the decorrelation procedure. We set

$$d_i = c_i - t b_i = a_i + (\gamma - t) b_i \quad (19)$$

Now, we search for  $t$ , which minimizes the correlation function

$$f = \left[ \frac{\sum_i [(d_i - \bar{d})(b_i - \bar{b})]^2}{\sum_i (d_i - \bar{d})^2 \sum_i (b_i - \bar{b})^2} \right]^{1/2} \quad (20)$$

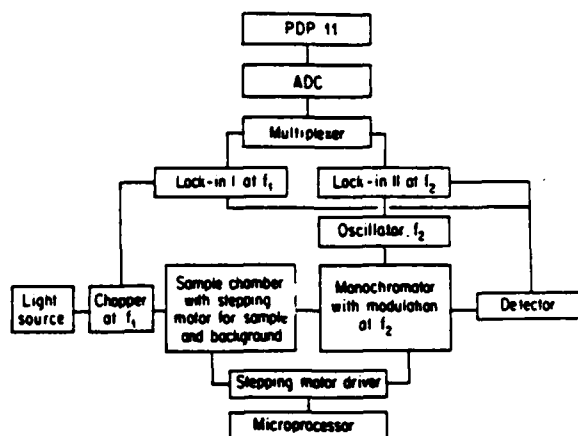


Fig. 1. Block diagram of the infrared wavelength modulated system.

when  $\gamma = t$ ,  $d_i = a_i$ . Here,  $d_i = a_i$  independent of  $b_i$  is assumed. If desired, Eq. (17) can be integrated numerically. In this study, the trapezoidal integration of Eq. (17) was performed.

## D. Implementation and Operation of the System

### 1. Construction

The block diagram of the system is shown in Fig. 1. We have converted a Perkin-Elmer 301 spectrophotometer into a single beam system for improved SNR by using a sample-in and sample-out scheme. The sample-in and sample-out mechanism was accomplished with a linear translator assembly unit driven by a stepping motor. The wave-number drive was also performed by a stepping motor at preset intervals to scan the spectral regions of interest. Both stepping motors are driven by a dual-channel step motor drive unit. The intervals of stepping of sample-in and sample-out stepping motor and the wave-number driving motor as well as the data-collecting system as a whole are controlled by an on-line microprocessor (Motorola M6800 microprocessor) in a cycle for each set of data.

Sinusoidal sweeping of the light beam across the exit slit of the monochromator was accomplished by a vibrating mirror at 11 Hz. We have chosen this low frequency in spite of the 1/f noise in anticipation of the need of a slow detector such as a thermocouple, bolometer, or Golay cell, and most important to avoid the subharmonics of the background chopper channel, which is 39 Hz. The amplitude of modulation is adjustable through the output voltage of the scanner driver and can result in a wide range of modulation for  $\Delta\lambda/\lambda \sim 10^{-2}$  to investigate the broad structures of solids in the infrared region of the spectrum.

As shown in the block diagram of the system in Fig. 1, two lock-in amplifiers are employed. Lock-in amplifier I measures the intensity of the chopped radiation at 39 Hz with sample-in and sample-out settings at a fixed wavelength. The lock-in amplifier II, which is fed with the 11-Hz reference frequency derived from the vibrating mirror, measures the derivative signal with

sample-in and sample-out settings. The sample-in and sample-out mechanism is a stepping motor coupled with a translation stage. With appropriate combinations of gratings, filters, and light sources, the system can be operated in the spectral region from ultraviolet to infrared ( $\sim 12 \mu\text{m}$ ). The main light sources in this study were a tungsten lamp in the visible and near infrared and a globar in the infrared. The detectors used were PbSnTe, PbS, and a silicon photodiode for appropriate spectral regions.

## 2. Operation

With the sample-in settings, two data points were taken; one from lock-in *I*, which is in the intensity of radiation transmitted by the sample, and the other from lock-in *II*, which is the derivative signal. The same set of data is taken with the sample-out setting yielding the equivalent for the background. Those two sets of data are fed into a multiplexer and then digitized by an ADC. The digitized result can be either punched on paper tape by a teletype or fed into the on-line computer (PDP 11/23) directly for numerical processing. By appropriate combinations of these sets of data, we can form a logarithmic derivative of intensity as a function of energy or direct transmission. A computer program was written to obtain the numerical values and graphs of derivative of the absorption coefficient, integrated result, and direct transmission as a function of energy.

All these data-taking processes are done in a sequence at one wavelength, and after a cycle the system moves to the next wavelength. This data-collecting cycle, which is controlled by a microprocessor (Motorola M6800), is operated in the following sequences. The block diagram of the data-taking cycle is shown in Fig. 2, which performs in the following cycle:

- (1) The M6800 sends out pulses to the stepping motor driver which drives two stepping motors: one for the linear translator assembly unit and another one for wavelength drive.
- (2) The stepping motor which is attached to the linear translator assembly unit takes the sample in or out of the path of the light beam.
- (3) While the sample mount is translating, the wavelength drive is stepped by the second stepping motor.
- (4) Then the system waits for a certain time before taking the first set of data. In this study, we have chosen the waiting time to be approximately three times the lock-in time constant.
- (5) At the end of the waiting time, two data points are taken: one from the lock-in *I*, which is the intensity of the background radiation, and one from lock-in *II*, which is the derivative signal of the background radiation.
- (6) The microprocessor sends out reverse pulses to the driver to step the stepping motor backward so the linear translator assembly unit will bring the sample mount to the sample-in position. This brings the sample in the path of the light beam.
- (7) Waiting time starts.

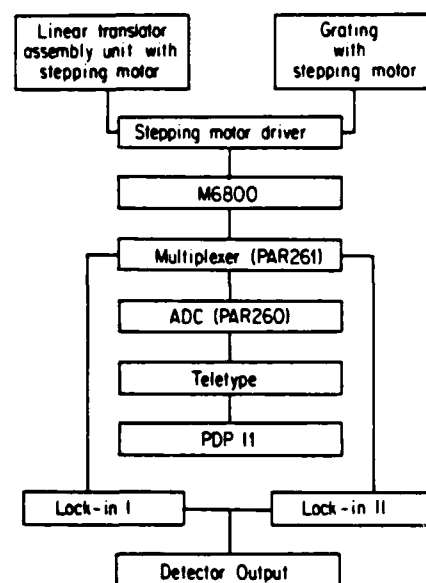


Fig. 2. Block diagram of control system for data-taking cycle.

(8) At the end of the waiting time, two similar data points are taken, except with the sample-in this time.

This completes one data-taking cycle at one wavelength. The interval of the linear translation of the sample mount and the wavelength drive as well as the length of the waiting time can be adjusted by changing the appropriate program parameters fed to the microprocessor. The program of the microprocessor is taped on a cassette tape and played by a cassette player at the beginning of the run of the system.

## III. Experimental Results and Discussions

### A. Treatment of Data

Before a detailed discussion of the experimental results and the interpretation of the spectra of the individual substances measured, we shall present the method of presentation of data and the mode of analysis.

In the intrinsic spectral regions, values of the absorption coefficient were determined from transmission measurements. In the extrinsic spectral regions, that is, impurity dominating regions, the integrated derivative data were normalized to the laser calorimetry measurement at indicated discrete laser lines.<sup>16</sup> This representation of the data allows us to display the fine structure excursions in absorption above and below the calorimetric point. In a number of cases a second calorimetric point was measured at the other end of the spectrum. It was found that the absorption coefficient derived from this second measurement agreed with the integrated value obtained from wavelength modulation data.

To discriminate the effect of atmospheric absorption on a sample, we ran each sample in two different ambient conditions, one in atmospheric ambient, the other in dry nitrogen ambient. The latter was accomplished by flushing the whole system by dry nitrogen gas flowing

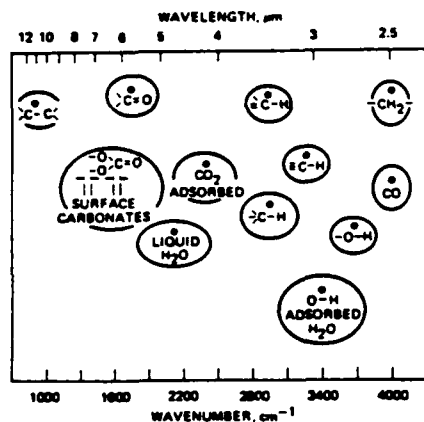


Fig. 3. Correlation chart of carbonates, C—H, O—H, and water frequency.

into the system throughout the entire run. When the sample was placed in a dry  $N_2$  atmosphere, a continuous change in the spectral distribution of the absorption was observed until the spectra stabilized after the sample had been in this gaseous ambient for an hour.

Correlation-type charts have been published that represent a tabulation of molecular-ion vibrational frequencies as means of identifying possible surface and volume impurities in alkali-halide laser window materials.<sup>17</sup> If one considers a frequency overlay of possible impurities that can be present in concentration of 0.1 ppm, one finds that a quasi-continuous absorption would be expected throughout the 2.6–12- $\mu m$  region due to the overlap of the Lorentzian tails of the various absorption bands. It has been felt that a heterogeneous distribution of a conglomeration of chemical compositions which can be deposited on the surface from the environment would produce a uniform absorption throughout the infrared spectral regions.<sup>17</sup> However, the distinct absorption bands observed in this study indicate the possibility of specifically identifying dominant absorption centers. Figure 3 shows a correlation chart of carbonates, C—H, O—H, and water frequencies which prove to be the common bulk and surface impurities encountered in this study.

## B. Discussions

In Table I we show the origins of the samples used in this study.

### 1. Potassium Bromide

Several different reactive atmosphere process (RAP) grown samples from various sources have been studied. The dimensions of the samples varied, that is, 2.5 cm in diameter and 1–7 cm in length. The absorption spectrum of a typical KBr sample obtained with a conventional double-beam spectrometer is shown in Fig. 4. Virtually no absorption structure is present in the extrinsic spectral region above the noise level of the instrument, confirming the relative purity of the sample. Calculated values of absorption coefficients from the exponential behavior of the multiphonon processes from Eq. (1) at 10.6- and 5.3- $\mu m$  wavelength regions predict

Table I. Origins of Samples Used in This Study

KBr	Naval Research Laboratory Oregon State University
KCl	Hughes Research Laboratories
BaF <sub>2</sub>	Harshaw
MgF <sub>2</sub>	Optovac
SrF <sub>2</sub>	Hughes Research Laboratories
CaF <sub>2</sub>	Harshaw
NaF	Optovac
LaF <sub>3</sub>	Hughes Research Laboratories
NaCl	Hughes Research Laboratories
LiF	Meller
MgO	Optovac

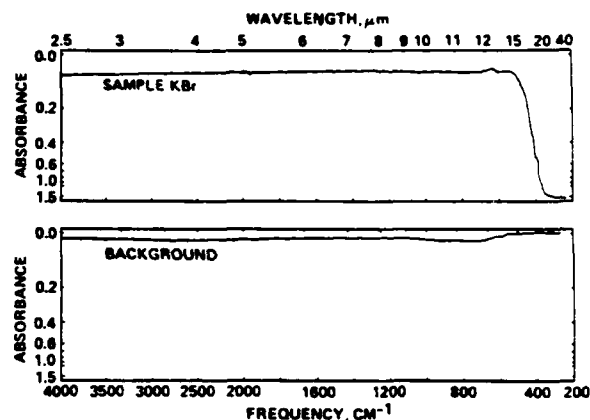


Fig. 4. Absorption spectrum of a typical KBr sample obtained by a conventional double-beam instrument.

$2 \times 10^{-7}$  and  $8 \times 10^{-18} \text{ cm}^{-1}$ , respectively.<sup>18</sup> The actual measurements at best show  $4.2 \times 10^{-4} \text{ cm}^{-1}$  at 10.6  $\mu m$  and  $2.1 \times 10^{-4} \text{ cm}^{-1}$  at 5.3  $\mu m$ , respectively.<sup>1</sup> Therefore, in these spectral regions, the absorptions are mainly due to extrinsic origins.

In Fig. 5 we show a typical result of our study of KBr in two different ambients. In general, for the spectral region from 2.5  $\mu m$  to 12  $\mu m$ , the samples in this study show a structure around 2.5  $\mu m$ , multiple structures between 3 and 4.0  $\mu m$ , a sharp peak at 4.2  $\mu m$ , a band centered at 4.8  $\mu m$ , multiple structures between 6 and 8  $\mu m$ , a valley near 9  $\mu m$ , and a peak at 10.6  $\mu m$  at the levels of absorption coefficient of  $\sim 10^{-5} \text{ cm}^{-1}$ . Since the relative magnitudes of these structures differ in different samples, the indications are that these bands have extrinsic origins. Although the spectra differ in detail, the clustering of the spectral lines in similar spectral regimes indicate common origins of the spectra. The magnitudes and linewidths of some of the bands vary when the samples are in a dry  $N_2$  atmosphere compared with a laboratory ambient, indicating that a portion of the absorption is due to surface physical adsorption. The structures that persist even when the samples are flushed in dry  $N_2$  may be due to surface chemisorbed species or volume impurities. The surface character of some of these bands was confirmed by performing similar measurements on 1-mm thick samples. Absorption coefficients of the order of  $10^{-5} \text{ cm}^{-1}$  were observed on thick and thin samples with slight differences in the spectral distribution. Due to

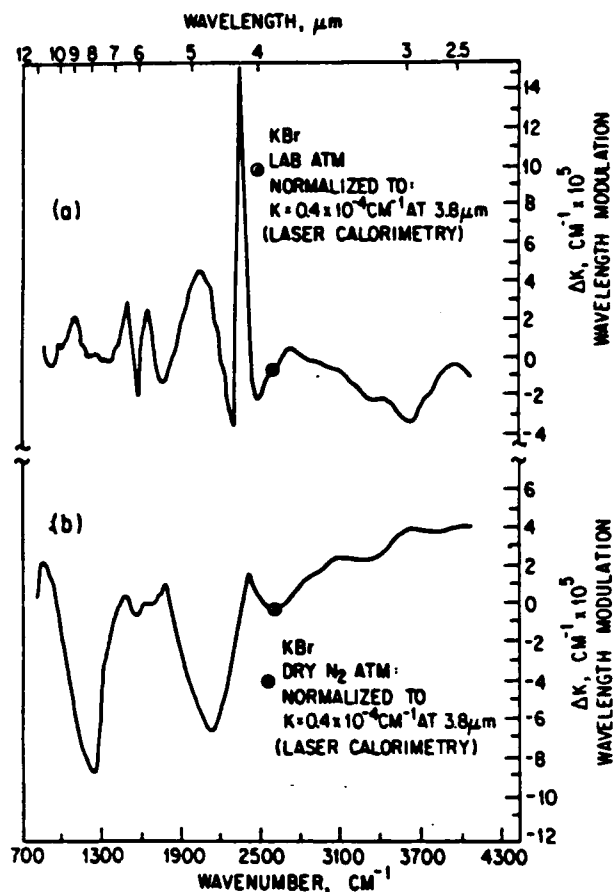


Fig. 5. Wavelength modulation absorption spectra of KBr;  $K$  is the absorption coefficient in  $\text{cm}^{-1}$ : (a) in the laboratory atmosphere; (b) in a dry  $\text{N}_2$  atmosphere.

the complex superposition of the bands, it was difficult to distinguish unambiguously which bands would scale with a thickness that would identify volume absorption. The  $4.2\text{-}\mu\text{m}$  band was observed with the same intensity for all thicknesses, confirming a surface origin. The continuous variation of the spectral features with the thickness of sample that remains at  $\sim 10^{-5}\text{-cm}^{-1}$  levels indicates that, at this level of absorption, we have a combination of volume and surface absorption or there is an inhomogeneous distribution of volume impurities.

The region between 2 and  $4\text{ }\mu\text{m}$  reveals several structures, while previous measurements by laser calorimetry have indicated a peak near  $2.7\text{ }\mu\text{m}$  which has usually been associated with the stretching frequency of the isolated  $\text{OH}^-$  radicals.<sup>19</sup> However, the laser calorimetry measurements are performed with a multiline laser at a few discrete wavelengths and so can only infer a broad band with the great possibility of missing peaks or valleys.

In this study, a prominent peak is observed at  $3850\text{ cm}^{-1}$ , which is shifted from the peak that is observed at  $3610\text{ cm}^{-1}$  in deliberately doped KBr.<sup>20</sup> It is not clear that such a large shift could occur due to different crystallographic locations of  $\text{OH}^-$  in the lattice. The

magnitude and linewidth of this peak vary from sample to sample. In addition, placing a sample in  $\text{N}_2$  gas atmosphere results in spectral changes that indicate that part of this band may be due to surface adsorption. However, there is a shoulder in this line near  $3700\text{ cm}^{-1}$  that persists in dry  $\text{N}_2$  ambient and can be associated with adsorbed  $\text{H}_2\text{O}$ .

The region between 3 and  $4.0\text{ }\mu\text{m}$  shows a superposition of structures that could be attributed to various C—H bonds. The origin of these groups can result from surface contaminants due to alcohol that is used to disperse the grinding compounds used in the surface polishing of the crystals. However, some of these bands may be due to volume absorption since some of the spectra scale with sample thickness. Volume absorption due to C—H bonds can be due to carbonaceous fractions, which can result from organic materials such as water-soluble alcohols that decompose on melting and are incorporated in the crystals.

A unique example of physical adsorption taking place on a surface of KBr is seen at  $4.2\text{ }\mu\text{m}$ . This strong narrow band with varying intensity is observed at  $2358\text{ cm}^{-1}$  on all samples of KBr. This is close to the gas-phase value of  $2349\text{ cm}^{-1}$  for the  $\text{CO}_2$  vibration. Since this band is easily suppressed by flushing with dry  $\text{N}_2$  gas, it is readily identified as due to a physically adsorbed species. When the sample is returned to atmospheric ambient, this band returns. It was observed that the  $\text{CO}_2$  adsorption varies from sample to sample for the laboratory ambient. It is not unreasonable to expect physical adsorption to depend on surface variations or impurities in the substrate.

The band at  $4.8\text{ }\mu\text{m}$  is most likely due to surface-adsorbed liquid water as the adsorption in this region is markedly reduced in a dry  $\text{N}_2$  ambient; some of the additional structure in the  $2.7\text{-}\mu\text{m}$  region can be due to the vibrational structure of water as it is also reduced by dry  $\text{N}_2$  flushing.

The bands between  $5.5$  and  $8.0\text{ }\mu\text{m}$  are the most persistent of all structures seen in all the KBr samples. Measurements on thin samples still reveal these structures, which lends evidence that these are due to surface chemical adsorption. The position of these bands is consistent with the vibrational frequencies of various surface carbonate complexes.<sup>21</sup>

It is interesting to note that the data reveal a peak in absorption at  $10.6\text{ }\mu\text{m}$  and a valley around  $9\text{ }\mu\text{m}$ . It is possible to identify the  $10.6\text{-}\mu\text{m}$  peak as due to the C—C vibration. It is our interpretation that the laser calorimetry data indicate a possible minimum in absorption near the  $\text{CO}_2$  laser line at  $9.27\text{ }\mu\text{m}$ .<sup>22</sup> The wavelength modulation data definitely establish this valley.

The absorption between  $5.5$  and  $8.0\text{ }\mu\text{m}$  seems to be due to surface carbonates. However, the absence of absorption at  $1070\text{ cm}^{-1}$  signals that the species are in the form of carboxylates. Therefore, we can infer the presence of chemisorbed carbonates not only by the presence of absorption in the  $5.5\text{--}8.0\text{-}\mu\text{m}$  region but also by the absence of absorption at  $9.27\text{ }\mu\text{m}$ . The  $10.6\text{-}\mu\text{m}$  ( $960\text{-cm}^{-1}$ ) region corresponds to the 7–8-phonon region for KBr; the intrinsic multiphonon absorption of KBr



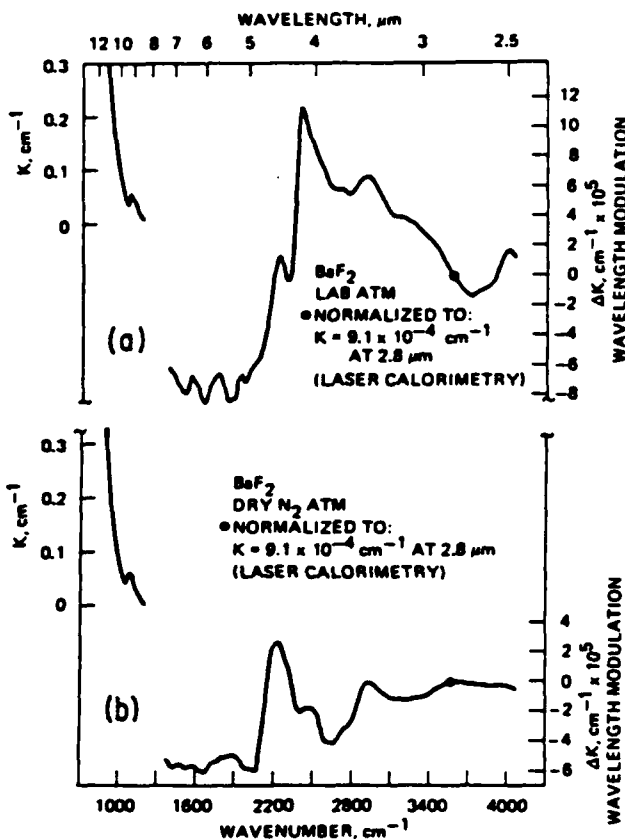


Fig. 6. Wavelength modulation absorption spectra of  $\text{BaF}_2$ ;  $K$  is the absorption coefficient in  $\text{cm}^{-1}$ : (a) in the laboratory atmosphere; (b) in a dry  $\text{N}_2$  atmosphere.

at  $10.6 \mu\text{m}$  is expected to be  $2 \times 10^{-7} \text{ cm}^{-1}$ , but our results show that, even at this region, the main mechanisms of absorption are dominated by impurities, that is,  $K \sim 10^{-4} \text{ cm}^{-1}$ , therefore, masking intrinsic multiphonon contribution to the absorption.

## 2. Barium Fluoride

By similar analysis with KBr, we can readily identify several main features of  $\text{BaF}_2$  in Fig. 6(a). A prominent band at  $4.2 \mu\text{m}$  can be associated with the physisorption of atmospheric  $\text{CO}_2$ . The bands in the  $4\text{--}6\text{-}\mu\text{m}$  region can be due to atmospheric water, while the bands in the  $3\text{--}4\text{-}\mu\text{m}$  region can be assigned to an overlap of hydrocarbon bands. Internal reflection spectrum of an ethylene-glycol-polished  $\text{BaF}_2$  plate and a water-polished  $\text{BaF}_2$  plate showed the absorption structure at  $2915 \text{ cm}^{-1}$  ( $3.43 \mu\text{m}$ ), and it was attributed to C—H stretching absorption from residual organic material used in cutting or preparing the plates.<sup>18</sup> The bands in the  $6\text{--}8\text{-}\mu\text{m}$  region are associated with carbonates. The fact that the bands in the  $3\text{--}4\text{-}\mu\text{m}$  and  $4\text{--}6\text{-}\mu\text{m}$  regions are largely due to physisorbed species is confirmed by the decrease in absorption in the dry  $\text{N}_2$  atmosphere data shown in Fig. 6(b).

The region between  $6$  and  $8 \mu\text{m}$  in  $\text{BaF}_2$  shows considerable structures whose magnitudes vary only slightly with dry  $\text{N}_2$  flushings. These structures can be

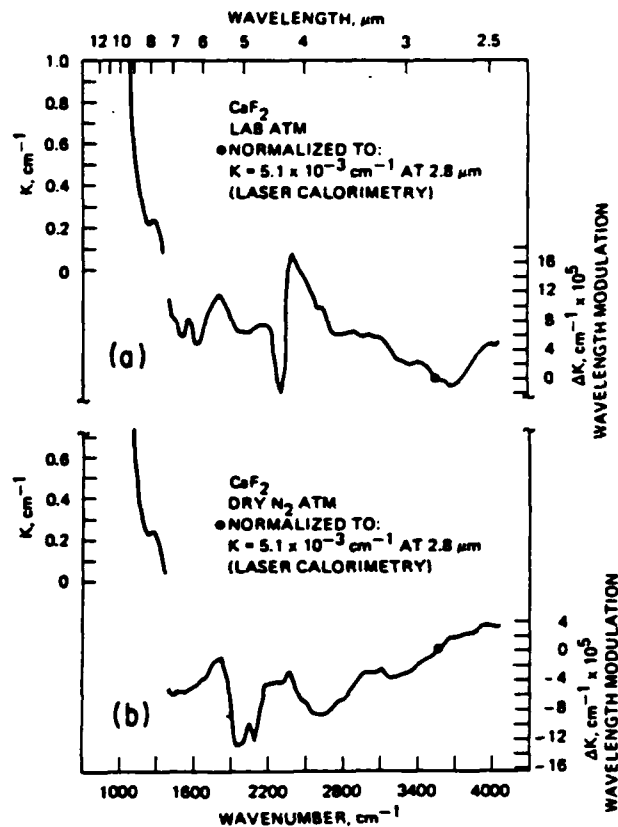


Fig. 7. Wavelength modulation absorption spectra of  $\text{CaF}_2$ ;  $K$  is the absorption coefficient in  $\text{cm}^{-1}$ : (a) in the laboratory atmosphere; (b) in a dry  $\text{N}_2$  atmosphere.

associated with the chemisorbed carbonates. The small structure at  $5.6 \mu\text{m}$  can be associated with chemisorbed carbonyl. Photoacoustic measurements on  $\text{BaF}_2$  and  $\text{SrF}_2$  using a CO laser that was tunable to discrete lines in the  $6\text{--}8\text{-}\mu\text{m}$  region have revealed a steplike structure in the surface adsorption,<sup>23</sup> while our results show distinct bands. A structure around  $1100 \text{ cm}^{-1}$  can be due to surface contaminations of secondary or tertiary alcohol which is commonly used as a surface polishing chemical agent, isopropyl alcohol, for example.

The relationship between physisorbed  $\text{CO}_2$  at  $4.2 \mu\text{m}$  and the formation of the carbonates  $\text{CO}_3^{2-}$  on  $\text{BaF}_2$  can be seen if we compare the data on  $\text{BaF}_2$  in two different ambients. Namely, higher adsorption of  $\text{CO}_2$  at  $4.2 \mu\text{m}$  gives rise to the formation of more carbonates  $\text{CO}_3^{2-}$  around  $6.5 \mu\text{m}$ .

## 3. Calcium Fluoride

The  $\text{CaF}_2$  data in the laboratory ambient are shown in Fig. 7(a). Here we can see the similar distribution of bands as exhibited by  $\text{BaF}_2$ : adsorbed  $\text{CO}_2$  at  $4.2 \mu\text{m}$ , overlap of various hydrocarbons in the  $3\text{--}4\text{-}\mu\text{m}$  region, liquid water around  $4.8 \mu\text{m}$ , carbonyls around  $5.6 \mu\text{m}$ , and carbonates in the  $6\text{--}7.5\text{-}\mu\text{m}$  region. Comparison of Figs. 7(a) and (b) reveals several features. The fact that the  $\text{CO}_2$  band is suppressed in dry  $\text{N}_2$  atmosphere confirms the nature of physisorbed  $\text{CO}_2$  on the surface.

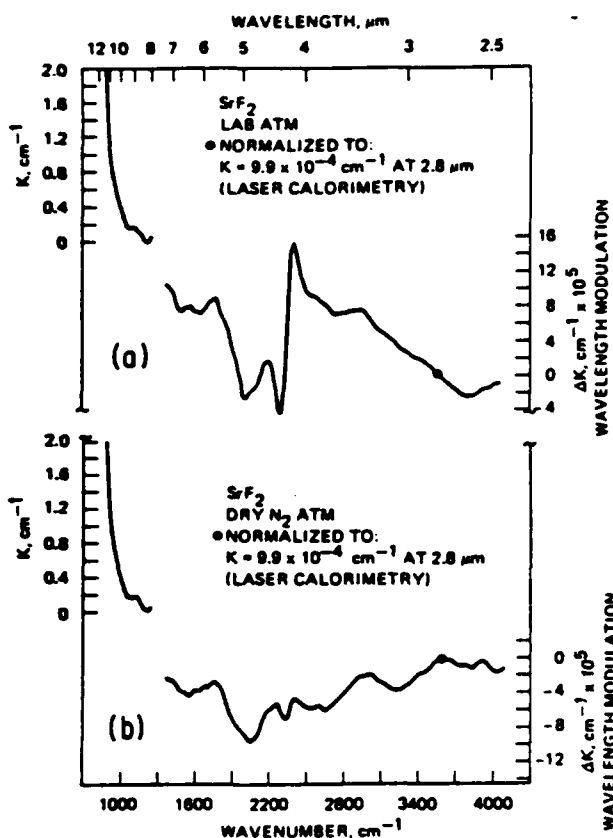


Fig. 8. Wavelength modulation absorption spectra of  $\text{SrF}_2$ ;  $K$  is the absorption coefficient in  $\text{cm}^{-1}$ : (a) in the laboratory atmosphere; (b) in a dry  $\text{N}_2$  atmosphere.

Carbonyl around  $5.6 \mu\text{m}$  appears to be chemisorbed species. We note here that a band at  $6.5 \mu\text{m}$  in Fig. 7(a) disappears in (b) completely. This band must be due to physisorbed carbonates. The relationship of physisorbed  $\text{CO}_2$  and carbonates in two different ambients clearly indicates the active participation of adsorbed  $\text{CO}_2$  in the formation of physisorbed carbonates. This is particularly clear in  $\text{CaF}_2$ , even though we can see this relationship in most of the samples studied. A structure around  $8 \mu\text{m}$  is again due to the surface contamination. From Fig. 7(a) and (b) we can conclude that these are chemisorbed species. They can be surface-polishing chemical agents such as secondary and tertiary alcohol.

#### 4. Strontium Fluoride

The  $\text{SrF}_2$  sample used was from a press-forged RAP boule. In Fig. 8(a) we show data of  $\text{SrF}_2$  in the laboratory atmosphere, where we can see all the main features of  $\text{BaF}_2$  and  $\text{CaF}_2$ : hydrocarbon in the  $3\text{--}4\text{-}\mu\text{m}$  region,  $\text{CO}_2$  at  $4.2 \mu\text{m}$ , liquid water around the  $4.5\text{-}\mu\text{m}$  region, carbonyls around  $5.6 \mu\text{m}$ , and various carbonates in the  $6\text{--}7.5\text{-}\mu\text{m}$  region. In Fig. 8(a) we note the emergence of a structure around  $2.8 \mu\text{m}$ . This can be due to  $\text{OH}^-$  in bulk. Judging from the dry  $\text{N}_2$  gas atmosphere data in Fig. 8(b), C—H bonds in the  $3\text{--}4 \mu\text{m}$  region must be due to chemisorbed species. In Fig. 8(b) we again see

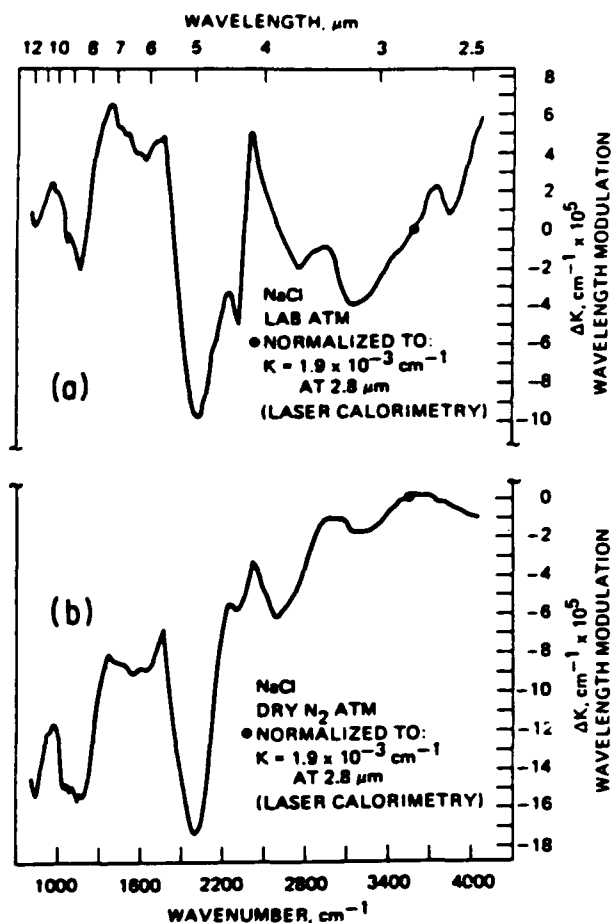


Fig. 9. Wavelength modulation absorption spectra of  $\text{NaCl}$ ;  $K$  is the absorption coefficient in  $\text{cm}^{-1}$ : (a) in the laboratory atmosphere; (b) in a dry  $\text{N}_2$  atmosphere.

that the disappearance of carbonate at  $6.5 \mu\text{m}$  can be attributed to the suppression of physisorbed  $\text{CO}_2$ . A small structure at the tail of the intrinsic region is due to the chemisorbed species on the surface from the surface polishing chemicals.

#### 5. Sodium Chloride

The  $\text{NaCl}$  data in both the laboratory and dry  $\text{N}_2$  atmosphere, Figs. 9(a) and (b), respectively, show prominent structures. Although the spectral distribution is different in detail in two different ambients, we still can identify the structures:  $10\text{--}11\text{-}\mu\text{m}$  ( $>\text{C}=\text{CH}_2$  alcohols),  $6\text{--}8\text{-}\mu\text{m}$  (carbonates),  $5.6\text{-}\mu\text{m}$  (carbonyl),  $4.8\text{-}\mu\text{m}$  (liquid water), the  $4.2\text{-}\mu\text{m}$  ( $\text{CO}_2$ ),  $4\text{-}\mu\text{m}$  (C—H), and  $2.8\text{-}\mu\text{m}$  ( $\text{OH}^-$ ) bands. The prominence of the bands in both ambients is consistent with the greater surface activities which are expected for  $\text{NaCl}$  as compared to the other substances in this study. Comparison of Figs. 9(a) and (b) reveals the difference between chemisorbed species and physisorbed species.

A vibrational frequency of  $\text{CO}_2$  adsorbed on  $\text{NaCl}$  shifts only slightly ( $4\text{--}5 \text{ cm}^{-1}$ ) with respect to the gas-phase frequency. The molecule is only weakly

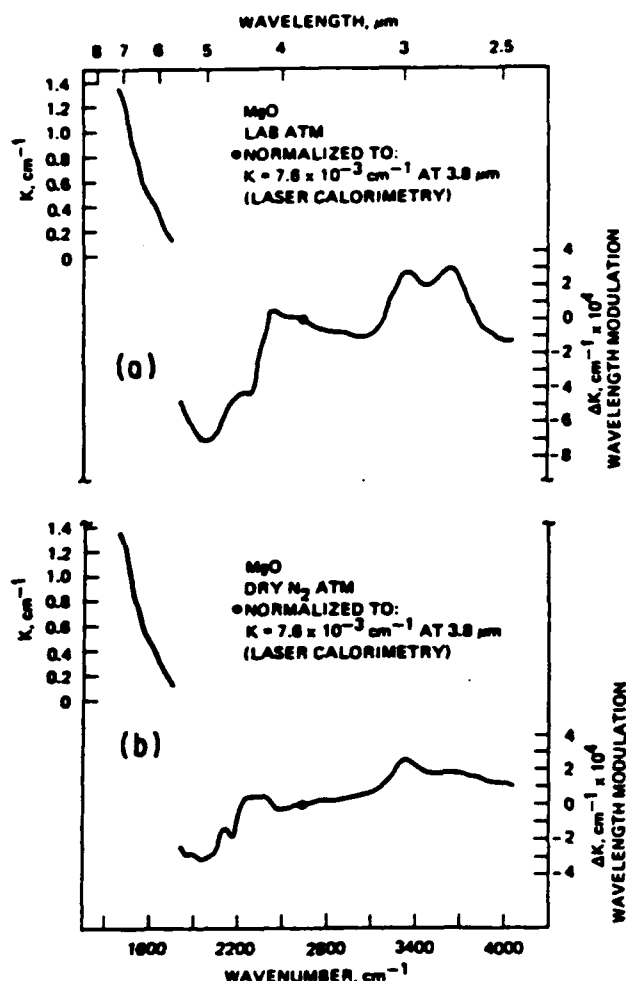


Fig. 10. Wavelength modulation absorption spectra of MgO;  $K$  is the absorption coefficient in  $\text{cm}^{-1}$ : (a) in the laboratory atmosphere; (b) in a dry  $\text{N}_2$  atmosphere.

perturbed by the surface field, and the energy of interaction with the adsorbent is not high. The ease of removal of  $\text{CO}_2$  on evacuation was observed.<sup>24</sup> It is interesting to note that the intensity of absorption due to  $\text{CO}_2$  can be reduced by flushing alone as this study shows.

#### 6. Magnesium Oxide

The data for MgO are shown in Fig. 10. The most prominent features seen in the laboratory ambient are a doublet in the 2.8–3.0- $\mu\text{m}$  region (water and  $\text{OH}^-$ ), some trace of a possible  $\text{CO}_2$  at 4.2  $\mu\text{m}$ , a structure in the 4–6- $\mu\text{m}$  region (liquid water), and very slight structure in the 3–4- $\mu\text{m}$  region (hydrocarbon). It is interesting to note that, of the doublet in the laboratory ambient, it is only the 3.0- $\mu\text{m}$  band which survives dry  $\text{N}_2$  flushings with a noticeable suppression of the 2.8- $\mu\text{m}$  band. In a previous study<sup>6</sup> of MgO, impurity bands were observed between 3.8 and 2.7  $\mu\text{m}$ . Our study clearly shows that the 3.0- $\mu\text{m}$  band is due to bulk or chemisorbed  $\text{OH}^-$ , while the 2.8- $\mu\text{m}$  band is due to physisorbed  $\text{OH}^-$ .

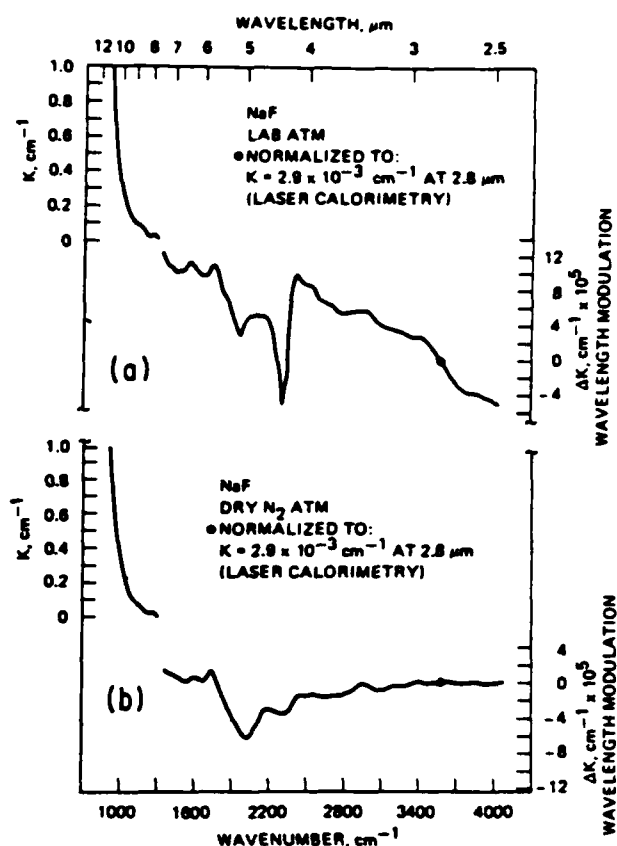


Fig. 11. Wavelength modulation absorption spectra of NaF;  $K$  is the absorption coefficient in  $\text{cm}^{-1}$ : (a) in the laboratory atmosphere; (b) in a dry  $\text{N}_2$  atmosphere.

The region of intrinsic absorption in MgO shows some fluted structures in the multiphonon absorption tail. The rise  $\sim 1600 \text{ cm}^{-1}$  agrees with the shoulder previously studied in the multiphonon spectra of MgO and was attributed to a four TO phonon process by suitably averaging over the dispersion curves.<sup>25</sup>

#### 7. Sodium Fluoride

Comparison of the NaF data in Fig. 11 shows a large decrease of the band heights in the 2.5–4.0- $\mu\text{m}$  region, but the familiar patterns shown in  $\text{BaF}_2$ ,  $\text{SrF}_2$ , and  $\text{CaF}_2$  are still apparent. The relationship between the adsorbed  $\text{CO}_2$  and surface carbonates at 6.5  $\mu\text{m}$  is clear. In both Figs. 11(a) and (b) we can observe a little break  $\sim 1100 \text{ cm}^{-1}$ ; this corresponds to the regime of three phonon spectrum.<sup>26</sup> But it can as well be due to surface contamination of chemisorbed species of some alcohol which is often used as surface polishing reagents—tertiary alcohol, for example.

#### 8. Magnesium Fluoride

The  $\text{MgF}_2$  laboratory atmosphere data shown in Fig. 12 reveal a cluster of bands similar to those observed in  $\text{BaF}_2$ . Again the ubiquitous  $\text{CO}_2$  at 4.2  $\mu\text{m}$  is evident. The 2.8- $\mu\text{m}$  and 4–6- $\mu\text{m}$  regions reveal the liquid water and  $\text{OH}^-$  bands, while the 3–4- $\mu\text{m}$  region reveals the

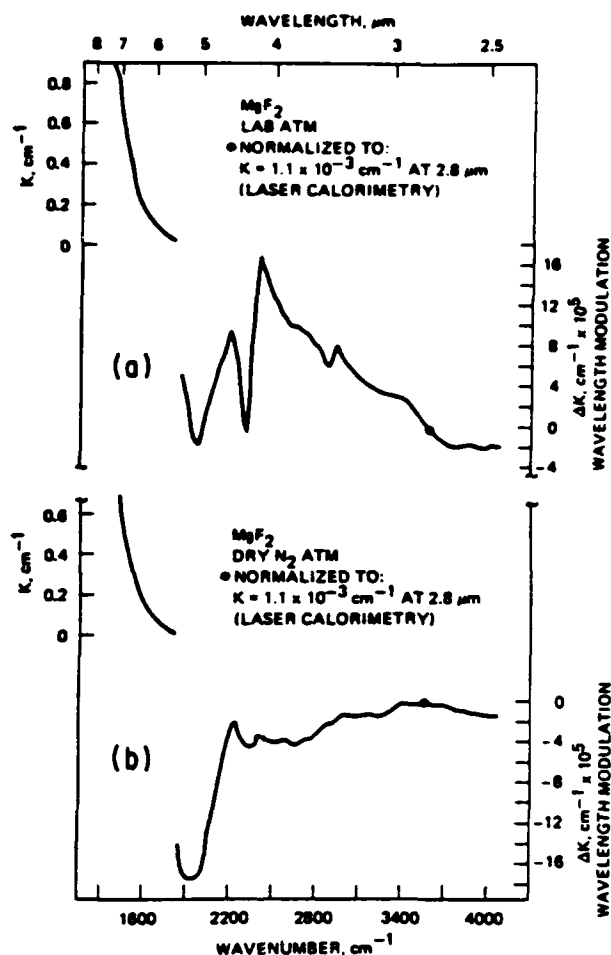


Fig. 12. Wavelength modulation absorption spectra of  $\text{MgF}_2$ ;  $K$  is the absorption coefficient in  $\text{cm}^{-1}$ : (a) in the laboratory atmosphere; (b) in a dry  $\text{N}_2$  atmosphere.

possible overlay of C—H bands. The 6–9- $\mu\text{m}$  bands seen in  $\text{BaF}_2$  seem to be absent or are obscured by the strong water band in the 4–6- $\mu\text{m}$  region. The  $\text{MgF}_2$  data in dry  $\text{N}_2$  atmosphere in Fig. 12(b) show a dramatic suppression of all the above bands. The remaining structure can be due to volume or chemisorbed species: the rise in the neighborhood of 2.8 and 4.8  $\mu\text{m}$  can be due to  $\text{OH}^-$  and liquid water, respectively.

#### 9. Lanthanum Fluoride

The  $\text{LaF}_3$  data in the laboratory atmosphere shown in Fig. 13(a) reveal the  $\text{CO}_2$  band at 4.2  $\mu\text{m}$ , the possible carbonates in the 6–8- $\mu\text{m}$  region and  $\text{OH}^-$  band near 2.8  $\mu\text{m}$ . However, it should be noted that the bands in the 3–4- $\mu\text{m}$  region due to C—H vibrations which have been prominent in  $\text{BaF}_2$ ,  $\text{SrF}_2$ ,  $\text{MgF}_2$ ,  $\text{CaF}_2$ , and  $\text{NaF}$  seem to be absent or greatly suppressed. In the dry  $\text{N}_2$  atmosphere data shown in Fig. 13(b), the peak near 2.8  $\mu\text{m}$  possibly due to  $\text{OH}^-$  is about the same height as shown in Fig. 13(a). The structure around 1200  $\text{cm}^{-1}$  is due to chemisorbed surface contamination, tertiary alcohol, for example.

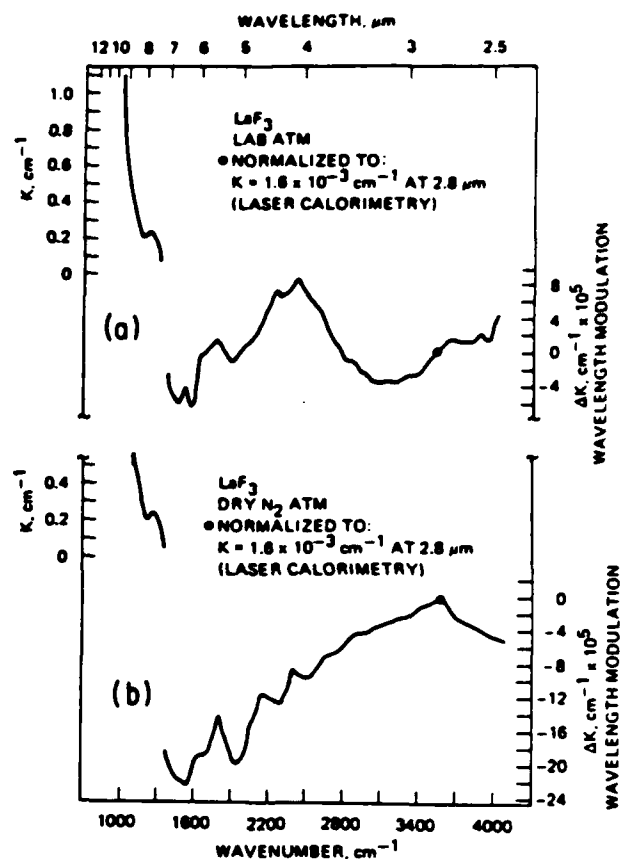


Fig. 13. Wavelength modulation absorption spectra of  $\text{LaF}_3$ ;  $K$  is the absorption coefficient in  $\text{cm}^{-1}$ : (a) in the laboratory atmosphere; (b) in a dry  $\text{N}_2$  atmosphere.

#### 10. Lithium Fluoride

The  $\text{LiF}$  data in Fig. 14 show little structure indicating that  $\text{LiF}$  is the least surface active of all the substances studied. The absence of the 4.2- $\mu\text{m}$  band, which was visible in all the substances studied, should be noted. The only band which seems to be noticeable is the 4.5- $\mu\text{m}$  band in both ambients, and this can be due to water.

#### 11. Potassium Chloride

If we examine the data of  $\text{KCl}$  shown in Fig. 15 in the light of the discussion of the identification of the bands seen in other alkali-halides ( $\text{KBr}$ , for example), similar features can be discerned. It is interesting to note that the adsorbed  $\text{CO}_2$  band is markedly suppressed in  $\text{KCl}$  relative to  $\text{KBr}$ . The band around 1400  $\text{cm}^{-1}$  can be due to the chemisorbed species of surface carbonates. The band around 1900  $\text{cm}^{-1}$  can be due to some type of carbonyl.

#### IV. Summary

The infrared wavelength modulated spectrometer system that we have developed has the capabilities of detecting a change in absorption of a part in  $10^5$  out of a relatively smooth background in the spectral region from 2.5 to 12  $\mu\text{m}$ . This sensitivity can be realized from

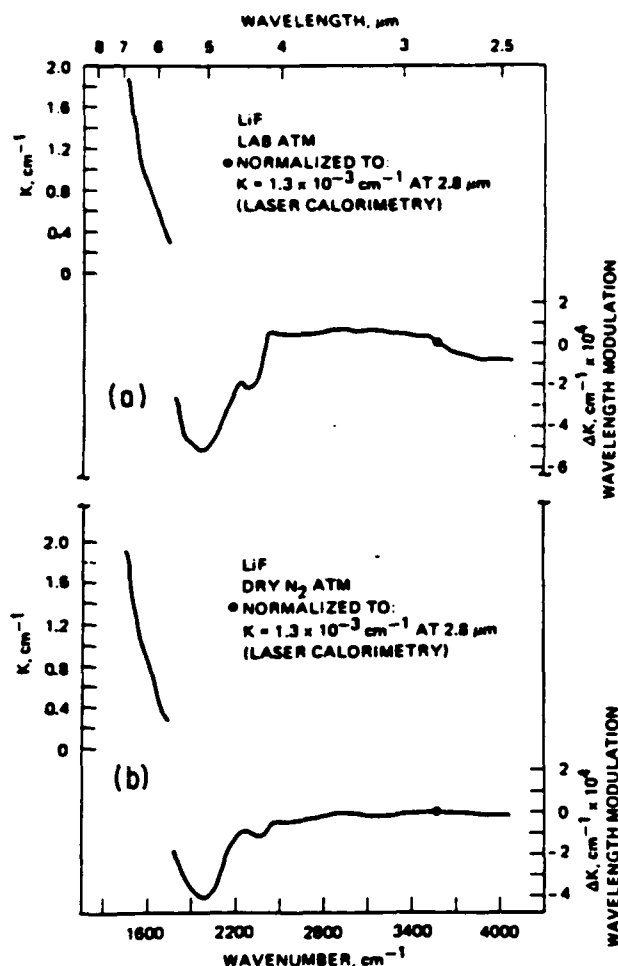


Fig. 14. Wavelength modulation absorption spectra of LiF;  $K$  is the absorption coefficient in  $\text{cm}^{-1}$ : (a) in the laboratory atmosphere; (b) in a dry  $\text{N}_2$  atmosphere.

the visible to the further infrared using appropriate detectors. For the first time the continuous spectral distribution of extrinsic absorption at levels of  $10^{-5} \text{ cm}^{-1}$  were measured on KCl, KBr,  $\text{CaF}_2$ , LiF, NaCl, NaF,  $\text{LaF}_3$ ,  $\text{BaF}_2$ ,  $\text{MgF}_2$ ,  $\text{SrF}_2$ , and MgO enabling an identification of physisorption, volume, and surface chemisorption of impurities. The use of the infrared wavelength modulated spectroscopy of this work can be of great utility in monitoring crystal growth and surface preparation for optical materials for high-power laser and lightguiding systems requiring extremely low absorption levels. The system is capable of detecting a hundredth of a monolayer of surface species on a single crystal surface and so can play a role in catalysis studies.

This work was supported in part by the U.S. Army Research Office DAAG-29-K-0164, the Air Force Office of Scientific Research 78-3665, and the California-MICRO Program.

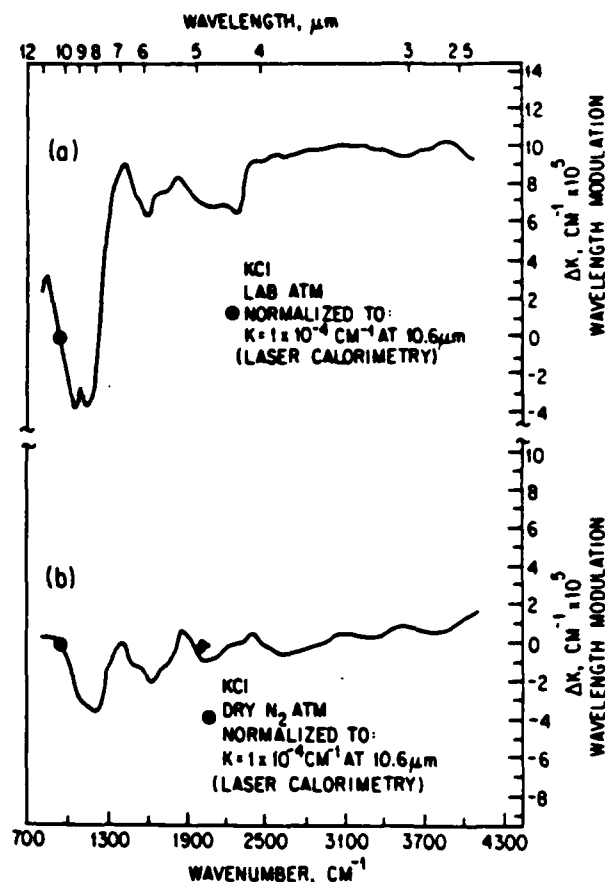


Fig. 15. Wavelength modulation absorption spectra of KCl;  $K$  is the absorption coefficient in  $\text{cm}^{-1}$ : (a) in the laboratory atmosphere; (b) in a dry  $\text{N}_2$  atmosphere.

## References

1. B. Bendow, in *Solid State Physics*, Vol. 33, F. Seitz and D. Turnbull, Eds. (Academic, New York, 1978), p. 249.
2. T. F. Deutsch, *J. Phys. Chem. Solids* **34**, 2091 (1973).
3. M. Sparks and L. J. Sham, *Solid State Commun.* **11**, 1451 (1972).
4. C. J. Duthler, *J. Appl. Phys.* **45**, 2668 (1974).
5. M. Hass, J. W. Davison, P. H. Klein, and L. L. Boyer, *J. Appl. Phys.* **45**, 3959 (1974).
6. J. A. Harrington, D. A. Gregory, and W. F. Otto, Jr., *Appl. Opt.* **15**, 1953 (1976).
7. M. Cardona, *Modulation Spectroscopy* (Academic, New York, 1969).
8. B. O. Seraphin and N. Bottka, *Phys. Rev.* **145**, 628 (1966).
9. G. W. Gobeli and E. O. Kane, *Phys. Rev. Lett.* **15**, 142 (1965).
10. B. Batz, *Solid State Commun.* **4**, 241 (1966).
11. E. Y. Wang, W. A. Albers, and C. E. Bleil, in *Proceedings, II-VI Semiconducting Compounds, 1967 Conference*, D. G. Thomas, Ed. (Benjamin, New York, 1967), p. 136.
12. M. Welkowsky and R. Braunstein, *Rev. Sci. Instrum.* **43**, 399 (1972).
13. R. Stearns, J. Steele, and R. Braunstein, *Rev. Sci. Instrum.* **54**, 984 (1983).
14. K. L. Shaklee, J. E. Rowe, and M. Cardona, *Phys. Rev.* **174**, 828 (1968).

15. M. Burd, R. Stearns, and R. Braunstein, *Phys. Status Solidi* (B) 117, 101 (1983).
  16. The laser calorimetric measurements were performed by Robert Curran of the Hughes Laboratories.
  17. M. Flannery and M. Sparks, in *Laser Damage in Optical Materials*, 1977, A. J. Glass and A. J. Guenther, Eds., NBS Spec. Publ. 509 (U.S. GPO, Washington, D.C., 1977), p. 5.
  18. T. F. Deutsch, *J. Electron. Mater.* 4, 663 (1975).
  19. M. Hass, J. A. Harrington, D. A. Gregory, and J. W. Davison, *Appl. Phys. Lett.* 28, 610 (1976).
  20. P. Handler and D. E. Aspnes, *Phys. Rev. Lett.* 17, 1095 (1966).
  21. M. L. Hair, *Infrared Spectroscopy in Surface Chemistry* (Marcel Dekker, New York, 1967).
  22. J. R. Howe and J. A. Harrington, *J. Appl. Phys.* 47, 4926 (1976).
  23. A. Hordvik, *Appl. Opt.* 16, 2827 (1977).
  24. Y. Kozirovski and M. Folman, *Trans. Faraday Soc.* 62, 1431 (1966).
  25. J. T. Gourly and W. A. Runciman, *J. Phys. C* 6, 583 (1973).
  26. D. W. Pohl, in *Optical Properties of Highly Transparent Solids*, S. S. Mitra and B. Bendow, Eds. (Plenum, New York, 1975).
-

# Status of point defects in HgCdTe<sup>a)</sup>

C. E. Jones

*Santa Barbara Research Center, Goleta, California 93117*

K. James and J. Merz

*University of California at Santa Barbara, Goleta, California 93117*

R. Braunstein, M. Burd, and M. Eetemadi

*University of California at Los Angeles, Los Angeles, California 90024*

S. Hutton and J. Drumheller

*Montana State University, Bozeman, Montana 59717*

(Received 15 October 1984; accepted 15 October 1984)

This paper reviews the status of point defect studies in HgCdTe and presents new data on the characterization of impurities in CdTe, on shallow and deep acceptors in arsenic-doped HgCdTe, and on the ability of electron paramagnetic resonance (EPR) to detect defects in HgCdTe. Point defects are important in controlling carrier concentrations, minority-carrier lifetimes, and noise in HgCdTe. Shallow impurities from dopants are fairly well understood and their effects follow what is expected from the periodic table. Intrinsic defects such as the mercury vacancy, which is believed to act as a shallow acceptor, are less well understood and suffer from a lack of characterization techniques that can identify individual defects. Deep-level defects are present with concentrations proportional to the shallow acceptor concentrations. These centers often control lifetime and noise. Many of these have been electrically characterized, but not identified. Theoretical work by several groups to calculate defect levels has begun. At present, the errors in this work are larger than the HgCdTe band gaps, but the calculated trends are important. Experimental data on identified deep levels are needed both for guiding material improvement and for improving the theoretical modeling.

## I. INTRODUCTION

The point defect studies considered in this paper are vacancies, interstitials, impurity atoms, and complexes. The effects of extended defects such as dislocations, grain boundaries, precipitates, and voids are not covered. In the simplest terms, the defects that introduce shallow levels in the HgCdTe band gap are important in controlling the free carrier type and concentration, while the defects with deep electronic levels in the gap can control minority-carrier lifetimes and noise.

The first section of this paper reviews the status of shallow defect doping and characterization, and the second section deals with deep level defect studies. This section also reviews some of the theoretical work on point defects in HgCdTe and makes some suggestions for future research.

## II. SHALLOW LEVEL DEFECTS

Shallow level defects have been introduced into Hg<sub>1-x</sub>Cd<sub>x</sub>Te both by annealing to adjust the mercury vacancy concentration, and by impurity doping. This section reviews the intrinsic defect reactions which give a basis for modeling the annealing behavior. It also reviews what is known about residual impurities and dopants in Hg<sub>1-x</sub>Cd<sub>x</sub>Te.

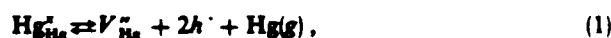
### A. Undoped HgCdTe

The carrier concentration in annealed, undoped HgCdTe is usually assumed to be due to mercury-vacancy acceptors. In many compound semiconductors, however, impurities that move into the metal ion vacancy have been found to be

the real acceptors. The data for CdTe and HgCdTe at present is mixed and incomplete. These data are reviewed here.

The enthalpy needed to produce a mercury vacancy in  $x = 0.2$  material is 2.2 eV compared with 4.7 eV estimated for producing the cadmium vacancy.<sup>1,2</sup> Because of the low formation energy for the mercury vacancy this species dominates the annealing effects. Heating to higher temperatures with low Hg overpressures tends to produce vacancies, and heating to low or moderate temperatures in high mercury overpressures tends to fill the vacancies. The defect kinetics for this have been modeled by Vydyanath<sup>1</sup> and data and predicted curves are shown in Fig. 1 for  $x = 0.2$  material.

The basic reactions are assumed to be



and



where  $x$ ,  $\cdot$ , and  $\cdot\cdot$  refer to neutral, negative, and positive elements, respectively, and the subscripts give the site. Each reaction corresponds to a mass action equation for the concentrations of the reactants, giving

$$K_{V_{\text{Hg}}}^{\cdot\cdot} = [V_{\text{Hg}}^{\cdot\cdot}][h^{\cdot}]^2/P_{\text{Hg}} \quad (3)$$

and

$$K_{\text{Hg}} = [\text{Hg}_{\text{Hg}}^{\cdot\cdot}][e^{\cdot}]^2/P_{\text{Hg}}. \quad (4)$$

The model includes assumptions that at the annealing temperatures the negative ion contribution is dominated by mercury vacancies, and that tellurium interstitials, impurities, and complexes can be neglected. As shown in Fig. 1, for high hole concentrations above  $10^{16} \text{ cm}^{-3}$ , the theory can be

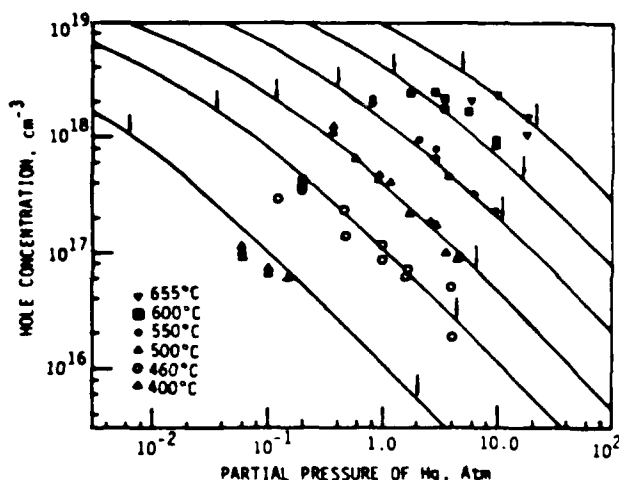


FIG. 1. Hole concentrations at 77 K as a function of partial pressure of Hg and anneal temperature for undoped  $\text{Hg}_{1-x}\text{Cd}_x\text{Te}$ . The solid lines are values calculated by a solid-state reaction model formulated by Vydyanath. Arrows define the material existence region.

fit well to the data. Similar data for  $x = 0.4$  material is able to explain the shift from  $[V_{\text{Hg}}] \sim P_{\text{Hg}}^{-1}$  shown in Eq. (3) to  $[V_{\text{Hg}}] \sim P_{\text{Hg}}^{-1/3}$  as being due to the change in the hole concentration at the annealing temperatures from intrinsic to vacancy-acceptor dominated.<sup>3</sup>

Comparison of undoped- with copper-doped material suggests that the mercury-vacancy acceptor in undoped material is a double acceptor. This shows up in the decreased mobility due to doubly charged ionic scattering in undoped material and in the defect introduction rates.<sup>1</sup>

Raman spectroscopy data obtained by Pollak *et al.*<sup>4</sup> have identified a defect mode with spherical symmetry, called the clustering mode, at  $136 \text{ cm}^{-1}$  in  $x = 0.2 \text{ HgCdTe}$  that would fit the vacancy symmetry and not that of a substitutional ion.<sup>4</sup> Rhiger and Cornilsen have found that this center is more intense in annealed  $\text{HgCdTe}$  with higher acceptor concentrations and presumably higher vacancy concentrations.<sup>5</sup>

The annealing data of Vydyanath and the Raman data suggest that the mercury vacancy is present in  $\text{HgCdTe}$  and that impurities moving into the vacancy at room temperature do not dominate for material with high mercury vacancy concentrations, i.e., above  $10^{16} \text{ cm}^{-3}$ .

While the mercury vacancy model seems to fit the data for  $\text{HgCdTe}$ , the metal vacancy is not seen as the dominant acceptor in  $\text{ZnS}$ ,  $\text{ZnSe}$ , and possibly  $\text{CdTe}$ . The vacancy is produced by the usual annealing or growth techniques, but residual impurities such as copper, silver, lithium, or sodium move into the vacancy producing single-level shallow acceptors.<sup>6</sup> Because of the ability of some defects to diffuse at room temperature the simple intrinsic defects are lost to substitutional impurities or complex formation.

In  $\text{CdTe}$  the evidence for impurity domination of the acceptor concentrations are based on luminescence data. Luminescence data for  $\text{CdTe}$  at low temperatures is shown in Fig. 2. From left to right (from high to low energies) free exciton (FE) luminescence is seen, excitons bound to shallow

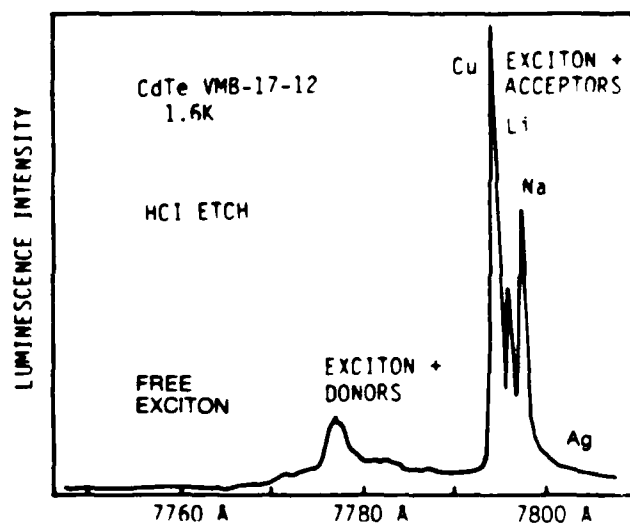


FIG. 2. Luminescence from  $\text{CdTe}$  at 1.6 K showing the recombination bands for the free exciton, exciton bound to shallow neutral donors, and excitons bound to neutral acceptors. The identifications are due to Molva *et al.*<sup>8</sup>

donors, then excitons bound to a series of shallow acceptors; off the figure at longer wavelengths ( $\sim 8250$  to  $8900 \text{ Å}$ ) donor-acceptor pair luminescence is also seen. Molva *et al.*<sup>7,8,9</sup> have done furnace diffusion impurity doping and have identified the major acceptor bands seen in  $\text{CdTe}$  with copper, lithium, sodium, and silver; these are labeled in the figure.

Energies identified for the shallow acceptors in  $\text{CdTe}$  are  $E_v + 0.147 \text{ eV}$  for copper,  $E_v + 0.059 \text{ eV}$  for sodium,  $E_v + 0.058 \text{ eV}$  for lithium,  $E_v + 0.263 \text{ eV}$  for gold,  $E_v + 0.107 \text{ eV}$  for silver,  $E_v + 0.056 \text{ eV}$  for nitrogen,  $E_v + 0.068 \text{ eV}$  for phosphorus, and  $E_v + 0.092 \text{ eV}$  for arsenic.<sup>10</sup> Figure 3

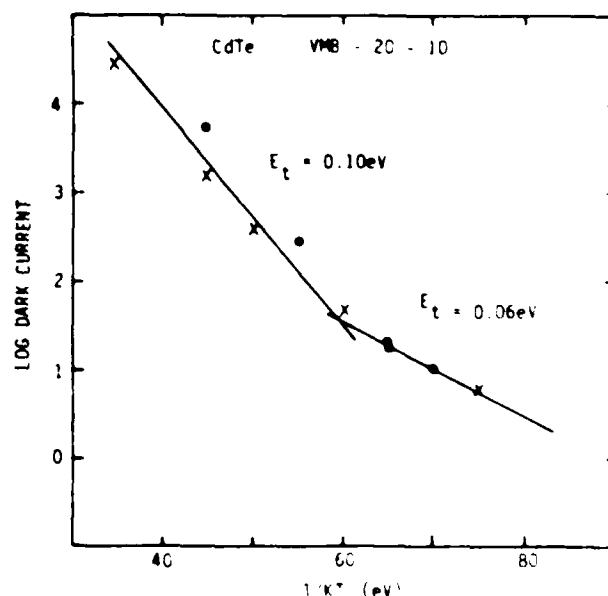


FIG. 3. Conductivity vs temperature for p-type  $\text{CdTe}$ , showing activation energies similar to those identified by luminescence for silver and alkali acceptors.



shows conductivity versus temperature data for a sample of CdTe.<sup>11</sup> The major shallow acceptors seen have energies of 0.11 and 0.06 eV, corresponding to the silver and alkali levels identified in the luminescence. Braunstein *et al.*<sup>11</sup> have shown the same levels in CdTe by photoinduced transient currents, a photoexcited DLTS technique that works in high-resistivity materials. These data are shown in Fig. 4.

It is very important to verify the identifications of the luminescence bands or the defect energy levels in CdTe. Magnetic field studies have shown that these bands are due to substitutional  $T_d$  symmetry centers, not vacancies.<sup>12</sup> Using the identified shallow acceptors, several techniques including luminescence, Hall effect, resistivity, photoinduced currents, and optical absorption can be used to characterize the acceptor levels, which may be due to copper, silver, sodium, or lithium in CdTe. Dean<sup>13</sup> has argued that bound exciton luminescence from the neutral vacancy may not be possible. The vacancy may be present and have an energy level similar to one of the other acceptors, and just not be seen in luminescence. The available data, however, suggest that the shallow acceptors in "undoped" CdTe are probably due to impurities, possibly copper, silver, and alkalis.

Low-temperature luminescence was reported for HgCdTe by Hunter and McGill,<sup>14</sup> but the bands were very broad, and it was not possible to resolve individual bound exciton bands for different acceptors. This makes luminescence impurity characterization and identification using a magnetic field<sup>12</sup> and stress perturbation studies (as was done in CdTe) very difficult in the HgCdTe alloys. Techniques to distinguish the various electrically active impurities in HgCdTe need to be further developed.

For lower carrier concentration levels, less than  $10^{16}$   $\text{cm}^{-3}$  copper, silver, and the alkalis may be important in controlling carrier type and concentration in "undoped" HgCdTe also. This has been described in several papers,<sup>15-17</sup> and the effect of lithium build-up in ion-implantation regions was reported by Bubulac *et al.*<sup>18</sup> In  $n$ -type undoped HgCdTe the carrier concentration is set by the residual donor impurities and not by the intrinsic defects, such as the mercury interstitial. Yoshikawa *et al.*<sup>19</sup> have suggested that

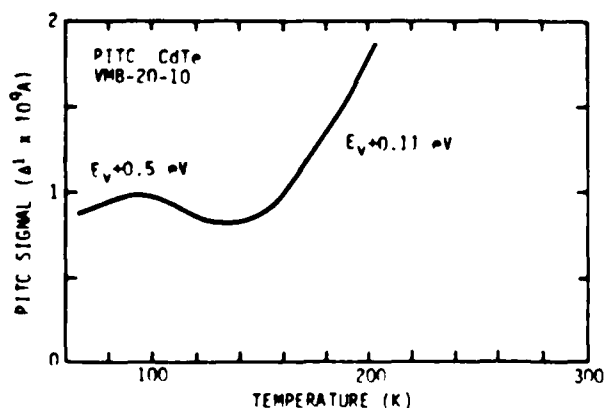


FIG. 4 Defect levels in semi-insulating CdTe as determined by photoinduced transient currents, again showing the same impurity energy level as seen in conductivity and luminescence.

an oxygen-related defect is one of the important residual donors. By decreasing the oxygen content of LPE HgCdTe the residual donor concentration could be reduced to the mid- $10^{13}$   $\text{cm}^{-3}$  level.

## B. Doped HgCdTe

Shallow impurity doping in HgCdTe<sup>20-22</sup> has been reported by several groups. The group I and group III elements tend to substitute for mercury and act as single acceptors and donors, respectively. The group V and VII elements act similarly on the tellurium sites. Silicon and germanium, which could go either way, seem to favor producing donors on the mercury sites. These trends are shown in a simplified periodic table in Fig. 5. No activity has yet been identified with carbon. One old rule of thumb that has fallen by the wayside is that all group I and group III elements are fast diffusers. Boron and indium implants have shown slow diffusion fronts after annealing, and indium-doped epitaxial layers have shown minimal interdiffusion after annealing. Indium, when evaporated as a metal on the surface of HgCdTe, seems to react with the material, possibly producing vacancies that cause the anomalously high indium diffusion for these conditions. No electrical activity has been observed for group II element zinc, at concentrations up to  $10^{19}$   $\text{cm}^{-3}$ .

Vydyanath *et al.*, have studied copper, indium, phosphorus, and iodine doping in HgCdTe and have modeled the solid-state defect reactions expected.<sup>3,23-25</sup> Electrically active indium is measurably lower than the total indium concentration and formation of the  $\text{In}_2\text{Te}_3$  compound is suggested. The modeling also suggests donor-acceptor pairs in iodine- and phosphorus-doped material involving  $(\text{I}_{\text{Te}} \text{V}_{\text{Hg}})^-$ ,  $(\text{P}_{\text{Hg}} \text{P}_{\text{I}})^0$ ,  $(\text{P}_{\text{Hg}} \text{V}_{\text{Hg}})^-$ , and  $(\text{P}_{\text{Hg}} \text{V}_{\text{Hg}})^+$ , where  $\text{I}_{\text{Te}}$  is iodine on a tellurium site, and  $\text{P}_{\text{Hg}}$  is phosphorus on a mercury site.

## C. Discussion

Mercury vacancy introduction explains the acceptor introduced by annealing in HgCdTe, but for low carrier concentrations such impurities as copper, silver, alkalis, and oxygen may be important. CdTe may be impurity-dominated even after annealing to produce vacancies. Doping follows the trends expected from the periodic table. Impurity characterization techniques for measurement of electrically

I	II	III	IV	V	VI	VII
Li	Be	B	C	N	O	F
Na	Mg	Al	Si	P	S	Cl
K	Ca	Sc	Ti	V	Cr	
Cu	Zn	Ga	Ge	As	Se	Br
Ag	Cd	In	Sn	Sb	Te	I
Au	Hg	Pb		Bi		
ACCEPTOR		DONOR	AMPHOTERIC		ACCEPTOR	DONOR

FIG. 5 Schematic Periodic Table showing the effect of doping on the carrier type in HgCdTe.

active copper, silver, alkali, and donor concentrations need to be verified for CdTe, and are not at all well-developed for HgCdTe. Several areas for further work include the following: determining if the Cd vacancy exists at room temperature in CdTe, characterizing the energy levels, sites and concentrations for interstitial atoms (which at present are completely unknown) verifying with impurity characterization techniques the assumed solid-state defect reactions, and determining the importance of defect complexes.

### III. DEEP-LEVEL IMPURITIES

Figure 6 shows the 77 K minority-carrier lifetime in undoped and arsenic-doped  $\text{Hg}_{0.7}\text{Cd}_{0.3}\text{Te}$  as a function of the total acceptor concentration. Similar data for undoped HgCdTe have been reported by Tobin<sup>26</sup> and Pollak *et al.*<sup>27</sup> In both cases shown in Fig. 6, the minority-carrier lifetime is inversely proportional to the acceptor concentration. The minority-carrier lifetime for the arsenic-doped material is three to ten times longer than that in equivalent undoped material. At low temperatures the expression for minority-carrier lifetime, due to recombination through deep traps, has the simple form

$$\tau = (\sigma_n \langle v_m \rangle N_T)^{-1}, \quad (5)$$

where  $\sigma$  = minority-carrier capture cross section at the deep defect,  $\langle v_m \rangle$  = minority-carrier average thermal velocity, and  $N_T$  = trap concentration.

The data in Fig. 6 suggest that there is a deep recombination center with a concentration  $N_T$  directly proportional to the shallow acceptor concentration. The deep center and the shallow acceptor do not have to be the same defect. The proportionality holds for any defect or complex involving the shallow acceptor due to mass action, as follows:

$$\begin{aligned} (\text{shallow acceptor}) + (\text{another defect}) &\xrightleftharpoons{K} (\text{complex}), \\ [\text{complex}] &= k [\text{acceptor}][\text{defect}], \end{aligned} \quad (6)$$

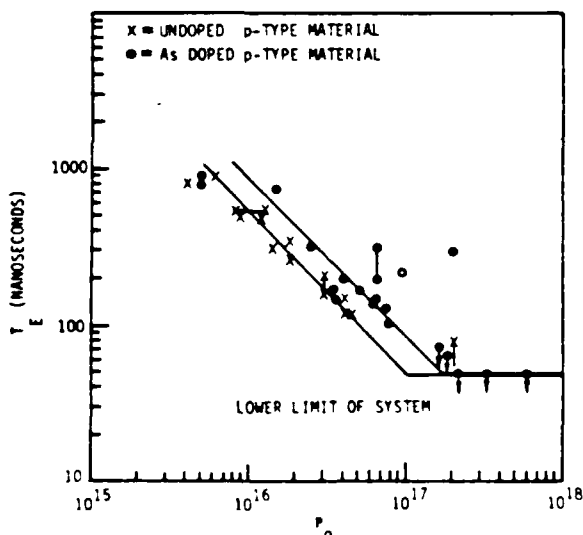


FIG. 6 Low temperature (77 K) minority-carrier lifetime in undoped and arsenic-doped  $\text{Hg}_{0.7}\text{Cd}_{0.3}\text{Te}$  ( $x = 0.3$ ) as a function of the total acceptor concentration (from W. A. Radford and C. E. Jones)

where the brackets denote concentrations and  $K$  is the mass action proportionality constant. Equation 6 shows that the concentration of a complex involving the shallow acceptor will be proportional to the acceptor concentration.

In earlier work, Jones *et al.*<sup>28,29</sup> have presented DLTS data characterizing the traps in undoped, copper-doped, and gold-doped HgCdTe. The DLTS technique is able to identify the trap energies, capture cross sections, and concentrations. These are the parameters needed to calculate the effect of a trap on the minority-carrier lifetime and noise.

For undoped HgCdTe, two traps are commonly observed at  $E_V + 0.4E_{gap}$  and  $E_V + 0.7E_{gap}$ , as well as the shallow acceptor level at  $E_V + 0.015$  eV, believed to be due to the mercury vacancy. The deep levels may be related to different charge states of the same defect, since increasing the electron flux during trap filling causes the one electron trap peak to decrease as the second increases. The concentrations of these defects have ranged from approximately equal to the shallow acceptor concentrations, to 1/100 of this value. This is another point suggesting the deep defect is a related defect, not another charge state of the shallow acceptor. The capture cross sections are larger for electron capture ( $\sigma_n \approx 10^{-16} \text{ cm}^2$ ) than for hole capture ( $\sigma_p \approx 10^{-19} \text{ cm}^2$ ), suggesting a donorlike defect. This is also contrary to the suggestion that these centers may be the second acceptor level of the mercury vacancy. The energies, capture cross sections, and concentrations for these deep levels were found to fit the minority-carrier lifetime and thermal-noise currents for the devices with no adjustable parameters.<sup>27</sup>

In copper-doped material, two new deep level defects were seen. The fact that the deep defects can be changed is important, since this indicates that the trapping and noise generation may be controllable with the proper dopant. The deep levels again appeared donorlike ( $\sigma_n > \sigma_p$ ) but their energies were fixed at  $E_V + 0.05$  eV and  $E_V + 0.15$  eV, even though  $x$  and the band gap were varied.

In the gold-doped samples different deep levels were seen in different samples, suggesting several different complexes could be formed depending on the other impurities or defects

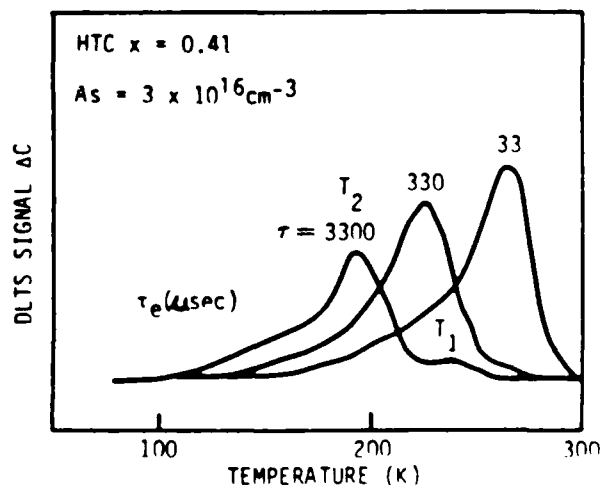


FIG. 7. DLTS spectra from arsenic-doped ( $3 \times 10^{16} \text{ cm}^{-3}$ )  $x = 0.41$   $\text{Hg}_{0.7}\text{Cd}_{0.3}\text{Te}$

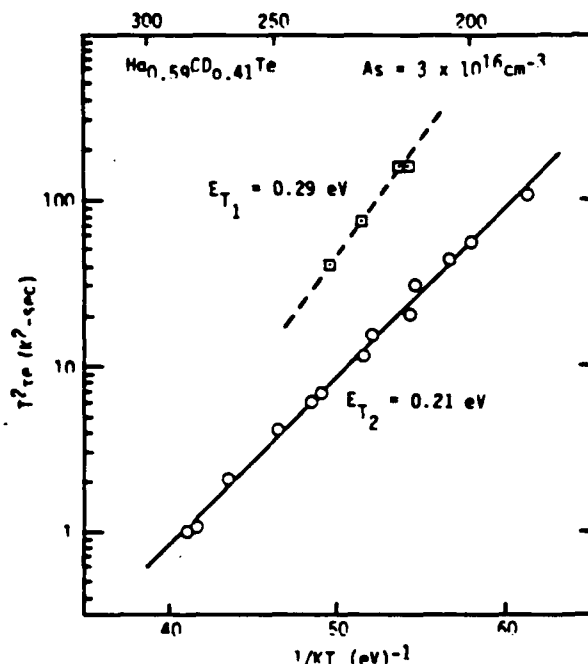


FIG. 8. Energy levels for two hole traps in arsenic-doped  $x = 0.41$   $\text{Hg}_{1-x}\text{Cd}_x\text{Te}$  as determined from the temperature dependence of the trap emission time constant  $\tau_p$ .

present, or on the thermal history. Again, the deep centers seemed donorlike with  $\sigma_n > \sigma_p$ . For both the gold and copper doping the dopant-related deep levels limited the minority-carrier lifetime, and dominated the noise generation.

New data have been obtained on arsenic-doped material. Arsenic predominantly substitutes on the tellurium site as an acceptor at  $E_v + 0.01$  eV for arsenic concentrations in the  $10^{16}$   $\text{cm}^{-3}$  range, or less. At high concentrations the activation energy is lowered due to overlap of acceptor wave functions, and  $E_a = E_v + 0.004$  eV at arsenic concentrations of  $5 \times 10^{17}$   $\text{cm}^{-3}$ . DLTS data for  $x = 0.4$   $\text{HgCdTe}$  doped to  $3 \times 10^{16}$   $\text{cm}^{-3}$  are shown in Fig. 7. One major peak is ob-

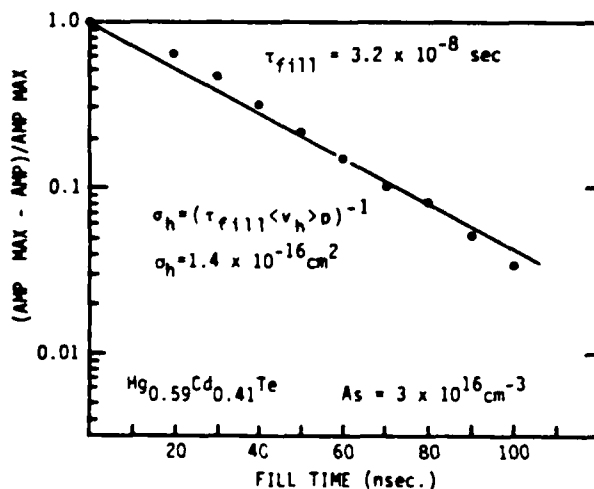


FIG. 9. Capture cross section for the arsenic-related trap determined from the trap filling-time constant.

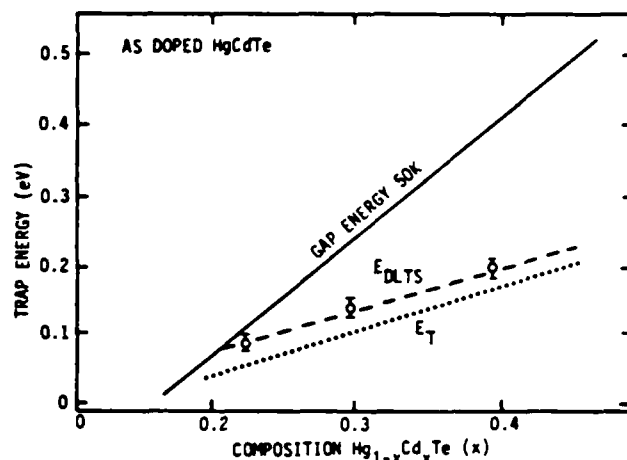


FIG. 10. The DLTS measured activation energies for the arsenic-related defect in  $\text{Hg}_{1-x}\text{Cd}_x\text{Te}$  ( $E_{\text{DLTS}}$ ) and the estimated defect energies, after correcting for the temperature dependence of the capture cross section ( $E_T$ ), are shown as a function of composition.

served with a concentration near  $3 \times 10^{16}$   $\text{cm}^{-3}$ . A smaller peak at higher temperatures is seen at a concentration of  $10^{15}$   $\text{cm}^{-3}$ . The emission rates as a function of temperature are shown in Fig. 8, and they yield uncorrected DLTS activation energies of 0.21 and 0.29 eV. The capture cross sections for holes can be determined from the time needed to fill the centers. These data are shown in Fig. 9.

The major center in the arsenic-doped material has  $\sigma_n = 10^{-20}$   $\text{cm}^2$  and  $\sigma_p \approx 10^{-16}$   $\text{cm}^2$ . The major center acts as if it is a multiple acceptor, with both hole and electron capture taking place on a negative center. The minor center acts donorlike, with electron capture being easier than hole capture. This minor center in this sample seems to be the one predominantly seen in undoped  $\text{HgCdTe}$ . Because of its small minority-carrier (electron) capture cross section, the major center does not control the minority carrier lifetime; the minor center does. In the arsenic-doped material the carrier concentration can be controlled by the arsenic doping level, while the minority-carrier lifetime can be controlled to some extent by annealing to remove mercury vacancies, which also lowers the concentration of the center commonly observed in undoped material.

Data for  $x = 0.2$  and  $x = 0.3$  material have also been taken, and the energy levels for the center that seems to be arsenic-related are shown in Fig. 10. The energy level scales with the band gap, as do the levels seen in undoped material, but in contrast to the levels in copper-doped material, which were fixed relative to the valence band.

### A. Defect Identification

While the deep-level defects have been characterized electrically, and their concentrations related to different shallow acceptors, there are still no firmly identified deep-level defects. Theoretical calculations of defect energy levels so far only provide an indication of trends, since the accuracy is probably on the order of  $\pm 0.5$  eV, much larger than the  $\text{HgCdTe}$  band gap. In a simplified picture, the energy levels

of a defect depend on the potential chosen, and on the overlap of the defect wave function with the wave function of the host crystal having the same symmetry. Chen and Sher<sup>30</sup> recently compared the expected energy levels for defects in CdTe using four different literature calculations for the CdTe wave functions and energies. Even using the same potential, a defect could shift in energy from near the valence band to near the conduction band, depending on the model used for the CdTe.

A few firmly identified deep levels in HgCdTe would help establish the theoretical parameters, and would provide extensive leverage in allowing the energies of many other defect centers to be estimated with usable accuracy. One general trend in the calculations is the change in a defect level as the  $\text{Hg}_{1-x}\text{Cd}_x\text{Te}$   $x$  value is changed.<sup>31,32</sup>  $p$ -type states on the tellurium site are fixed relative to the valence band, while the  $s$ -states on tellurium and the  $s$ - and  $p$ -states on the mercury site tend to scale with the band gap.

The centers in undoped and arsenic-doped HgCdTe scaled with the band gap, suggesting mercury site defects, while the levels in copper-doped HgCdTe stayed fixed relative to the valence band, suggesting tellurium-site defects.

Preliminary data on two other experimental techniques that may help identify defect models have recently been obtained. Amirtharaj *et al.*,<sup>4</sup> reported work with polarized Raman scattering on single-crystal material, and were able to distinguish symmetries for scattering centers. Electron paramagnetic resonance (EPR) techniques can be used to determine defect atomic components and defect symmetries, and have been very important in identifying defects and defect

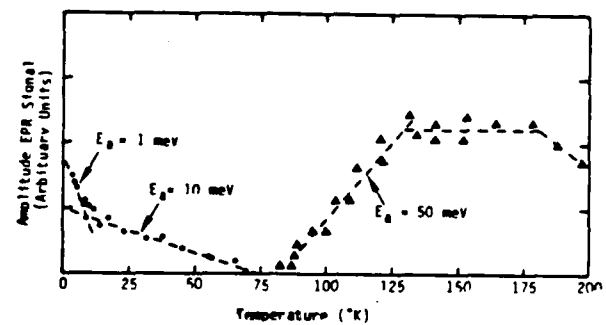


FIG. 11. Temperature dependence for the EPR centers observed in  $p$ -type undoped  $\text{Hg}_{1-x}\text{Cd}_x\text{Te}$ ,  $x = 0.3$ .

reactions in silicon and GaAs. Initial EPR work with CdTe was often without success, and it was not known whether the alloy effects would broaden the HgCdTe spectra so much that they would be undetectable. Initial studies by Hutton, Drumheller, and Jones have revealed several EPR centers in undoped  $x = 0.3$  HgCdTe. One, or possibly two, shallow acceptors are seen near  $g = 2.35$  to  $2.5$ , one with an activation energy of  $1 \text{ meV}$ , the other with  $E_a = 10 \text{ meV}$ , which may be the mercury vacancy. A deep center near  $g = 3.0$  with an activation energy of  $0.050 \text{ eV}$  seems to have  $(111)$  wave-function symmetry. The temperature dependencies of the EPR centers are shown in Fig. 11.

While detailed structures still have to be worked out for both the Raman and EPR centers, it is encouraging to know that these techniques will work in HgCdTe alloys.

TABLE I. Deep-level centers seen in  $\text{Hg}_{1-x}\text{Cd}_x\text{Te}$ .

Material	Levels	Data	Suggested models
Undoped HgCdTe	2 levels at $E_v + 0.4 E_g$ and $E_v + 0.7 E_g$	Donorlike ( $\sigma_n > \sigma_p$ ). Levels probably different states of the same defect. Concentration varies from 1 to 1/100 [Hg] vac. concentration. These control lifetime and noise in undoped material.	Hg interstitial, Si, C, or Cl on Hg site, or Te antisite.
Cu doped	2 levels $E_v + 0.05 \text{ eV}$ $E_v + 0.150 \text{ eV}$ . Fixed relative to $E_v$	Donorlike. These control lifetime and noise in Cu doped material.	Cu on Te site, or Cu complex with a donor.
As doped	Several different levels seen in different samples.	Donorlike.	As related multiple complexes.
As doped	One level near $1/2 E_{gap}$ with the common undoped defects, seen depending on the anneal.	Acceptorlike ( $\sigma_p > \sigma_n$ ). Not a good recombination center.	Complex of As.

## B. Discussion of deep-level defects

A summary of the data on deep levels in HgCdTe is given in Table I. Several comments on the status of deep level studies can be made; (a) Detailed electrical data on trap energies, capture cross sections, and concentrations have been obtained, (b) the deep levels are important in controlling minority-carrier lifetimes and noise in HgCdTe, and (c) there are no firmly identified deep-level centers in HgCdTe.

## IV. CONCLUSIONS

Foreign elements dope HgCdTe as expected from the Periodic Table, but characterization techniques that can identify different electrically active shallow-level impurities need to be developed. Little is known of the role of interstitials, especially the mercury interstitial in HgCdTe. It is not known how important interstitials or complexes are in ion implantation or radiation damage effects. The solid-state reaction models have given a framework for estimating the major defect concentrations as a function of annealing. These reaction models need to be reinforced with independent measurements of identified defect concentrations. For lower doping levels residual impurities are very important in HgCdTe. Good progress has been made on electrically characterizing the deep-level centers. Further work on identifying centers in HgCdTe with Raman, EPR, or optical techniques is needed to guide the material development and theoretical work.

## ACKNOWLEDGMENTS

The authors would like to thank AFWAL Materials Laboratory and NV&EOL for support for DLTS and EPR work, respectively. The authors would also like to thank W. A. Radford, M. H. Kalisher, and R. P. Ruth for discussions of this paper, and several scientists, including D. R. Rhiger, F. Pollack, A. B. Chen, A. Sher, J. Dow, R. H. Vydyanath, and C. W. Myles for discussing their own current research progress with us during preparation of this paper. The CdTe studies are part of a joint SBRC program with UCLA and UCSB, supported by SBRC IR&D funds and by the State of California MICRO Program.

\*Partially supported by AFWAL/ML, WPAFB, and NV&EOL, under Contract No. F33615-82-C-5122.

- <sup>1</sup>H. R. Vydyanath, *J. Electrochem. Soc.* **128**, 2609 (1981).
- <sup>2</sup>S. S. Chern, H. R. Vydyanath, and F. A. Kroger, *J. Solid State Chem.* **14**, 361 (1975).
- <sup>3</sup>H. R. Vydyanath, J. C. Donovan, and D. A. Nelson, *J. Electrochem. Soc.* **128**, 2625 (1981).
- <sup>4</sup>P. M. Amirharaj, K. K. Tiong, P. Parayanthal, Fred H. Pollak, and J. K. Furdyna (these proceedings).
- <sup>5</sup>D. Rhiger and B. C. Cornilsen, Paper N8, Electronic Materials Conference, Santa Barbara, CA, June 20-22, 1984.
- <sup>6</sup>O. J. Fitzpatrick, C. J. Werkhoven, T. F. McGee, P. M. Harnack, S. P. Herko, R. N. Bkargava, and J. P. Dean, *IEEE Trans. Electron. Devices* **28**, 440 (1981).
- <sup>7</sup>J. P. Chamonal, E. Molva, and J. L. Pautrat, *Solid State Commun.* **43**, 801 (1982).
- <sup>8</sup>E. Molva, J. P. Chamonal, G. Milchberg, K. Saminadazar, B. Pajot, and G. Neu, *Solid State Commun.* **44**, 351 (1982).
- <sup>9</sup>E. Molva, J. P. Chamonal, and J. L. Pautrat, *Phys. Status Solidi B* **109**, 635 (1982).
- <sup>10</sup>E. Molva, K. Saminadayer, J. L. Pautrat, and E. Ligeon, *Solid State Commun.* **48**, 955 (1983).
- <sup>11</sup>Unpublished results obtained by R. Braunstein, M. Burd, and M. Etemadi of UCLA, and C. Jones of SBRC.
- <sup>12</sup>E. Molva and Le Si Dang, *Phys. Rev. B* **27**, 6222 (1983).
- <sup>13</sup>J. P. Dean, *J. Lumin.* **21**, 75 (1979).
- <sup>14</sup>A. T. Hunter and T. P. McGill, *J. Vac. Sci. Technol.* **21**, 205 (1982).
- <sup>15</sup>H. F. Schaake, J. H. Tregilgas, J. D. Beck, M. A. Kinch, and B. E. Gnade (these proceedings).
- <sup>16</sup>J. Tregilgas, J. Beck, and B. Gnade (these proceedings).
- <sup>17</sup>J. Tregilgas and B. Gnade (these proceedings).
- <sup>18</sup>L. O. Bubulac, W. E. Tennant, R. A. Riedel, J. Bajaj, and D. D. Edwall, *J. Vac. Sci. Technol. A* **1**, 1646 (1983).
- <sup>19</sup>M. Yoshikawa, S. Veda, K. Maruyama, and H. Takigawa (these proceedings).
- <sup>20</sup>C. L. Jones, M. J. T. Quelch, P. Capper, and J. J. Gosney, *J. Appl. Phys.* **53**, 9080 (1982).
- <sup>21</sup>E. S. Johnson and J. L. Schmit, *J. Electron. Mater.* **6**, 25 (1977).
- <sup>22</sup>M. Kalisher, Presented at Sixth American Conference on Crystal Growth, Atlantic City, NJ, 1984.
- <sup>23</sup>H. R. Vydyanath and F. A. Kroger, *J. Electron. Mater.* **11**, 111 (1982).
- <sup>24</sup>H. R. Vydyanath, R. C. Abbotta, and D. A. Nelson, *J. Appl. Phys.* **54**, 1323 (1982).
- <sup>25</sup>H. R. Vydyanath, *J. Electrochem. Soc.* **128**, 2619 (1981).
- <sup>26</sup>S. P. Tobin, M. S. thesis, Massachusetts Institute of Technology, 1979.
- <sup>27</sup>D. L. Polla, R. L. Aggarwal, D. A. Nelson, J. F. Shanley, and M. B. Reine, *Appl. Phys. Lett.* **43**, 941 (1983).
- <sup>28</sup>C. E. Jones, V. Nair, J. Lindquist, and D. L. Polla, *J. Vac. Sci. Technol.* **21**, 187 (1982).
- <sup>29</sup>C. A. Merilainen and C. E. Jones, *J. Vac. Sci. Technol. A* **1**, 1637 (1983).
- <sup>30</sup>A. B. Chen and A. Sher, *Bull. Am. Phys. Soc.* **29**, 251 (1984).
- <sup>31</sup>A. Kolayaski, O. F. Sankey, and J. D. Dow, *Phys. Rev. B* **25**, 6367 (1982).
- <sup>32</sup>C. W. Myles and O. F. Sankey, *Phys. Rev. B* **29**, 6810 (1984).

phys. stat. sol. (b) 180, 595 (1985)

Subject classification: 13.1 and 20.1; 1.2; 21.1

Department of Physics, University of California, Los Angeles<sup>1)</sup>

# Wavelength-Modulated Spectra of the Optical Properties of $\beta'$ -Cu<sub>2</sub>Zn<sub>1-x</sub> from 1.5 to 5.1 eV at the $\beta' \rightleftharpoons \alpha + \beta'$ Phase Transition<sup>2)</sup>

By

R. STEARNS<sup>3)</sup>, R. BRAUNSTEIN, and L. MULDAWER<sup>4)</sup>

Wavelength-modulated derivative spectra of the reflectivity of  $\beta'$ -Cu<sub>2</sub>Zn<sub>1-x</sub> are determined between 1.5 and 5.1 eV for compositions near the  $\beta' \rightleftharpoons \alpha + \beta'$  phase transition. The alloys are annealed and quenched in the  $\beta'$  phase on both sides of the phase transition. Both the intraband and interband properties show marked changes at the transition. The Drude effective mass increases dramatically for the  $\beta'$  phase in the region where  $\alpha + \beta'$  composition is thermodynamically preferred, indicating flattening of the bands. Shifts in interband properties also show a marked change at the phase transition, with the conduction bands showing a much greater sensitivity than the d-bands.

Wellenlängen-modulierte Ableitungsspektren des Reflexionskoeffizienten von  $\beta'$ -Cu<sub>2</sub>Zn<sub>1-x</sub> werden zwischen 1,5 und 5,1 eV für Zusammensetzungen nahe des  $\beta' \rightleftharpoons \alpha + \beta'$ -Phasenübergangs bestimmt. Die Legierungen werden in der  $\beta'$ -Phase auf beiden Seiten des Phasenübergangs getempert und abgeschreckt. Sowohl die Interband- als auch die Intrabandeigenschaften zeigen ausgeprägte Änderungen am Übergang. Drudes effektive Masse steigt für die  $\beta'$ -Phase in dem Bereich, wo die  $\alpha + \beta'$ -Zusammensetzung thermodynamisch bevorzugt ist, dramatisch an, was ein Abflachen der Bänder anzeigt. Verschiebungen der Interbandeigenschaften bestätigen diese Deutung und weisen auf konkurrierende physikalische Mechanismen hin, die diese Verschiebungen verursachen.

## 1. Introduction

Ordered beta brass ( $\beta'$ -CuZn) is a traditional prototype binary alloy obeying the Hume-Rothery rules [1]. Its theoretical electronic band structure, Fermi surface phase stability, optical and other properties have been the subjects of extensive study [2 to 8]. The wavelength-modulated spectra of the optical properties of a series of compositions of this alloy system have been studied in the hope that they will help lead to a better determination of the Cu and Zn potentials.

The individual shapes of conduction and Cu d-bands are, according to calculations [2], largely independent of small variations in crystal potential; however, the relative position of the d-bands and conduction bands were shown to be very sensitive to the nature of the potential. The bands originating from the d- and lower core electrons of the elements depend primarily on the nature of the potentials within a radius of one atomic unit [3]. Self-consistent free-atom potentials provide a reasonably accurate description of the fields experienced by these electrons. It is the behavior of the potential between 1 at. unit and the atomic cell boundary which is most uncertain.

<sup>1)</sup> Los Angeles 90024, USA.

<sup>2)</sup> Work supported in part by the U.S. Army Research Office, Durham, North Carolina, and by the Air Force Office of Scientific Research.

<sup>3)</sup> Current address: Newport Corporation, Fountain Valley, CA 92708, USA.

<sup>4)</sup> Permanent address: Temple University, Philadelphia, PA 19122, USA.

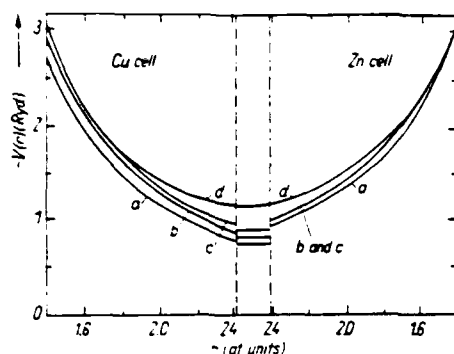


Fig. 1. Comparison of crystal potentials for  $\beta'$ -CuZn based on modification of free-atom potentials (from [3])

The energies of the valence electrons are very sensitive to variations of the potential in this region and to changes of the constant potential  $V_0$  between muffin-tin spheres. The conduction bands can be shifted relative to the d-bands simply by altering the slopes of the potentials beyond a radius of 1 at. unit or by adjusting  $V_0$ . This is illustrated in Fig. 1 for several possible potentials chosen for Cu and Zn. The resulting band profiles for the stoichiometric alloy along the  $[110]$  direction in the cubic Brillouin zone are shown in Fig. 2. It can be seen that the d-bands are effectively shifted with respect to the conduction bands for various choices of potentials.

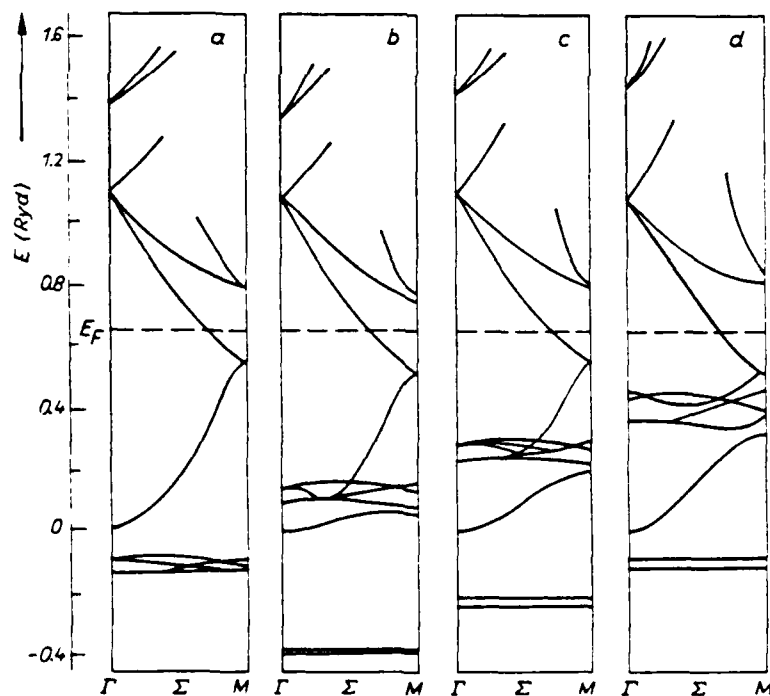


Fig. 2. Comparison of band profiles in  $(\Gamma\Sigma M)$  direction resulting from potentials of Fig. 1 (from [3])

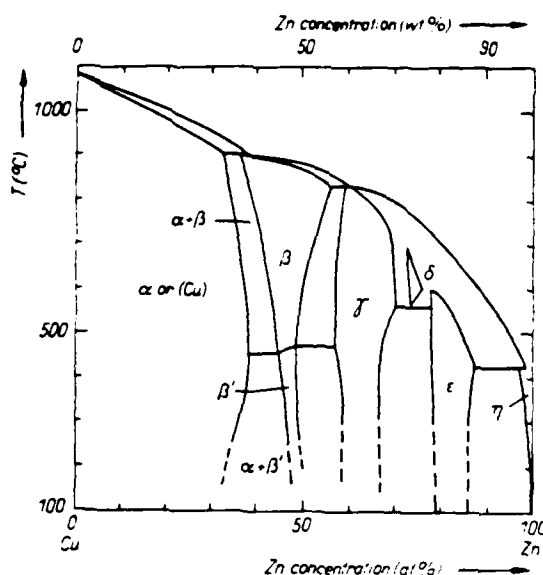


Fig. 3. Phase diagram of CuZn alloy system (from [9])

The phase diagram of the CuZn alloy system is given in Fig. 3 (cf. [9]). The  $\beta'$ -phase is an ordered alloy of the CsCl(B2) type. This phase exists at low temperature within a narrow range of compositions. At higher temperatures it disorders to the  $\beta$ -phase which is a random alloy with a body-centered cubic structure. It should be noted that the  $\beta \rightarrow \beta'$  transformation cannot be suppressed by quenching [10]. At lower zinc compositions the  $\beta'$ -phase goes into an  $\alpha + \beta'$  phase. Pure  $\beta'$ -phase material may be quenched from the  $\beta$ -phase even in the composition range where the  $\alpha + \beta'$  phase is thermodynamically preferred at room temperature.

It should be instructive, then, to examine the optical properties, with their implications for band structure, as the  $\beta' \rightleftharpoons \alpha + \beta'$  phase boundary is crossed. If samples are obtained which have pure  $\beta'$ -composition on both sides of the boundary, the effects of the changes in the crystal potential due to the thermodynamic stresses involved when the crystal is not in its lowest energy state may be studied. The intent of this study is to provide experimental data concerning the optical properties of this alloy system near this phase boundary, in order to stimulate continued theoretical interest in this problem.

## 2. Sample Preparation

A series of samples was produced by melting high-purity copper and zinc in sealed evacuated quartz tubes. Sample composition was determined by a microprobe analysis. The three samples were found to be  $\text{Cu}_{0.54}\text{Zn}_{0.46}$ ,  $\text{Cu}_{0.52}\text{Zn}_{0.48}$ , and  $\text{Cu}_{0.50}\text{Zn}_{0.50}$ . The samples were cut with a string saw and polished, the final polish being with  $0.3 \mu\text{m}$  alpha alumina polishing compound. They were then annealed for 1 h at high temperature in the  $\beta$ -phase, again in evacuated quartz tubes. The samples were quenched to room temperature and given a final light polish to remove any oxide layer. A final low-temperature anneal at  $100^\circ\text{C}$  relieved any residual cold-work. This temperature was low enough to prevent dezincification or precipitation of the  $\alpha$ - or  $\gamma$ -phase.



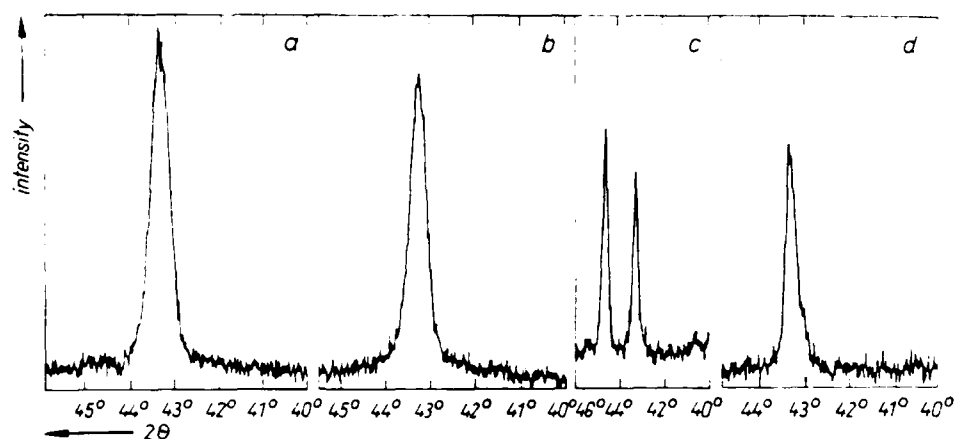


Fig. 4. X-ray diffraction scans of  $\text{Cu}_x\text{Zn}_{1-x}$  samples as a function of  $2\theta$ , where  $\theta$  is the X-ray incident angle, is evident at  $2\theta = 43.3^\circ$ .  $\alpha$ -phase would appear at  $42.2^\circ$ . a)  $x = 0.54$ , b)  $0.52$ , c)  $0.50$  showing martensite line at  $44.7^\circ$ , d) pure  $\beta$ -phase material in  $x = 0.50$  sample after low-temperature anneal to eliminate martensite

Crystal structures of the samples were determined by X-ray diffraction analysis. Fig. 4 a and b show the scans of the  $\text{Cu}_{0.54}\text{Zn}_{0.46}$  and  $\text{Cu}_{0.52}\text{Zn}_{0.48}$  samples. The diffraction line at  $43.3^\circ$  in each is due to  $\beta$ -phase material. If there were any  $\alpha$ -phase material present, it would reveal itself by producing a line at  $42.2^\circ$ . Thus, we may conclude that these are pure  $\beta$ -phase samples. Fig. 4c shows the first scan of the  $\text{Cu}_{0.50}\text{Zn}_{0.50}$  sample, showing an additional line present at  $44.7^\circ$  for this sample. This is due to a martensitic phase, which is a deformation of the  $\beta$ -phase. This is caused by unrelieved thermal stresses which occur in the quenching process [11]. An additional 48 h low-temperature anneal was given to relieve these stresses. This produced the results shown in Fig. 4d, which indicate that pure  $\beta$ -phase material has again been obtained.

### 3. Experimental Method

Wavelength-modulation spectroscopy [12, 13] was used because of the unambiguous lineshapes obtained by the technique and the resulting ease of interpretation of those results. The theory of wavelength-modulation spectroscopy is well detailed elsewhere [14, 15]. The theory of lineshapes near a three-dimensional critical point was given by Batz [16, 17]. It is sufficient here to give the theoretical lineshapes for the sake of

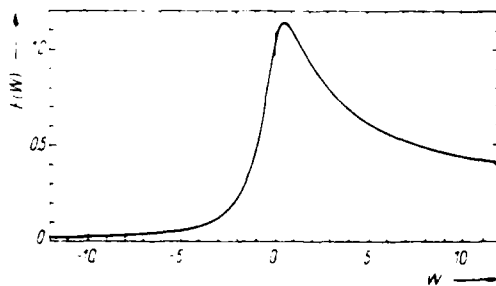


Fig. 5. Universal function,  $F(W)$ , derived by Batz [16, 17] for lineshapes near critical points as seen in wavelength modulation spectroscopy.  $F(W) = [W^2 + 1]^{-1/2} [(W^2 + 1)^{1/2} + W]^{1/2}$ , where  $W$  is the reduced frequency  $(\omega - \omega_g)/\eta$ ,  $\hbar\omega_g$  is the interband energy at the critical point and  $\eta$  is a phenomenological broadening parameter

Table 1  
Derivative of critical points with broadening included in terms of  $F(W)$

critical point	$2\eta^{1/2} \frac{d\epsilon_1}{d\omega}$	$2\eta^{1/2} \frac{d\epsilon_2}{d\omega}$
$M_0$	$F(-W)$	$F(W)$
$M_1$	$-F(W)$	$F(-W)$
$M_2$	$-F(-W)$	$-F(W)$
$M_3$	$F(W)$	$-F(-W)$

$$F(W) = [(W^2 + 1)^{1/2} + W]^{1/2} / (W^2 + 1)^{1/2}; W = (\omega - \omega_0)/\eta.$$

reference. All three-dimensional critical-point lineshapes may be expressed in terms of a single function,  $F(W)$ , which is reproduced in Fig. 5. The behavior of critical points in terms of  $F(W)$  is listed in Table 1. Derivative data with a resolution of 0.02 eV were taken between 1.50 and 5.10 eV.

The ultimate limit of the wavelength modulation derivative spectrometer used in this investigation is to be able to detect a derivative signal of the order of  $\Delta R/R \approx 10^{-5}$ . It is important to remember that when the experimental signal is actually of this order, the signal-to-noise ratio is about one. This will also be seen in the integral optical functions. Also, when the derivative is nearly flat, the same considerations may lead to noise in the optical functions. We may express this analytically as saying that the error bars will be larger when  $\Delta R/R$  is small or when  $d(\Delta R/R)/d\lambda$  is small.

This is the source of the anomalous structure which will be seen at the low energy end of these spectra. This is also the source of the noise in the high-energy regions which make exact assignment of d-band-to-conduction band transitions impossible.

#### 4. Experimental Results

The logarithmic derivatives of this series of samples, which are the direct experimental results, are illustrated in Fig. 6. These are integrated to yield the reflectivities shown in Fig. 7. In order to analyze these results, the dielectric function must first be calculated.

The Kramers-Krönig dispersion relation must be used to find the phase shift, so that other optical properties may be calculated from the reflectivity and the phase shift. To perform the integrals involved, the reflectivities must be extrapolated over the entire energy spectrum. On the infrared side, a Hagen-Rubens extrapolation (cf. [18]) is used to match the low-energy end of the experimental spectrum and a reflectivity of 100% at zero energy. The data of Muldawer and Goldman [19] are used from 5.1 to 18 eV. At higher energies, a constant reflectivity was used. This brings us into consistency with the other work [19], so results may be compared. Using this information, the real and imaginary parts of the dielectric function,  $\epsilon_1$  and  $\epsilon_2$ , are calculated. These are found in Fig. 8. Their derivatives are found numerically and are displayed in Fig. 9.

There are several points to note about the reflectivity data. The position of the main minimum in the reflectivity moves from lower to higher energy as the copper concentration decreases. The minima are at 2.48, 2.64, and 2.68 eV for 50, 48, and 46% zinc, respectively. This is in agreement with the results of Muldawer and Goldman [19]. The depth of the reflectivity minimum increases as the zinc concentration increases. At 50% zinc the minimum reflectivity is 35.2%, while at 46% zinc the minimum is at 16.9%.

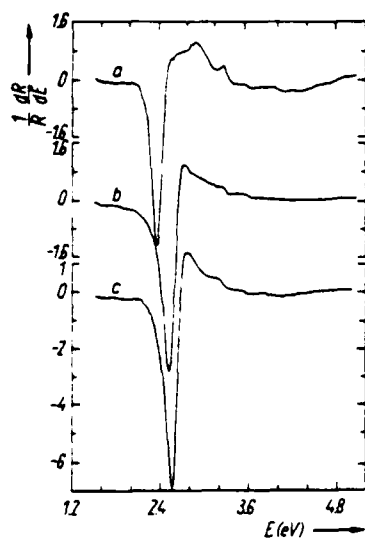


Fig. 6

Fig. 6. Wavelength-modulated derivative of the reflectivity of  $\text{Cu}_x\text{Zn}_{1-x}$ . (a)  $x = 0.50$ , (b) 0.52, (c) 0.54

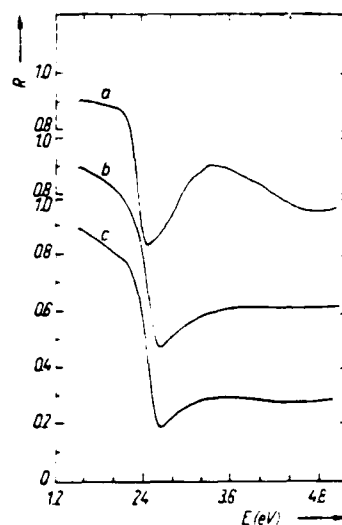


Fig. 7

Fig. 7. Reflectivity,  $R$ , of  $\text{Cu}_x\text{Zn}_{1-x}$ , which is found by integrating the data of Fig. 6. (a)  $x = 0.50$ , (b) 0.52, (c) 0.54

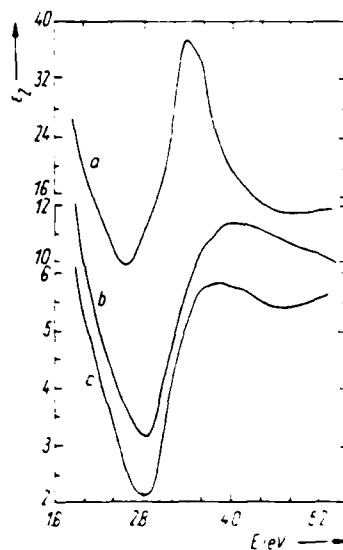
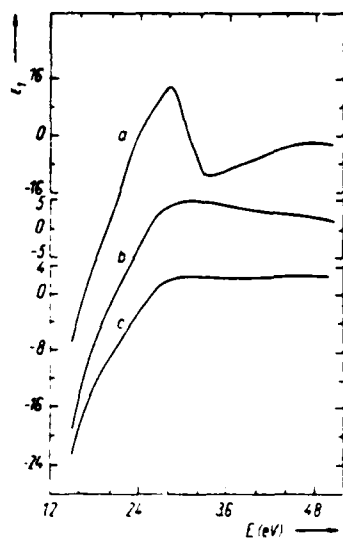


Fig. 8. Real part ( $\epsilon_1$ ) and imaginary part ( $\epsilon_2$ ) of the dielectric function of  $\text{Cu}_x\text{Zn}_{1-x}$ . (a)  $x = 0.50$ , (b) 0.52, (c) 0.54

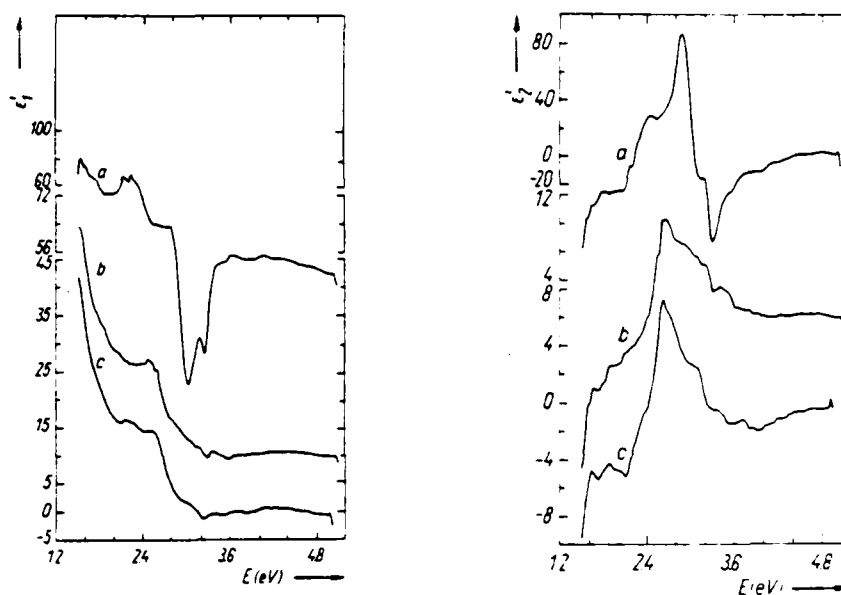


Fig. 9. Derivatives with respect to energy of  $\epsilon_1$ ,  $\epsilon_1'$  and with respect to  $\epsilon_2$ ,  $\epsilon_2'$ , of  $\text{Cu}_x\text{Zn}_{1-x}$ . (a)  $x = 0.50$ , (b) 0.52, (c) 0.54

The final note is that the reflectivity at higher energies is essentially featureless and does not show the structure which has been reported [19]. In this matter, it is similar to the data which Jan and Vishnubhatla [20] obtained for CuZn. The reasons for this will be discussed in the later section on interband transitions.

### 5. Intraband Transitions

The intraband and interband contributions to the dielectric function have been separated using a method of deconvolution which was previously described [21, 22]. The values of the Drude effective mass and relaxation time for each alloy composition are given in Table 2.

The relaxation times are slightly higher than others have found by optical means for this alloy system [19, 20]. However, it should be noted that the relaxation times calculated from resistivity data are an order of magnitude larger than those found by optical means [19].

Table 2  
Drude optical parameters

composition		effective mass to free-electron mass $m^*/m_0$	relaxation time ( $10^{-13}$ s)
(% Cu)	(% Zn)		
54	46	1.89	2.64
52	48	1.17	2.13
50	50	1.20	3.69

The most striking feature of the data in Table 2 is the change in effective mass. The values of 1.20 for 50% and 1.17 for 48% zinc are not far from the value of 1.4 reported for 50% zinc [20]. The effective mass of 1.89 free-electron masses found for the 46% zinc sample represents a significant departure from the other compositions. This means that there is a considerable flattening of the energy bands near the Fermi surface when the  $\beta' \rightarrow \alpha + \beta'$  phase transition has been crossed (Fig. 3) at the lower zinc concentration.

### 6. Plasma Resonance

Before making interband assignments, we need to look at the structure which dominates the experimental spectrum, the main plasma resonance which is responsible for the main dip in the reflectivity. The plasma resonance occurs when the real part of the dielectric function goes through zero. In the CuZn system this happens at a point very near to the onset of interband transition. For the 50% zinc sample, the plasma resonance is at 2.45 eV, while for the 48% and 46% zinc samples the resonance is at 2.57 and 2.59 eV. The peak in the energy loss function (Fig. 10) due to the plasma resonance is greatly damped because of the relatively large values of  $\epsilon_2$  in the region. This is because of the proximity of the onset of interband transitions to the plasma resonance.

### 7. Fermi Level-to-Conduction Band Transitions

Once the Drude parameters have been determined, they may be used in the classical Drude expressions for the dielectric function to subtract the intraband contribution from the total experimentally determined dielectric function. The remaining functions are the interband parts of the dielectric function. The real parts of this,  $\epsilon_{1b}$ , are displayed in Fig. 11, left part, while the imaginary parts,  $\epsilon_{2b}$ , are given in Fig. 11, right part, for the three samples. The derivatives of these are shown in Fig. 12, left and right part, respectively. These results are now used to analyze and assign the interband transitions in the alloy system.

The band structure of ordered beta-brass as calculated by Amar and co-workers [3, 4] is shown in Fig. 13. The derivatives of interband parts of the dielectric function

which have been measured may now be compared to the band calculations using the theory of Batz [16, 17] for wavelength-modulation data.

The onset of interband transitions has previously been identified as the Fermi level to conduction band transitions,  $\Sigma_4 \rightarrow \Sigma_1$  and  $T_3 \rightarrow T_1$  [2, 4]. The critical point of the transition, then, is  $M_5 \rightarrow M_1$ . It would be expected that there would be a double structure due to the transition  $M_5 \rightarrow M_3$ . The above band structure shows a value of 2.0 eV

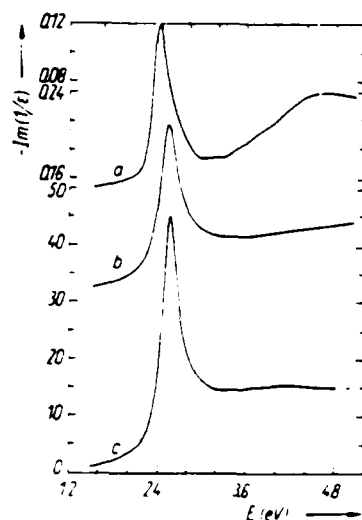


Fig. 10. Energy loss function of  $\text{Cu}_x\text{Zn}_{1-x}$  (a)  $x = 0.50$ , (b) 0.52, (c) 0.54

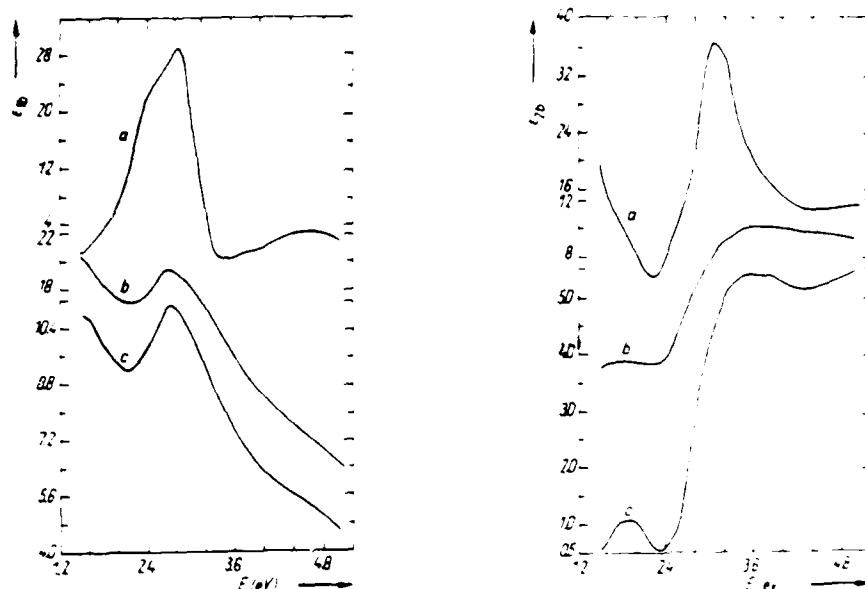


Fig. 11. Real part ( $\epsilon_{1b}$ ) and imaginary part ( $\epsilon_{2b}$ ) of the bound part of the dielectric function of  $\text{Cu}_x\text{Zn}_{1-x}$ , determined by subtracting the Drude contribution from the data of Fig. 8 (left part). (a)  $x = 0.50$ , (b) 0.52, (c) 0.54

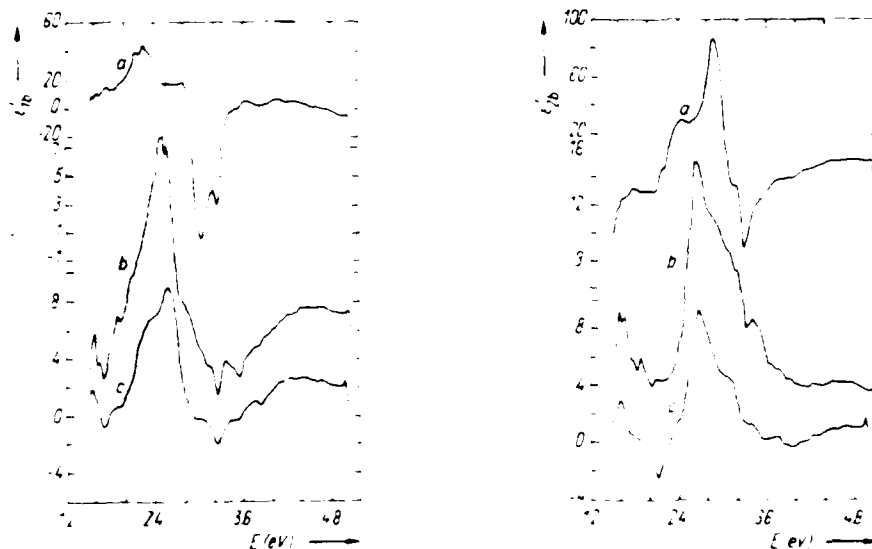


Fig. 12. Derivative with respect to energy of  $\epsilon_{1b}$ ,  $\epsilon_{1b}'$  and with respect to  $\epsilon_{2b}$ ,  $\epsilon_{2b}'$  of  $\text{Cu}_x\text{Zn}_{1-x}$ . (a)  $x = 0.50$ , (b) 0.52, (c) 0.54. With reference to the band structure in Fig. 13 obtained from [3, 4], the following transitions are identified for  $\text{Cu}_{0.50}\text{Zn}_{0.50}$ :  $M_3' \rightarrow M_1$  (3.16 eV),  $M_3' \rightarrow M_2$  (3.29 eV),  $T_2 \rightarrow T_4$  (3.7 eV); for  $\text{Cu}_{0.52}\text{Zn}_{0.48}$ :  $M_3' \rightarrow M_1$  (3.36 eV),  $M_3' \rightarrow M_2$  (3.6 eV),  $T_2 \rightarrow T_4$  (3.7 eV); for  $\text{Cu}_{0.54}\text{Zn}_{0.46}$ :  $M_3' \rightarrow M_1$  (3.01 eV),  $M_3' \rightarrow M_2$  (3.29 eV),  $T_2 \rightarrow T_4$  (3.6 eV)

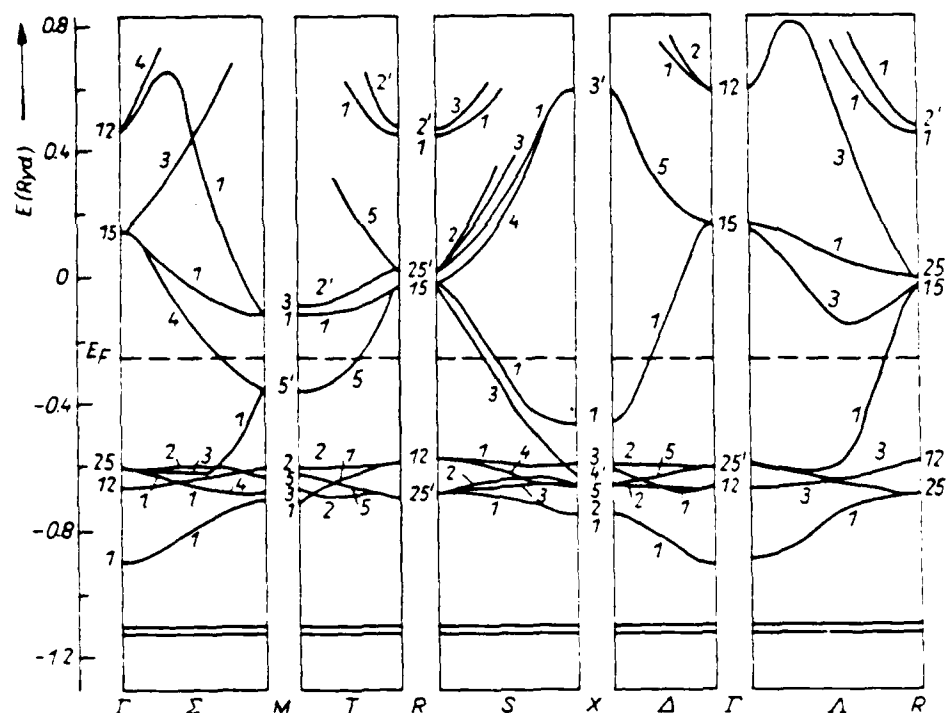


Fig. 13. Band structure of  $\beta'$ -CuZn calculated by Amar and co-workers [3, 4]

for the onset of transition  $T_5 \rightarrow T_1$  and 2.3 eV for the transition  $\Sigma_4 \rightarrow \Sigma_1$ . It shows that the  $M_5 \rightarrow M_1$  transition has an energy of 3.3 eV. Therefore, we should expect to see a break in the derivative of the dielectric function due to the onset at about 2.0 eV followed by an enhancement near 2.3 eV. This would then be followed by a double-extreme-point structure near 3.3 eV.

We can also determine from the band structure the type of three-dimensional critical point to expect. The band at  $M_5$  has greater curvature than the conduction band at  $M_1$ . Therefore, the transition  $M_5 \rightarrow M_1$  is a maximum of the optical band, an  $M_5$  critical point. This is not the case, however, for the  $M_5 \rightarrow M_3$  transition. The conduction band rises much faster than the valence band in the  $\Sigma$ -direction, but is again shallower than the valence band in the  $T$ -direction of the Brillouin zone. Therefore, the optical band has a saddle-point type of critical point for this transition.

In the derivative of  $\epsilon_{1b}$  for  $\text{Cu}_{0.50}\text{Zn}_{0.50}$  (Fig. 12 (curve a), left part), the critical point structure is found in the double dip structure centered at about 3.1 eV. Since an  $M_5$  critical point has a positive derivative in  $\epsilon_{1b}$  at the critical point, the  $M_5 \rightarrow M_1$  transition is associated with the positive peak at the center of the double structure. The associated structure in the derivative of  $\epsilon_{2b}$  (Fig. 12 (curve a), right part) is the local dip in the descending derivative at 3.14 eV. The centrum of these two structures is the location of the critical point, 3.16 eV. The assignment of the  $M_5 \rightarrow M_3$  given to the local minimum in the derivative of  $\epsilon_{1b}$  at 3.26 eV. The corresponding structure in the derivative of  $\epsilon_{2b}$  is the minimum at 3.32 eV. The position of the critical point is thus at

3.29 eV. This is in close agreement with the calculations of Amar and co-workers [3, 4], but is somewhat higher in energy than the theory of Skriver and Christensen [8] and the results of Muldewer and Goldman [19].

The onsets of these transitions are associated with breaks in the derivatives at lower energies. There are breaks in the derivatives at 2.1 and 2.2 eV which could be assigned to onsets at  $T_4 \rightarrow T_1$  and  $\Sigma_4 \rightarrow \Sigma_1$ , respectively. The break at 2.5 eV could then be assigned to the onset at  $T_4 \rightarrow T_2$ , although this should be regarded as speculative.

In Cu<sub>0.52</sub>Zn<sub>0.48</sub>, the onsets of the transitions have remained at pretty much the same energies, while the critical points have moved to higher energies. Note (in Fig. 12 (curve b), left and right part) that the double structure at the critical points remains, but it has moved to higher energy, in agreement with [19]. The  $M_3 \rightarrow M_1$  critical point is at 3.36 eV and the  $M_3 \rightarrow M_2$  critical point is at 3.60 eV. This also represents a slightly greater separation between the two conduction bands. There are again breaks in the derivative spectra at 2.1, 2.2, and 2.6 eV, for this composition, which have the same interpretation as the corresponding structures seen in the 50% copper sample.

The Cu<sub>0.54</sub>Zn<sub>0.46</sub> presents a considerably different picture of the interband transitions as measured by the derivatives of  $\epsilon_{1b}$  and  $\epsilon_{2b}$  (Fig. 12 (curve c), left and right part). The  $M_3 \rightarrow M_1$  critical point is at 3.01 eV and the  $M_3 \rightarrow M_2$  critical point is at 3.29 eV. The break at 1.9 eV is the onset of transitions to the lower conduction band and the break at 2.4 eV is due to transitions to the upper conduction band.

For each of the samples in this investigation, the derivative of  $\epsilon_{2b}$  is dominated by a large negative dip which is due to the  $M_3 \rightarrow M_1$  transition. The peak due to the  $M_3 \rightarrow M_2$  transition is a perturbation which is superimposed on the major dip. The critical-point energies are greater for Cu<sub>0.52</sub>Zn<sub>0.48</sub> than for Cu<sub>0.50</sub>Zn<sub>0.50</sub>, but are then again lower for the Cu<sub>0.54</sub>Zn<sub>0.46</sub> sample. This indicates that there are competing forces whose interplay determines the transition energies.

### 8. d-Band Transitions

The band structure of Fig. 13 shows that the Cu d-bands lie 4 to 6 eV below the Fermi surface. There are several points in the Brillouin zone where d-band to Fermi-surface transitions are possible, with the energies of the onsets being approximately equal. However, the critical-point structure of the transitions will not be seen because the transition at the actual extremum of the optical band would be a filled state-to-filled state transition. For example, the band picture shows that the transition  $T_2 \rightarrow T_3$  occurs at about 4.1 eV. The critical point of this transition is at  $M_2 \rightarrow M_3$ . The band is filled at  $M_3$ , so the extremal point will not be seen.

When this kind of transition occurs, the critical structure is missing and only relatively small breaks in the derivatives of  $\epsilon_b$  are seen. In addition, it is unlikely that these d-band-to-Fermi surface transitions will cause large structures in the  $\Delta R/\bar{R}$  derivative data, and this is confirmed in our experimental data. This is distinctly different from other reflectivity data [19], where a series of structures are seen extending from 3.7 eV to higher energies. The reason for this discrepancy is not clear.

In the 48% and 50% Zn samples, there is evidence for breaks in the derivatives, as discussed, at about 3.7 eV. In the 46% Zn sample, the first such break occurs at 3.6 eV. These results are slightly lower than the band structure of Amar and Johnson [3, 4] would indicate. Skriver and Christensen [8] show that the d-bands lie 3 to 5 eV below the Fermi surface, which would be considerably lower than our results. Thus, the d-band-to-Fermi surface energy difference is much less affected by the crossing of the phase boundary than are the Fermi surface-to-conducting band energy differences, in agreement with [19].



### 9. Conclusions

There are three major experimental facts arising from this investigation which need to be brought together to provide a unified picture of the physics of this alloy system. They are:

- (i) The effective mass for intraband transitions has a sharp, large increase as we go from the  $\beta'$ -field to the  $\alpha + \beta'$  field, while maintaining a  $\beta'$ -structure.
- (ii) The energy differences for the valence band-to-conduction band critical points first rise upon going to lower composition and then drop significantly upon crossing the phase boundary.
- (iii) The onset of d-band-to-valence band transitions moves to lower energy as the Zn concentration decreases, but the effect is much less than in (2).

We note from these observations that there is a considerable flattening of the valence bands upon crossing the phase boundary. There is also a downward shifting of both the conduction and the Cu d-bands with respect to the valence bands, although the shift of the conduction bands is much greater than the shift of the d-bands. The explanation of these results must form the basis for future band calculations in this alloy system.

### References

- [1] W. HUME-ROTHERY, *J. Inst. Metals* **35**, 309 (1926).
- [2] K. H. JOHNSON and H. AMAR, *Phys. Rev.* **139**, A760 (1965).
- [3] H. AMAR, K. H. JOHNSON, and K. P. WANG, *Phys. Rev.* **148**, 672 (1966).
- [4] H. AMAR and K. H. JOHNSON, in: *Optical Properties and Electronic Structures of Metals and Alloys*, Ed. F. ABELES, North Holland Publ. Co., Amsterdam 1966 (p. 586).
- [5] F. J. ARLINGHAUS, *Phys. Rev.* **157**, 491 (1967).
- [6] F. J. ARLINGHAUS, *Phys. Rev.* **186**, 609 (1969).
- [7] V. L. MORUZZI, A. R. WILLIAMS, and J. F. JANAK, *Phys. Rev. B* **9**, 3316 (1974).
- [8] H. K. SKRIVER and N. E. CHRISTENSEN, *Phys. Rev. B* **8**, 3778 (1973).
- [9] M. HANSEN, *Constitution of Binary Alloys*, McGraw-Hill Publ. Co., New York 1958.
- [10] M. HANSEN, *Z. Phys.* **59**, 466 (1930).
- [11] F. SEITZ, *The Physics of Metals*, McGraw-Hill Publ. Co., New York 1943.
- [12] M. WELKOWSKY and R. BRAUNSTEIN, *Rev. sci. Instrum.* **43**, 399 (1972).
- [13] R. STEARNS, J. STEELE, and R. BRAUNSTEIN, *Rev. sci. Instrum.* **54**, 984 (1983).
- [14] M. CARDONA, *Modulation Spectroscopy*, Academic Press, New York 1969.
- [15] M. WELKOWSKY, Ph. D. Thesis, University of California, Los Angeles 1971.
- [16] B. BATZ, Ph. D. Thesis, Univ. Libre de Bruxelles, 1967.
- [17] B. BATZ, *Solid State Commun.* **4**, 241 (1965).
- [18] N. F. MOTT and H. JONES, *The Theory of the Properties of Metals and Alloys*, Dover Publ., New York 1958.
- [19] L. MULDOWER and H. J. GOLDMAN, see [4] (p. 574).
- [20] J. P. JAN and S. S. VISHNUBHATLA, *Canad. J. Phys.* **45**, 2505 (1967).
- [21] M. BURD, R. STEARNS, and R. BRAUNSTEIN, *phys. stat. sol. (b)* **117**, 101 (1983).
- [22] R. STEARNS, Ph. D. Thesis, University of California, Los Angeles 1982.

(Received March 4, 1985)

phys. stat. sol. (b) 129, 735 (1985)

Subject classification: 13.1 and 20.1; 21.1; 21.6

Department of Physics, University of California, Los Angeles<sup>1)</sup>

## Optical Properties of $\beta'$ -AuZn by Wavelength-Modulated Derivative Spectroscopy<sup>2)</sup>

By

R. STEARNS<sup>3)</sup>, R. BRAUNSTEIN, and L. MULDAWER<sup>4)</sup>

Derivative spectra of the optical properties of  $\beta'$ -AuZn are obtained using wavelength-modulated spectroscopy between 1.5 and 5.1 eV. Assignments are made for the interband transition at the M point of the Brillouin zone which fix the transition energies with an accuracy previously unattained.

Es werden Ableitungsspektren der optischen Eigenschaften von  $\beta'$ -AuZn mittels wellenlängenmodulierter Spektroskopie zwischen 1,5 und 5,1 eV erhalten. Für den Interbandübergang am M-Punkt der Brillouin-Zone werden Zuordnungen gemacht, welche die Übergangsenergien mit einer bisher unerreichten Genauigkeit festlegen.

### 1. Introduction

$\beta'$ -AuZn is nearly a perfect prototype of the ordered alloy of the CsCl structure. The  $\beta'$ -phase is an ordered phase of two interlocking simple cubic sublattices, one for each atomic constituent; the cube corners of each sublattice form the cube centers for the other sublattice. The principal problem in calculating the band structure of this alloy system is similar to that in other alloys, that is, the problem of specification of the potentials to give proper placement of the Au d-bands.

The best band structure calculation available places the Au d-bands with an accuracy of 0.5 eV [1]. Previous experimental studies of this alloy system [2, 3] have not shed much light on this problem since they mainly dealt with the principal band edge, which does not involve the lower lying d-bands.

This current study reports the wavelength-modulated spectrum of  $\beta'$ -AuZn for the first time. The results which follow give specific assignment to some of the transitions involving the Au d-bands. The spectrum of  $(1/R) (dR/dE)$  has been determined between 1.5 and 5.1 eV, and other optical properties have been calculated after a Kramers-Kronig analysis of the data was performed.

The ordered  $\beta$ -phase of AuZn is stable over a narrow range of atomic composition, bracketing the stoichiometric  $\beta'$ -Au<sub>50</sub>Zn<sub>50</sub>, as shown in Fig. 1. At room temperature, the boundaries of the  $\beta'$ -phase are Au<sub>48</sub>Zn<sub>52</sub> and Au<sub>52.5</sub>Zn<sub>47.5</sub>, with the phase boundaries widening with increasing temperature [4]. This phase has the structure of CsCl (B2) type [5], with a lattice constant  $a = 0.3128$  nm at 49.5 at% Zn [6]. It may also be noted from Fig. 1 that this system has no disordered  $\beta$ -phase at higher temperature as is seen, for example, in the CuZn alloy system [4].

<sup>1)</sup> Los Angeles, California 90024, USA.

<sup>2)</sup> Work supported in part by the U.S.A. Research Office, Durham, North-Carolina, and by the A.F. Office of Scientific Research.

<sup>3)</sup> Current address: Newport Corporation, Fountain Valley, CA 92708, USA.

<sup>4)</sup> Permanent address: Temple University, Philadelphia, PA 19122, USA.

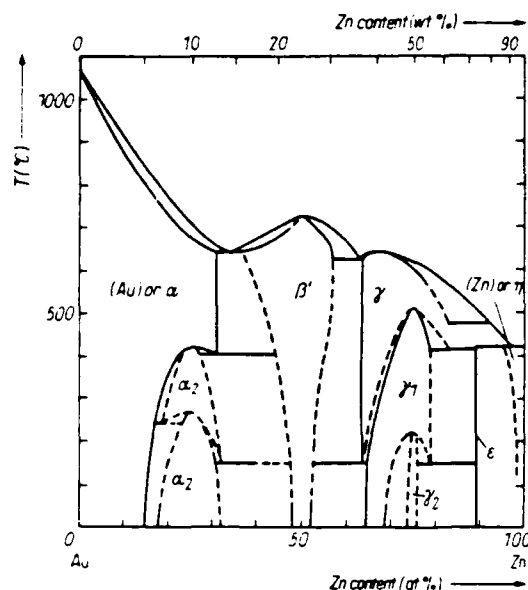


Fig. 1. Phase diagram of the  $Au_{1-x}Zn_x$  alloy system. Dashed lines indicate boundaries which have not been firmly established [4]

## 2. Sample Preparation

The AuZn sample which was used in this investigation was prepared from 0.9998 pure Au and 0.99999 pure Zn. The AuZn mixture was sealed in a tube at a pressure of less than  $10^{-6}$  mm Hg and shaken in the liquid state 5000 times before quenching to room temperature. The sample was subsequently annealed at 600 °C for 24 h in order to homogenize it, and was then again quenched to room temperature. After cutting and polishing, it was given another anneal near 200 °C in order to remove any cold work introduced during the finishing process. The final composition of the sample, as determined by assay for Au content by the U.S. Mint, is  $\beta'$ - $Au_{51.9}Zn_{48.1}$ .

## 3. Experimental Method

Wavelength-modulated spectroscopy [7, 8] was used because of the unambiguous lineshapes obtained by the technique and the resulting ease of interpretation of these lineshapes. The theory of wavelength-modulation spectroscopy is well detailed elsewhere [9, 10]. The theory of the lineshapes near a three-dimensional critical point was given by Batz [11, 12]. It is sufficient here to give the theoretical lineshapes for the sake of reference. All three-dimensional critical-point lineshapes may be expressed in terms of a single function,  $F(W)$ , which is reproduced in Fig. 2. The behavior of

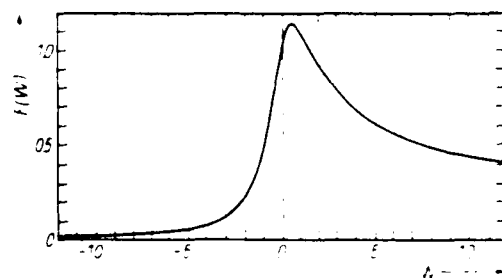


Fig. 2. Universal function,  $F(W)$ , derived by Batz [11, 12] for lineshapes near critical points as seen in wavelength modulation spectroscopy.  $F(W) = [W^2 - 1]^{-1/2} \times [(W^2 + 1)^{1/2} + W]^{1/2}$ , where  $W$  is the reduced frequency  $(\omega - \omega_c)/\eta$ ,  $\hbar\omega_c$  is the interband energy at the critical point and  $\eta$  is a phenomenological broadening parameter

Table 1

Derivative of critical points with broadening included in terms of  $F(W)$   
 $(F(W) = [(W^2 + 1)^{1/2} + W]^{1/2} / (W^2 + 1)^{1/2}, W = (\omega - \omega_g)/\eta)$

critical point	$2\eta^{1/2} \frac{d\epsilon_1}{d\omega}$	$2\eta^{1/2} \frac{d\epsilon_2}{d\omega}$
$M_0$	$F(-W)$	$F(W)$
$M_1$	$-F(W)$	$F(-W)$
$M_2$	$-F(-W)$	$-F(W)$
$M_3$	$F(W)$	$-F(-W)$

critical points in terms of  $F(W)$  is listed in Table 1. Derivative data with a spacing of 0.02 eV between data points were taken between 1.50 and 5.10 eV. The depth of modulation,  $\Delta\lambda/\lambda$ , was about  $1.5 \times 10^{-3}$  at the Hg green line and varied in a manner that was approximately proportional to energy. Thus, the resolution of the data should be better than the spacing of the data points.

#### 4. Experimental Results

The logarithmic derivative of the reflectivity (Fig. 3) was determined experimentally and integrated to yield the complete reflectivity spectrum from 1.5 to 5.1 eV (Fig. 4). The general shape of the reflectivity curve in Fig. 4 agrees with previous results [2, 3], but shows shifting of major structures and has additional fine structure. The minimum at 3.2 eV and the maximum at 3.78 eV are at higher energies than in the other work. The sharp dip in the reflectivity at about 2 eV accounts for the color of the material, which could be described as a ruddy brass. This may be similar to the yellow-pink described by Jan and Vishnubhatla [3] and the "pale purple" seen by Muldower [2].

In order to determine the other optical properties of AuZn, a Kramers-Kronig analysis of the data was undertaken. In order to perform the integration which is involved, extrapolations of the reflectivity to the infrared and ultraviolet regions of the spectrum were necessary. The data of Jan and Vishnubhatla [3] were used for the region from 5.1 to 10 eV. Contributions to the integrals from even high energies are

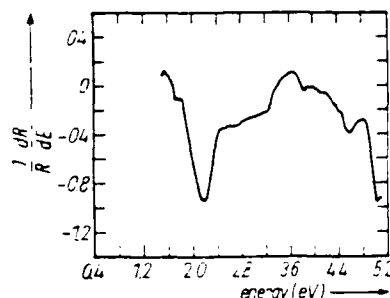


Fig. 3

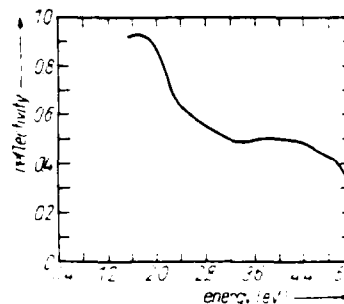


Fig. 4

Fig. 3.  $(1/R)(dR/dE)$  for  $\beta'$ -AuZn. This is the direct experimental result of wavelength-modulated derivative spectroscopy

Fig. 4. Reflectivity of  $\beta'$ -AuZn. The reflectivity is determined by integrating the results of Fig. 3

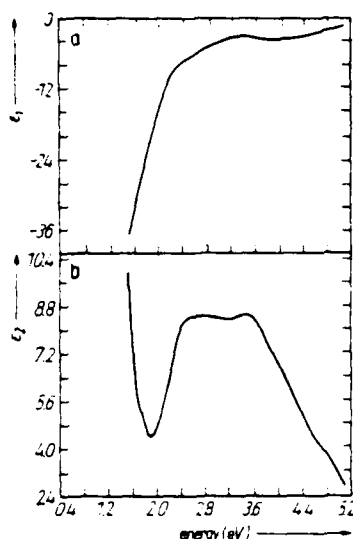


Fig. 5

Fig. 5. Real and imaginary parts of the dielectric function, a)  $\epsilon_1$  and b)  $\epsilon_2$  [15]. These are determined by a Kramers-Kronig analysis of the reflectivity in Fig. 4

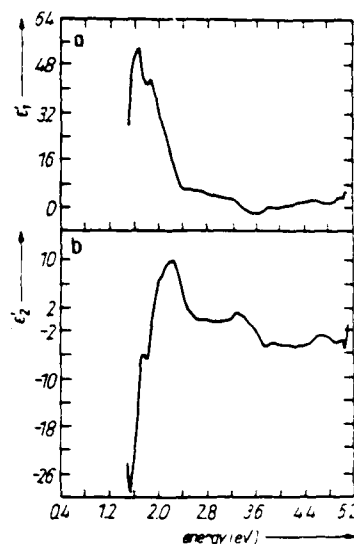


Fig. 6

Fig. 6. Derivatives of the real and imaginary parts of the dielectric function, a)  $\epsilon_1'$  and b)  $\epsilon_2'$

small, due to the local nature of the integrals. A principal effect of a different choice of far uv extrapolation is the addition of a dc level to the optical constants. Muldower and Goldman [13] found that for  $\beta$ -CuZn alloys, the reflectivity actually increases between 12 and 18 eV. Therefore, in order to provide a reasonable comparison with other alloys of the CsCl structure, a constant reflectivity was used for energies greater than 10 eV. In the infrared, a Hagen-Rubens extrapolation (cf. [14]) to a reflectivity of 100% at zero energy was used. The extrapolations were normalized to the experimental data. These are small discontinuities at the points where the spectral regions meet. This can cause localized anomalous structure at the end points of the data. However, due to the local nature of the Kramers-Kronig integrals, this structure will not effect the general structure of the experimental spectra.

Fig. 5 shows the real and imaginary parts of the dielectric function,  $\epsilon_1$  and  $\epsilon_2$ , and Fig. 6 their derivatives,  $\epsilon_1'$  and  $\epsilon_2'$ , which are calculated from the results of the Kramers-

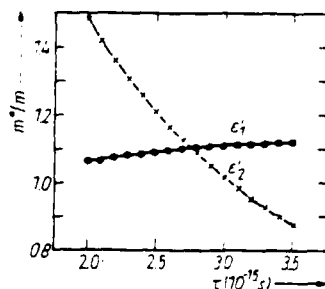


Fig. 7. Determination of the Drude parameters of  $\beta'$ -AuZn. The curves represent two functions,  $m^*(\tau)$  ( $m^*$  effective mass,  $\tau$  relaxation time), one for the real part and one for the imaginary part of  $\epsilon'$ . Each function gives the value of  $m^*$  which best deconvolutes [14, 15] the Drude and bound parts of the dielectric function for a given value of  $\tau$ . The crossing of these functions ( $\tau = 2.76 \times 10^{-15}$ ,  $m^*/m = 1.10$ ) is the point where the same values of  $m^*$  and  $\tau$  minimize the decorrelation function of both  $\epsilon_1'$  and  $\epsilon_2'$ . This intersection is the physical result for the Drude parameters [14, 15]

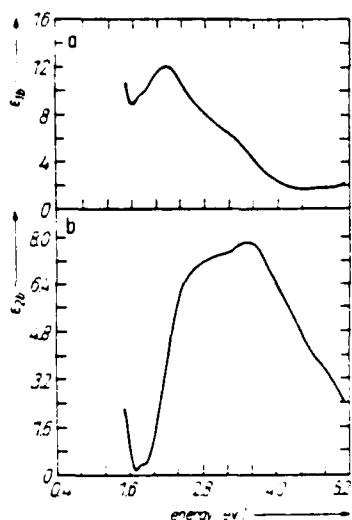


Fig. 8

Fig. 8. Bound parts of the dielectric function,  $\epsilon_{1b}$  and  $\epsilon_{2b}$  [15], which result when the Drude contributions are subtracted from  $\epsilon_1$  and  $\epsilon_2$ .

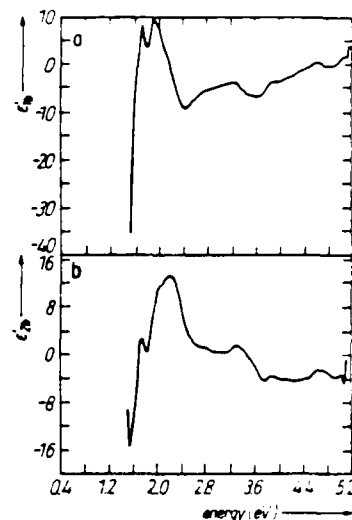
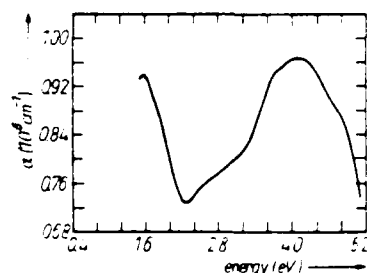


Fig. 9

Fig. 9. Derivatives with respect to energy of the bound parts of the dielectric function,  $\epsilon'_{1b}$  and  $\epsilon'_{2b}$ . With reference to the band structure in Fig. 11 obtained from [11], the following transitions are identified:  $M_{7-} \rightarrow M_{6+}$  (1.67 eV),  $M_{7-} \rightarrow M_{7-}(E_F)$  (2.06 eV),  $M_{6-} \rightarrow M_{6+}$  (2.28 eV),  $M_{7-} \rightarrow M_{7+}$  (3.26 eV),  $M_{6-} \rightarrow M_{7-}$  (3.86 eV),  $M_{6+}(d) \rightarrow M_{7-}$  (4.4 eV),  $M_{6+}(d) \rightarrow M_{6+}$  (4.61 eV).

Kronig integral. These data are then used to find the Drude parameters, the effective mass, and relaxation time, by deconvoluting the Drude-like terms and bound terms as described elsewhere [15, 16]. Fig. 7 shows the curves generated from the derivatives of the dielectric functions to separate the free- and bound-electron contributions. Their intersection determines the values of the Drude parameters [14, 15]. The Drude effective mass was found to be 1.10 times the free-electron mass and the relaxation time was found to be  $2.76 \times 10^{-16}$  s. The value for the effective mass compares favorably with the previous value of 1.2 [3]. The relaxation time for AuZn is not given elsewhere; the value here is about 2 to 3 times the relaxation time for CuZn [13]. Fig. 8 and 9 are the bound-electron contributions to the dielectric function,  $\epsilon_{1b}$  and  $\epsilon_{2b}$ , and their derivatives,  $\epsilon'_{1b}$  and  $\epsilon'_{2b}$ , which are obtained when the Drude parameters are used to subtract the free-electron contributions from the dielectric function.

Fig. 10. Absorption coefficient,  $\alpha$ , of  $\beta'$ -AuZn

Finally, the absorption coefficient is given in Fig. 10. The general shape is the same as previously reported [3], but the maximum is at 4.1 instead of 3.2 eV. This also illustrates the shift in major structure noted in the discussion of the reflectivity.

### 5. Interband Transitions

The band structure which was previously calculated for AuZn is given in Fig. 11 [1]. Assignment of interband transitions is made using the data found from the derivatives of the bound parts of the dielectric function. The proper lineshape for each transition is determined by first finding the type of critical point involved in the transition from band theory and comparing that with the lineshapes of Table 1. Finding that a transition, determined from Fig. 9, has a lineshape as expected near the predicted energy lends confidence to interband transition assignments.

#### 5.1 Fermi level to higher bands

The band structure in Fig. 11 shows that the onset of interband transitions is due to transitions from the Fermi level to higher conduction bands at the M point, that is, the (110) direction, in the Brillouin zone. The lowest-energy transitions are  $M_{7-} \rightarrow M_{6-}$  and  $M_{6-} \rightarrow M_{6+}$ . The band calculation has a critical gap of 2.0 eV for  $M_{7-} \rightarrow M_{6-}$  with an onset at 1.6 eV for this transition. The  $M_{6-} \rightarrow M_{6+}$  transition has a critical point energy of 2.6 eV and an onset of 1.8 eV, according to Fig. 11. The experimental data yield lower values for these energies.  $M_{7-} \rightarrow M_{6-}$  is at 1.67 eV. This is probably the reason why the reflectivity is rising at the low-energy end of the spectrum.

$M_{6-} \rightarrow M_{6+}$  is found to be at 2.28 eV, as given by the dip in  $\epsilon_{2b}$  at 2.4 eV and the peak in  $\epsilon_{1b}$  at 2.2 eV. Both transitions involved here are shifted to a lower energy by

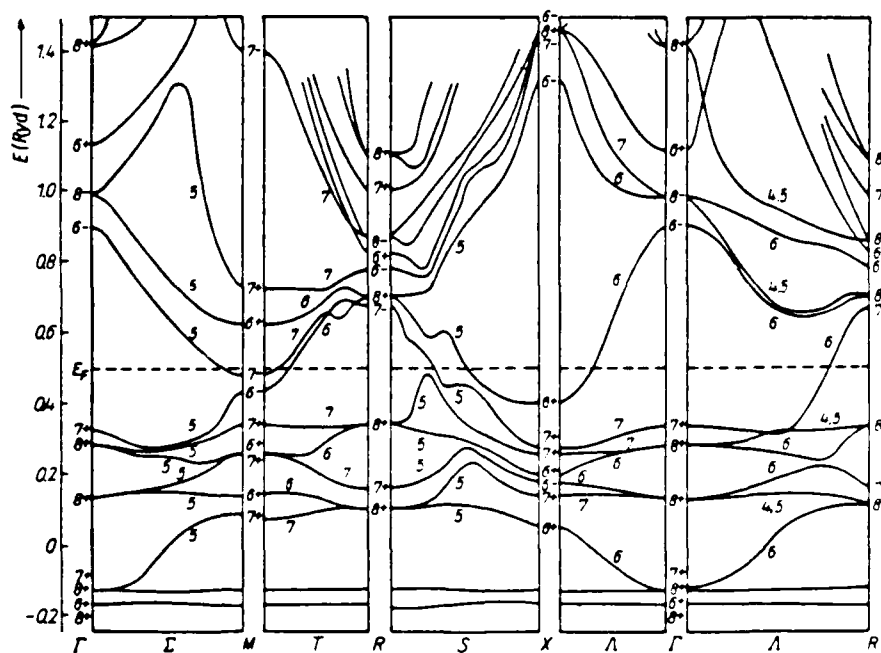


Fig. 11. Band structure of 9'-AuZn as calculated by Connolly and Johnson [1]

about 0.3 eV. This leads to a conclusion that the  $M_{6+}$  conduction band should be shifted down by about that energy with respect to the Fermi level. If this is done, that would place the onset of the second transition below the experimental energy range.

The transitions from the Fermi level to the second higher conduction band occur in the intermediate part of the spectrum. The band picture predicts that the transitions  $M_{7-} \rightarrow M_{7+}$  and  $M_{6-} \rightarrow M_{7+}$  will be at 3.3 and 3.9 eV, respectively. The experimental data show these to be at 3.26 and 3.86 eV. These assignments give an internal consistency to the results. By subtracting transition energies, a value for the  $M_{6-} \rightarrow M_{7-}$  gap may be obtained. The low and intermediate energy assignments give 0.61 and 0.60 eV, respectively, for this difference. The difference between these two values is less than the resolution of the experimental data.

### 5.2 Transitions involving d-bands

There is one other structure in the lower-energy portion of the spectrum. This is due to transitions from the upper Au d-band to the Fermi level. The actual critical point from the highest lying  $M_{7+}$  to the  $M_{7-}$  conduction band at the Fermi level cannot be seen because the upper level is filled. However, the transition has an onset at the point where the valence band crosses the Fermi level. By inspection of the band structure of Fig. 11, it is apparent that this critical point is of the  $M_0$  (minimum) type. Fig. 12 shows, in accordance with Table 1, how the lineshapes for  $\epsilon_1$  and  $\epsilon_2$  behave near an  $M_0$  critical point. In this figure,  $\omega_c$  is the critical point gap and  $\omega_0$  is the point of the actual onset. The dashed line shows how the transition lineshape will actually behave. Note that the structure in  $\epsilon_1$  is quite small compared to the structure which would be observed in  $\epsilon_2$ . This behavior can actually be seen in the experimental spectrum at 2.06 eV. The observation of this transition is an illustration of the strength of modulation spectroscopy, since this observation would be very difficult in a standard reflectivity experiment.

The onset is observed at 2.06 eV, compared to 2.2 eV as predicted by the band structure. Fig. 13 shows how some of the bands might be shifted to match the observations made so far (along with some other shifts which will be discussed in the remainder of this discussion). The  $M_{6-}$  point is shifted down in energy by 0.3 eV, while  $M_{7-}$  remains the same. The  $M_{7-}$  and  $M_{6-}$  partially filled valence bands are unchanged with respect to these two bands. The  $M_{7+}$  Au d-band is shifted upward by about 0.2 eV, in accordance with the observed structure.

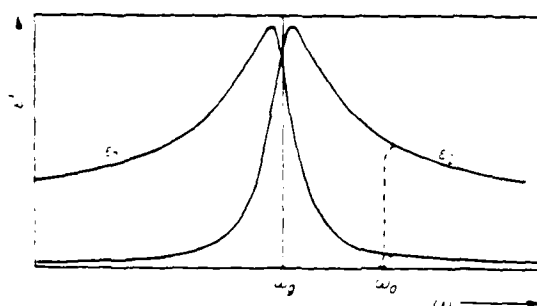


Fig. 12. Lineshapes near an  $M_0$  critical point as determined from Fig. 2 and Table 1. If the upper band involved in the transition is partially filled, then the critical point itself will not be seen in the experimental spectrum since it is a filled-state to filled-state transition. Transitions will begin at an energy,  $\hbar\omega_0$ , at which there are empty final states. The dashed lines in the figure show the expected experimental results for such a situation.



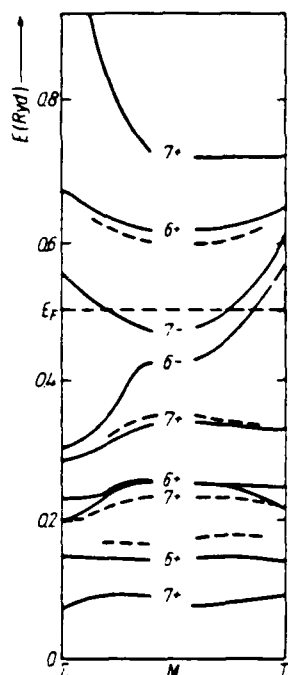


Fig. 13. Adjustments of the  $\beta'$ -AuZn bands near the M point of the Brillouin zone to fit the experimental results. The solid lines are reproduced from Fig. 11 and the dashed lines are the adjustments of the bands which are suggested by the experimentally determined transition assignments

If the modification of the  $M_{6+}$  conduction band is correct, the transition from the second Au d-band to this upper band would be at 4.6 eV. A major structure is observed centered at 4.61 eV. Since it follows the lineshape for the  $M_0$  transition which is predicted by the band picture, this structure is assigned to the  $M_{6-}$  (d-band)  $\rightarrow M_{6+}$  (cond.) transition.

Also, the  $M_{6+}$  modification, along with the proposed shift in the  $M_{7+}$  d-band, brings the  $M_{7+} \rightarrow M_{6-}$  transition to almost the same energy as the  $M_{7-} \rightarrow M_{7+}$  transition discussed previously. The convolution of these two critical points can be seen in the additional structure at about 3.4 eV.

The last major structure in this experimental spectrum is at 5.0 eV. A possible assignment for this structure is the d-band to conduction band transition  $M_{7-} \rightarrow M_{6-}$ . However, this would require breaking the degeneracy of the intermediate Au d-bands as suggested by Fig. 13. An exact assignment is difficult since anomalous structure due to end-point problems may have some effect on the apparent optical functions, as discussed previously.

The only transition which we would hope to see from the lowest Au d-band is to the Fermi level. Again, the actual critical point is filled, so all that will be seen is a small break in the spectrum at the point where the d-band to Fermi level transition has its onset. The band structure gives an energy of 4.8 eV for the onset of this transition. There are no breaks between the structures at 4.6 and 5.0 eV. This transition is assigned to the small structure at 4.4 eV. This necessitates raising the lower Au d-band as shown in Fig. 13. This structure is right at the limits allowed by the noise level in the data, so this assignment must be regarded as tentative.

## 6. Conclusions

The experimental results which have been described are summarized in Table 2. These results should help in the placement of the Au d-bands in the AuZn alloy system. In the band structure of Connolly and Johnson [1], the four Au d-bands had a total width of 2.8 eV at the M point, while using the results from our work, this same width is about 2.5 eV. This should be a more accurate result, since the placement of the d-bands in the previous calculation was  $\pm 0.5$  eV. These results should allow a more accurate calculation of the crystal potential for band structure calculations.

Table 2  
Summary of experimental results

transition	predicted energy (eV) [1]	experimental energy $\Delta E$ (eV)
$M_{7-} \rightarrow M_{6-}$	2.0	1.67
$M_{6-} \rightarrow M_{6-}$	2.6	2.28
$M_{7-} \rightarrow M_{7-}$	3.3	3.26
$M_{6-} \rightarrow M_{7-}$	3.9	3.86
$M_{7-}$ (upper d) $\rightarrow M_{7-}(E_F)$	2.2 (onset)	2.06 (onset)
$M_{6-}$ (mid. d) $\rightarrow M_{6+}$ (cond.)	5.0	4.61
$M_{7-} \rightarrow M_{6+}$	5.0	$\approx 5.0$
$M_{6-}$ (lower d) $\rightarrow M_{7-}(E_F)$	4.8 (onset)	4.4 (onset)
$R_{8+} \rightarrow R_{7-}$	4.6	4.6
$R_{8+} \rightarrow R_{8+}$	4.8	5.0

Drude effective mass  $m^*/m = 1.10$ .

Drude relaxation time  $\tau = 2.76 \times 10^{-13}$  s.

#### References

- [1] J. W. D. CONNOLLY and K. H. JOHNSON, Proc. III. Material Research Symposium, Electronic Density of States, Nat. Bur. Standards, Gaithersburg (MD) 1967.
- [2] L. MULDAWER, Phys. Rev. 127, 1551 (1962).
- [3] J. P. JAN and S. S. VISHNUBHATLA, Canad. J. Phys. 45, 2205 (1967).
- [4] M. HANSEN, Constitution of Binary Alloys, McGraw-Hill Publ. Co., New York 1958.
- [5] A. WESTGREN and G. PERAGMEN, Phil. Mag. 50, 311 (1925).
- [6] N. V. AGEEV and D. H. SHOYLSHET, Izv. Sektora fiz.-khim. Anal. 13, 165 (1940).
- [7] M. WELKOWSKY and R. BRAUNSTEIN, Rev. sci. Instrum. 43, 399 (1972).
- [8] R. STEARNS, J. STEELE, and R. BRAUNSTEIN, Rev. sci. Instrum. 54, 984 (1983).
- [9] M. CARDONA, Modulation Spectroscopy, Academic Press, New York 1969.
- [10] M. WELKOWSKY, Ph. D. Thesis, Univ. of California, Los Angeles 1971.
- [11] B. BATZ, Ph. D. Thesis, Univ. Libre de Bruxelles, 1967.
- [12] B. BATZ, Solid State Commun. 4, 241 (1965).
- [13] L. MULDAWER and H. J. GOLDMAN, in: Optical Properties and Electronic Structure of Metals and Alloys, Ed. F. ABELES, North-Holland Publ. Co., Amsterdam 1966 (p. 574).
- [14] N. F. MOTT and H. JONES, The Theory of the Properties of Metals and Alloys, Dover Publ., Inc., New York 1958.
- [15] M. BURD, R. STEARNS, and R. BRAUNSTEIN, phys. stat. sol. (b) 117, 101 (1983).
- [16] R. STEARNS, Ph. D. Thesis, Univ. of California, Los Angeles 1982.

(Received February 22, 1985)

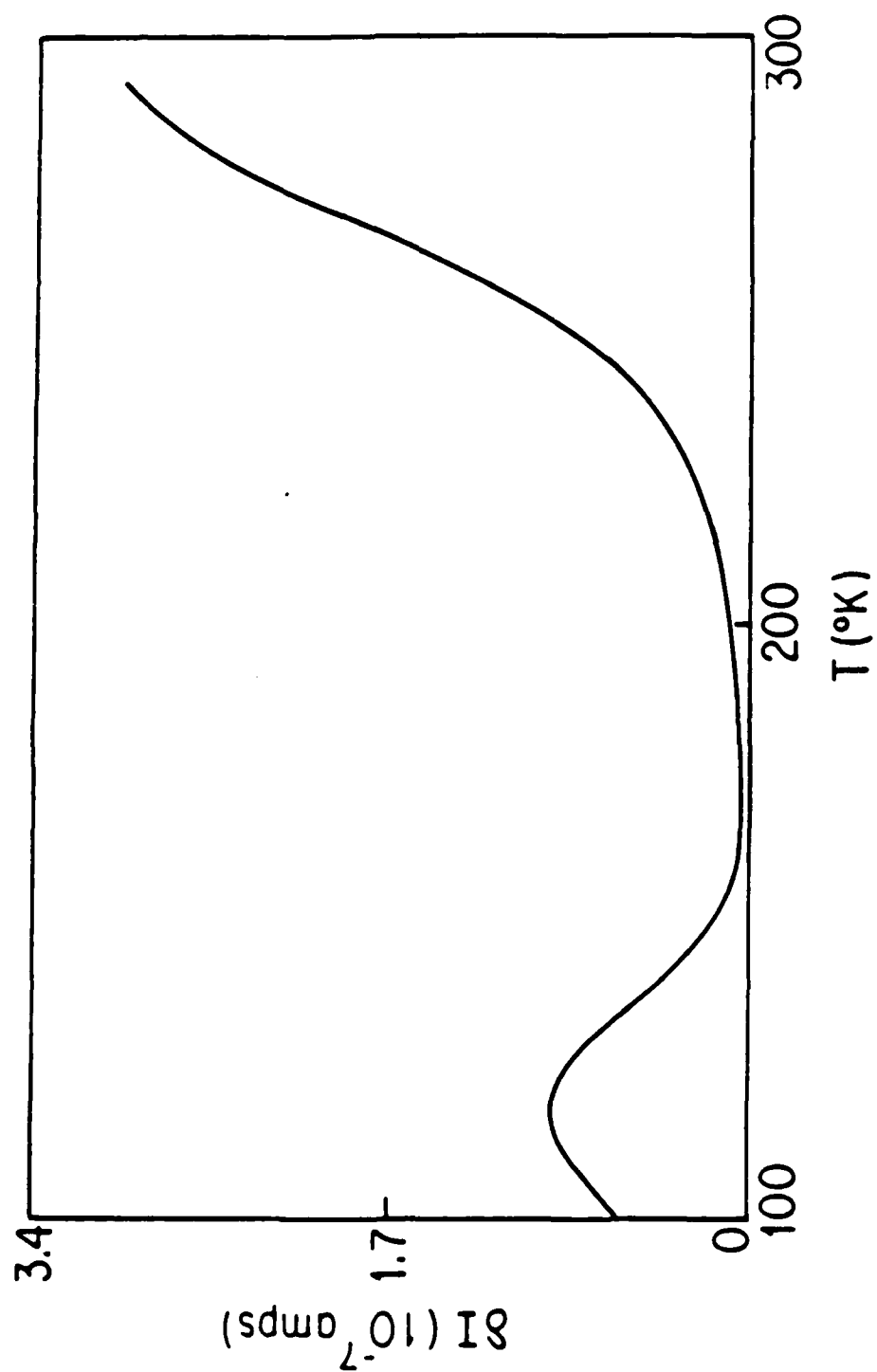


Fig. 5

## Deep level derivative spectroscopy of semiconductors by wavelength modulation techniques

R. Braunstein, S. M. Eetemadi, and R. K. Kim

Department of Physics, University of California,  
Los Angeles, California 90024

### Abstract

An infrared wavelength modulated absorption spectrometer capable of measuring changes in the absorption coefficient of levels of  $10^{-3} \text{ cm}^{-1}$  in the spectral range 0.2-20 microns was employed to study bulk and surface absorption in semiconductors. The results of the study of deep levels in semi-insulating GaAs, surface layers on Si, GaAs, and HgCdTe, oxygen complexes in floating-zone silicon, and determination of strain in ion implanted layers are presented.

### Introduction

The utilization of semiconductors in devices for the amplification, detection, generation, and signal processing of high frequency electromagnetic radiation in very high density configurations requires an intimate knowledge of the impurities and structure imperfections which affect device performance. It has been a scientific and technological challenge to develop nondestructive techniques to detect such imperfections and to develop a conceptual framework for understanding their microscopic electronic structure. In fashioning high density arrays of semiconductor devices, it is essential to start with well characterized, homogeneous substrates to obtain near-identical properties of individual circuit elements. Aside from knowing how to select the initial "winning" substrate, subsequent device processing can introduce unknown impurities or defects which can degrade device performance and consequently it would be desirable to have a technique which is capable of following the evaluation of a semiconductor's characteristics from its initial growth through the device processing phases.

A powerful array of electron spectroscopies<sup>1</sup> exist for detecting chemical impurities but these require an ultra-high-vacuum environment and are not readily adaptable to analytical procedures which can ultimately be used on the production line. There exists an immense variety of junction techniques employing some form of deep level transient spectroscopy (DLTS) to study deep level defects whose variation depends on which junction parameter is finally measured.<sup>2</sup> However, apart from technical details, the end result one desires to extract from these measurements are the optical and thermal emission cross sections for electrons and holes, as well as the concentration of levels. In general excited state, thresholds for transitions between levels, and intra-center transitions between levels are not easily determined using the above techniques. The presence of high electric fields at the junctions adds complications to the interpretation of the data. In addition, thermal processing of the test structures can introduce further defects. Direct optical absorption measurements yield the quantities of interest, but at the level of sensitivity of DLTS techniques, on the order of  $10^{12}$ - $10^{14}/\text{cm}^3$ , it is not possible to employ conventional techniques. Consequently consideration has been given to optical modulation spectroscopies for detecting small structures out of a broad background.<sup>3</sup> A family of derivative spectroscopy techniques has been developed where the modulation parameter may be the electric field, stress temperature, or wavelength of the probing light beam. Recently, wavelength modulation photoresponse spectroscopies have evolved to measure photo-induced changes in voltage,<sup>4</sup> capacitance,<sup>5</sup> and current<sup>6</sup> from which the absorption coefficients are inferred. An examination of wavelength modulation photoresponse spectroscopies in contrast to direct wavelength modulation absorption/reflection indicates that the latter is the most suitable technique for studying deep levels since it yields unambiguous line shapes.<sup>7</sup>

We have developed an infrared wavelength modulated system capable of measuring changes in absorption coefficients at levels of  $10^{-3} \text{ cm}^{-1}$  out of a broad background in the spectral range 0.2-20 microns.<sup>8</sup> Since it is not necessary to make electrical contact to the sample one obviates possible contamination by thermal processing necessary for DLTS or photoresponse techniques. In addition, being an optical technique there are no restrictions on the resistivity of the sample. In this report we will discuss the use of this system in a number of studies concerned with characterization of semiconductors.

### Infrared wavelength modulation system

The theory of operation of the infrared wavelength modulation system, its construction, and implementation has been previously reported.<sup>8</sup> For the purposes of the present discussion we shall indicate some general aspects of its operation. In one form of this system we have employed a Perkin-Elmer 301 spectrometer in a single beam sample-in and sample-out scheme shown in Fig. 1. The sample-in, sample-out and spectrometer wave-number positions are preset at intervals by stepping motors, these and the data collecting system are controlled by an on-line microprocessor (Motorola M6800) or a CAMAC based PDP 11/23 computer; a block diagram of the control system is shown in Fig. 2. The modulation of the wavelength is accomplished by the sinusoidal sweeping the output of the light beam across the exit slit of the monochromator by a vibrating mirror; this method of modulation is equally good for any wavelength and the amplitude can be continuously varied up to  $\Delta\lambda/\lambda = 10^{-2}$ . The system employs two lock-in amplifiers. As

shown in Figs. 1 and 2, lock-in amplifier I measures the intensity of the chopped radiation at frequency  $f_1$  at a fixed wavelength with the sample-in and the sample-out while lock-in amplifier II, at frequency  $f_2$ , measures the derivative signal also with the sample-in and sample-out. Appropriate light sources, filters and detectors are employed for a given spectral region. At the end of a data taking cycle the energy derivative of the absorption as well as its integral are calculated by a PDP 11/23 computer and the results plotted. The constant of integration is supplied by the direct measurement of the absorption in a convenient spectral region.

#### Derivative absorption spectroscopy of GaAs:Cr

The above infrared wavelength modulated system was employed in a detailed study of the derivative absorption of GaAs:Cr.<sup>9</sup> Figures 3 and 4 show the integrated derivative data of semi-insulating GaAs:Cr at 300 K with various degrees of shallow donor-acceptor compensations. All the samples were semi-insulating and contained  $\sim 10^{16}/\text{cm}^3$  Cr. The samples in Fig. 3 were highly compensated while those in Fig. 4 were slightly more p- or n-type, respectively. The extensive fine structures with variation in absorption coefficient of  $\Delta K \sim 10^{-1}$  to  $10^{-2} \text{ cm}^{-1}$  out of a relatively smooth background absorption of  $1\text{--}2 \text{ cm}^{-1}$  should be noted. Previously reported conventional optical absorption measurements revealed a few plateau-like structures, indicating that they had only observed the envelope of the absorption in this region.<sup>10</sup> The detailed extensive fine structure observed can be correlated with an energy level scheme of  $(\text{Cr}^{3+}\text{--}\text{Cr}^{2+})$  ions in GaAs shown in Fig. 5 and interpreted in terms of transitions from Cr-ions to the valence and conduction bands and excited states. The complexity of the spectra is due to coupling of Cr to donor or acceptor complexes, and the subtle changes are due to the degree of compensation and consequent position of the Fermi level in these four semi-insulating samples. A complete analysis indicates that a comparable number of Cr atoms are at tetragonal and trigonal sites and can explain the rapid diffusion of Cr in GaAs.<sup>9</sup>

#### Semi-insulating LEC GaAs

An extensive study was made on semi-insulating GaAs grown by the liquid encapsulated Czochralski technique (LEC). These studies were performed in the spectral region 0.3–1.5 eV and the temperature range 80–300 K. In these samples, we observed a number of structures due to EL2, other defects, and impurities. Several fine structures were observed which can be interpreted in terms of intra-center transitions between levels of impurities split by the crystal field; the data were obtained with our derivative spectrometer and the integrated results are discussed below.

Figure 6 shows the absorption of semi-insulating LEC GaAs at 300 K. The threshold at 1.4 eV is the onset of the direct band-to-band transition, while the threshold at 1.0 eV is the onset of the EL2 defect. The small structure between 0.3 and 0.5 eV and threshold at 0.5 eV should be noted. The sensitivity of our measurement allows us to give credence to changes in absorption coefficient  $\sim 10^{-3} \text{ cm}^{-1}$ . As the temperature is reduced to 160 K, we note the emergence of structure shown in Fig. 7 on a vastly expanded scale. When the sample temperature is reduced to 80 K, the structure with a threshold at 1.0 eV at room temperature abruptly quenches when the sample is illuminated with band gap light; see Fig. 8. When the sample temperature is increased and the measurement performed without band gap light present, the EL2 threshold returns. The metastability of this level and its possible identification as an anti-site defect of GaAs have been previously discussed.<sup>11</sup>

Figure 9 shows the structure observed in Fig. 8 on a vastly expanded scale possibly by the precision of our measurement. Note should be taken of the sharp structure at 0.36–0.38 eV, a broad peak at 0.4 eV, structure between 0.42–0.5 eV, and the threshold at 0.5 eV. Similar structures are observed in the same spectral region for other undoped LEC GaAs samples, but with changes in the relative intensities of the various structures. The structures at 0.36–0.38 eV and the threshold at 0.5 eV seem to be correlated, indicating they are due to the same level. The structures at 0.36–0.38 eV are very similar to that which is observed for deliberately Fe doped in a number of semiconductors,<sup>12</sup> and so can be identified as an intra-center transition of  $\text{Fe}^{2+}$  in GaAs. (Estimating the oscillator strength for Fe, our samples contain  $\sim 10^{16} \text{ Fe}/\text{cm}^3$ .) The threshold at 0.5 eV whose intensity scales with this intra-center transition corresponds to the transition from the valence band to the Fe levels. This is further substantiated by the fact that the position of this threshold moves with a temperature coefficient similar to the GaAs band gap; a similar observation has been made from Hall measurements.<sup>13</sup> The resonant-like band around 0.4 eV with its possible fine structure seems to be an intra-center transition. Photo-induced-transient spectroscopy (P.I.T.S.) electrical measurements made on the same samples as the optical measurements reveal levels at 0.4 and 0.8 eV, the latter being due to EL2. A level at 0.4 eV has been reported in semi-insulating GaAs by a number of measurements<sup>14</sup> which was originally ascribed to oxygen in O-doped GaAs. Recently a combination of temperature-dependent Hall-effect measurements, spark-source mass spectroscopy, and secondary ion mass spectroscopy measurements have indicated that neither oxygen nor any other impurity can account for the 0.4 eV level and consequently it is probably due to a pure defect.

Thermal annealing and quenching experiments on a range of LEC GaAs samples revealed that some of these levels are probably due to structure imperfections.<sup>15</sup> The subtle changes in these levels could readily be followed by our wavelength modulation technique.

### Surface Absorption

The sensitivity of our system enables us to study surface absorption. Although the primary aim of this report is to demonstrate the power of infrared wavelength modulation spectroscopy as a characterization technique for bulk semiconductors, we shall show some examples of measurements on alkali halides<sup>8</sup> since recently a great deal of material preparation studies have taken place to improve these materials for light guiding applications. First we shall discuss an example of measurements on KBr which reveal both surface and bulk absorption. These clean alkali halides are potentially useful insulators in MIS structures. Subsequently we describe some examples of surface absorption on semiconductor.

The absorption spectra of a typical KBr crystal obtained with a conventional double-beam spectrometer are shown in Fig. 10. This crystal was grown from material which was selectively ion filtered and reactive gas treated for purification prior to crystal growth. As can be seen, virtually no absorption structure can be seen above the noise level of the instrument, confirming the relative purity of the sample.

Figure 11a shows the integrated derivative spectra of the above KBr sample taken with the sample in the laboratory atmosphere. The richness of the observed spectra should be noted in contrast to the featureless spectral shown in Fig. 10 for the same sample. The right-hand ordinate in Fig. 11 indicates the absorption coefficient at  $3.8 \mu\text{m}$  as inferred from a laser calorimeter measurement with a DF laser; the left-hand ordinate indicates the relative change of absorption obtained by integrating the wavelength modulation derivative data. The depth of the modulation of the monochromator frequency used to obtain these data was  $10 \text{ cm}^{-1}$ . The zero of the  $\Delta K \text{ cm}^{-1}$  wavelength modulation result is registered with the absorption calibration point of  $0.4 \times 10^{-4} \text{ cm}^{-1}$  obtained by laser calorimetry. Therefore, to obtain the actual absorption coefficient at a particular wavelength, one merely adds or subtracts the appropriate  $\Delta K$  value at a given frequency to the  $0.4 \times 10^{-4} \text{ cm}^{-1}$  value. This type of representation of the data allows us to display the fine structure excursions in absorption above and below the calorimetric point. Successive runs on this sample reveal that the structure shown in Fig. 11 is reproducible within a mean deviation of  $\Delta K = 10^{-6} \text{ cm}^{-1}$ . Consequently, the noise level is at the level of the width of the drafting lines. The data points were taken at  $5 \text{ cm}^{-1}$  frequency intervals. The sample thickness was  $4 \text{ cm}$ .

When this sample is placed in a dry  $\text{N}_2$  atmosphere, a continuous change in the spectral distribution of the absorption is observed until the spectra stabilize after the sample has been in this gaseous ambient for an hour. The dominant features of the spectra of this sample when in the laboratory atmosphere displayed in Fig. 11a are: a band near  $2.5 \mu\text{m}$  with the fine structure, multiple structure between  $3$  to  $4 \mu\text{m}$  with fine structure, a sharp strong band at  $4.2 \mu\text{m}$ , a band at  $5 \mu\text{m}$ , and multiple structures between  $6$  to  $12 \mu\text{m}$ . The data shown in Fig. 11b are for this same sample in a dry  $\text{N}_2$  atmosphere. Although there is a distinct change in the spectra in Fig. 11b compared to Fig. 11a, some of the original prominent features can still be recognized. The sharp peak at  $4.2 \mu\text{m}$  is greatly reduced, and the band at  $5 \mu\text{m}$  is gone, while some of the original structure between  $5.8$  and  $12.0 \mu\text{m}$  is still present; however, a valley develops around  $9 \mu\text{m}$ . Analysis of the observed spectra has allowed us for the first time to identify volume and surface impurities in highly pure KBr and other alkali halides.<sup>8</sup>

Using our infrared wavelength modulation system, we have been able to study the growth of native oxides on freshly etched silicon surfaces. We can easily detect the  $9 \text{ micron}$   $\text{SiO}_2$  absorption band in a  $10 \text{ \AA}$  layer of silicon with a signal-to-noise ratio of  $100/1$ , indicating that we have the capabilities of studying the growth of a fraction of a monolayer of adsorbed species. An example of this band is shown in Fig. 12 immediately after the silicon surface was etched with HF. Studies of oxides on GaAs and HgCdTe have enabled us to study the formation of OH<sup>-</sup> in oxides on GaAs as well as the presence of  $\text{TeO}_2$  on HgCdTe due to various surface treatments.

### Determination of strain in layered semiconductors

In the growth of semiconductor layers by various epitaxial techniques such as M.B.E., L.P.E., and C.V.D., and the doping of layers by ion implantation and other techniques, an important technological problem is the assessment of the homogeneity of doping, alloy composition, and strain in the layers. We have used our wavelength techniques to determine shifts in various critical points as a function of doping and strain in several semiconductors.

One of the major fabrication processes used in the fabricate of n-type channel FET's on semiconducting GaAs is the utilization of ion implantation. The assessment of defects subsequent to implantation and annealing is of prime importance, especially so for shallow implanted layers  $\sim 1000 \text{ \AA}$ . We have observed the effects of ion implantation by the nondestructive methods of wavelength modulation. Local strain was observed by measuring the shift of the imaginary part of the dielectric function of GaAs in the neighborhood of the  $E_1$  and  $E_1 + \Delta$  critical point. Implants of Be, Sb, S, In, and double implanted Sb and Be were studied. The implanting fluxes were of the order of  $10^{13}/\text{cm}^2$ , compared to ion unimplanted GaAs, positive and negative shifts of the energy of the critical point were observed, indicating that we are able to distinguish contraction or expansion of the lattice.

In addition, we found that the intensity of  $\epsilon_2$  the imaginary part of the dielectric function at the  $E_1 + \Delta$  critical point decreased as a function of n-type doping. These results can be interpreted in terms of screening of the hyperbolic exciton associated with this critical point.

### Difference wavelength modulation spectroscopy of oxygen in floating-zone silicon

The use of infrared spectroscopy to identify relative amounts of oxygen in silicon is routine.<sup>16</sup> Usually the concentration of dissolved oxygen is deduced from the infrared absorption at about 9  $\mu\text{m}$  ( $1100\text{ cm}^{-1}$ ). The relationship between the intensity of this band and the dissolved oxygen has been demonstrated reliably in experiments by comparing the absorption in samples containing the oxygen isotopes  $\text{O}^{16}$  and  $\text{O}^{18}$ .<sup>17,18</sup>

It has been shown that this band is associated with interstitial oxygen and is due to an infrared-active antisymmetric type of vibration of the  $\text{Si-O}$  "molecule".<sup>19</sup> This model has been questioned and it has been suggested<sup>20</sup> that the oxygen in silicon is in a bound state, forming fine second-phase  $\text{SiO}_2$  particles and the absorption at 9  $\mu\text{m}$  is due to this oxygen. Attempts have been made to explain the changes of optical and electrical properties of silicon after various heat treatments by the phase transitions of these second-phase particles of  $\text{SiO}_2$ .<sup>20</sup> Other workers showed that absorption spectra of silicon samples around 9  $\mu\text{m}$  with relatively low oxygen concentration have a complex structure. They observed a peak at  $1128\text{ cm}^{-1}$ , and another peak at  $1135\text{ cm}^{-1}$ , and they attributed these peaks to dissolved oxygen in the lattice and in the second-phase  $\text{SiO}_2$  particles, respectively. They suggested that other electrically inactive states of oxygen in silicon might exist, and there might be a threshold oxygen concentration which is necessary for any significant formation of  $\text{SiO}_4$  complexes to occur.

Nearly all previous optical studies of oxygen in silicon were performed on silicon samples grown by the Czochralski method, which presumably have oxygen contents in the range of  $10^{17}$ – $10^{18}$  atoms/ $\text{cm}^3$ . Practically no information is available on the state of oxygen in float-zone grown silicon. The reason for this, we believe, is that float-zone grown silicon has low oxygen content ( $\sim 10^{16}$  atoms/ $\text{cm}^3$ ), and the detection limit of conventional differential absorption methods is  $\sim 1 \times 10^{16}$  atoms/ $\text{cm}^3$ . Oxygen concentration in the range of  $\sim 10^{16}$  atoms/ $\text{cm}^3$  contributes  $\sim 0.5\text{ cm}^{-1}$  to the absorption coefficient at about 9  $\mu\text{m}$ . In addition, the intrinsic lattice band of silicon contributes  $\sim 0.8\text{ cm}^{-1}$  to the absorption coefficient at about 9  $\mu\text{m}$ . This fact clearly indicates the difficulty of the study of the samples with low oxygen content.

But we believe that the mechanism of oxygen complex formation and thermal donors can be understood better if we can understand how the oxygen complex formation is initiated for low oxygen content. In this spirit, we initiated the study of oxygen in silicon with low oxygen content ( $\sim 10^{15}$  atoms/ $\text{cm}^3$ ) using an infrared difference wavelength modulation technique. Several float-zone grown silicon samples were studied, all with oxygen content below the detection limit of conventional methods  $\sim 1 \times 10^{16}$  atoms/ $\text{cm}^3$ . Measurements were made on different sections of the same ingot, that is, the seed-end and the tail-end of the dimensions  $\sim 2\text{ cm}$  in diameter and 1 cm in thickness.

Our infrared wavelength modulation technique<sup>22</sup> was employed to study the 9  $\mu\text{m}$  absorption band of these samples at room temperature. To eliminate the absorption due to the intrinsic lattice vibration of silicon and surface effects, we used a sample-in and sample-out procedure, which enables a comparison of the derivative of the absorption of a sample with a reference sample. With this procedure, the derivative spectrum of the difference of the absorption between a sample and the reference crystal is obtained. A conventional spectrophotometer run of the reference crystal, which is a seed-end of another float-zone silicon, showed just a trace of oxygen at 9  $\mu\text{m}$ ; that is, at 9  $\mu\text{m}$  the oxygen contributes approximately  $0.15\text{ cm}^{-1}$  to the absorption coefficient. From this we can approximate the oxygen content of reference crystal to be  $\sim 10^{15}$  atoms/ $\text{cm}^3$ . The detector used in this study was PbSnTe at liquid nitrogen temperature.

The integrated results of these derivative spectra of the difference for a series of samples are shown in Figs. 13, 14, 15, and 16. The figures show the relative variations of absorption of samples with respect to the reference crystal. Therefore, the positive side of the absorption of the sample in the figures means more absorption and negative side of the absorption means less absorption than the reference crystal at the appropriate wavenumbers. In all the figures, the upper drawing is the experimental result of the seed-end and the lower one is the result of the tail-end of the same ingot with respect to the reference crystal with  $\sim 10^{15}$  oxygen atoms/ $\text{cm}^3$ .

In this study, it should be noted that since we are taking the derivative of the difference of absorption at appropriate frequencies between sample and the reference crystal, the shift or the different width of the bands of the crystals represent changes relative to the reference crystal. Consequently, it is interesting to note that because of the sensitivity of the difference derivative technique ( $\Delta k \sim 10^{-3}\text{ cm}^{-1}$ ), the subtle spectra changes introduced by various heat treatments can be studied by comparing it with the reference even though the change of spectral distribution caused by heat treatment on the sample by itself is difficult to determine.

In Fig. 13, we note that a band emerges at  $1123\text{ cm}^{-1}$  (8.9  $\mu\text{m}$ ) in the tail-end (lower figure). It is not clear exactly what complex is responsible for this band. We can clearly see a shoulder at  $1108\text{ cm}^{-1}$  (8.9  $\mu\text{m}$ ) in the tail-end (lower figure) which appears to be  $\text{Si}_2\text{O}$ . The results on two different ingots are shown in Figs. 14 and 15 and we can see about the same level<sup>2</sup> absorption due to  $\text{Si}_2\text{O}$  at  $1108\text{ cm}^{-1}$  in both parts of the same ingot. However, we can immediately note that the spectral distribution changes even within the same ingot depending on which part of the ingot the sample is taken from. This is not unreasonable if we consider the fact that the crystals are float-zone samples and the sensitivity of our system.

As shown in all of the figures, at low oxygen content the infrared absorption mechanism in the 9  $\mu\text{m}$  region is complicated. This indicates the existence of oxygen in different energy states. This is understandable if we keep in mind the fact that, although oxygen is interstitial in the sense that it does not occupy a lattice site, it can occupy slightly different positions of varying energy.<sup>23</sup> During growth, oxygen atoms are randomly trapped in the silicon lattice, and at room temperature thermal agitation permits the oxygen atom to occupy a number of slightly different configurations of varying energy.

In Fig. 16 the absorption is stronger than the previous samples; it appears that if the oxygen content exceeds a certain value  $\sim 10^{16}$  atoms/cm<sup>3</sup>, the absorption mechanism at 1108 cm<sup>-1</sup> dominates. This band at 1108 cm<sup>-1</sup> we attribute to the form of freely dissolved Si<sub>2</sub>O "quasimolecule." In the above figure we can also note a band at 1048 cm<sup>-1</sup> (9.5  $\mu\text{m}$ ) in both seed and tail-ends; this band might be related to still another complex which can be formed if the oxygen content reaches a certain value ( $\sim 10^{16}$  atoms/cm<sup>3</sup>).

In concluding, we summarize our results:

- 1) Even though the use of float-zone silicon as an oxygen free reference is a common practice, our results show the float-zone silicon also contains oxygen.
- 2) The state of oxygen in silicon is in the form of complexes.
- 3) If the oxygen concentration exceeds a certain value, the oxygen in Si<sub>2</sub>O "quasimolecule" starts dominating the infrared absorption mechanism at about 9  $\mu\text{m}$ .
- 4) Different parts of the same ingot of float-zone grown silicon have different oxygen content which is responsible for infrared absorption around 9  $\mu\text{m}$ .
- 5) Our wavelength modulation system can detect the variation in the absorption coefficient of  $\sim 10^{-6}$  cm<sup>-1</sup>. If we approximate the scattering cross section of oxygen responsible for absorption at 9  $\mu\text{m}$  to be  $\sim 10^{-18}$  cm<sup>2</sup>, we have the capability of detecting oxygen at levels of  $\sim 10^{12}$  atoms/cm<sup>3</sup>!

#### Summary

In this paper we have shown that infrared wavelength modulation is a sensitive and versatile spectroscopic characterization technique for a variety of semiconductor technology problems. In particular the results of a study of deep levels in semi-insulating GaAs, surface layers in Si, GaAs, and HgCdTe, oxygen complexes in floating-zone Si, as well as the determination of strain in ion implanted layers were presented.

#### Acknowledgments

The support of this work by the Air Force Office of Scientific Research under AFOSR-83-0169B, the Army Research Office-Durham under DAAG29-81-K-0164, and the State of California - MICRO program is gratefully acknowledged.

#### References

1. Czanderna, A. W., editor, Methods of Surface Analysis, Vol. 1, Elsevier Scientific Publishing Co., Amsterdam-Oxford-New York, 1975.
2. Lang, D. V., in Thermally Stimulated Relaxation in Solids, edited by P. Bräunlich, Springer-Verlag, Berlin-Heidelberg, New York, 1979.
3. Willardson, R. K., and Beer, A. C., editors, Semiconductors and Semimetals, Vol. 9, Academic Press, New York, 1977.
4. Lagowski, J., Walukiewicz, W., Slusarczyk, M. M. G., and Gatos, H. C., J. Appl. Phys. 50, 5059 (1979).
5. Kamieniecki, E., Lagowski, J., and Gatos, H. C., J. Appl. Phys. 51, 1863 (1980).
6. T. Nishino and Y. Hamakawa, Phys. Stat. Sol. (b) 50, 345 (1972).
7. Eetemadi, S. M., and Braunstein, R., to be published.
8. Kim, R. K., and Braunstein, R., Appl. Opt. 23, 1166 (1984).
9. Braunstein, R., Kim, R. K., Matthews, D., and Braunstein, M., Physica 117B and 118B (1983).
10. Clerjaud, B., Hennel, A. M., and Martinez, G., Solid State Comm. 33, 983 (1980).
11. Martin, G., Appl. Phys. Lett. 39, 747 (1981).
12. Barnowski, J. M., Allen, J. W., and Pearson, G. L., Phys. Rev. 160, 627 (1967).
13. R. W. Haisty, Appl. Phys. Lett. 7, 208 (1965).
14. Look, D. C., Chaudhuri, S., and Sizelove, J. R., Appl. Phys. Lett. 42, (a) (1983).
15. Eetemadi, S. M., and Braunstein, R., to be published.
16. Patel, J. R., in Semiconductor Silicon, edited by H. R. Huff, R. J. Kriegler, and Y. Takeishi, Electrochemical Society, Princeton, 1981, p. 189.
17. Kaiser, W., Phys. Rev. 105, 1751 (1957).
18. Kaiser, W., Frisch, H. L., and Reiss, H., Phys. Rev. 112, 1546 (1958).
19. Kaiser, W., Keck, P. H., and Lange, C. F., Phys. Rev. 101, 1264 (1956).
20. Malyshev, V. A., Sov. Phys. Semicond. 8, 92 (1974).



21. Ryzhkova, E. M., Trapeznikova, I. I., Chelnokov, V. E., and Yakovenko, A. A., Sov. Phys. Semicond. 11, 628 (1977).
22. Braunstein, R., Kim, R. K., and Braunstein, M., Laser Induced Damage in Optical Materials: 1979, Boulder, CO, USA. 30-31 Oct. 1979 (Washington D. C., U.S.A.: NBS 1980), pp. 99-117.
23. Hrostowski, H. J., and Kaiser, R. K., Phys. Rev. 107, 966 (1957).

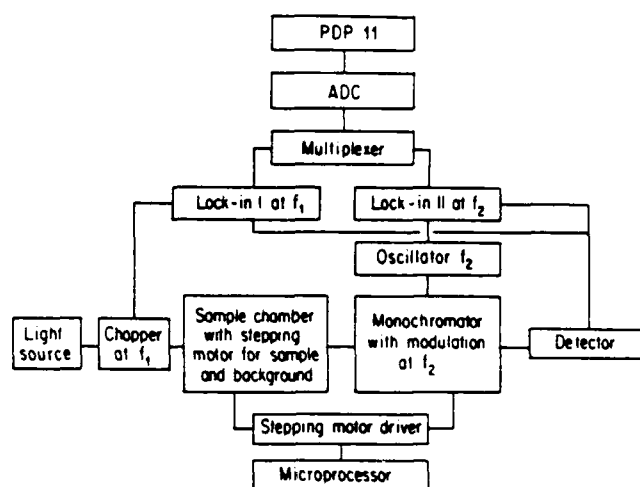


Figure 1. Block diagram of the infrared wavelength modulated system.

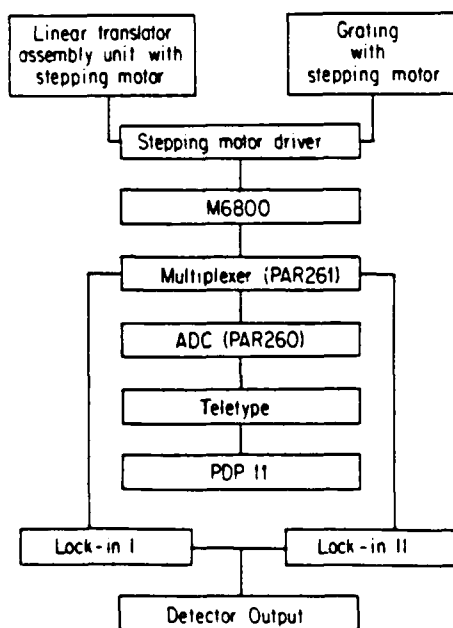


Figure 2. Block diagram of control system for data-taking cycle.

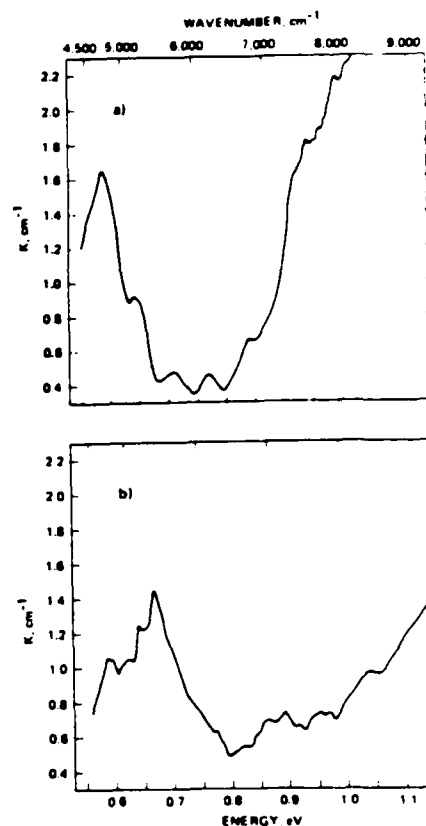
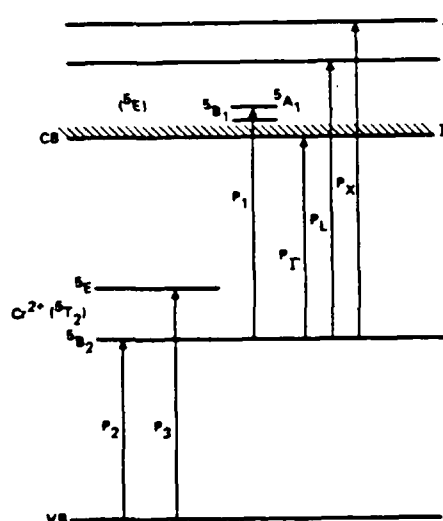


Figure 4. a) p-type, b) n-type GaAs:Cr.



SI-GaAs-(LEC)  
Sample: M039T  
T = 300K

Energy (eV)	Absorption Coefficient (cm <sup>-1</sup> )
0.2	0.1
0.5	0.2
0.8	0.5
1.0	1.0
1.2	2.0
1.3	2.5
1.4	4.0

Figure 6. Wavelength modulation absorption spectra of LEC-GaAs at 300 K.

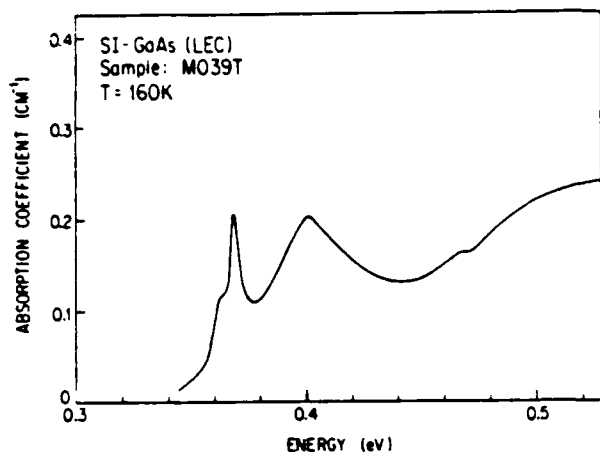


Figure 7. Wavelength modulation absorption spectra of LEC-GaAs at 160 K.

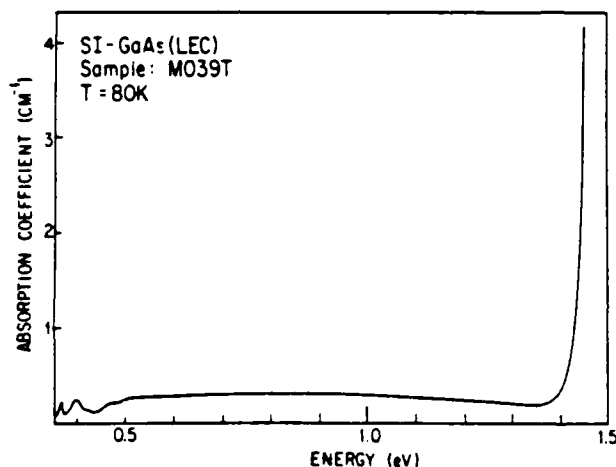


Figure 8. Wavelength modulation absorption spectra of LEC-GaAs at 80 K with EL2 photo-quenched.

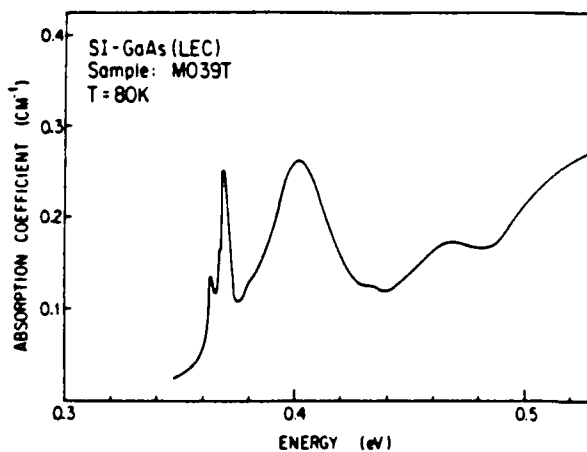


Figure 9. Wavelength modulation absorption spectra of LEC-GaAs at 80 K on a vastly expanded scale compared to Fig. 8.

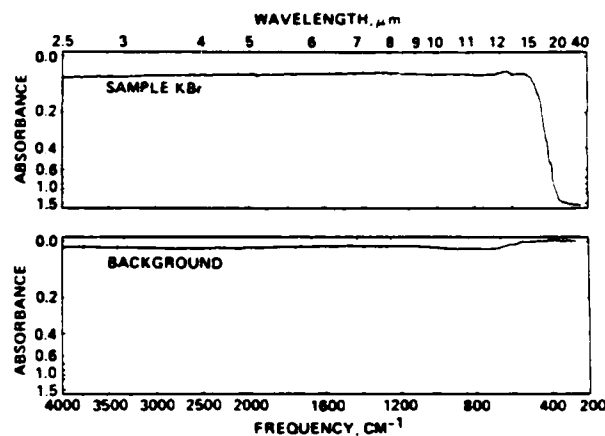


Figure 10. Absorption spectrum of a typical KBr sample obtained by a conventional double-beam instrument.

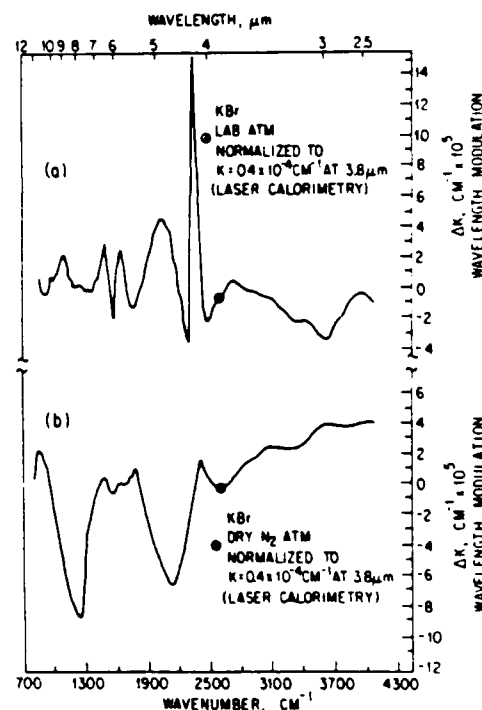


Figure 11. Wavelength modulation absorption spectra of KBr;  $\Delta K$  is the change in the absorption coefficient in  $\text{cm}^{-1}$ ; (a) in the laboratory atmosphere; (b) in a dry  $\text{N}_2$  atmosphere.

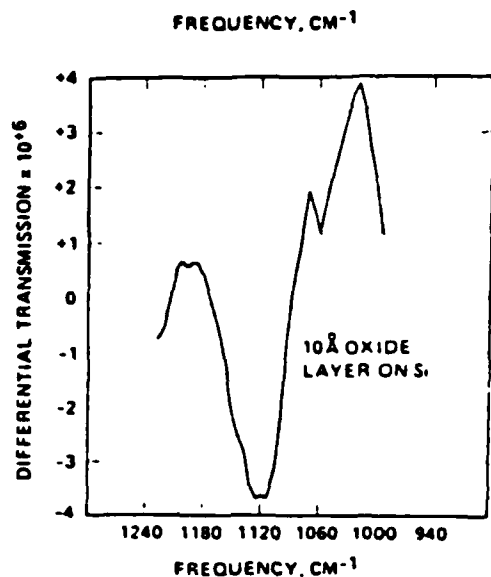


Figure 12. Wavelength modulation absorption spectra of a 10 Å oxide layer of Si.

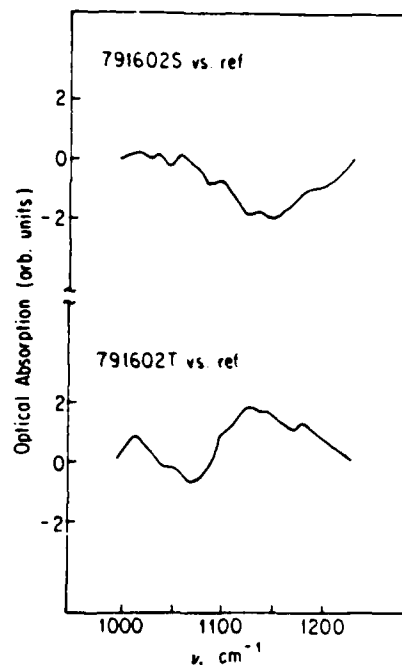


Figure 13.

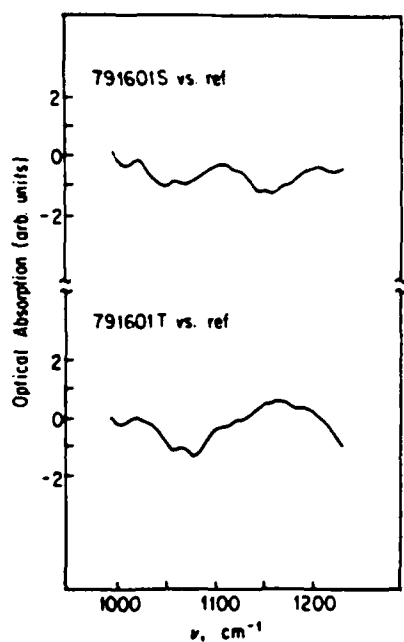


Figure 14.

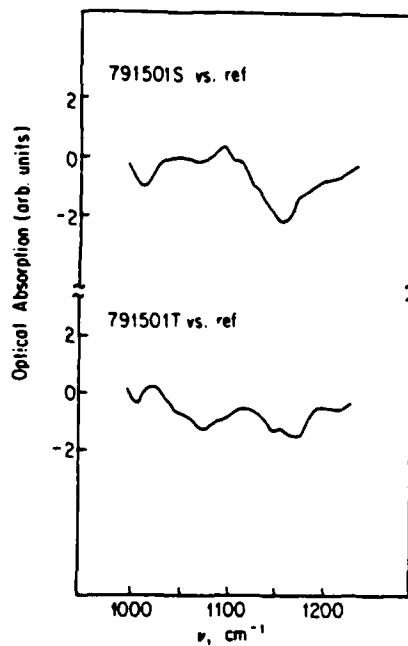


Figure 15.

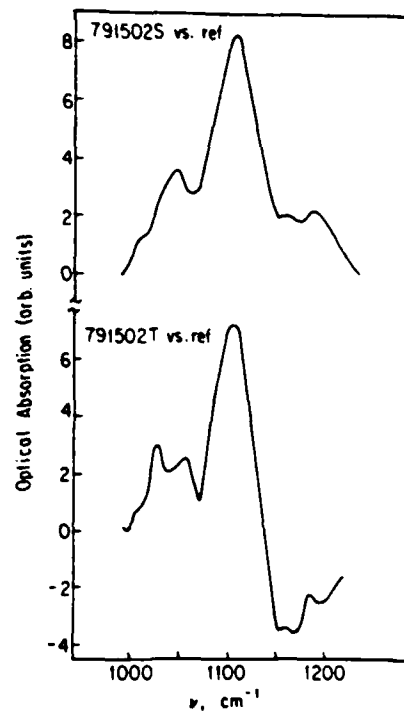


Figure 16.

Figures 13, 14, 15, 16. The relative optical absorption of the seed (top curve) and tail-end (bottom curve) of 791602, 791601, 791501, and 791502, respectively, float-zone Si ingots with respect to a Si reference containing  $\sim 10^{15}$  oxygen atoms/cm<sup>3</sup>.

# Reexamination of the wavelength modulation photoresponse spectroscopies

S. M. Eetemadi and R. Braunstein

Department of Physics, University of California, Los Angeles, California 90024

(Received 15 April 1985; accepted for publication 29 July 1985)

Reexamination of the wavelength modulation photoresponse spectroscopies showed that the line shapes obtained by these methods are subject to distortions from several sources of spurious interference spectra. A comparison is made between the wavelength modulation absorption/reflection and the wavelength modulation photoresponse spectroscopies; it is concluded that the former are the most suitable modulation techniques for studies requiring unambiguous line shapes.

## I. INTRODUCTION

Optical modulation spectroscopy has been extensively used in the past to study the optical absorption and reflection of materials.<sup>1-3</sup> Being a derivative technique in nature, it is far more sensitive than conventional spectroscopic methods for detecting small structures out of a broad background. Various modulation parameters such as applied electric field, stress, temperature, and wavelength of the probing light beam have been combined with absorption and reflection spectroscopy to form a whole family of derivative spectroscopy techniques. More recently, other derivative techniques combining the wavelength modulation and the photoresponse (photoinduced changes in voltage,<sup>4</sup> capacitance,<sup>5</sup> and current<sup>6</sup>) spectroscopies have been introduced as a new approach to the study of absorption in semiconductors.

In this paper we present a reexamination of the wavelength modulation photoresponse spectroscopies in general. Some of the limitations of these techniques, as well as the necessary precautions in interpreting the experimental results, are discussed. A comparison is made between wavelength modulation absorption/reflection and wavelength modulation photoresponse spectroscopies.

For wavelength modulation photoresponse measurements, samples are prepared in the form of a  $p$ - $n$  junction,<sup>6</sup> a metal-insulator semiconductor (MIS),<sup>4</sup> or a Schottky barrier<sup>5</sup> with semitransparent electrodes. The changes in the photoresponse induced in the space-charge region, by wavelength modulation of the incident light beam, are measured using a phase-locked amplifier synchronous with the wavelength modulator. The derivative photoresponse spectrum thus obtained has been interpreted as being proportional to the derivative of the absorption coefficient, and thus to the derivative of the photoionization cross section.<sup>4</sup> In particular, for the transitions involving photoionization of the deep levels, the derivative surface photovoltage (DSPV) is given by<sup>5</sup>

$$\frac{dV_s}{d\lambda} = -V_s I_0 A \frac{n_t}{N_D - N_A} \frac{d\sigma}{d\lambda}, \quad (1)$$

where  $V_s$  is the surface photovoltage,  $I_0$  is the incident photon flux,  $n_t$  is the concentration of the occupied traps being probed, and  $N_D - N_A$  is the net doping concentration. The

constant  $A$  depends on the thermal generation and recombination of the traps, and  $\sigma$  is the photoionization cross section.

Wavelength modulation reflection and transmission spectroscopies have a serious experimental difficulty because the spectra contain substantial spurious structures originating from the derivative of the background spectra which must be properly removed in order to obtain the true spectra of the sample itself. The structures in the background spectrum are due to the spectral dependence of the light source intensity, various optical components of the experimental system, and the atmospheric absorption, especially in the infrared region of the spectra. These structures have been successfully removed by various ingenious methods of background derivative subtractions,<sup>2</sup> including double-beam single detector<sup>7</sup> and single beam sample-in sample-out techniques.<sup>1</sup> However, the question of the effect of the background spectra on the derivative photoresponse results has not been addressed in the previous theoretical and experimental works on this subject.

To investigate the possible effects of the background spectra, a preliminary derivative surface photovoltage (DSPV) experiment was conducted on a silicon sample prepared in the form of a semitransparent MOS structure, and the result was compared with the derivative of the incident photon flux spectrum. Similarities between changes in the structures observed in both spectra were taken as an indication of possible superposition of the derivative of the background spectra on the DSPV spectra, and prompted us to reexamine the theory of the wavelength modulation surface photovoltage spectroscopy.

The result of our investigation showed that the proportionality relationship [Eq. (1)] between the DSPV and the derivative of the absorption coefficient is not valid in general. The DSPV spectra are rather a superposition of several terms, which includes the derivative of the background spectra, as well as the optical properties of the materials which are used to construct the MOS structure; these additional terms are the various sources of distortions depending on the spectral region under investigation. The following discussion is focused primarily on the wavelength modulation surface photovoltage. The analysis, however, applies equally to other modulation photoresponse spectroscopies, as well

## II. EXPERIMENTAL RESULTS

The derivative surface photovoltage measurements were performed on *n*-type silicon (100) substrates utilizing MOS structures. The experimental system used is described elsewhere.<sup>8</sup> The MOS structures were made by evaporating a 400 Å semitransparent gold electrode on an oxide layer (1000 Å thick) grown on silicon by a standard dry oxidation technique.<sup>9</sup>

Typical sub-band-gap derivative surface photovoltage spectra ( $dV_s/dE$ ) obtained at 83 K are shown in Figs. 1(a) and 2(a). To obtain a good signal-to-noise ratio it was necessary to keep the modulation amplitude and the spectral slit width of the monochromator fairly large ( $\Delta\lambda/\lambda \sim 10^{-2}$  when using a Golay detector). The derivatives of the incident photon spectra of a tungsten iodide source for the same instrument and spectral region with comparable amplitude of modulation were obtained using a PbS detector. These are shown for comparison in Figs. 1(b) and 2(b). With the sensitivity of the PbS detector a much better resolution ( $\Delta\lambda/\lambda \sim 2 \times 10^{-3}$ ) is also possible, as shown in Fig. 3.

The dominant structure in Fig. 1(a) is due to the inter-band transition near the indirect band gap of silicon with the emission and absorption of phonons. It is similar to other reported DSPV results.<sup>10</sup> The smaller structures, below 1.15 eV, may in principle be associated with the multiphonon absorption. However, they can also be considered to be a manifestation of similar structures in the derivative of the background spectra  $dI_0/dE$ , shown in Fig. 1(b). Comparison of Figs. 2(a) and 2(b) also suggests a strong correlation

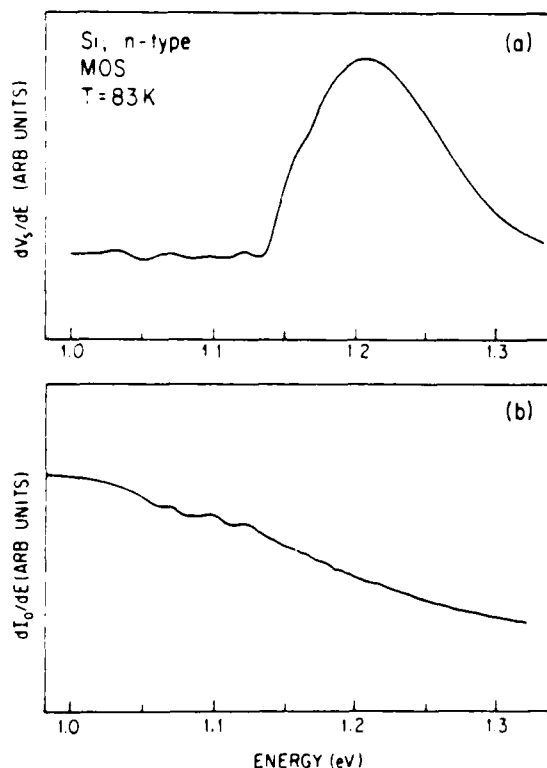


FIG. 1. (a) The derivative surface photovoltage spectra of silicon ( $T = 83$  K); (b) the derivation of the background spectra in the spectral range of 1.0–1.35 eV; amplitude of modulation ( $\Delta\lambda/\lambda$ ) =  $10^{-2}$ .

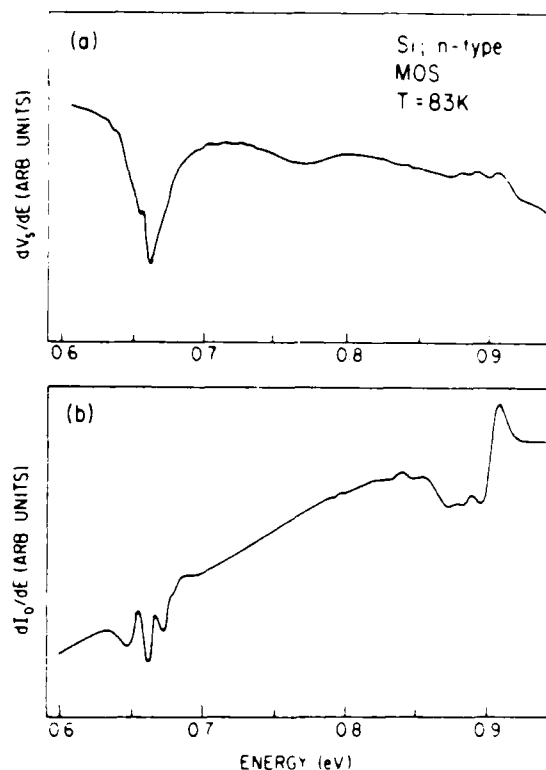


FIG. 2. (a) The derivative surface photovoltage spectra of silicon ( $T = 83$  K); (b) the derivative of the background spectra in the spectral range of 0.6–1.0 eV; amplitude of modulation ( $\Delta\lambda/\lambda$ ) =  $10^{-2}$ .

between the structures in the DSPV and the derivative of the background spectra near 0.65 and 0.9 eV. In fact, signatures of the derivative of the background spectra are quite commonly observed in the wavelength modulated spectra of the reflected and transmitted light beam, as predicted by the theory of the corresponding wavelength modulation spectroscopy. These can be corrected for by subtraction of the experimentally determined background.<sup>7</sup> In contrast, the theory of the DSPV, as formulated in Eq. (1), is not consis-

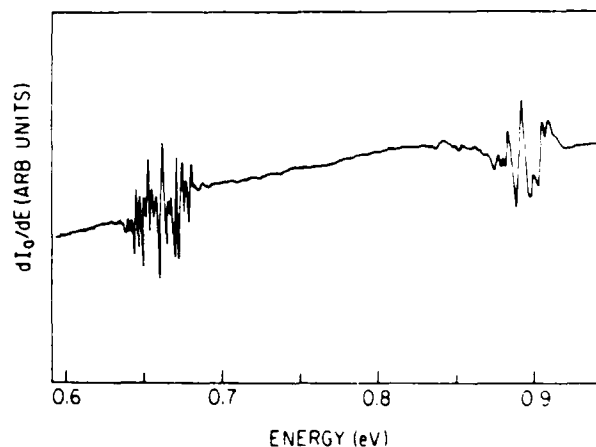


FIG. 3. Derivative of the background spectra in the spectral range of 0.76–1.0 eV using a tungsten source; amplitude of modulation ( $\Delta\lambda/\lambda$ ) =  $2 \times 10^{-3}$ .

tent with the above observation. In the next section we present our analysis of the theory of the DSPV spectroscopy, which shows that the DSPV spectra can contain signatures of the derivative of the background spectra, as well as other possible sources of distortions in the various regions of spectra.

### III. DERIVATIVE OF SURFACE PHOTOVOLTAGE (DSPV)

The theory of surface photovoltage has been treated by a number of authors.<sup>11</sup> For the purpose of this study, the changes in the surface potential of a semiconductor,  $V_s$ , induced by the light of intensity  $I_0$  and wavelength  $\lambda$  may be written, for small signals (surface photovoltage  $\ll$  surface potential), in the form<sup>11</sup>

$$V_s(\lambda) = I(\lambda) \alpha(\lambda) F(\lambda), \quad (2)$$

where

$$F = F(L_0, \alpha, T, E_f, \tau_b, n_b, p_b; \\ \times E_i, n_i, \sigma_{ph}^n, \sigma_{ph}^p, e_n, e_p, S).$$

$F$  is a complicated function of diffusion length  $L_0$ , absorption coefficient  $\alpha$ , temperature  $T$ , Fermi energy  $E_f$ , bulk carrier lifetime for electrons, holes, and concentrations  $\tau_b$ ,  $n_b$ ,  $p_b$ , respectively, deep levels energy  $E_i$ , concentration  $n_i$ , photoionization cross sections  $\sigma_{ph}^n$ , and  $\sigma_{ph}^p$  for electrons and holes, respectively, and their thermal emission rates  $e_n$  and  $e_p$ , in the semiconductor, as well as the effective surface recombination velocity  $S$ . The exact functional dependence of  $F$  on these parameters is not needed for our discussion; however, it is rather important to note its implicit wavelength dependence through  $\alpha(\lambda)$ ,  $\sigma_{ph}^n(\lambda)$ , and  $\sigma_{ph}^p(\lambda)$ .  $I(\lambda)$  is the actual photon flux entering the space-charge region of the semiconductor. Quite often in the past,  $I_0(\lambda)$ , which is the incident photon flux illuminating the MOS structure, has been used instead of  $I(\lambda)$ ; thus, ignoring the spectral dependence of the transmittance through the metal and the insulating layers of the structure,  $I(\lambda)$  and  $I_0(\lambda)$  are related by

$$I(\lambda) = I_0(\lambda) T(\lambda). \quad (3)$$

In essence, the wavelength dependence of  $T(\lambda)$  is due to the spectral dependence of the absorption coefficient of the light in the metal and insulator layers, the reflection coefficients at the interfaces, and the interference pattern due to the internal multiple reflections from the interfaces.

Combining Eqs. (2) and (3) we have

$$V_s = I_0(\lambda) T(\lambda) \alpha(\lambda) F(\lambda), \quad (4)$$

which forms the basis of our analysis of the wavelength modulation surface photovoltage.

If the wavelength of the incident light beam is modulated as

$$\lambda = \lambda_0 + \Delta \lambda \cos \omega t, \quad (5)$$

where  $\Delta \lambda$  and  $\omega$  are the amplitude and the frequency of modulation, respectively, then the surface photovoltage  $V_s(\lambda)$  becomes a periodic function of time,  $V_s(\lambda_0 + \Delta \lambda \cos \omega t)$ . For small  $\Delta \lambda$ , the derivative of the modulated surface photovoltage is given by

$$\begin{aligned} \frac{dV_s}{d\lambda} = & I_0(\lambda) T(\lambda) F(\lambda) \frac{d\alpha(\lambda)}{d\lambda} + T(\lambda) F(\lambda) \alpha(\lambda) \frac{dI_0}{d\lambda} \\ & + I_0(\lambda) F(\lambda) \alpha(\lambda) \frac{dT(\lambda)}{d\lambda} \\ & + I_0(\lambda) T(\lambda) F(\lambda) \frac{dF(\lambda)}{d\lambda}. \end{aligned} \quad (6)$$

It must be added that, in order to incorporate the response of the system to a time varying incident light intensity, the above equation must be multiplied by a frequency response function  $G(\omega)$ .<sup>12</sup> However, since this factor is to first-order independence of the wavelength, it is treated here as a constant of proportionality.

In contrast to Eq. (1), Eq. (6) shows that the DSPV signal is not, in general, proportional to  $d\alpha/d\lambda$ , and therefore its various terms introduce different degrees of distortion which depend on the relative size of their spectral changes in the spectral region of interest. The most notorious source of the distortion is the spectral changes of  $I_0(\lambda)$ , the background. The distortion introduced by  $I_0$  is present in all four terms of Eq. (6), but its effect is most dramatic in the second term, which contains  $dI_0/d\lambda$ . This term affects the DSPV spectra in the near infrared region of spectra which corresponds to the sub-band-gap transitions in some semiconductors (e.g., Si, GaAs), as well as in the ultraviolet region of the spectra where the interband transitions occur.

### IV. DISCUSSION: COMPARISON OF WAVELENGTH MODERATION PHOTO RESPONSE AND WAVELENGTH MODULATION ABSORPTION/REFLECTION SPECTROSCOPIES

The structure in the spectra of the transmittance  $T(\lambda)$  and its derivative  $dT/d\lambda$  are caused by the spectral changes of the optical constants in the metal and the insulating layers, and the reflection coefficient of the semiconductor, as well as the interference patterns generated because of the interfaces. In the present MOS structure the optical properties of Au, SiO<sub>2</sub>, and Si have to be considered. These factors are separately discussed below:

(a) The spectral changes of the reflectivity of gold  $R(\lambda)$ , as well as its logarithmic derivative  $dR/d\lambda$  occur in the 2.0–5.0 eV region of the spectra and are primarily due to the  $d$  band in Fermi-level transitions.<sup>13</sup> Structure in the spectrum of the derivative of its transmission coefficient in the 2.0–3.5 eV region, have also been observed.

(b) The optical constants of the insulating layer (SiO<sub>2</sub>) are fairly smooth in the 0.5–4.5 eV region of the spectrum,<sup>15</sup> and therefore are not expected to influence the line shapes of the interband transitions.

(c) The spectral changes caused by the interference pattern depend on the thickness of the layers, their index of refraction, and the spectral region of interest. Optical interference patterns have been studied for the MIS structures with various thicknesses of Au and SiO<sub>2</sub> layers on silicon substrates.<sup>16</sup> The signatures of such interference patterns have also been observed in the surface photovoltage spectra.<sup>17</sup>



(d) Finally, the spectral changes in the  $R(\lambda)$  and  $dR/d\lambda$  of the Si substrate contribute significantly to the spectra of  $T(\lambda)$  and  $dT/d\lambda$ , and hence to the DSPV spectra. The reflectivity of Si and its logarithmic derivative obtained by the wavelength modulation reflectance spectroscopy has been reported.<sup>18,19</sup>

It is therefore clear that the spectra of  $T(\lambda)$  and  $dT/d\lambda$  contain substantial structures that could significantly change the line shapes of the absorption obtained from the wavelength modulation surface photovoltage, as well as other forms of wavelength modulation photoresponse spectroscopies.

In contrast to the wavelength modulation absorption/reflection spectroscopy, removal of the background interferences  $I_0(\lambda)$  and  $dI_0/d\lambda$  from the DSPV spectra is very difficult. To date, no systematic method for its subtraction has been suggested. We suggest a technique utilizing a double-beam system in combination with a reference optical detector and feedback loops to suppress the spectral changes of  $I_0(\lambda)$  and  $dI_0/d\lambda$ .

For this purpose, the light beam from the exit slit of the monochromator in DSPV spectrometer needs to be split by a beam splitter. Both beams can therefore be wavelength modulated at frequency  $\omega_2$ . One of the beams can be used to illuminate the DSPV sample, while the other beam can be chopped at frequency  $\omega_1$  and then incident upon an optical detector. The output of the detector is fed into two lock-in amplifiers. One of the lock-in amplifiers (I) is tuned to  $\omega_1$  to measure the light intensity, and the other one is tuned to  $\omega_2$  to measure  $dI_0/d\lambda$ . Except for the beam splitter and the DSPV sample, this is similar to the infrared wavelength modulation spectrometer described elsewhere.<sup>1</sup> The output of the lock-in amplifier (I) can be used in a negative feedback loop to regulate the power supply of the light source. This arrangement will keep the light intensity constant as the wavelength is scanned. The output of the lock-in amplifier (II) can be used in another negative feedback loop to regulate an intensity modulator to keep  $dI_0/d\lambda$  equal to zero. The intensity modulator can be placed anywhere in the light path before the beam splitter. Its modulator frequency should be the same as the wavelength modulator, and its amplitude can be controlled by the negative feedback loop from the lock-in amplifier (II). One such intensity modulator has been used in a wavelength modulation reflectance spectrometer for the same purpose.<sup>19</sup> The two feedback loop systems eliminate  $dI_0/d\lambda$  and the spectral changes of the background  $I_0(\lambda)$  to the extent that it is smooth in the spectra region of interest. This is not possible in the absolute sense nor over the entire region of the spectrum. However, what is needed in practice, is to have detectors whose spectral responsivity are flat and smooth compared to the line shapes of the optical transitions under investigation.

In comparing the wavelength modulation techniques, the wavelength modulation absorption/reflection (WMA/R) spectroscopy has several advantages over the wavelength modulation photoresponse (WMPR). The WMA/R method

yields unambiguous line shapes for the optical transitions, which are therefore easier to interpret. In WMA/R, the only source of spurious signals is the background spectrum which can be completely removed in a systematic way, independent of the spectral responsivity of the detector. Finally, the WMA/R is a nondestructive method which can be applied directly to the bulk of the materials. In contrast, the WMPR measurements often require fabrication of devices in the form of MIS,  $p$ - $n$  junction, or Schottky barriers which could result in the introduction of process related impurities or defects into the samples, as well as the necessity of applying corrections for the optical properties of the materials used for fabricating the structures.

## V. CONCLUSIONS

We have shown that contrary to the previous assumptions, the DSPV in general is not proportional to the derivative of the absorption coefficient. A general formulation of the DSPV was derived which revealed the various possible sources of spurious interference spectra. The effects of these interferences on the line shapes of optical transitions were studied. A practical method for removal of the main source of the distortions, i.e., the background, was suggested.

## ACKNOWLEDGMENTS

The support of this work by the Air Force Office of Scientific Research under AFOSR-84-0169B, the Army Research Office-Durham under DAAG29-81-K-0164, and the State of California MICRO program is gratefully acknowledged.

<sup>1</sup>R. K. Kim and R. Braunstein, *Appl. Opt.* **23**, 1166 (1984).

<sup>2</sup>M. Cardona, *Modulation Spectroscopy* (Academic, New York, 1969).

<sup>3</sup>*Semiconductors and Semimetals*, Vol. 9, *Modulation Techniques*, edited by R. K. Willardson and A. C. Beer (Academic, New York, 1977).

<sup>4</sup>J. Lagowski, W. Walukiewicz, M. M. G. Slusarczyk, and H. C. Gatos, *J. Appl. Phys.* **50**, 5059 (1979).

<sup>5</sup>E. Kamieniecki, J. Lagowski, and H. C. Gatos, *J. Appl. Phys.* **51**, 1863 (1980).

<sup>6</sup>T. Nishino and Y. Hamakawa, *Phys. Status Solidi B* **50**, 345 (1972).

<sup>7</sup>R. Stearns, J. Steele, and R. Braunstein, *Rev. Sci. Instrum.* **54**, 984 (1983).

<sup>8</sup>S. M. Eetemadi, Ph.D. thesis (University of California at Los Angeles, 1984).

<sup>9</sup>A. S. Grove, *Physics and Technology of Semiconductor Devices* (Wiley, New York, 1967).

<sup>10</sup>L. L. Jastrzebski and J. Lagowski, *RCA Rev.* **41**, 181 (1980).

<sup>11</sup>D. L. Lile, *Surf. Sci.* **34**, 337 (1973), and references therein.

<sup>12</sup>S. M. Ryvkin, *Photoelectric Effects in Semiconductors* (Consultants Bureau, New York, 1964), Chap. III.

<sup>13</sup>M. Welkowsky, Ph.D. thesis (University of California, Los Angeles, 1971).

<sup>14</sup>R. Rosei, R. Antonangeli, and U. M. Grassano, *Surf. Sci.* **37**, 689 (1973).

<sup>15</sup>W. L. Wolfe, in *Handbook of Optics*, edited by W. G. Driscoll and W. Vaughan (McGraw-Hill, New York, 1973), Chap. 7.

<sup>16</sup>R. J. Powell, *J. Appl. Phys.* **40**, 5093 (1969).

<sup>17</sup>J. Lagowski, L. Jastrzebski, and G. W. Cullen, *J. Electrochem. Soc.* **128**, 2669 (1981).

<sup>18</sup>M. Welkowsky and R. Braunstein, *Phys. Rev. B* **5**, 497 (1972).

<sup>19</sup>R. Zucca and Y. R. Shen, *Appl. Opt.* **12**, 1293 (1973).

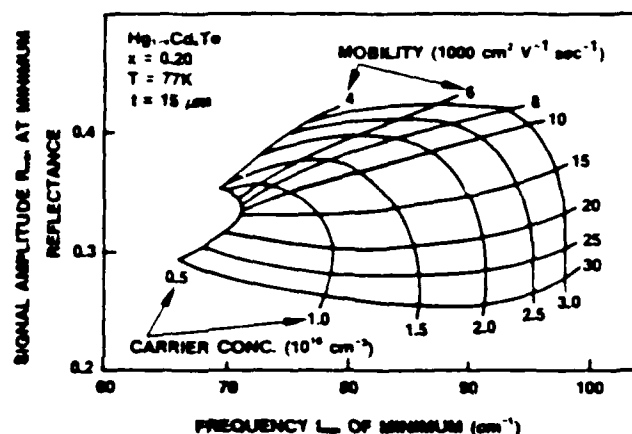


FIG. 5. Calculated carrier concentration and mobility from fit to far-infrared reflectivity minimum amplitude and frequency, for epitaxial layer at 77 K, with  $x = 0.2$  and thickness  $15 \mu\text{m}$ .

Comparisons of the resistivities, carrier concentrations, and mobilities obtained by modeling the full far-infrared reflectance spectra and by Hall-effect analyses are shown in Figs. 2, 3, and 4. The resistivity values agree within a factor of 2, while the carrier concentration and mobility data show different systematic displacements at room temperature and at 77 K, causing an increased data scatter. The use of more accurate temperature-dependent values of effective mass is expected to bring all of the far-infrared data to within a factor of 2 of Hall-effect values.

A simpler and faster method for determining the resistivity, carrier concentration, and mobility is to determine the position and amplitude of the reflectivity minimum between the free-carrier region and the HgTe-like vibrational mode. This type of analysis has been reported for GaAs<sup>1</sup> and CdTe.<sup>2</sup> The minimum occurs at the frequency  $\omega_-$ , the lower coupled plasmon-phonon mode. If the mobility  $\mu$  is large, this is given by

$$2\omega_-^2 = (\omega_p^2 + \omega_l^2) - [(\omega_p^2 - \omega_l^2)^2 + 4\omega_p^2\omega_l^2(1 - \epsilon_-/\epsilon_s)]^{1/2}, \quad (5)$$

where  $\omega_l$  is the dominant HgTe-like longitudinal optical lattice frequency ( $\omega_l = (\epsilon_s/\epsilon_-)^{1/2}\omega_1$ ) and  $\epsilon_-$  and  $\epsilon_s$  are the high-frequency and static dielectric constants, respectively. Parametric curves relating the carrier concentration and mobility to the frequency and reflectivity amplitude at the minimum have been calculated. An example for  $n$ -type HgCdTe with  $x = 0.2$  at 77 K is shown in Fig. 5. Resistivities, carrier concentrations, and mobilities estimated in this way are shown for room-temperature data in Figs. 2, 3, and 4. While good results are shown in the figures, the accuracy of this reflectivity-minimum analysis is lower for  $p$ -type material than for  $n$ -type. Furthermore, multilayer structures, such as those having an  $n$ -type skin on a  $p$ -type base, or layers with mixed conduction (as occurs in an intrinsic sample), do not exhibit a well-defined minimum. Other structures in the reflectance data can also interfere with the determination of the location of the minimum, as is shown in Fig. 1. When a distinct minimum can be seen, the analysis is quick and reasonably accurate.

### III. RAMAN SCATTERING

In Raman scattering, the plasmon-phonon mode produces a peak instead of a minimum. As in the reflectance-minimum analysis, the peak frequency can be used to determine  $\omega_p^2$  and the free-carrier concentration.<sup>7,8</sup> For HgCdTe, the peaks have been found to occur in regions where other Raman modes make the identification of the plasmon-phonon mode difficult and make it insensitive to carrier concentrations below  $10^{16} \text{ cm}^{-3}$ . Raman scattering is sensitive to a surface layer  $\sim 100 \text{ \AA}$  deep. This makes Raman spectroscopy potentially useful for measuring carrier concentrations in ion-implanted materials, but it is too insensitive for general epitaxial layer screening.

### IV. EDDY-CURRENT ABSORPTION

In eddy-current absorption, a wafer is placed between an rf source and a pickup coil. The power loss due to eddy currents induced in the sample is proportional to the conductivity times the thickness of the layer.<sup>6</sup> Two commercial instruments<sup>12</sup> were tested, with similar results. Data in Fig. 6 show a variation between eddy-current and current-voltage resistivity values of a factor of approximately 3. In this case, the current-voltage analysis was done on a small piece cleaved off the edge of the wafer, while the eddy-current measurements were done on the remaining wafer, which could have caused some of the data scatter shown.

The eddy-current technique tests a large area, requiring a minimum sample size of  $\sim 5/8 \times 5/8$  in. Both vendors supply a standard resistivity meter and a high-sensitivity meter. The standard range is appropriate for bulk HgCdTe wafers, while the high-sensitivity range is needed for thin epitaxial layers. The technique does not have enough sensitivity to indicate any absorption in CdTe semi-insulating substrate material. The measurements are simple and take only a few seconds to perform, but their accuracy for determining resistivity is only within a factor of 3.

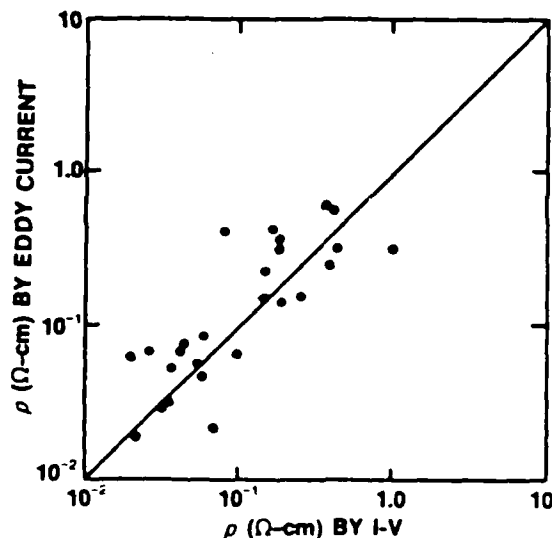


FIG. 6 Resistivity measured by eddy-current and current-voltage techniques.

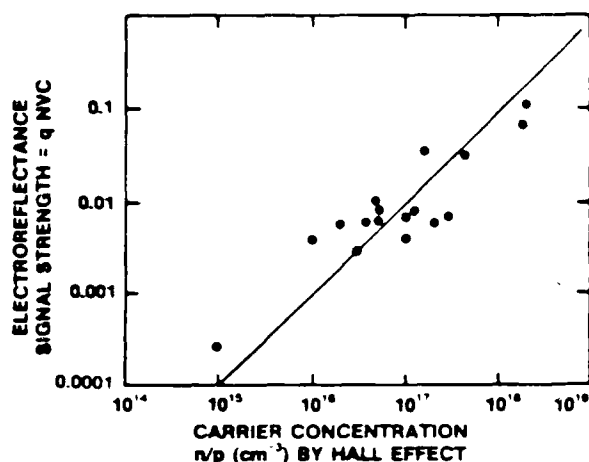


FIG. 7. Electroreflectance signal strength as function of free-carrier concentration in sample.

The parameter of more importance is usually carrier concentration. In Si, where mobilities can be accurately estimated for any given doping concentration, the resistivity measurement can be used to give carrier concentration values by means of the relation  $\rho = Ne\mu$ . In HgCdTe, the error in resistivity multiplied by the uncertainty in the mobility produces errors of over an order of magnitude in estimating carrier concentrations. This makes the technique less important for HgCdTe than it is for Si.

## V. ELECTROREFLECTANCE

Electroreflectance involves immersing the sample in an electrolyte so that an ac electric field can be applied to the surface. The ac field modulates the reflectance, giving a normalized reflectance spectrum at a singularity in a band density of state represented by<sup>13</sup>

$$\frac{\Delta R_{ac}}{R_{dc}} = \text{Re} \left\{ \frac{qNVCe^{i\theta}}{[E_s - E_{ph} + i\Gamma]^{1/2}} \right\}, \quad (6)$$

where  $\Delta R_{ac}$  = ac reflectance;  $R_{dc}$  = reflectance;  $N$  = doping density;  $V$  = ac modulation voltage;  $E_s$  = energy of the singularity;  $E_{ph}$  = incident light energy;  $n = 5$  for the  $E_s$  singularity;  $\theta$  = a phase factor;  $\Gamma$  = a broadening factor; and  $C$  is a constant including the oscillator strength of the optical transition.

Experimentally, the reflectance signal from a photomultiplier is divided and sent to an ac amplifier and to a dc amplifier; the latter is used in a feedback loop on the photomultiplier power supply to keep  $R_{dc}$  constant. The ac amplifier output is then proportional to  $\Delta R_{ac}/R_{dc}$ . The ratio removes any amplitude fluctuation effects in the signal due to the lamp or the optics. A computer is used to fit the observed data to Eq. (6), with the signal strength ( $qNVC$ ),  $\theta$ ,  $E_s$ , and  $\Gamma$  being the fitting parameters. The signal strength is proportional to the net doping density  $N$  and independent of the phase  $\theta$  or the broadening  $\Gamma$ .

Without standards, absolute values of  $N$  are difficult to obtain using this technique, as the voltage drops are difficult to measure in the electrolyte, the surface layers, and the

semiconductor. For this study, the same samples were used for both Hall-effect measurements and electroreflectance measurements at room temperature. Full-temperature Hall-effect data are needed for  $p$ -type samples, since the net doping density is not given by single-temperature Hall-effect data in the transition region from extrinsic to intrinsic conductivity.

Data in Fig. 7 show a good one-to-one relationship between the free-carrier concentration as determined by the Hall effect and the electroreflectance signal strength. The scatter in the data is within a factor of approximately 2. The data include both  $n$ - and  $p$ -type samples, with  $x$  values between  $x = 0.2$  and  $x = 0.35$ . The low scatter in the data implies that the factor  $C$  in Eq. (6) is approximately constant over this range in  $x$ .

The technique has been used in measuring relative free-carrier concentrations and in determining electrical junction locations in double-layer devices that have been either bevel-etched or step-etched. Photorefectance techniques in which light of above-band-gap energy is used to excite carriers that induce a surface field may allow the measurements to be made without contacts and at low temperatures, as well.<sup>14</sup>

## VI. CONCLUSIONS

Of the techniques studied, far-infrared reflection gives the most complete and most accurate noncontact characterization of electrical properties. It can be used to determine resistivity, free-carrier concentration and mobility, and to map these values over the area of a wafer to be processed. The agreement of the far-infrared values and Hall-effect values is within a factor of 2 for resistivity and within a factor of 3 for carrier concentration and mobility. More accurate temperature-dependent effective mass values should bring the carrier concentration and mobility data to the same agreement as is seen in the resistivity data. The data analysis using the reflectivity minimum, while easier and faster than a full fit to the data, at present does not work well for  $p$ -type or mixed-conduction samples.

Interference of other effects with the plasmon-phonon mode in Raman spectra makes this technique too inaccurate for general use in screening material for carrier concentration values.

Commercially available eddy-current resistivity equipment allows for the rapid measurement of this parameter for epitaxial HgCdTe layers, with the values agreeing within a factor of 3 with current-voltage data. The technique is not sensitive enough to screen semi-insulating CdTe substrates, however.

Electroreflectance signal strength can be used to give relative doping density values at room temperature that are useful in mapping wafer uniformity or in profiling bevel-etched or step-etched samples.

## ACKNOWLEDGMENTS

The authors wish to thank Professor Paul Raccach of the University of Illinois, Chicago, and Professor Fred Pollak of Brooklyn College of CUNY for their help and advice in setting up SBRC's electroreflectance measurement apparatus.

They would also like to thank George Whiteman, Joseph Rosbeck, Ralph Ruth, and Karen Kormos of SBRC for their help in this study.

\*<sup>1</sup> Supported at SBRC by AFWAL/ML, under Contract No. F33615-84-C-5083 and at UCLA jointly by SBRC and the State of California through a State MICRO Program.

<sup>1</sup>S. Perkowitz and J. Brecher, *Infrared Phys.* **13**, 321 (1973).

<sup>2</sup>S. Perkowitz and R. H. Thorland, *Phys. Rev. B* **9**, 545 (1974).

<sup>3</sup>W. E. Tennant and J. A. Cape, *Phys. Rev. B* **13**, 2540 (1976).

<sup>4</sup>S. Perkowitz, *Infrared and Millimeter Waves Vol. 8, Electromagnetic Waves in Matter*, Part I, edited by K. J. Button (Academic, New York, 1983), pp. 71-122.

<sup>5</sup>S. Perkowitz, *J. Electron Mater.* **14**, 551 (1985).

<sup>6</sup>G. L. Miller, D. A. H. Robinson, and J. D. Wiley, *Rev. Sci. Instrum.* **47**, 799 (1976).

<sup>7</sup>A. Mooradian and G. B. Wright, *Phys. Rev. Lett.* **16**, 999 (1966).

<sup>8</sup>V. I. Zemski, E. L. Ivchenko, D. N. Mirlin, and I. I. Reshina, *Solid State Commun.* **16**, 221 (1975).

<sup>9</sup>F. H. Pollak, C. E. Okeke, P. E. Vanier, and P. M. Raccach, *J. Appl. Phys.* **49**, 4216 (1978).

<sup>10</sup>J. Baars, A. Hurne, W. Rothmund, C. R. Fritzsche, and T. Jakobus, *J. Appl. Phys.* **53**, 1461 (1982).

<sup>11</sup>R. Dornhaus and G. Nimtz, *The Properties and Applications of the HgCdTe Alloy System, Solid State Physics* (Springer, Berlin, 1976), p. 37.

<sup>12</sup>Tencor Instruments, 2400 Charleston Road, Mountain View, CA 94043 and Lehigh Electronics, Box 323, Lehigh, PA 18235.

<sup>13</sup>R. L. Brown, L. S. Schoonveld, L. L. Abels, S. Sundaram, and P. M. Raccach, *J. Appl. Phys.* **52**, 2950 (1981).

<sup>14</sup>P. M. Amirtharaj, J. H. Dinan, J. J. Kennedy, P. R. Boyd, and O. J. Glembocki, *J. Vac. Sci. Technol.* **4**, 2028 (1986).

# Wavelength modulation absorption spectroscopy of deep levels in semi-insulating GaAs

S. M. Eetemadi and R. Braunstein

*Department of Physics, University of California, Los Angeles, California 90024*

(Received 18 March 1985; accepted for publication 4 June 1985)

Infrared wavelength modulation absorption spectroscopy was used in the spectral region of 0.3–1.45 eV and the temperature range of 80–300 K, to study deep level impurities and defects in undoped semi-insulating GaAs grown by the liquid encapsulated Czochralski technique. The measurements revealed two resonant type peaks with fine structure near 0.37 and 0.40 eV, as well as thresholds and plateaus at higher energies. The sensitivity of the measurements allows us to give credence to changes in the absorption coefficient at levels  $\sim 10^{-3} \text{ cm}^{-1}$ . The absorption band at 0.37 eV is interpreted as being due to the intra-center transition between levels of accidental iron impurity, split by the crystal field. The absorption band near 0.40 eV, can be annealed out by heat treatment, and is considered to belong to a multilevel defect complex. Utilizing the photo-quenching behavior of the absorption in the spectral region of 0.6–1.4 eV, it was shown that conventional room temperature optical absorption may give erroneous results in measuring the concentration of the EL2 levels, because of appreciable absorption due to other residual deep levels in this spectral region, as revealed by the sensitivity of the wavelength modulation technique.

## I. INTRODUCTION

Deep levels in semiconductors continue to be the subject of considerable theoretical<sup>1–3</sup> and experimental<sup>4–6</sup> research as our understanding of these levels is far from complete. The presence of deep levels in semiconductors at concentrations of  $10^{15}/\text{cm}^3$  or even less, can significantly affect the carrier lifetime, mobility, and the rate of radiative transitions, and thus performance of microelectronic and optoelectronic devices made from these materials. The fascinating features of the physics of deep levels, coupled with great technological interest in this field has intensified searches for sensitive experimental techniques for their detection and characterization at these low levels of concentrations.

The various space charge spectroscopy techniques (such as TSC, DLTS, and DLOS)<sup>4–5</sup> developed in recent years are commonly employed electrical measurements to detect deep levels. With very good sensitivities, they can provide thermal activation energy, carrier capture cross section, and concentration of deep levels (and optical cross section in some cases). The main drawback of these techniques, however, is that measurements are carried out in space charge regions, i.e., in the presence of high-electric fields ( $\sim 10^4$ – $10^5$  V/cm), the effect of which on the emission rate is not thoroughly understood.<sup>3</sup> Furthermore, these measurements require fabrication of *p-n* junctions, of Schottky barriers, or ohmic contacts which could result in the introduction of process related impurities and or defects into the sample. In addition, the above techniques employing essentially thermal processes usually do not yield excited states of levels. Photoluminescence type experiments, although very sensitive for shallow levels,<sup>7,8</sup> have limited sensitivity in the case of deep levels due to appreciable phonon coupling, resulting in competition between different possible radiative and nonradiative mechanisms.

Extrinsic optical absorption spectroscopy has been

among the most favored techniques of studying impurity and defect levels at high level of concentrations.<sup>9,10</sup> These measurements are done on bulk materials, and therefore, are free from high-electric fields and process related impurity or defects. The absorption coefficient along with its spectral and temperature dependence can give information about the photoionization energy, excited states, temperature dependence of the level, electron-phonon coupling, and the symmetry of the localized wavefunction as well as their concentration.<sup>3</sup> However, conventional optical absorption techniques usually suffer from poor sensitivity at low levels of concentration of the order of  $10^{12}$ – $10^{16} \text{ cm}^{-3}$  usually encountered for deep levels. Consequently, considerations have been given to optical derivative spectroscopies which can measure absorption coefficients at levels of  $10^{-3}$  to  $10^{-5} \text{ cm}^{-1}$ .<sup>11</sup>

Several modulation schemes have been developed in optical derivative spectroscopy. Electro-modulation, piezo-modulation, thermo-modulation, and wavelength modulation are examples of this technique, depending on whether the modulating parameter is the applied electric field, strain, temperature, or the wavelength of the probing light beam.<sup>12,13</sup> However, these techniques have primarily been used to study the intrinsic optical properties of materials.

The techniques of extrinsic electro-absorption has been used in some cases to study deep levels in semiconductors.<sup>14</sup> They have not, however, been extensively employed, since they require high-resistivity material in order that sufficiently high-electric fields can be applied to obtain adequate modulation. In addition, the present knowledge of the effect of electric fields on the properties of deep levels is not sufficient for a complete interpretation of the experimental results.

Wavelength modulation absorption spectroscopy, in contrast, allows one to obtain the derivative spectrum by modulating the wavelength of the probing light beam, and

thus has a straightforward relationship to the conventional absorption measurements with improved sensitivity.<sup>15</sup> The difficulty in this case is the presence of spurious structures in the spectrum due to background derivative spectra, which poses a serious problem especially in the infrared region of spectra. In the present work, the modulation of the wavelength was obtained by oscillating the diagonal mirror before the exit slit of a conventional monochromator. The transmitted intensity through the sample and its derivative, as well as the incident intensity and its derivative, are measured using a sample in-sample out technique; an on-line computer system was employed for collecting data and numerically decorrelating the spectral absorption of the sample from the background.<sup>16</sup> The implementation of this system is described in detail in Sec. II.

Undoped semi-insulating GaAs substrates, grown by liquid encapsulated Czochralski technique (LEC) are currently being used for the fabrication of high speed GaAs devices. Deep levels play a crucial role in controlling the carrier concentration and, hence, the resistivity of the substrates. Therefore much attention has been focused on detection and characterization of the deep levels in this technologically important material.

A detailed study of the derivative absorption of GaAs:Cr has been reported.<sup>17</sup> In the present study, we have employed a modified wavelength modulation absorption spectrometer to study the deep levels in semi-insulating GaAs prepared by the LEC techniques. The spectrometer was used in the spectral region of 0.3–1.45 eV and the temperature range of 80–300 K, to study deep level impurities and defects in undoped semi-insulating (SI) GaAs. The measurements revealed two resonant type peaks with fine structures near 0.37 and 0.40 eV, as well as thresholds and plateaus at higher energies. The sensitivity of our measurements allows us to give credence to changes in the absorption coefficient at levels  $\sim 10^{-3} \text{ cm}^{-1}$ . The absorption band at 0.37 eV is interpreted as being due to the intra-center transition

between levels of accidental iron impurity, split by the crystal field. The absorption band near 0.40 eV, annealed out as a result of heat treatment, and therefore is considered to belong to a multilevel defect complex.

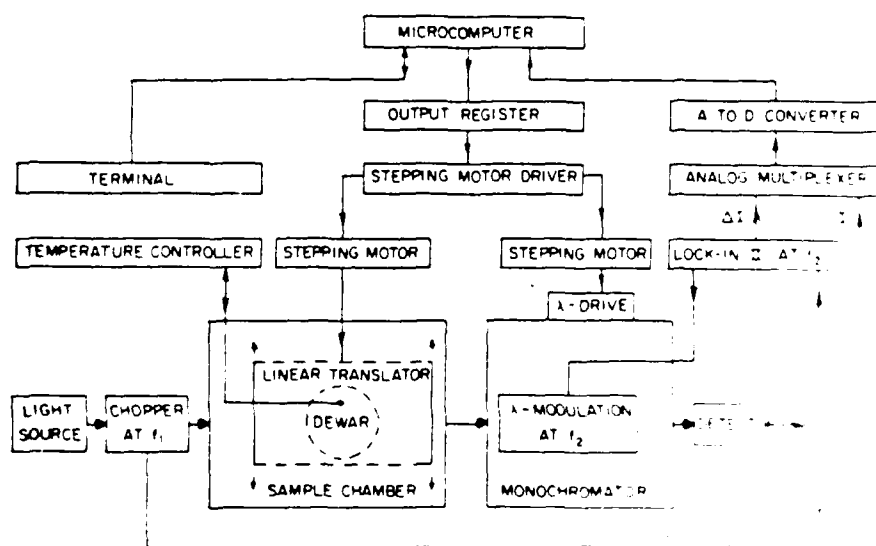
The spectrum between 0.6 and 1.45 eV was identified as being due to a native defect commonly referred to as EL2.<sup>18</sup> Utilizing the unusual photo-quenching behavior<sup>19</sup> of this level we were able to re-examine the accuracy of the conventional room temperature optical absorption, commonly used in measuring the EL2 concentration, and showed that these methods typically can have up to 20% error.

## II. EXPERIMENTAL TECHNIQUES

Our previously reported wavelength modulated spectrometer<sup>16</sup> has been modified (for the low temperature operation) by adding to it a low temperature optical dewar essential to this work. We have also improved the stability, reproducibility, and control of the modulating system, as well as the signal processing. The schematic diagram of the system is shown in Fig. 1.

A liquid transfer refrigerator, with an optical window shroud and a sample holder suitable for the sample in-sample out technique, and a digital temperature indicator and controller, were used for the low temperature operation. A tungsten/halogen light source, and quartz windows were used for the spectral range of 0.55–1.50 eV. For the infrared region, a Globar light source and potassium chloride windows were used. The detector throughout the spectral range was a Golay cell.

The modulation of the wavelength was accomplished by sinusoidal oscillation of a diagonal mirror, located before the exit slit of the monochromator, and mounted on a piezoelectric transducer. The internal oscillator of a lock-in amplifier was used to drive the scanner through a current amplifier driver circuit. The new modulation system has several advantages over the one previously employed.



AD-A181 016

CHARACTERIZATION OF INFRARED PROPERTIES OF LAYERED  
SEMICONDUCTORS(U) CALIFORNIA UNIV LOS ANGELES DEPT OF  
PHYSICS R BRAUNSTEIN 20 FEB 87 AFOSR-TR-87-0721

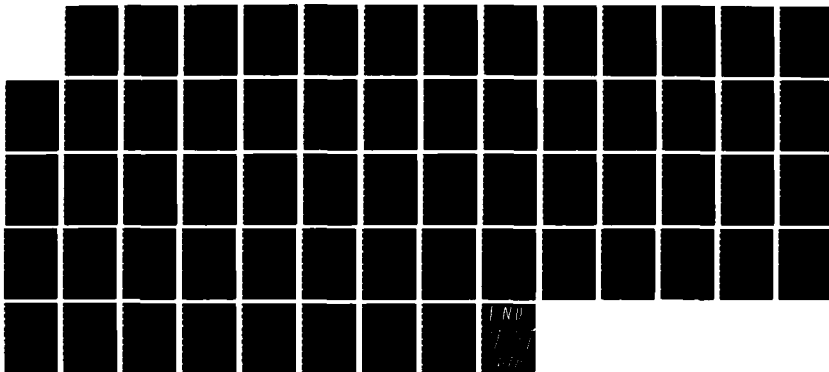
272

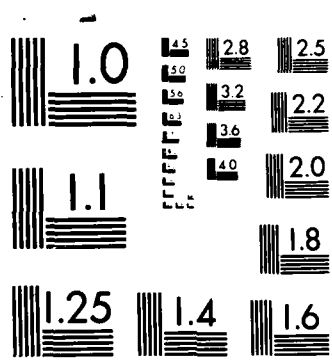
UNCLASSIFIED

AFOSR-83-0169

F/G 20/12

NL







tunable (1–100 Hz), has high amplitude and frequency stability, and allows large wavelength excursions. With the new system, the amplitude of modulation can be controlled from 0.2 to 150 Å precision. There was no wobbling, and no cross talk with other mechanically vibrating components. These features were desirable for reducing noise and drift, as well as optimizing the modulation frequency compatible with the detector response, and consistent with the chopper frequency to avoid harmonic or subharmonic pickup. It can also be used to conveniently and very precisely calibrate the spectral slit width, the depth of modulation, and to select these quantities for optimum resolution, signal-to-noise ratio, and minimum distortion in the derivative signal, for a given spectral region. A dc offset feature of this scanner also allows one to set the monochromator calibration electrically rather than mechanically. Data was taken at discrete energies with a resolution set by the slit width and depth of modulation, which for this work was 0.00075–0.0015 eV.

An on-line computer steps the sample, in and out of the light beam, as well as, steps the wavelength, and collects data from the output of lock-in amplifiers at controllable rates for additional signal averaging. These operations are conveniently done using a LSI-11/23 computer and its peripherals

in the form of a CAMAC system. The data taking cycle is shown in Fig. 2. The method of data analysis is similar to that previously employed.<sup>16</sup> The wavelength modulation technique yields essentially the energy derivative of the absorption coefficient. To obtain the value of the absorption coefficient, one numerically integrates the observed derivative spectra, and normalizes it to the absorption coefficient obtained by a direct loss measurement in the same apparatus at fixed wavelengths where the absorption coefficient can be measured with good precision.

The undoped semi-insulating GaAs samples used in this work were cut from five different ingots, all grown in pyrolytic boron nitride crucibles, by the liquid encapsulated Czochralski technique, with  $B_2O_3$  as the encapsulant. They had resistivities greater than  $10^7 \Omega \text{ cm}$ , and Hall mobilities of 4570–6319  $\text{cm}^2/\text{V s}$ . They were typically 3 mm thick and the surfaces were polished with Br-methanol. The samples were grown by the Hughes Research Laboratory, Malibu.

### III. RESULTS

Figure 3 shows the absorption spectra of an undoped semi-insulating GaAs at 300 K. The threshold near 1.4 eV is the onset of the interband transition, while the spectra between 0.7 and 1.4 eV is the characteristic absorption of a deep level due to a presumably native defect complex, commonly referred to as the EL2 level.<sup>19</sup> The small structures between 0.3 and 0.5 eV, and the threshold at 0.5 eV should be noted. In conventional absorption spectroscopy these small variations would be buried in the systems noise, whereas with our technique, variations as small as  $10^{-3} \text{ cm}^{-1}$  have significance. As the temperature is reduced to 160 K, we note the sharpening of the thresholds, and emergence of distinct resonance type structures, shown in Fig. 4. The structures below 0.52 eV are shown in Fig. 5 on a vastly expanded scale made possible by the precision of our measurement. Upon lowering the temperature to 80 K the structures sharpen further, and some finer ones appear, as seen in Fig. 6. Note should be taken of the sharp structure at 0.36–0.38 eV,

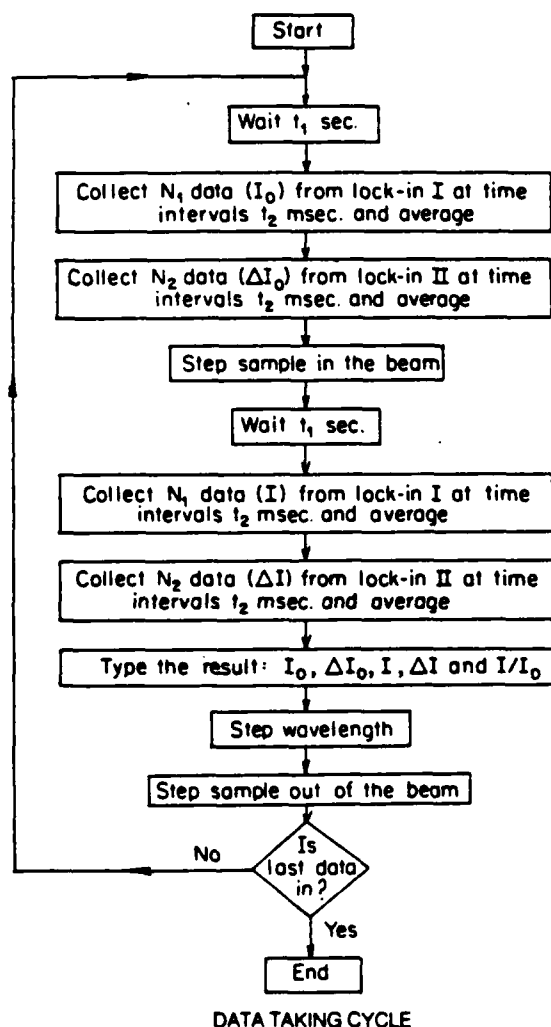


FIG. 2. Block diagram of the data taking cycle.

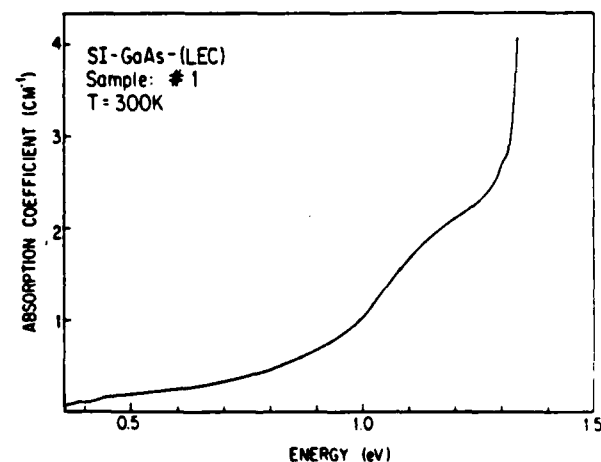


FIG. 3. Absorption spectra of sample 1 SI GaAs (LEC);  $T = 300 \text{ K}$ , spectral range: 0.3–1.5 eV.

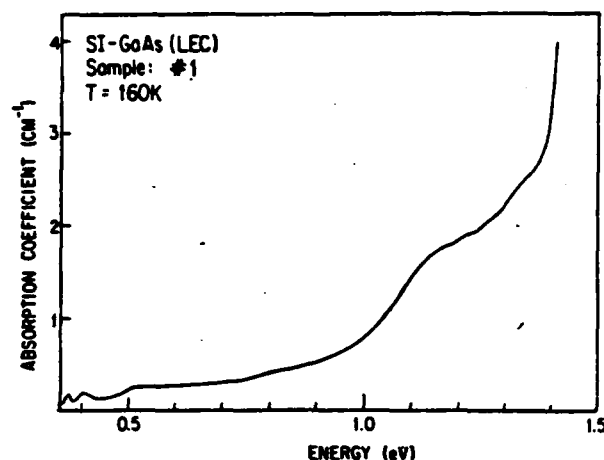


FIG. 4. Absorption spectra of sample 1 SI GaAs (LEC);  $T = 160$  K, spectral range: 0.3–1.5 eV.

a broad peak at 0.4 eV with side lobes, and the threshold near 0.5 eV. Figures 7–10 show the observed structures in the same spectral region and temperature for other undoped GaAs samples. It should be noted that the general shape of the resonant structure at 0.36–0.38 eV remains unchanged as its intensity varies from Figs. 6–9. In contrast, the broad peak at 0.4 eV changes its intensity as well as the details of its shape. No distinct pattern was observed in the structures at 0.43–0.47 eV. Figure 11 shows the spectra of the sample after the sample had been annealed in a  $N_2$  atmosphere at 450 °C for 4 h. the difference between this and Fig. 6 should be noted. The peak at 0.4 eV has been annealed out as a result of heat treatment.

When the temperature was lowered to below 140 K, and the sample was illuminated with a 50-W tungsten halogen lamp, the structures between 0.7 and 1.3 eV quenched (see Fig. 12) and remained in the quenched state for several hours even after the background illumination had been turned off. The magnitude and the details of the shape of the post-

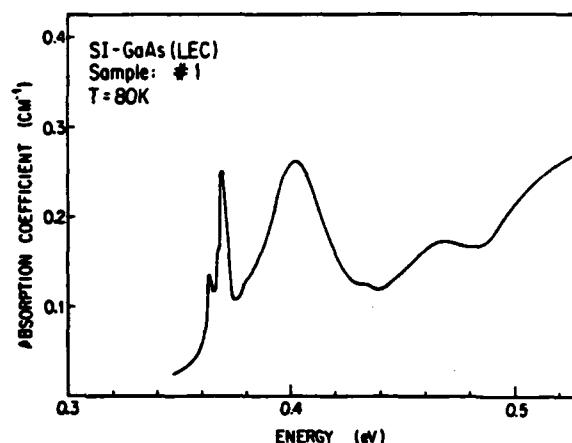


FIG. 6. Absorption spectra of sample 1 SI GaAs (LEC);  $T = 80$  K, spectral range: 0.3–0.52 eV.

quenched spectra varied from sample to sample. Its magnitude at 1.2 eV was 10–20% of the total room temperature absorption coefficient at the same energy.

#### IV. DISCUSSION

The above results are discussed in the following subsections. In Sec. IV A the resonant spectra at 0.37 is discussed and attributed to accidental iron impurities. Section IV B is devoted to the comparison of the spectra at 0.4 eV among the various samples, as well as its behavior under heat treatment, and is considered to be the signature of a multilevel defect complex. The results of our observation in the spectral range of 0.7–1.4 eV are discussed in Sec. IV C.

##### A. Iron in undoped GaAs

In the spectra below 0.55 eV, the sharp peak at 0.37 eV can be attributed to the presence of iron in these materials; a similar absorption peak has been reported in GaAs sub-

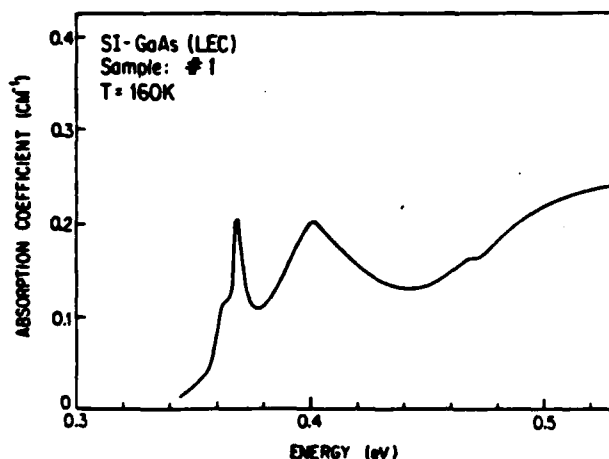


FIG. 5. Absorption spectra of sample 1 SI GaAs (LEC);  $T = 160$  K, spectral range: 0.3–0.52 eV.

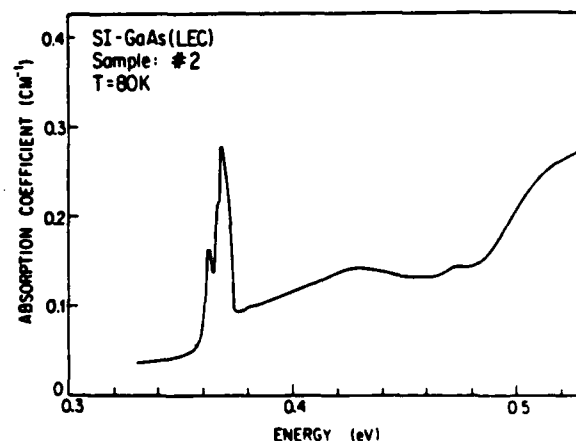


FIG. 7. Absorption spectra of sample 2 SI GaAs (LEC);  $T = 80$  K, spectral range: 0.3–0.52 eV.

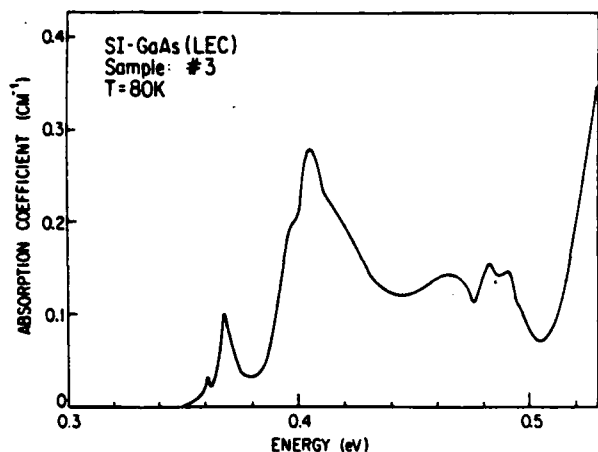


FIG. 8. Absorption spectra of sample 3 SI GaAs (LEC);  $T = 80$  K, spectral range: 0.3–0.52 eV.

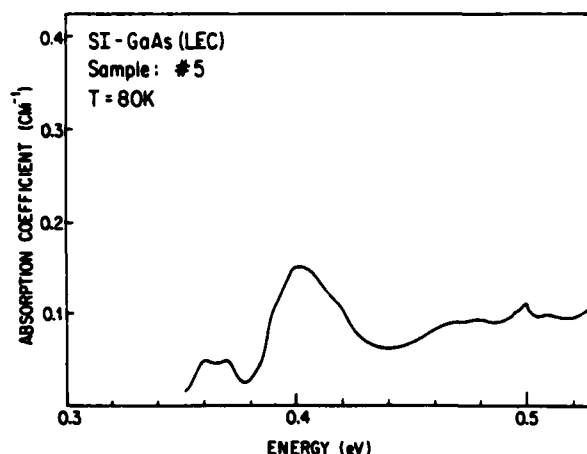


FIG. 10. Absorption spectra of sample 5 SI GaAs (LEC);  $T = 80$  K, spectral range: 0.3–0.52 eV.

strates intentionally doped with iron.<sup>10</sup> Sharp zero-phonon photoluminescence lines near 0.37 eV has also been seen in iron doped GaAs materials.<sup>20</sup> Similar structures in absorption and photoluminescence have also been observed for iron in other III–V compounds as well.<sup>10,20</sup> Paramagnetic resonance experiments have shown that iron is incorporated substitutionally in the Ga sublattice, and acts as a deep acceptor.<sup>21</sup> At the Ga site, Fe loses three electrons to the bonds, becoming  $\text{Fe}^{3+}$  in a  $3d^5$  configuration, and when an electron is trapped, a  $\text{Fe}^{2+}$  in a  $3d^6$  configuration is created.

The energy levels of  $\text{Fe}^{2+}$  in  $3d^6$  configuration derived on the basis of the crystal field theory up to the second-order term in the spin-orbit correction have been reported in the literature.<sup>22</sup> At a site of tetrahedral symmetry ( $T_d$ ), the lowest free ion term,  $^5D$ , of  $\text{Fe}^{2+}$  ( $3d^6$ ), is split by the crystal field into a ground state doublet  $^5E$  and  $^5T_2$  excited state. Allowance for the spin-orbit coupling lifts the degeneracy of the  $^5T_2$  level and in the second-order approximation it lifts also the degeneracy of the  $^5E$  levels, as shown in Fig. 13. The

absorption and luminescence peaks mentioned above are due to the internal transitions between  $^5E$  and  $^5T_2$  multiplets.

The central peak at 0.37 eV in Figs. 5–9 can be attributed to the zero-phonon transition from the lowest  $^5E$  multiplet to the lowest level of  $^5T_2$  multiplet. The structure appearing as a weak shoulder on the low energy side of the line and about less than 2 meV away from the main peak can also be attributed to a zero-phonon transition from the second lowest level of  $^5E$  to lowest level of  $^5T_2$ . This transition has been reported as well resolved into a separate peak when the measurement is done at about liquid Helium temperature.<sup>10</sup> From the position of the main two zero-phonon lines, and Fig. 13, we obtain a value of  $\Delta \sim 3000 \text{ cm}^{-1}$  for the crystal field energy, in agreement with the reported values of  $\Delta$  in the III–V compounds.<sup>3</sup> The other side structures are harder to interpret, partly because it is difficult to distinguish between vibronic and electronic levels. As for the Jahn–Teller distortion, its effect on the  $^5E$  states is not pronounced but it alters the splitting of  $^5T_2$  levels.<sup>23</sup> Such changes would be

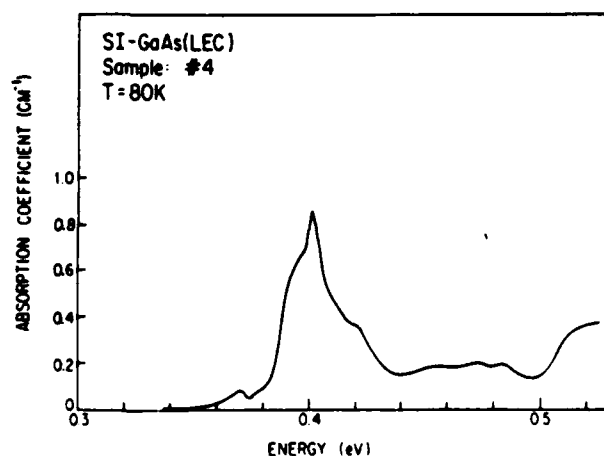


FIG. 9. Absorption spectra of sample 4 SI GaAs (LEC);  $T = 80$  K, spectral range: 0.3–0.52 eV.

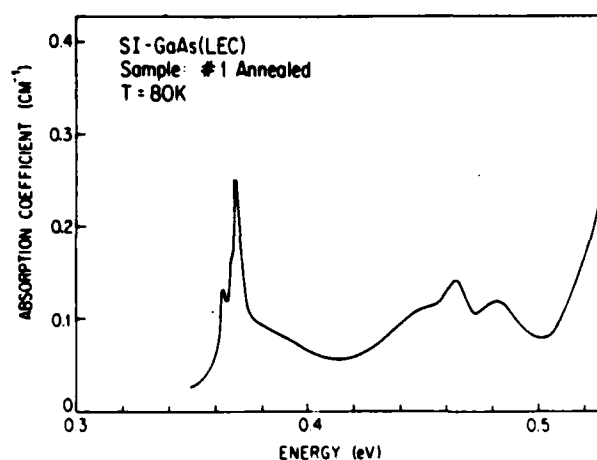


FIG. 11. The post-annealed absorption spectra of sample 1 SI GaAs (LEC);  $T = 80$  K, spectral range: 0.3–0.52 eV.

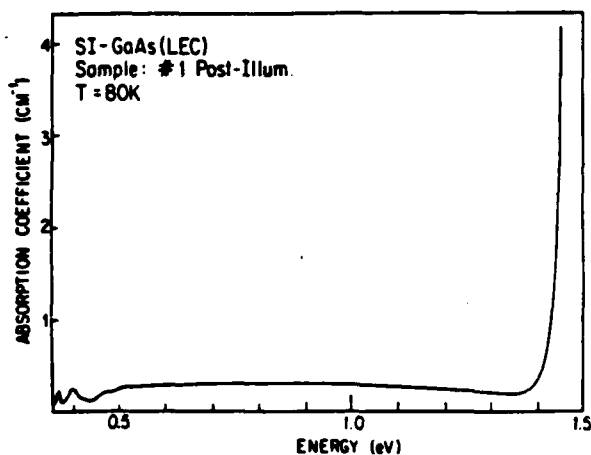


FIG. 12. The post-illumination absorption spectra of sample 1 SI GaAs (LEC);  $T = 80$  K, spectral range: 0.3–0.52 eV.

observable in transitions involving higher energy levels of  $^5T_2$ . Unfortunately, these transitions cannot be seen in our data, because they have much smaller oscillator strengths<sup>10,23</sup> and therefore are buried under the structures due to other residual impurities or defects.

A detailed analysis of iron levels is not the main concern of this work. For that, one would have to study these levels in substrates doped with iron at concentrations much above that of the residual impurities and defects. Our aim in this work was rather to make a broad survey of deep levels in the undoped SI GaAs substrates. To our knowledge this is the first observation of the distinct iron signature in the bulk of as-grown undoped semi-insulating GaAs by optical absorption or emission techniques. Estimating the value of the oscillator strength, the lowest detected concentration of  $Fe^{2+}$  was  $5 \times 10^{15} \text{ cm}^{-3}$  in our work. Although  $Fe^{2+}$  in GaAs does have a distinct photoluminescence signature at 0.37 eV, to our knowledge no such emission band has been reported in the undoped as-grown materials. Emission lines, however, do appear after the substrates are heated to about 700 °C

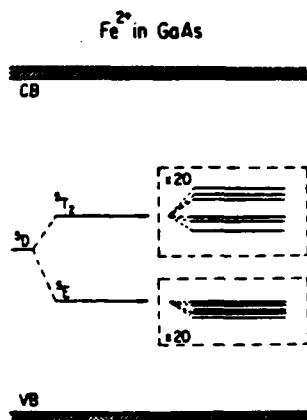


FIG. 13. Energy level scheme of the  $^3D$  level of  $Fe^{2+}$  ( $3d^6$ ) in GaAs.

because of accumulation of iron in the near surface region at concentrations of  $10^{17}$ – $10^{18} \text{ cm}^{-3}$ .<sup>24</sup> Therefore it is significant that we have been able to detect Fe at levels of  $10^{15} \text{ cm}^{-3}$ . It should also be noted that in the absence of absorption bands due to other residual deep levels—interfering with the iron absorption spectra—the sensitivity of our present measurement would allow detection of iron at an order of magnitude below the above concentration level.

The threshold near 0.5 eV whose intensity scales with the intra-center transition at 0.37 eV can be identified with a transition from the valence band to the lower multiplet of  $Fe^{2+}$ . This is further substantiated by the fact that the position of this threshold moves with a temperature coefficient of  $(5.0 \pm 0.5) \times 10^{-4} \text{ eV/K}$ , which is similar to the temperature coefficient of the GaAs band gap; a similar observation has been made from Hall measurements.<sup>25</sup> A deep acceptor level at about 0.5 eV from the valence band, due to iron impurity has also been reported by several investigators.<sup>26,27</sup>

One might also expect to observe thresholds at higher energies due to the photoionization of electrons from  $Fe^{2+}$  levels to the conduction band. Figures 3 and 4 show absorption thresholds in the range of 0.7 to 1.4 eV. However, in Sec. IV C it will be shown that these thresholds bear no relation to the presence of iron. They are rather attributed to another level commonly referred to as EL2,<sup>19</sup> which is believed to originate from a native defect sample. The absorption spectra due to EL2 can be quenched out at 80 K if the sample is illuminated by band gap light (see Sec. IV C). The remaining spectra shown in Fig. 12 does not contain any strong photoionization threshold. We therefore conclude that the magnitude of the photoionization cross section for electronic transition from the  $Fe^{2+}$  levels to the conduction band is very small. It can be argued that since the site symmetry of iron is tetrahedral, transitions from  $d$ -orbitals to conduction band  $s$ -like orbitals may be strongly prohibited by the selection rules.

## B. Multilevel defect complex

Another dominant absorption band common to all the substrates we studied is the resonant spectra whose peak is near 0.4 eV, with a peak absorption coefficient typically below  $0.4 \text{ cm}^{-1}$ , a half width of about 30 meV, and usually with two side lobes. Being a peak rather than a threshold it can be interpreted as being due to an electronic transition between levels associated with the same center. The peak magnitude, and the detail shape of this structure as well as its sidebands varied from sample to sample as seen from Figs. 5–10, indicating that it is not associated with a simple multilevel impurity. It is more likely that this structure is due to a complex defect formed during the crystal growth or in the cooling period following the growth, whose exact structure is sensitively dependent upon the thermal history of the sample. To explore the possible origin of this level, sample 1 was cleaned, etched and annealed in a nitrogen atmosphere for 4 h, at a temperature of 450 °C. In contrast to the spectra of sample 1 shown in Fig. 6, the post-annealed spectra, shown in Fig. 11, indicated that the spectra at 0.4 eV has been annealed out. We thus conclude that (i) the structure is a defect or defect complex; (ii) this defect introduces two main levels

into the gap separated by 0.4 eV; (iii) these levels may split into more levels depending on the exact nature of the defect's immediate surrounding or additional complexing. These additional complexes could vary from sample to sample if they do not have identical thermal history. This would account for variations of the fine structures of the spectra among the samples. To our knowledge this is the first observation of this multilevel defect in semi-insulating GaAs by optical techniques. A possibly related level has been observed by the photo-induced transient spectroscopy (P.I.T.S.) in these samples.<sup>28</sup> However, an exact correlation between the levels observed by the wavelength modulation absorption and the level detected by P.I.T.S. must take into account the fact that the latter essentially yields information on the thermal emission from the level to the band, whereas the former gives information about the intra-center transitions.

### C. The EL2 in SI GaAs

The absorption spectra in the 0.6–1.4 eV shown in Figs. 3 and 4, are due to a deep level known as the EL2 which is associated with a native defect.<sup>18</sup> This defect is responsible for producing undoped semi-insulating GaAs by compensating the shallow impurities.<sup>29,30</sup> The exact origin and microscopic structure of this defect is still subject to considerable debate. Many of the investigations on this defect have involved studies of the correlation between the distribution pattern across the wafer, of the EL2 concentration, dislocation density, resistivity, as well as their relation to the stoichiometry of the melt, and conditions of the crystal growth.<sup>31,32</sup> Central to many of these studies is the precise measurement of the EL2 concentration and its distribution. Optical absorption spectroscopy, at room temperature, has commonly been used for this purpose, since it provides a convenient and nondestructive way of measuring the local concentration of the EL2 with good spatial resolution.<sup>19</sup> In this method the value of the absorption coefficient at about 1.2 eV is taken to be a measure of the EL2 concentration. However, we have shown that the presence of other residual deep levels, even at low concentrations, may give rise to appreciable absorption spectra in the neighborhood of the EL2 spectra.<sup>33</sup> Hence the apparent near-infrared absorption spectra cannot be *a priori* attributed to the EL2 levels alone.

The EL2 level has been shown to exhibit unusual properties, among them, the quenching of photoluminescence,<sup>34</sup> photocapacitance,<sup>35</sup> and optical absorption,<sup>19</sup> at low temperature ( $T < 140$  K). In particular, the near-infrared absorption spectra due to EL2 quenches out at low temperature after the sample is illuminated with light of  $0.9 < h\nu < 1.35$  eV and remains in the quenched state for many hours, even after the background illumination has been turned off. The sensitivity of the wavelength modulation absorption spectroscopy together with the photo-quenching behavior of the EL2 allowed us to separate the EL2 spectra in the total absorption spectra and to observe the absorption spectra due to all other residual deep levels. Figure 12 shows the absorption due to all the deep levels other than the EL2 in the spectral region of 0.3–1.5 eV. The spectra of another GaAs sample in the spectral region of 0.5–1.5 eV is also shown in Fig. 14, in which the solid curve is the room temperature spectra and

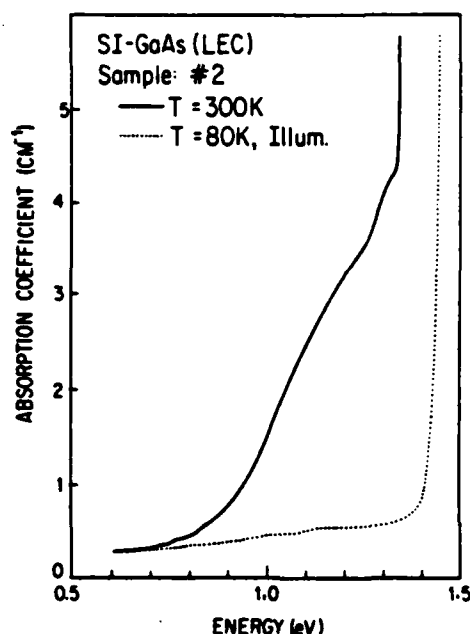


FIG. 14. The total absorption spectra at 300 K (solid curve) and the residual absorption spectra after photoquenching at 80 K (dotted curve) of sample 2 SI GaAs (LEC).

the dotted curve is the post-quenched spectra (at 80 K) due to residual absorption. As is seen from these figures, the post-quenched spectra do not exhibit any strong threshold associated with the photoionization of electrons from the iron impurity levels. In surveying several samples of undoped semi-insulating GaAs we found that in a typical sample, up to 20% of the room temperature optical absorption coefficient may be due to residual deep levels other than the EL2.<sup>33</sup>

Therefore, in cases where the EL2 concentration and distribution must be measured with better than 10% accuracy,<sup>32</sup> room temperature optical absorption is not adequate. In such cases, the use of infrared wavelength modulation absorption in conjunction with photoquenching<sup>33</sup> represent a more accurate method of measuring the EL2 concentration.

### V. CONCLUSIONS

In summary, wavelength modulation absorption was used to investigate the deep levels in semi-insulating undoped GaAs grown by the liquid encapsulated technique which is currently of high technological interest. Extensive low temperature measurements permitted observation of structures with fine details in the spectra of the SI GaAs at 0.37 and 0.4 eV. The structures near 0.37 eV were identified as intra-center transitions between the levels of accidental iron impurities incorporated in the Ga sublattice. To our knowledge this was the first observation of the iron absorption spectra in the semi-insulating GaAs at such low levels of concentration. The structure at 0.4 eV was considered as being due to an intra-center transition associated with a growth related multilevel defect complex. The fine details of

this structure were found to be sensitive to the thermal history of the sample, and the whole structure was annealed out at about 450 °C. Such a level and its characteristics have not been previously reported.

Measurements at liquid nitrogen temperature also allowed us to utilize the photoquenching behavior of the absorption bands in the spectral region of 0.7–1.45 eV to assess the accuracy of the conventional room temperature optical absorption spectroscopies in measuring the deep level concentrations. It was demonstrated that the nonselectivity of such measurements may give erroneous results in measuring the concentration of specific deep levels, because of appreciable absorption due to the collective contribution of other residual deep levels. This result holds special significance in the current investigations on the origin of the nonuniform distribution of the main electron trap, the EL2 level, in undoped GaAs.

## ACKNOWLEDGMENTS

The support of this work by the Air Force Office of Scientific Research under AFOSR-83-0169B, the Army Research Office-Durham under DAAG29-81-K-0164, and the State of California-MICRO program is gratefully acknowledged.

- <sup>1</sup>A. G. Milnes, *Deep Impurities in Semiconductors* (Wiley, New York, 1973).
- <sup>2</sup>S. T. Pantelides, *Rev. Mod. Phys.* **50**, 797 (1978).
- <sup>3</sup>M. Jaros, *Deep Levels in Semiconductors* (Hilger, London, 1982).
- <sup>4</sup>C. T. Sah, *Solid State Electron.* **19**, 975 (1976).
- <sup>5</sup>G. L. Miller, D. V. Lang, and L. C. Kimerling, *Annu. Rev. Mater. Sci.* **7**, 377 (1977).
- <sup>6</sup>G. M. Martin, in *Semi-Insulating III-V Materials, Nottingham 1980*, edited by G. J. Rees (Shiva, Orpington, U. K.), p. 13.
- <sup>7</sup>J. J. Hopfield, G. D. Thomas, and M. Gerabenzon, *Phys. Rev. Lett.* **10**, 162 (1963).

- <sup>8</sup>E. Cohen and M. D. Sturge, *Phys. Rev. B* **15**, 4020 (1977).
- <sup>9</sup>E. Burstein, G. S. Picus, B. Henvis, and R. Wallis, *J. Phys. Chem. Solids* **1**, 65 (1956).
- <sup>10</sup>J. M. Baranowski, J. W. Allen, and G. L. Pearson, *Phys. Rev.* **160**, 627 (1967).
- <sup>11</sup>R. Braunstein, R. K. Kim, and M. Braunstein, in *Proceedings of the Symposium on Laser Induced Damage in Optical Materials*, Natl. Bur. Stand.-SP-620, Boulder, CO, 1980 (Natl. Bur. Stand., Washington DC, 1981), pp. 29–43.
- <sup>12</sup>M. Cardona, *Modulation Spectroscopy* (Academic, New York, 1969).
- <sup>13</sup>*Semiconductors and Semimetals, Vol. 9, Modulation Techniques*, edited by R. K. Willardson and A. C. Beer (Academic, New York, 1977).
- <sup>14</sup>A. D. Jonath, E. Voronkov, and R. H. Bube, *J. Appl. Phys.* **46**, 1754 (1975).
- <sup>15</sup>M. Welkowsky and R. Braunstein, *Rev. Sci. Instrum.* **43**, 399 (1972).
- <sup>16</sup>R. K. Kim and R. Braunstein, *Appl. Opt.* **23**, 1166 (1984).
- <sup>17</sup>R. Braunstein, R. K. Kim, D. Matthews, and M. Braunstein, *Physica* **117B** and **118B** (1983).
- <sup>18</sup>G. M. Martin, A. Mitonneau, and A. Mircea, *Electron. Lett.* **13**, 191 (1977).
- <sup>19</sup>G. M. Martin, *Appl. Phys. Lett.* **39**, 747 (1981).
- <sup>20</sup>W. H. Koschel, S. G. Bishop, and B. D. McCombe, in *Proceedings of the 13th Internat'l Conference on Physics of Semiconductors*, Rome, 1976 (North-Holland, Amsterdam, 1976), p. 1065.
- <sup>21</sup>E. M. Ganapol'skii, *Sov. Phys. Solid State* **15**, 269 (1973).
- <sup>22</sup>W. Low and M. Weger, *Phys. Rev.* **118**, 1119 (1960).
- <sup>23</sup>G. A. Slack, F. S. Ham, and R. M. Chrenko, *Phys. Rev.* **152**, 376 (1966).
- <sup>24</sup>P. E. R. Nordquist, P. B. Klein, S. G. Bishop, and P. G. Siebermann, *Inst. Phys. Conf. Ser.* **56**, 569 (1981).
- <sup>25</sup>R. W. Haisty, *Appl. Phys. Lett.* **7**, 208 (1965).
- <sup>26</sup>V. I. Fistul, L. Ya. Pervova, E. M. Omelyanovskii, and E. P. Rashevskaya, *Sov. Phys. Semicond.* **8**, 311 (1974).
- <sup>27</sup>D. V. Lang and R. A. Logan, *J. Electron. Mater.* **4**, 1053 (1975).
- <sup>28</sup>M. R. Burd (private communication).
- <sup>29</sup>D. E. Holmes, R. T. Chen, K. R. Elliott, and C. G. Kirkpatrick, *Appl. Phys. Lett.* **40**, 46 (1982).
- <sup>30</sup>H. Winston, *Solid State Technol.* **26**, 145 (1983).
- <sup>31</sup>M. R. Brozel, I. Grant, R. M. Ware, and D. J. Stirland, *Appl. Phys. Lett.* **42**, 610 (1983).
- <sup>32</sup>D. E. Holmes, R. T. Chen, K. R. Elliott, and C. G. Kirkpatrick, *Appl. Phys. Lett.* **43**, 305 (1983).
- <sup>33</sup>S. M. Etemadi and R. Braunstein (unpublished).
- <sup>34</sup>P. W. Yu, *Appl. Phys. Lett.* **44**, 330 (1984).
- <sup>35</sup>G. Vincent and D. Bois, *Solid State Commun.* **27**, 431 (1978).

# Noncontact electrical characterization of epitaxial HgCdTe<sup>a)</sup>

C. E. Jones, M. E. Boyd, and W. H. Konkel  
*Santa Barbara Research Center, Goleta, California 93117*

S. Perkowitz  
*Physics Department, Emory University, Atlanta, Georgia 30322*

R. Braunstein  
*Physics Department, University of California, Los Angeles, California 90024*

(Received 15 December 1985; accepted 14 March 1986)

It is important to be able to nondestructively characterize ("screen") the electrical properties of those areas of HgCdTe epitaxial material that will later be made into devices. This paper compares several noncontact techniques for measuring resistivity, carrier concentration, and mobility with the standard Hall-effect technique. The noncontact techniques examined are far-infrared reflection, Raman scattering, eddy-current absorption, and electroreflectance. Of these techniques, far-infrared reflection was found to be the best noncontact technique for measuring resistivity, carrier concentration, and mobility. Resistivity values were within a factor of 2 of Hall-effect values, while carrier concentration and mobility values that depend on an assumed effective mass were within a factor of 3. In Raman scattering, interference between the free-carrier plasmon-phonon mode and other modes makes it an inaccurate method for estimating carrier concentration. Eddy-current absorption is useful for quickly measuring epitaxial layer resistivities to within a factor of 3 of Hall-effect values, while electroreflectance gives a relative value for the surface doping density, which is useful in layer profiling.

## I. INTRODUCTION

It is important to know the electrical properties of HgCdTe starting material before it is processed into devices. The standard techniques for doing this, Hall-effect and capacitance-voltage testing, involve applying contacts to and processing a small piece of the sample, which takes this region out of production and does not characterize the actual material used for device processing.

This paper describes the use of far-infrared reflection, Raman spectroscopy, and eddy-current absorption to provide noncontact electrical characterization of epitaxial HgCdTe so that the characterized material can still be used for device processing. Electroreflectance data for carrier concentration is also presented, since this technique requires only a single edge contact. These techniques are all nondestructive and, except for eddy-current absorption, allow mapping of electrical parameters over the area of the starting material.

Far-infrared reflection has been used to estimate resistivity, carrier concentration, and mobility in GaAs,<sup>1</sup> CdTe,<sup>2</sup> and PbSnTe.<sup>3</sup> The method is described in a review article,<sup>4</sup> and initial data for HgCdTe has been reported by one of the present authors.<sup>5</sup> Eddy-current absorption is a standard noncontact technique used in the Si industry for measuring resistivity in wafers.<sup>6</sup> In the Raman technique, a coupled plasmon-phonon mode is excited in the surface region ( $\sim 100$  Å in depth). The mode frequency can be used to determine the surface-region free-carrier concentration.<sup>7,8</sup> In the electroreflectance technique, the signal strength is proportional to the surface-region doping density. Surface mapping of doping densities has been demonstrated for GaAs.<sup>9</sup> The issues in the present work are to determine the usefulness of these techniques for HgCdTe epitaxial layer

analysis and to compare techniques that measure the same electrical parameters.

Several of these techniques involve reflected light: i.e., far-infrared reflection, Raman scattering, and electroreflectance. The skin depth for good conductors  $\delta = c/(2\pi\nu\sigma)^{1/2}$  varies inversely with the square root of the optical conductivity and the square root of the frequency. Order-of-magnitude values are  $\sim 100$  Å for the visible region excitations used in Raman and electroreflectance and micrometers for the far-infrared reflection. The eddy-current absorption technique averages over the total layer thickness.

## II. FAR-INFRARED REFLECTION

Free-carrier absorption in a semiconductor is proportional to (wavelength)<sup>2</sup>, and in the far infrared it becomes strong enough to be used to determine the resistivity, free-carrier concentration, and mobility. The far-infrared spectra were taken at 300 and 77 K using a Fourier-transform spectrometer covering the range from 10 to 250 cm<sup>-1</sup>. The samples were both *n*- and *p*-type epitaxial layers of Hg<sub>1-x</sub>Cd<sub>x</sub>Te with doping concentrations ranging from 10<sup>15</sup> to 10<sup>18</sup> cm<sup>-3</sup> and compositions in the range  $x = 0.2$  to 0.4. The samples were  $\sim 0.5 \times 0.5$  cm and were used for both the van der Pauw Hall-effect measurements and the far-infrared reflectance measurements.

Typical data are shown in Fig. 1, in which the dots are the measured data points and the solid line is a modeled fit to the data. The least-squares fit to the reflectance comes from a model for the complex index of refraction  $\tilde{n}$  that includes the free-carrier contribution, the lattice vibrational modes, and defect vibrational modes. These are identified in Fig. 1. The

## II. EXPERIMENTAL RESULTS

The derivative surface photovoltage measurements were performed on *n*-type silicon (100) substrates utilizing MOS structures. The experimental system used is described elsewhere.<sup>8</sup> The MOS structures were made by evaporating a 400 Å semitransparent gold electrode on an oxide layer (1000 Å thick) grown on silicon by a standard dry oxidation technique.<sup>9</sup>

Typical sub-band-gap derivative surface photovoltage spectra ( $dV_s/dE$ ) obtained at 83 K are shown in Figs. 1(a) and 2(a). To obtain a good signal-to-noise ratio it was necessary to keep the modulation amplitude and the spectral slit width of the monochromator fairly large ( $\Delta\lambda/\lambda \sim 10^{-2}$  when using a Golay detector). The derivatives of the incident photon spectra of a tungsten iodide source for the same instrument and spectral region with comparable amplitude of modulation were obtained using a PbS detector. These are shown for comparison in Figs. 1(b) and 2(b). With the sensitivity of the PbS detector a much better resolution ( $\Delta\lambda/\lambda \sim 2 \times 10^{-3}$ ) is also possible, as shown in Fig. 3.

The dominant structure in Fig. 1(a) is due to the inter-band transition near the indirect band gap of silicon with the emission and absorption of phonons. It is similar to other reported DSPV results.<sup>10</sup> The smaller structures, below 1.15 eV, may in principle be associated with the multiphonon absorption. However, they can also be considered to be a manifestation of similar structures in the derivative of the background spectra  $dI_0/dE$ , shown in Fig. 1(b). Comparison of Figs. 2(a) and 2(b) also suggests a strong correlation

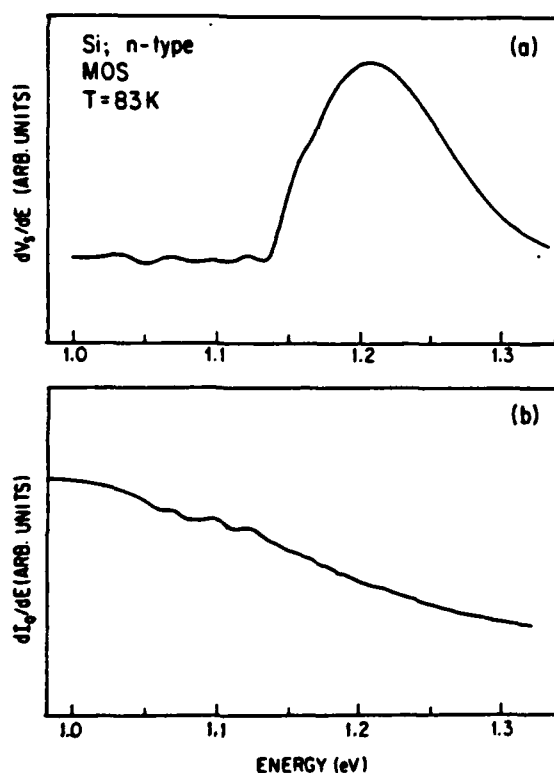


FIG. 1. (a) The derivative surface photovoltage spectra of silicon ( $T = 83$  K); (b) the derivative of the background spectra in the spectral range of 1.0–1.35 eV; amplitude of modulation ( $\Delta\lambda/\lambda$ ) =  $10^{-2}$ .

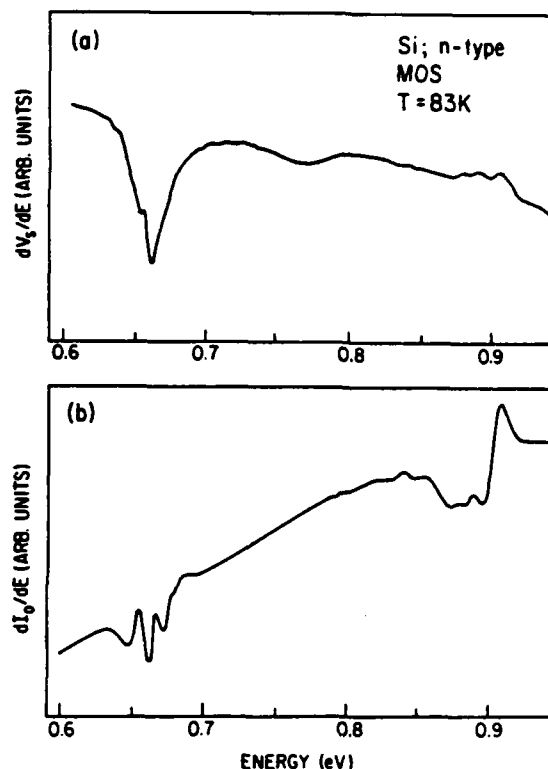


FIG. 2. (a) The derivative surface photovoltage spectra of silicon ( $T = 83$  K); (b) the derivative of the background spectra in the spectral range of 0.6–1.0 eV; amplitude of modulation ( $\Delta\lambda/\lambda$ ) =  $10^{-2}$ .

between the structures in the DSPV and the derivative of the background spectra near 0.65 and 0.9 eV. In fact, signatures of the derivative of the background spectra are quite commonly observed in the wavelength modulated spectra of the reflected and transmitted light beam, as predicted by the theory of the corresponding wavelength modulation spectroscopy. These can be corrected for by subtraction of the experimentally determined background.<sup>7</sup> In contrast, the theory of the DSPV, as formulated in Eq. (1), is not consis-

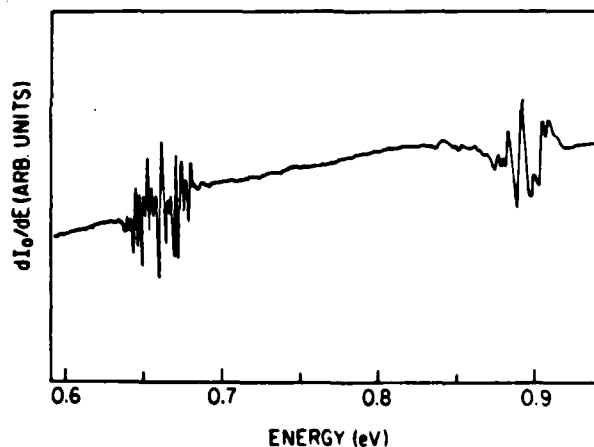


FIG. 3. Derivative of the background spectra in the spectral range of 0.76–1.0 eV using a tungsten source; amplitude of modulation ( $\Delta\lambda/\lambda$ ) =  $2 \times 10^{-3}$ .



tent with the above observation. In the next section we present our analysis of the theory of the DSPV spectroscopy, which shows that the DSPV spectra can contain signatures of the derivative of the background spectra, as well as other possible sources of distortions in the various regions of spectra.

### III. DERIVATIVE OF SURFACE PHOTOVOLTAGE (DSPV)

The theory of surface photovoltage has been treated by a number of authors.<sup>11</sup> For the purpose of this study, the changes in the surface potential of a semiconductor,  $V_s$ , induced by the light of intensity  $I_0$  and wavelength  $\lambda$  may be written, for small signals (surface photovoltage  $\ll$  surface potential), in the form<sup>11</sup>

$$V_s(\lambda) = I(\lambda) \alpha(\lambda) F(\lambda), \quad (2)$$

where

$$F = F(L_0, \alpha, T, E_f, \tau_b, n_b, p_b; \\ \times E_i, n_i, \sigma_{ph}^n, \sigma_{ph}^p, e_n, e_p, S).$$

$F$  is a complicated function of diffusion length  $L_0$ , absorption coefficient  $\alpha$ , temperature  $T$ , Fermi energy  $E_f$ , bulk carrier lifetime for electrons, holes, and concentrations  $\tau_b$ ,  $n_b$ ,  $p_b$ , respectively, deep levels energy  $E_i$ , concentration  $n_i$ , photoionization cross sections  $\sigma_{ph}^n$ , and  $\sigma_{ph}^p$  for electrons and holes, respectively, and their thermal emission rates  $e_n$  and  $e_p$ , in the semiconductor, as well as the effective surface recombination velocity  $S$ . The exact functional dependence of  $F$  on these parameters is not needed for our discussion; however, it is rather important to note its implicit wavelength dependence through  $\alpha(\lambda)$ ,  $\sigma_{ph}^n(\lambda)$ , and  $\sigma_{ph}^p(\lambda)$ .  $I(\lambda)$  is the actual photon flux entering the space-charge region of the semiconductor. Quite often in the past,  $I_0(\lambda)$ , which is the incident photon flux illuminating the MOS structure, has been used instead of  $I(\lambda)$ ; thus, ignoring the spectral dependence of the transmittance through the metal and the insulating layers of the structure,  $I(\lambda)$  and  $I_0(\lambda)$  are related by

$$I(\lambda) = I_0(\lambda) T(\lambda). \quad (3)$$

In essence, the wavelength dependence of  $T(\lambda)$  is due to the spectral dependence of the absorption coefficient of the light in the metal and insulator layers, the reflection coefficients at the interfaces, and the interference pattern due to the internal multiple reflections from the interfaces.

Combining Eqs. (2) and (3) we have

$$V_s = I_0(\lambda) T(\lambda) \alpha(\lambda) F(\lambda), \quad (4)$$

which forms the basis of our analysis of the wavelength modulation surface photovoltage.

If the wavelength of the incident light beam is modulated as

$$\lambda = \lambda_0 + \Delta \lambda \cos \omega t, \quad (5)$$

where  $\Delta \lambda$  and  $\omega$  are the amplitude and the frequency of modulation, respectively, then the surface photovoltage  $V_s(\lambda)$  becomes a periodic function of time,  $V_s(\lambda_0 + \Delta \lambda \cos \omega t)$ . For small  $\Delta \lambda$ , the derivative of the modulated surface photovoltage is given by

$$\begin{aligned} \frac{dV_s}{d\lambda} = & I_0(\lambda) T(\lambda) F(\lambda) \frac{d\alpha(\lambda)}{d\lambda} + T(\lambda) F(\lambda) \alpha(\lambda) \frac{dI_0}{d\lambda} \\ & + I_0(\lambda) F(\lambda) \alpha(\lambda) \frac{dT(\lambda)}{d\lambda} \\ & + I_0(\lambda) T(\lambda) F(\lambda) \frac{dF(\lambda)}{d\lambda}. \end{aligned} \quad (6)$$

It must be added that, in order to incorporate the response of the system to a time varying incident light intensity, the above equation must be multiplied by a frequency response function  $G(\omega)$ .<sup>12</sup> However, since this factor is to first-order independence of the wavelength, it is treated here as a constant of proportionality.

In contrast to Eq. (1), Eq. (6) shows that the DSPV signal is not, in general, proportional to  $d\alpha/d\lambda$ , and therefore its various terms introduce different degrees of distortion which depend on the relative size of their spectral changes in the spectral region of interest. The most notorious source of the distortion is the spectral changes of  $I_0(\lambda)$ , the background. The distortion introduced by  $I_0$  is present in all four terms of Eq. (6), but its effect is most dramatic in the second term, which contains  $dI_0/d\lambda$ . This term affects the DSPV spectra in the near infrared region of spectra which corresponds to the sub-band-gap transitions in some semiconductors (e.g., Si, GaAs), as well as in the ultraviolet region of the spectra where the interband transitions occur.

### IV. DISCUSSION: COMPARISON OF WAVELENGTH MODERATION PHOTO RESPONSE AND WAVELENGTH MODULATION ABSORPTION/REFLECTION SPECTROSCOPIES

The structure in the spectra of the transmittance  $T(\lambda)$  and its derivative  $dT/d\lambda$  are caused by the spectral changes of the optical constants in the metal and the insulating layers, and the reflection coefficient of the semiconductor, as well as the interference patterns generated because of the interfaces. In the present MOS structure the optical properties of Au, SiO<sub>2</sub>, and Si have to be considered. These factors are separately discussed below:

(a) The spectral changes of the reflectivity of gold  $R(\lambda)$ , as well as its logarithmic derivative  $dR/d\lambda$  occur in the 2.0–5.0 eV region of the spectra and are primarily due to the  $d$  band in Fermi-level transitions.<sup>13</sup> Structure in the spectrum of the derivative of its transmission coefficient in the 2.0–3.5 eV region, have also been observed.

(b) The optical constants of the insulating layer (SiO<sub>2</sub>) are fairly smooth in the 0.5–4.5 eV region of the spectrum,<sup>15</sup> and therefore are not expected to influence the line shapes of the interband transitions.

(c) The spectral changes caused by the interference pattern depend on the thickness of the layers, their index of refraction, and the spectral region of interest. Optical interference patterns have been studied for the MIS structures with various thicknesses of Au and SiO<sub>2</sub> layers on silicon substrates.<sup>16</sup> The signatures of such interference patterns have also been observed in the surface photovoltage spectra.<sup>17</sup>

(d) Finally, the spectral changes in the  $R(\lambda)$  and  $dR/d\lambda$  of the Si substrate contribute significantly to the spectra of  $T(\lambda)$  and  $dT/d\lambda$ , and hence to the DSPV spectra. The reflectivity of Si and its logarithmic derivative obtained by the wavelength modulation reflectance spectroscopy has been reported.<sup>18,19</sup>

It is therefore clear that the spectra of  $T(\lambda)$  and  $dT/d\lambda$  contain substantial structures that could significantly change the line shapes of the absorption obtained from the wavelength modulation surface photovoltage, as well as other forms of wavelength modulation photoresponse spectroscopies.

In contrast to the wavelength modulation absorption/reflection spectroscopy, removal of the background interferences  $I_0(\lambda)$  and  $dI_0/d\lambda$  from the DSPV spectra is very difficult. To date, no systematic method for its subtraction has been suggested. We suggest a technique utilizing a double-beam system in combination with a reference optical detector and feedback loops to suppress the spectral changes of  $I_0(\lambda)$  and  $dI_0/d\lambda$ .

For this purpose, the light beam from the exit slit of the monochromator in DSPV spectrometer needs to be split by a beam splitter. Both beams can therefore be wavelength modulated at frequency  $\omega_2$ . One of the beams can be used to illuminate the DSPV sample, while the other beam can be chopped at frequency  $\omega_1$  and then incident upon an optical detector. The output of the detector is fed into two lock-in amplifiers. One of the lock-in amplifiers (I) is tuned to  $\omega_1$  to measure the light intensity, and the other one is tuned to  $\omega_2$  to measure  $dI_0/d\lambda$ . Except for the beam splitter and the DSPV sample, this is similar to the infrared wavelength modulation spectrometer described elsewhere.<sup>1</sup> The output of the lock-in amplifier (I) can be used in a negative feedback loop to regulate the power supply of the light source. This arrangement will keep the light intensity constant as the wavelength is scanned. The output of the lock-in amplifier (II) can be used in another negative feedback loop to regulate an intensity modulator to keep  $dI_0/d\lambda$  equal to zero. The intensity modulator can be placed anywhere in the light path before the beam splitter. Its modulator frequency should be the same as the wavelength modulator, and its amplitude can be controlled by the negative feedback loop from the lock-in amplifier (II). One such intensity modulator has been used in a wavelength modulation reflectance spectrometer for the same purpose.<sup>19</sup> The two feedback loop systems eliminate  $dI_0/d\lambda$  and the spectral changes of the background  $I_0(\lambda)$  to the extent that it is smooth in the spectra region of interest. This is not possible in the absolute sense nor over the entire region of the spectrum. However, what is needed in practice, is to have detectors whose spectral responsivity are flat and smooth compared to the line shapes of the optical transitions under investigation.

In comparing the wavelength modulation techniques, the wavelength modulation absorption/reflection (WMA/R) spectroscopy has several advantages over the wavelength modulation photoresponse (WMPR). The WMA/R method

yields unambiguous line shapes for the optical transitions, which are therefore easier to interpret. In WMA/R, the only source of spurious signals is the background spectrum which can be completely removed in a systematic way, independent of the spectral responsivity of the detector. Finally, the WMA/R is a nondestructive method which can be applied directly to the bulk of the materials. In contrast, the WMPR measurements often require fabrication of devices in the form of MIS,  $p$ - $n$  junction, or Schottky barriers which could result in the introduction of process related impurities or defects into the samples, as well as the necessity of applying corrections for the optical properties of the materials used for fabricating the structures.

## V. CONCLUSIONS

We have shown that contrary to the previous assumptions, the DSPV in general is not proportional to the derivative of the absorption coefficient. A general formulation of the DSPV was derived which revealed the various possible sources of spurious interference spectra. The effects of these interferences on the line shapes of optical transitions were studied. A practical method for removal of the main source of the distortions, i.e., the background, was suggested.

## ACKNOWLEDGMENTS

The support of this work by the Air Force Office of Scientific Research under AFOSR-84-0169B, the Army Research Office-Durham under DAAG29-81-K-0164, and the State of California MICRO program is gratefully acknowledged.

- <sup>1</sup>R. K. Kim and R. Braunstein, *Appl. Opt.* **23**, 1166 (1984).
- <sup>2</sup>M. Cardona, *Modulation Spectroscopy* (Academic, New York, 1969).
- <sup>3</sup>*Semiconductors and Semimetals*, Vol. 9, *Modulation Techniques*, edited by R. K. Willardson and A. C. Beer (Academic, New York, 1977).
- <sup>4</sup>J. Lagowski, W. Walukiewicz, M. M. G. Slusarczyk, and H. C. Gatos, *J. Appl. Phys.* **50**, 5059 (1979).
- <sup>5</sup>E. Kamieniecki, J. Lagowski, and H. C. Gatos, *J. Appl. Phys.* **51**, 1863 (1980).
- <sup>6</sup>T. Nishino and Y. Hamakawa, *Phys. Status Solidi B* **50**, 345 (1972).
- <sup>7</sup>R. Stearns, J. Steele, and R. Braunstein, *Rev. Sci. Instrum.* **54**, 984 (1983).
- <sup>8</sup>S. M. Etemadi, Ph.D. thesis (University of California at Los Angeles, 1984).
- <sup>9</sup>A. S. Grove, *Physics and Technology of Semiconductor Devices* (Wiley, New York, 1967).
- <sup>10</sup>L. L. Jastrzebski and J. Lagowski, *RCA Rev.* **41**, 181 (1980).
- <sup>11</sup>D. L. Lile, *Surf. Sci.* **34**, 337 (1973), and references therein.
- <sup>12</sup>S. M. Ryvkin, *Photoelectric Effects in Semiconductors* (Consultants Bureau, New York, 1964), Chap. III.
- <sup>13</sup>M. Welkowsky, Ph.D. thesis (University of California, Los Angeles, 1971).
- <sup>14</sup>R. Rosei, R. Antonangeli, and U. M. Grassano, *Surf. Sci.* **37**, 689 (1973).
- <sup>15</sup>W. L. Wolfe, in *Handbook of Optics*, edited by W. G. Driscoll and W. Vaughan (McGraw-Hill, New York, 1973), Chap. 7.
- <sup>16</sup>R. J. Powell, *J. Appl. Phys.* **40**, 5093 (1969).
- <sup>17</sup>J. Lagowski, L. Jastrzebski, and G. W. Cullen, *J. Electrochem. Soc.* **128**, 2669 (1981).
- <sup>18</sup>M. Welkowsky and R. Braunstein, *Phys. Rev. B* **5**, 497 (1972).
- <sup>19</sup>R. Zucca and Y. R. Shen, *Appl. Opt.* **12**, 1293 (1973).

# Noncontact electrical characterization of epitaxial HgCdTe<sup>a)</sup>

C. E. Jones, M. E. Boyd, and W. H. Konkel  
*Santa Barbara Research Center, Goleta, California 93117*

S. Perkowitz  
*Physics Department, Emory University, Atlanta, Georgia 30322*

R. Braunstein  
*Physics Department, University of California, Los Angeles, California 90024*

(Received 15 December 1985; accepted 14 March 1986)

It is important to be able to nondestructively characterize ("screen") the electrical properties of those areas of HgCdTe epitaxial material that will later be made into devices. This paper compares several noncontact techniques for measuring resistivity, carrier concentration, and mobility with the standard Hall-effect technique. The noncontact techniques examined are far-infrared reflection, Raman scattering, eddy-current absorption, and electroreflectance. Of these techniques, far-infrared reflection was found to be the best noncontact technique for measuring resistivity, carrier concentration, and mobility. Resistivity values were within a factor of 2 of Hall-effect values, while carrier concentration and mobility values that depend on an assumed effective mass were within a factor of 3. In Raman scattering, interference between the free-carrier plasmon-phonon mode and other modes makes it an inaccurate method for estimating carrier concentration. Eddy-current absorption is useful for quickly measuring epitaxial layer resistivities to within a factor of 3 of Hall-effect values, while electroreflectance gives a relative value for the surface doping density, which is useful in layer profiling.

## I. INTRODUCTION

It is important to know the electrical properties of HgCdTe starting material before it is processed into devices. The standard techniques for doing this, Hall-effect and capacitance-voltage testing, involve applying contacts to and processing a small piece of the sample, which takes this region out of production and does not characterize the actual material used for device processing.

This paper describes the use of far-infrared reflection, Raman spectroscopy, and eddy-current absorption to provide noncontact electrical characterization of epitaxial HgCdTe so that the characterized material can still be used for device processing. Electroreflectance data for carrier concentration is also presented, since this technique requires only a single edge contact. These techniques are all nondestructive and, except for eddy-current absorption, allow mapping of electrical parameters over the area of the starting material.

Far-infrared reflection has been used to estimate resistivity, carrier concentration, and mobility in GaAs,<sup>1</sup> CdTe,<sup>2</sup> and PbSnTe.<sup>3</sup> The method is described in a review article,<sup>4</sup> and initial data for HgCdTe has been reported by one of the present authors.<sup>5</sup> Eddy-current absorption is a standard noncontact technique used in the Si industry for measuring resistivity in wafers.<sup>6</sup> In the Raman technique, a coupled plasmon-phonon mode is excited in the surface region ( $\sim 100$  Å in depth). The mode frequency can be used to determine the surface-region free-carrier concentration.<sup>7,8</sup> In the electroreflectance technique, the signal strength is proportional to the surface-region doping density. Surface mapping of doping densities has been demonstrated for GaAs.<sup>9</sup> The issues in the present work are to determine the usefulness of these techniques for HgCdTe epitaxial layer

analysis and to compare techniques that measure the same electrical parameters.

Several of these techniques involve reflected light: i.e., far-infrared reflection, Raman scattering, and electroreflectance. The skin depth for good conductors  $\delta = c / (2\pi\mu\omega)^{1/2}$  varies inversely with the square root of the optical conductivity and the square root of the frequency. Order-of-magnitude values are  $\sim 100$  Å for the visible region excitations used in Raman and electroreflectance and micrometers for the far-infrared reflection. The eddy-current absorption technique averages over the total layer thickness.

## II. FAR-INFRARED REFLECTION

Free-carrier absorption in a semiconductor is proportional to (wavelength)<sup>2</sup>, and in the far infrared it becomes strong enough to be used to determine the resistivity, free-carrier concentration, and mobility. The far-infrared spectra were taken at 300 and 77 K using a Fourier-transform spectrometer covering the range from 10 to 250 cm<sup>-1</sup>. The samples were both *n*- and *p*-type epitaxial layers of Hg<sub>1-x</sub>Cd<sub>x</sub>Te with doping concentrations ranging from 10<sup>15</sup> to 10<sup>18</sup> cm<sup>-3</sup> and compositions in the range  $x = 0.2$  to 0.4. The samples were  $\sim 0.5 \times 0.5$  cm and were used for both the van der Pauw Hall-effect measurements and the far-infrared reflectance measurements.

Typical data are shown in Fig. 1, in which the dots are the measured data points and the solid line is a modeled fit to the data. The least-squares fit to the reflectance comes from a model for the complex index of refraction  $\tilde{n}$  that includes the free-carrier contribution, the lattice vibrational modes, and defect vibrational modes. These are identified in Fig. 1. The

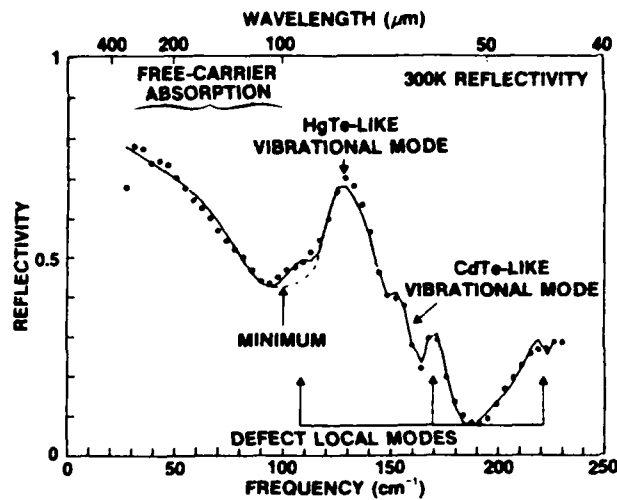


FIG. 1. Far-infrared reflectivity spectrum for HgCdTe epitaxial layer, showing free-carrier absorption region, HgTe- and CdTe-like vibrational modes, and structures at A, B, and C that may be defect local modes or interference effects.

equation used is

$$\tilde{n} = \left[ \epsilon_{\infty} + \sum_j \frac{S_j \omega_j^2}{\omega_j^2 - \omega^2 - i\omega\Gamma_j} - \frac{\omega_p^2 \epsilon_{\infty}}{\omega(\omega + i/\tau)} \right]^{1/2}, \quad (1)$$

where the second term on the right-hand side is a summation over lattice and impurity vibrational modes, each centered at a frequency  $\omega_j$  with a damping  $\Gamma_j$  and strength  $S_j$ , and the third term on the right-hand side is the free-carrier contribution, which determines the plasma frequency  $\omega_p$  and the carrier scattering time  $\tau$ . These, in turn, determine the carrier concentration, mobility, and resistivity by the expressions

$$N = \frac{\omega_p^2 m^* \epsilon_{\infty}}{4\pi e^2}, \quad (2)$$

$$\mu = \frac{e\tau}{m^*}, \quad (3)$$

and

$$\rho = \frac{1}{Ne\mu} = \frac{4\pi}{\omega_p^2 \tau}. \quad (4)$$

Figure 1 indicates that the dominant vibrational mode at 120  $\text{cm}^{-1}$  is the HgTe-like transverse optical mode, which we designate as  $\omega_1$ .

The electron effective mass values as a function of  $x$ ,  $T$ , and  $N$  were taken from work by Baars *et al.*,<sup>10</sup> while a value of 0.35 was used for the hole effective mass ratio.<sup>11</sup>

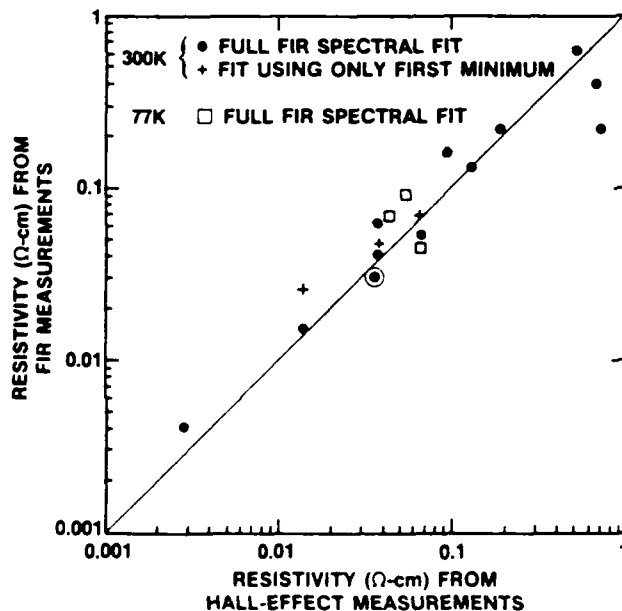


FIG. 2. Resistivity measured by far-infrared fitting and by Hall effect. (● 300 K full fit, □ 77 K full fit, + 300 K minimum fit).

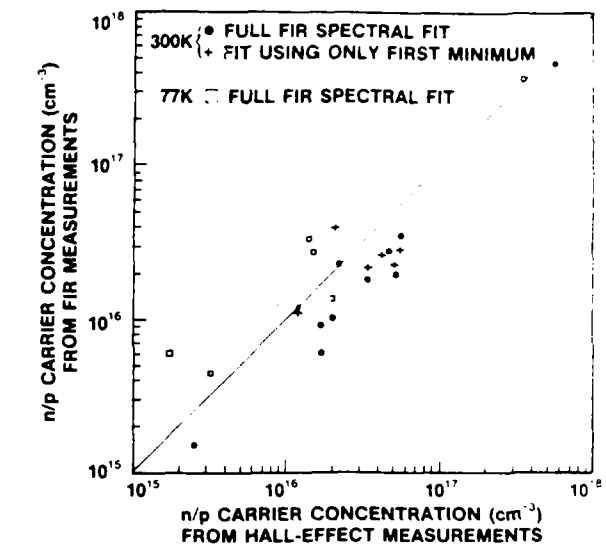


FIG. 3. Carrier concentration measured by far-infrared fitting and by Hall effect. (● 300 K full fit, □ 77 K full fit, + 300 K minimum fit).

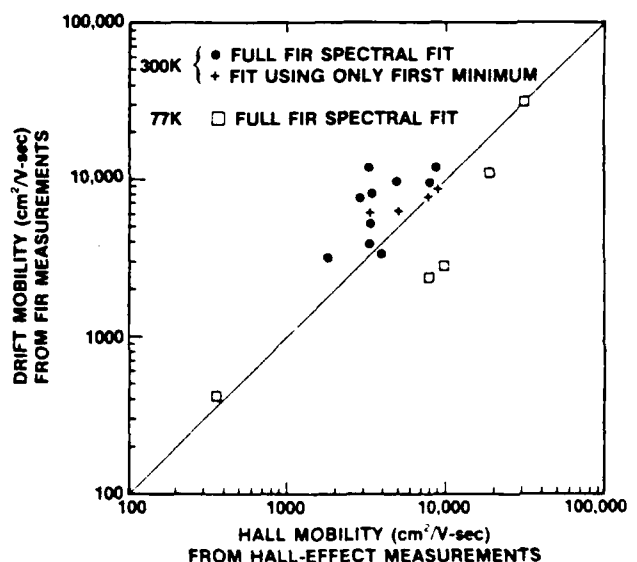


FIG. 4. Mobility measured by far-infrared fitting and by Hall effect (● 300 K full fit, □ 77 K full fit, + 300 K minimum fit).

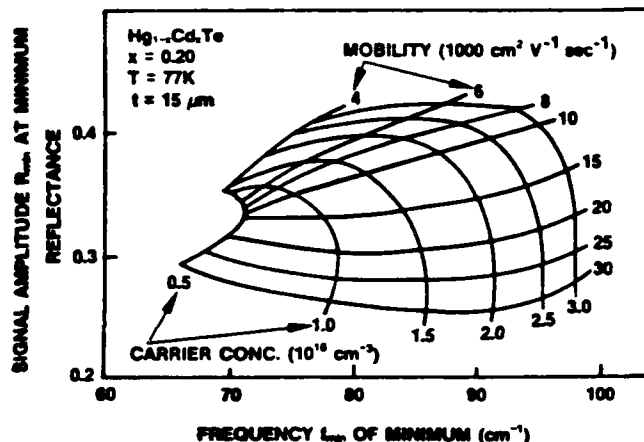


FIG. 5. Calculated carrier concentration and mobility from fit to far-infrared reflectivity minimum amplitude and frequency, for epitaxial layer at 77 K, with  $x = 0.2$  and thickness  $15 \mu\text{m}$ .

Comparisons of the resistivities, carrier concentrations, and mobilities obtained by modeling the full far-infrared reflectance spectra and by Hall-effect analyses are shown in Figs. 2, 3, and 4. The resistivity values agree within a factor of 2, while the carrier concentration and mobility data show different systematic displacements at room temperature and at 77 K, causing an increased data scatter. The use of more accurate temperature-dependent values of effective mass is expected to bring all of the far-infrared data to within a factor of 2 of Hall-effect values.

A simpler and faster method for determining the resistivity, carrier concentration, and mobility is to determine the position and amplitude of the reflectivity minimum between the free-carrier region and the HgTe-like vibrational mode. This type of analysis has been reported for GaAs<sup>1</sup> and CdTe.<sup>2</sup> The minimum occurs at the frequency  $\omega_-$ , the lower coupled plasmon-phonon mode. If the mobility  $\mu$  is large, this is given by

$$2\omega_-^2 = (\omega_p^2 + \omega_l^2) - [(\omega_p^2 - \omega_l^2)^2 + 4\omega_p^2\omega_l^2(1 - \epsilon_\infty/\epsilon_s)]^{1/2}, \quad (5)$$

where  $\omega_l$  is the dominant HgTe-like longitudinal optical lattice frequency  $\{\omega_l = (\epsilon_s/\epsilon_\infty)^{1/2}\omega_1\}$  and  $\epsilon_\infty$  and  $\epsilon_s$  are the high-frequency and static dielectric constants, respectively. Parametric curves relating the carrier concentration and mobility to the frequency and reflectivity amplitude at the minimum have been calculated. An example for  $n$ -type HgCdTe with  $x = 0.2$  at 77 K is shown in Fig. 5. Resistivities, carrier concentrations, and mobilities estimated in this way are shown for room-temperature data in Figs. 2, 3, and 4. While good results are shown in the figures, the accuracy of this reflectivity-minimum analysis is lower for  $p$ -type material than for  $n$ -type. Furthermore, multilayer structures, such as those having an  $n$ -type skin on a  $p$ -type base, or layers with mixed conduction (as occurs in an intrinsic sample), do not exhibit a well-defined minimum. Other structures in the reflectance data can also interfere with the determination of the location of the minimum, as is shown in Fig. 1. When a distinct minimum can be seen, the analysis is quick and reasonably accurate.

### III. RAMAN SCATTERING

In Raman scattering, the plasmon-phonon mode produces a peak instead of a minimum. As in the reflectance-minimum analysis, the peak frequency can be used to determine  $\omega_p^2$  and the free-carrier concentration.<sup>7,8</sup> For HgCdTe, the peaks have been found to occur in regions where other Raman modes make the identification of the plasmon-phonon mode difficult and make it insensitive to carrier concentrations below  $10^{16} \text{ cm}^{-3}$ . Raman scattering is sensitive to a surface layer  $\sim 100 \text{ \AA}$  deep. This makes Raman spectroscopy potentially useful for measuring carrier concentrations in ion-implanted materials, but it is too insensitive for general epitaxial layer screening.

### IV. EDDY-CURRENT ABSORPTION

In eddy-current absorption, a wafer is placed between an rf source and a pickup coil. The power loss due to eddy currents induced in the sample is proportional to the conductivity times the thickness of the layer.<sup>6</sup> Two commercial instruments<sup>12</sup> were tested, with similar results. Data in Fig. 6 show a variation between eddy-current and current-voltage resistivity values of a factor of approximately 3. In this case, the current-voltage analysis was done on a small piece cleaved off the edge of the wafer, while the eddy-current measurements were done on the remaining wafer, which could have caused some of the data scatter shown.

The eddy-current technique tests a large area, requiring a minimum sample size of  $\sim 5/8 \times 5/8$  in. Both vendors supply a standard resistivity meter and a high-sensitivity meter. The standard range is appropriate for bulk HgCdTe wafers, while the high-sensitivity range is needed for thin epitaxial layers. The technique does not have enough sensitivity to indicate any absorption in CdTe semi-insulating substrate material. The measurements are simple and take only a few seconds to perform, but their accuracy for determining resistivity is only within a factor of 3.

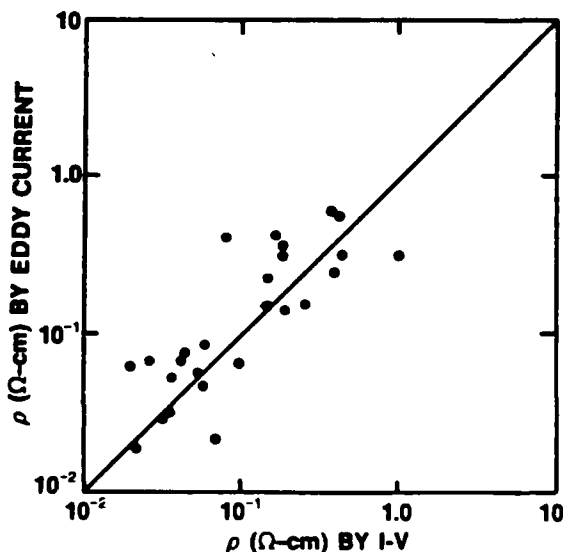


FIG. 6. Resistivity measured by eddy-current and current-voltage techniques.

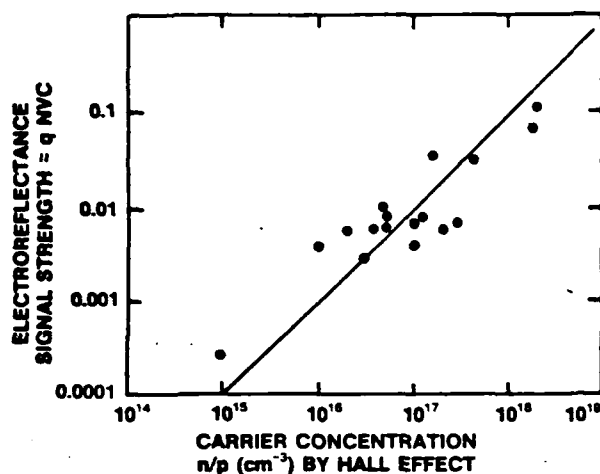


FIG. 7. Electroreflectance signal strength as function of free-carrier concentration in sample.

The parameter of more importance is usually carrier concentration. In Si, where mobilities can be accurately estimated for any given doping concentration, the resistivity measurement can be used to give carrier concentration values by means of the relation  $\rho = Ne\mu$ . In HgCdTe, the error in resistivity multiplied by the uncertainty in the mobility produces errors of over an order of magnitude in estimating carrier concentrations. This makes the technique less important for HgCdTe than it is for Si.

## V. ELECTROREFLECTANCE

Electroreflectance involves immersing the sample in an electrolyte so that an ac electric field can be applied to the surface. The ac field modulates the reflectance, giving a normalized reflectance spectrum at a singularity in a band density of state represented by<sup>13</sup>

$$\frac{\Delta R_{ac}}{R_{dc}} = \text{Re} \left\{ \frac{qNVCe^{\theta}}{[E_s - E_{ph} + i\Gamma]^{n/2}} \right\}, \quad (6)$$

where  $\Delta R_{ac}$  = ac reflectance;  $R_{dc}$  = reflectance;  $N$  = doping density;  $V$  = ac modulation voltage;  $E_s$  = energy of the singularity;  $E_{ph}$  = incident light energy;  $n = 5$  for the  $E_1$  singularity;  $\theta$  = a phase factor;  $\Gamma$  = a broadening factor; and  $C$  is a constant including the oscillator strength of the optical transition.

Experimentally, the reflectance signal from a photomultiplier is divided and sent to an ac amplifier and to a dc amplifier; the latter is used in a feedback loop on the photomultiplier power supply to keep  $R_{dc}$  constant. The ac amplifier output is then proportional to  $\Delta R_{ac}/R_{dc}$ . The ratio removes any amplitude fluctuation effects in the signal due to the lamp or the optics. A computer is used to fit the observed data to Eq. (6), with the signal strength ( $qNVC$ ),  $\theta$ ,  $E_s$ , and  $\Gamma$  being the fitting parameters. The signal strength is proportional to the net doping density  $N$  and independent of the phase  $\theta$  or the broadening  $\Gamma$ .

Without standards, absolute values of  $N$  are difficult to obtain using this technique, as the voltage drops are difficult to measure in the electrolyte, the surface layers, and the

semiconductor. For this study, the same samples were used for both Hall-effect measurements and electroreflectance measurements at room temperature. Full-temperature Hall-effect data are needed for  $p$ -type samples, since the net doping density is not given by single-temperature Hall-effect data in the transition region from extrinsic to intrinsic conductivity.

Data in Fig. 7 show a good one-to-one relationship between the free-carrier concentration as determined by the Hall effect and the electroreflectance signal strength. The scatter in the data is within a factor of approximately 2. The data include both  $n$ - and  $p$ -type samples, with  $x$  values between  $x = 0.2$  and  $x = 0.35$ . The low scatter in the data implies that the factor  $C$  in Eq. (6) is approximately constant over this range in  $x$ .

The technique has been used in measuring relative free-carrier concentrations and in determining electrical junction locations in double-layer devices that have been either bevel-etched or step-etched. Photorefectance techniques in which light of above-band-gap energy is used to excite carriers that induce a surface field may allow the measurements to be made without contacts and at low temperatures, as well.<sup>14</sup>

## VI. CONCLUSIONS

Of the techniques studied, far-infrared reflection gives the most complete and most accurate noncontact characterization of electrical properties. It can be used to determine resistivity, free-carrier concentration and mobility, and to map these values over the area of a wafer to be processed. The agreement of the far-infrared values and Hall-effect values is within a factor of 2 for resistivity and within a factor of 3 for carrier concentration and mobility. More accurate temperature-dependent effective mass values should bring the carrier concentration and mobility data to the same agreement as is seen in the resistivity data. The data analysis using the reflectivity minimum, while easier and faster than a full fit to the data, at present does not work well for  $p$ -type or mixed-conduction samples.

Interference of other effects with the plasmon-phonon mode in Raman spectra makes this technique too inaccurate for general use in screening material for carrier concentration values.

Commercially available eddy-current resistivity equipment allows for the rapid measurement of this parameter for epitaxial HgCdTe layers, with the values agreeing within a factor of 3 with current-voltage data. The technique is not sensitive enough to screen semi-insulating CdTe substrates, however.

Electroreflectance signal strength can be used to give relative doping density values at room temperature that are useful in mapping wafer uniformity or in profiling bevel-etched or step-etched samples.

## ACKNOWLEDGMENTS

The authors wish to thank Professor Paul Raccach of the University of Illinois, Chicago, and Professor Fred Pollak of Brooklyn College of CUNY for their help and advice in setting up SBRC's electroreflectance measurement apparatus.

They would also like to thank George Whiteman, Joseph Rosbeck, Ralph Ruth, and Karen Kormos of SBRC for their help in this study.

<sup>1</sup>Supported at SBRC by AFWAL/ML, under Contract No. F33615-84-C-5083 and at UCLA jointly by SBRC and the State of California through a State MICRO Program.

<sup>2</sup>S. Perkowitz and J. Brecher, *Infrared Phys.* 13, 321 (1973).

<sup>3</sup>S. Perkowitz and R. H. Thorland, *Phys. Rev. B* 9, 545 (1974).

<sup>4</sup>W. E. Tennant and J. A. Cape, *Phys. Rev. B* 13, 2540 (1976).

<sup>5</sup>S. Perkowitz, *Infrared and Millimeter Waves Vol. 8, Electromagnetic Waves in Matter, Part I*, edited by K. J. Button (Academic, New York, 1983), pp. 71-122.

<sup>6</sup>S. Perkowitz, *J. Electron Mater.* 14, 551 (1985).

<sup>7</sup>G. L. Miller, D. A. H. Robinson, and J. D. Wiley, *Rev. Sci. Instrum.* 47, 799 (1976).

<sup>8</sup>A. Mooradian and G. B. Wright, *Phys. Rev. Lett.* 16, 999 (1966).

<sup>9</sup>V. I. Zemski, E. L. Ivchenko, D. N. Mirlin, and I. I. Reshina, *Solid State Commun.* 16, 221 (1975).

<sup>10</sup>F. H. Pollak, C. E. Okeke, P. E. Vanier, and P. M. Raccach, *J. Appl. Phys.* 49, 4216 (1978).

<sup>11</sup>J. Baars, A. Hurrie, W. Rothmund, C. R. Fritzsche, and T. Jakobus, *J. Appl. Phys.* 53, 1461 (1982).

<sup>12</sup>R. Dornhaus and G. Nimtz, *The Properties and Applications of the HgCdTe Alloy System, Solid State Physics* (Springer, Berlin, 1976), p. 37.

<sup>13</sup>Tencor Instruments, 2400 Charleston Road, Mountain View, CA 94043 and Leighton Electronics, Box 323, Leighton, PA 18235.

<sup>14</sup>R. L. Brown, L. S. Schoonveld, L. L. Abels, S. Sundaram, and P. M. Raccach, *J. Appl. Phys.* 52, 2950 (1981).

<sup>15</sup>P. M. Amirtharaj, J. H. Dinan, J. J. Kennedy, P. R. Boyd, and O. J. Glembocki, *J. Vac. Sci. Technol.* 4, 2028 (1986).

## ARSENIC GROWTH ON THE GALLIUM ARSENIDE SURFACE DURING OXIDATION\*

R. Martin and R. Braunstein

Department of Physics, University of California,

Los Angeles, CA 90024

**Abstract** - Crystalline Arsenic was observed to grow on the surface of GaAs during exposure to continuous-wave laser radiation. A study of the time development of the Arsenic growth as revealed by Raman backscattering indicated that a surface diffusion process was responsible for limiting the growth process. Temperature measurements were performed from which the diffusion barrier energies were obtained for various GaAs samples. From these results the diffusion process was shown to depend on the Fermi level of the sample.

**Keywords:** Raman scattering, oxide growth, surface diffusion, barrier energies, GaAs, CdTe.



## 1. INTRODUCTION

The growth of an oxide on a III-V compound semiconductor surface is a topic of current research with both technical application and basic physical interest. It was discovered by Schwarz, et al[1], that when an anodic oxide layer is annealed at a suitable temperature, elemental Arsenic appears on the sample surface. Some study of the dynamics of Arsenic growth were pursued, however exact mechanisms have yet to be ascertained. Raman backscattering has been used in the present work to study the dynamics of the growth of crystalline Arsenic (c-As) on the GaAs surface; the growth rate has a dependence on the square-root of time. This type of time dependence is indicative of a diffusion process. The temperature dependence of the diffusion rate was measured on a variety of samples with different carrier concentration and surface orientation to obtain the diffusion barrier energy  $E$ . The results indicate a dependence of  $E$  on the Fermi level of the sample. A similar effect occurs on the surface of CdTe in that with sufficient heating elemental Te appears.

## 2. EXPERIMENTAL

By using 5145Å laser powers of 1-3 watts, with a spherical lens to focus the light on the GaAs sample, it was found by Raman backscattering that crystalline Arsenic forms on the surface. This is apparent in figs. 1 and 2, where each Raman spectrum was obtained using a low laser power of 0.5 watt. The sample was heated with the laser between each run with a laser power of two watts for a duration of one minute. Figure 1 is the spectrum of an unheated, doped sample and shows both the unscreened LO phonon from the depletion region, and the screened LO phonon from the bulk. Figure 2 shows the spectra from the same spot on the sample but after the high intensity illumination. A lower frequency peak is observed as well as a shoulder on the screened LO phonon peak. These two new features are recognized to be the Raman peaks of crystalline Arsenic (c-Arsenic)[1]. In the succeeding Raman spectra from the same spot on the sample it was observed that these Arsenic structures grew in intensity with the successive heatings via the laser.

The kinetics of the c-Arsenic formation was monitored by setting the spectrometer on the lower Arsenic Raman wavelength and recording its intensity as a function of time. The results of such an experiment is displayed in Fig. 3 where the abscissa is time and the ordinate is the intensity of the Arsenic Raman peak. If the Raman intensity is plotted as a function of the square-root of the time, the data is represented by a straight line as seen in Fig. 4. From this it may be concluded that a diffusion process is occurring.

Arsenic growth on GaAs surfaces has been seen in connection with oxide growth. The chemical reaction responsible for this is, according to Schwarz[2]:



That the As growth observed in the present work is a product of oxidation was concluded by noting that the As did not grow under the above experimental conditions in a vacuum. If indeed oxide was formed it should have been possible to observe the oxide by Raman scattering; however no  $\text{As}_2\text{O}_3$  lines were observed. It may be that the  $\text{As}_2\text{O}_3$  evaporated off of the surface, considering the vapor pressure of this compound [3], since these experiments were performed at temperatures of 400-550° Kelvin. Or, at any given time the actual amount of  $\text{As}_2\text{O}_3$  is too small to be seen if the reaction given above occurs very efficiently.  $\text{Ga}_2\text{O}_3$  has not been seen using Raman scattering on oxidized surfaces and it is generally believed that its scattering cross section is too small. If the reaction in equation (1) occurs, then we are left with a surface wherein there is mainly crystalline As and  $\text{Ga}_2\text{O}_3$ . The elemental As is thought to grow in the form of grains on the surface and as yet the physical form of the  $\text{Ga}_2\text{O}_3$  is undetermined. On these same samples, Auger and ESCA analyses were performed to see if  $\text{Ga}_2\text{O}_3$  may be detected and to determine the chemical states of the As. No shifts in the Ga ESCA peak were observed that corresponded to binding with Oxygen. These results are inconclusive, since the actual

area where the laser-induced As growth occurs is relatively small, so that ESCA signals from it may be too small to see.

### 3. DISCUSSION OF RESULTS

The process of oxide growth on GaAs is as yet not completely understood. What is known is that there is a commonality of the oxidation process among the majority of III-V compounds. III-V compounds will be henceforth denoted by AB where A and B designate column three and five elements respectively. What can occur is the following: The Oxygen first attaches to the B species on the surface due to the dangling bonds at this site. This may occur rapidly until there are a few monolayers of oxide present. This structure then becomes unstable since the  $A_2O_3$  binding is thermodynamically more stable, leaving behind elemental B. In general[4], the  $A_2O_3$  compounds are more stable and less volatile than the  $B_2O_3$  and B compounds. Therefore, the  $B_2O_3$  and B molecules will sublime if there is not a thick oxide layer to block this process. Furthermore, in order for oxidation to proceed it is necessary for the B atoms to diffuse out of said oxide layer in order to react with Oxygen, or, for the Oxygen to diffuse inward through the layer to react with the surface. Various experiments[5] using isotopes of Oxygen suggest that the Oxygen does not diffuse in.

A GaAs sample was heated at 300° C for an hour in an oxidizing

atmosphere. Prior to the heating, Raman scattering revealed the absence of elemental As on the surface. After the heating the Raman spectrum revealed a small amount of amorphous As but no  $\text{As}_2\text{O}_3$ . This temperature was larger than any obtained by laser heating, yet, the growth of crystalline As was not observed. Consequently, it is indicated that laser radiation enhanced the reactions occurring on the surface. Such enhancement has been observed elsewhere[6] in studies of oxide growth on GaAs and Si. It is hypothesized that the incident photons break bonds so that the surface reactions may occur more rapidly. When crystallization of As proceeds from the amorphous state a volume contraction of 17% occurs. Therefore, free surface must be exposed during crystallization, so that the oxidation continues without being limited by the diffusion of species through a thick oxide layer. Two different factors, then, cause the enhancement of oxidation in the laser heating process from the above considerations. The As atoms created on the free, exposed surfaces diffuse toward the crystalline As grains where they attach. This process is depicted in Fig. 5. The time dependence of the growth of the As peak yields information about surface-constrained As diffusion.

Diffusion in a solid occurs by the hopping of the atoms from site to site. There is an energy barrier that must be overcome by the diffusing atom as it moves from one site to a neighboring one. In addition there is a certain attempt frequency associated with for the atom's movement. By studying how the diffusion constant changes with temperature it is possible to determine the barrier energy  $E$ . This was accomplished by obtaining curves similar to Fig. 4 using different incident laser powers, and then finding the corresponding sample

temperatures. To find the temperature as a function of laser intensity, the results of Chang[7] were used. Chang, et al., measured the LO and TO peak positions of GaAs for varying temperatures. They found a peak shift of  $0.016 \text{ cm}^{-1}/^{\circ}\text{K}$  for both phonons. This result was applied here by measuring the LO peak position as a function of incident laser intensity. This data was reduced to obtain the graph of temperature vs. laser power in Fig. 6. The straight line is the least square fit of the data. By using the slopes of these graphs, and assuming that the sample temperature at zero laser power is  $300^{\circ}\text{K}$ , the temperature for each laser intensity used in the diffusion runs may be obtained.

If the Arsenic atoms are diffusing towards the crystalline Arsenic grains, then the results of the theory of the random walk are applicable here. The root-mean-square distance from the origin a randomly walking particle has traveled in the time  $t$  is given by:

$$(2) \quad \bar{r}^2 = (4Dt)^{1/2}$$

where  $D$  is the diffusion constant. The diffusion constant has a temperature dependence:

$$(3) \quad D = D_0 e^{-E/kT}$$

where  $E$  is the previously mentioned barrier energy. If the crystalline Arsenic grains are acting as sinks for the diffusing atoms then they must grow according to:

$$(4) \quad N_{AS}(t) = N_0 c (4Dt)^{1/2}$$

where  $c$  is a constant, the interpretation of which will be discussed later.  $N_0$  is the total number of Arsenic atoms generated in the process. It is assumed that this does not vary with the sample since the surfaces are rough enough so that the orientation is unimportant, and because for the case of the doped sample, the concentration of impurities on the surface is less than 1/10 of that of the intrinsic atoms. If  $I_0$  and  $\sigma$  are the incident light intensity and Raman scattering cross section respectively, then the time dependence of the crystalline Arsenic Raman peak is given by:

$$(5) \quad I_{AS}(t) = I_0 N_0 \sigma c (4Dt)^{1/2}.$$

The plots of Raman intensity as a function of the square root of time such as Fig. 4 then will have a slope equal to:

$$(6) \quad I_0 N_0 \sigma c (4D)^{1/2}.$$

The slopes of such graphs are taken for different temperatures of the sample and then divided by incident intensity to yield the normalized slopes:

$$(7) \quad \eta = N_o \sigma c \left[ 4D_o e^{-E/kT} \right]^{1/2}.$$

By squaring and taking the logarithm of both sides of the above equation we obtain

$$(8) \quad \log \eta^2 = \log 4D_o N_o^2 \sigma^2 c^2 - \frac{E}{kT}$$

which indicates that the slope of a plot of  $\log \eta^2$  versus  $1/T$  will yield the diffusion barrier energy  $E$ .

Table 1 lists the samples studied in the above described manner with their measured barrier energies. The graphs corresponding to equation 8 are displayed in Figs. 7-9. In these graphs the straight line is the least square fit of the experimental data points which are represented by the circles. By using radioactive tracer techniques, Goldstein[8] determined that the barrier energy for Arsenic in the bulk of a GaAs crystal is 10.2 ev. Since the barrier energies found in this



study are quite smaller than this, it is concluded that the diffusion observed here is constrained to the surface. These barrier energies may be compared with a result obtained by Schwarz[9], in a similar study, on c-As growth during annealing of an anodic oxide layer. Schwarz[9] obtained a barrier energy of approximately 2 ev by measuring the As peak intensity between successive anneals. The anneals for each series were performed at different temperatures. Only the first part of the As growth curve was obtained in this way. This part of the curve corresponds to the steepest part of the curve in Fig. 3. Schwarz[9] analyzed his data as linear in time to obtain the 2 ev barrier energy. The analysis performed in the present study utilized the whole curve and its observed dependence on the square-root of time. Also, the c-As growth observed here took place in connection with extreme light intensities. The energy measured by Schwarz[9] was interpreted to be a reaction barrier energy. With consideration of the results obtained here the 2 ev energy is interpreted to include an approximately 0.4 ev diffusion energy plus an approximate 1.6 ev "true" reaction barrier energy. The intense flux of 2.4 ev photons utilized here, could help the reactants overcome the reaction barrier energy, so that the diffusion part of the c-As growth is emphasized in the time-dependent measurements. This process is consistent with the previously noted enhancement of oxidation with extreme light intensities observed by other workers[6].

Furthermore, this model explains the  $N_0$  in equation 3 as being independent of temperature and laser light intensity. The temperature independence is seen by the chemical reaction occurring through interaction with photons in order to overcome the reaction barrier

energy. Laser intensity independence occurs through the necessity of Oxygen to encounter bare surface in order for the reaction to be initiated. The amount of bare surface is limited by the c-As grain size and the amount of  $\text{Ga}_2\text{O}_3$  present.

From table 1 it is seen that two of the sample surfaces had a (100) orientation, however one was semi-insulating and the other was n-type doped at approximately  $2 \times 10^{18}$  charge carriers/cm<sup>3</sup>. The difference in barrier energies could be ascribed to different charge states of the diffusing Arsenic atoms[10]. The difference in the position of the Fermi levels of the two samples will determine the charge state of the surface defects. Equation 7 not only yields the barrier energy, but also differences in the "sticking coefficient" c by using the intercepts of the plots in Figs. 7-9. This is seen by noting that, the intercept is equal to:

$$(9) \quad \log 4D_0 N_0^2 \sigma^2 c^2.$$

If the other parameters are invariant with respect to sample then the ratio of the sticking coefficients of the two samples may be found by:

$$(10) \quad \text{Int.}(1) - \text{Int.}(2) = \log \frac{c_1^2}{c_2^2}.$$

The sticking coefficient for the n-type sample is found to be 3.8

times as large as that of the semi-insulating sample. Again, the charge state of the migrating Arsenic atoms could explain this, since, there will be an image charge in the crystalline Arsenic grain when a diffusing atom comes near. This image charge causes an attractive force between the atom and the grain, hence the sticking coefficient is larger. This also means that the Arsenic atoms on the semi-insulating surface are neutral, while the atoms on the doped sample surface are charged and are acceptors, since they became occupied with increase in the Fermi energy. The above interpretation of the sticking coefficient gains further support in that the intercept for the (111) sample was roughly equal to that of the semi-insulating (100). By using the above analysis as described in equation 9, this means that the two samples have equal sticking coefficients. The (111) sample is Chromium doped and hence is also semi-insulating. Therefore, since its Fermi level is in the same place, the Arsenic atoms on its surface are in the same charge state as the (100) semi-insulating samples. A larger barrier energy for the (111) surface may be a result of a different morphology at this orientation. Various structures have been observed on this surface[3]. That these surfaces are good (100) or (111) planes is arguable. They probably have many hills and valleys, so that, ascribing to them properties associated with flat, planar surfaces of their respective orientations is only an approximation. The dominant difference in barrier energy for the three samples may be interpreted as being due to the charge state of the diffusing Arsenic atoms while surface orientation may play a weaker role

A similar study to that of GaAs was performed on surfaces of CdTe and HgCdTe when subjected to heat treatment. These measurements reveal

the growth of elemental Tellurium. The growth of Te is a major problem when using Raman scattering to study these materials. At room temperature relatively low incident light levels will induce its growth. A time dependent growth curve for the Te peak on an initially clean CdTe surface is shown in Fig. 10. There is a resemblance to the curve of Fig. 3 for the growth of As on GaAs. It was found that if the focusing of the incident light on GaAs were not done correctly, the As growth curves had a rough appearance as seen in Fig. 10 for CdTe. At only an empirically found critical distance between the focusing lens and the sample, was a relatively smooth growth curve be obtained. This is probably due to the size of the As grains, and possible over-excitation of the sample due to too high a light intensity. Sublimation effects may occur on an over-heated surface which will be more pronounced with smaller grain size. A similar critical focusing of incident light may exist for CdTe that would create smooth growth curves for Te. The curve in Fig. 10 is suggestive that a diffusion process is occurring for Te growth on CdTe that is like that of As on GaAs. This would be the subject of future studies in this laboratory.

#### 4. CONCLUSIONS

The present study of the time dependence of the growth of c-Arsenic during the oxidation of the surface of GaAs as monitored by Raman backscattering indicates that a surface diffusion process rather than

bulk diffusion is operative for the production of elemental Arsenic. An enhancement of the growth of c-Arsenic was observed due to 5145Å illumination. These measurements have shown that the surface diffusion barrier energies and sticking coefficients involved in Arsenic grain growth are determined by the charge state of the grains which is determined by the Fermi level of the GaAs substrate. Preliminary measurements on CdTe surfaces indicate similar results for the growth of elemental Te. The present work indicates that Raman backscattering is a useful tool for studying nucleation processes during interface growth.

#### REFERENCES

- \* This work was supported by the Air Force Office of Scientific Research under AFOSR-84-01698. The Army Research Office - Durham under DAAG 29-K-1064 and the State of California MICRO Program.
- 1. Schwartz G.P., Schwartz B., Distefano D., Gualtieri G.J. and Griffiths J.E., *Appl. Phys. Lett.*, **34(3)**, 205 (1979), p.270
- 2. Schwartz G.P., Insulating Films on Semiconductors, 270, (Springer-Verlag, Berlin, 1981), p.270

3. Wilmsen W., Physics and Chemistry of III-V Compound Semiconductor Interfaces, (Plenum Press 1985) p.403
4. Wilmsen C.W., *Thin Solid Films*, **39**, 105, (1976).
5. Watanabe K., Hashiba M., Hirahota Y., Nishino M., and Yamashina T., *Thin Solid Films*, **56**, 63 (1979)
6. Schafer S.A., and Lyon S.A., *J. Vac. Sci. Technol.*, **19(3)** p.494 (1981).
7. Chang R.K., Ralston J.M., and Keating D.E., Light Scattering Spectra of Solids, 369 (Springer-Verlag, 1969) p. 369
8. Goldstein B., *Phys. Rev.* **121(5)**, 1305 (1961).
9. Schwartz G.P., Gualtieri G.J., Griffiths J.E., and Schwartz J.E., *J. Electrochem Soc.*, **128(2)**, 410 (1981).
10. Boltaks B.I., Diffusion in Semiconductors, (Academic Press, New York, 1963) p.76

Table 1

Samples and measured diffusion barrier energies.

<u>Sample</u>	<u>Barrier Energy (ev)</u>
(100) semi-insulating	0.33
(100) n-type	0.50
(111) semi-insulating	0.43

Figure Captions

Figure 1. GaAs Raman spectrum before intense illumination.

Figure 2. GaAs Raman spectrum after intense illumination.

Figure 3. Intensity of c-As Raman peak as a function of time.

Figure 4. Intensity of c-As Raman peak as a function of the square root of time.

Figure 5. Growth of c-As grains on a surface.

Figure 6. Temperature of sample versus laser power for (100) semi-insulating GaAs.

Figure 7.  $\log \eta^2$  versus reciprocal temperatures for (100) semi-insulating GaAs.

Figure 8.  $\log \eta^2$  versus reciprocal temperatures for (100) n-type GaAs.

Figure 9.  $\log \eta^2$  versus reciprocal temperatures for (111) semi-insulating GaAs.

Figure 10. Intensity of c-Te Raman peak as a function of time.



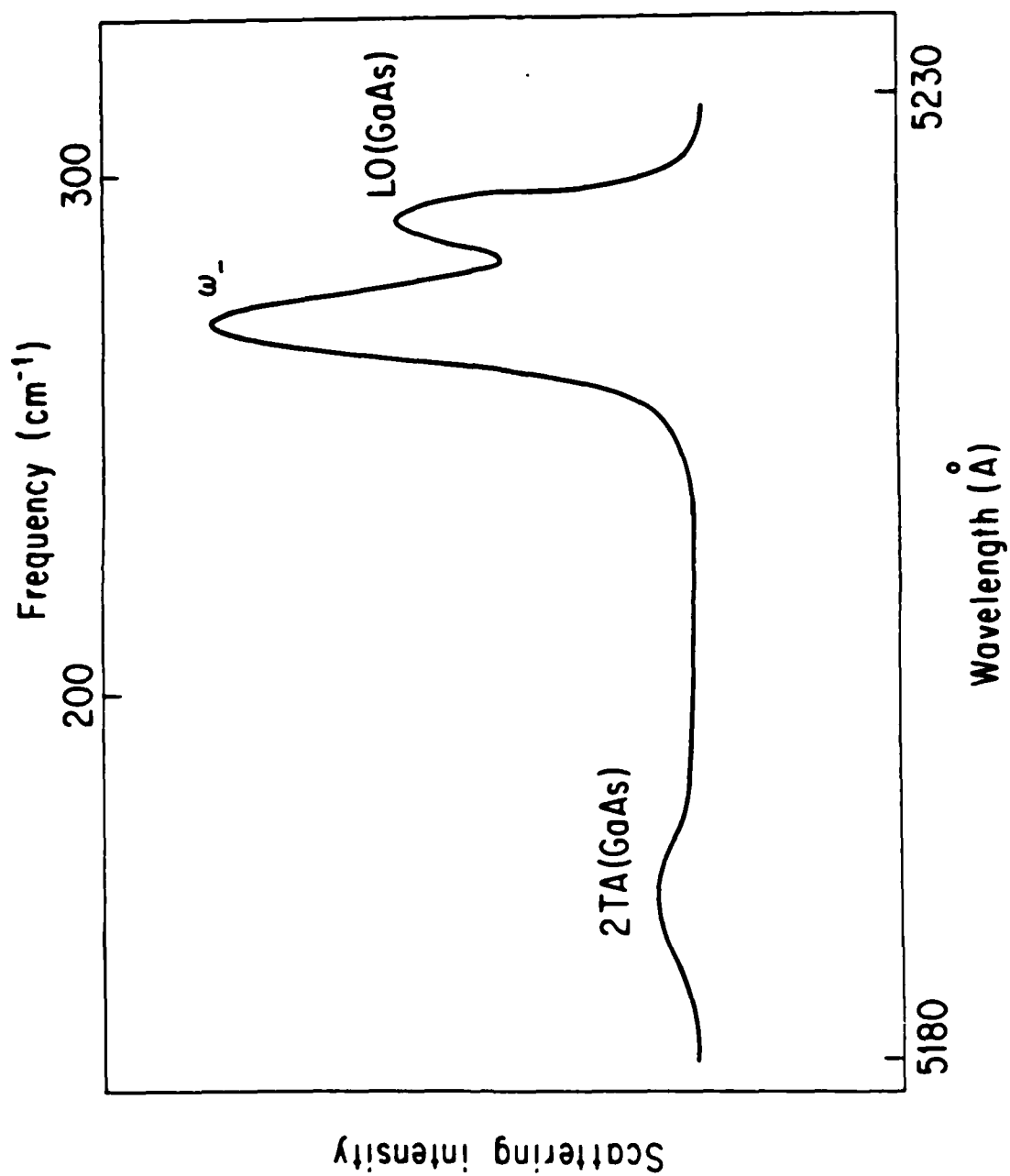


Figure 1

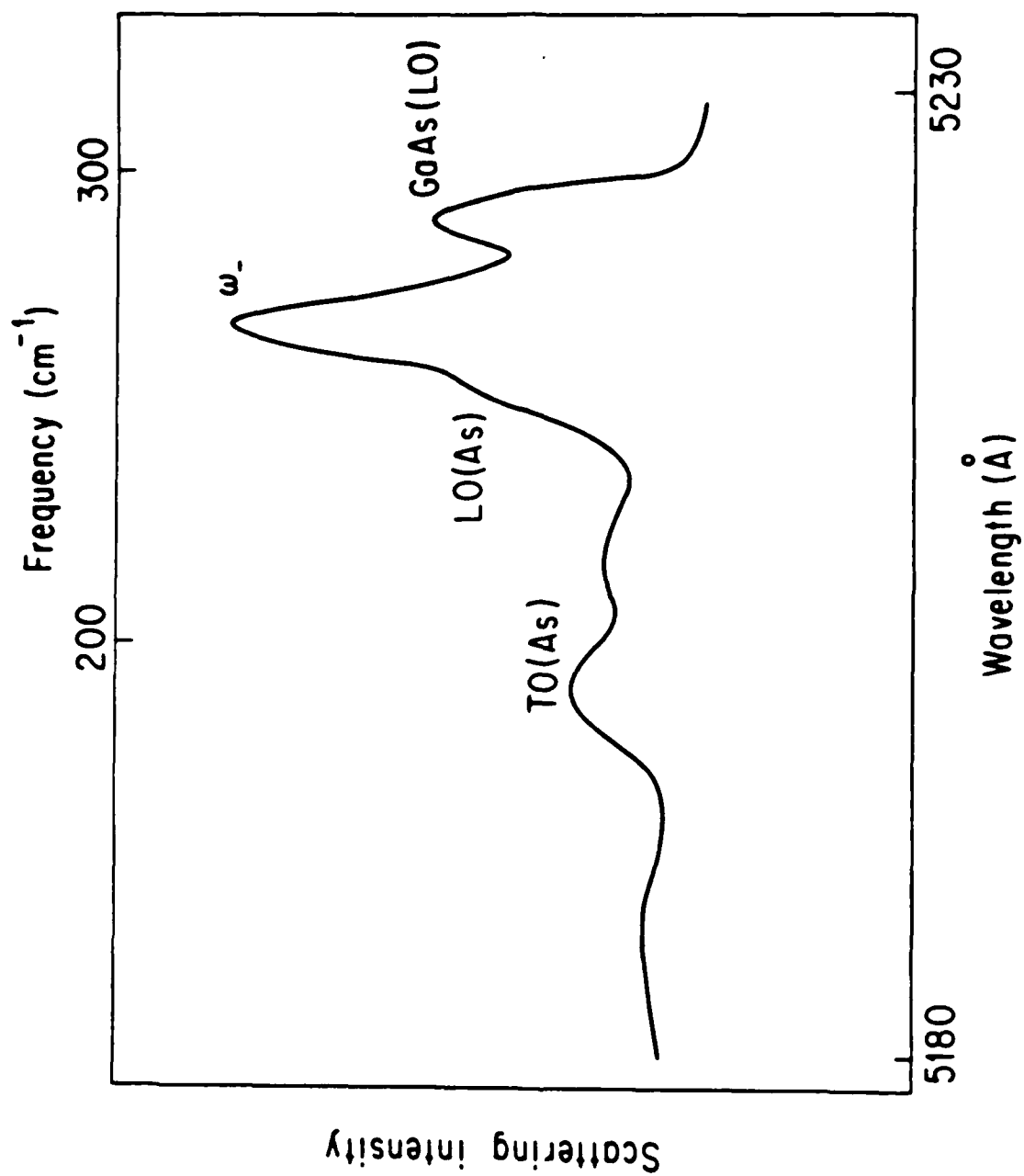


Figure 2

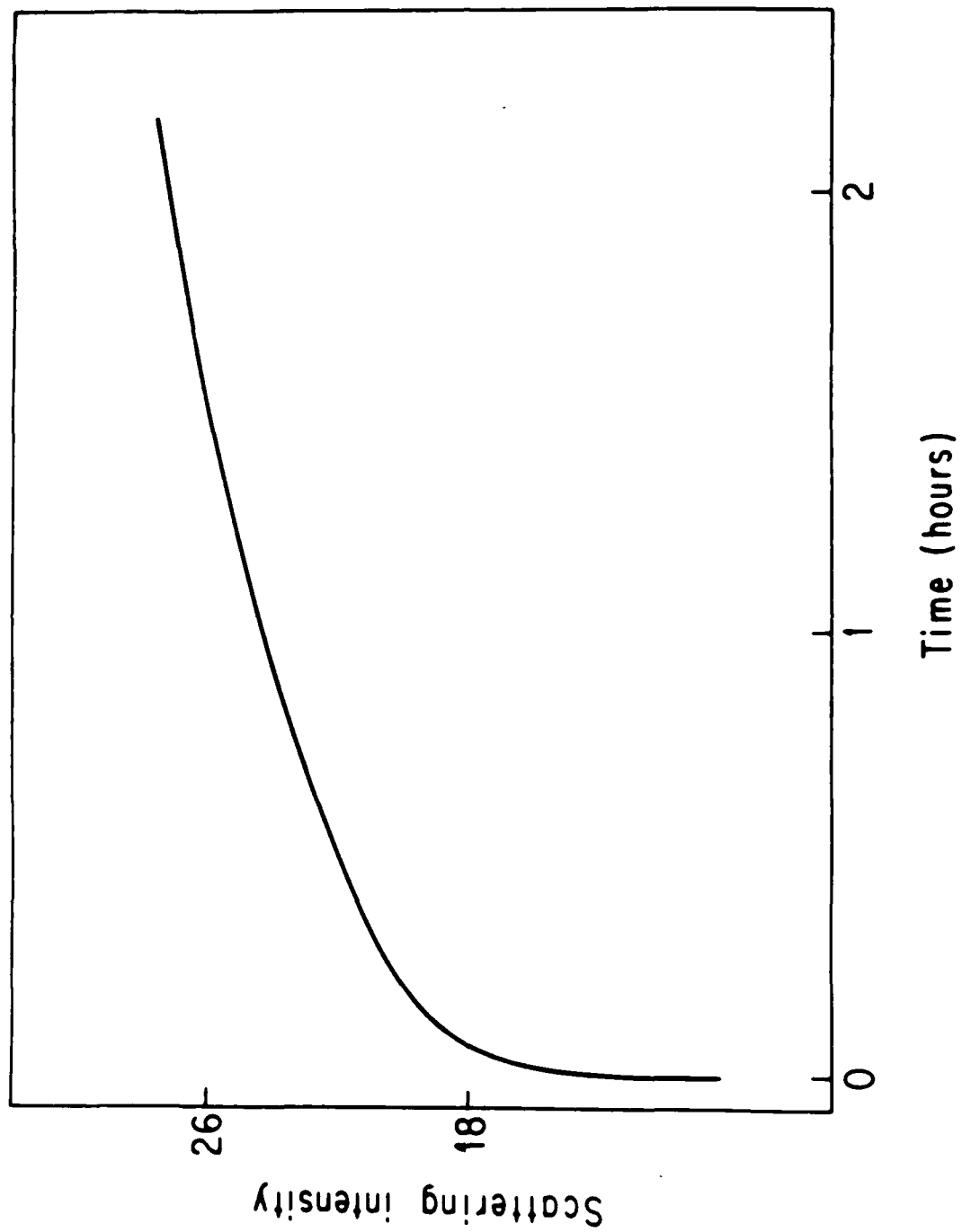


Figure 3

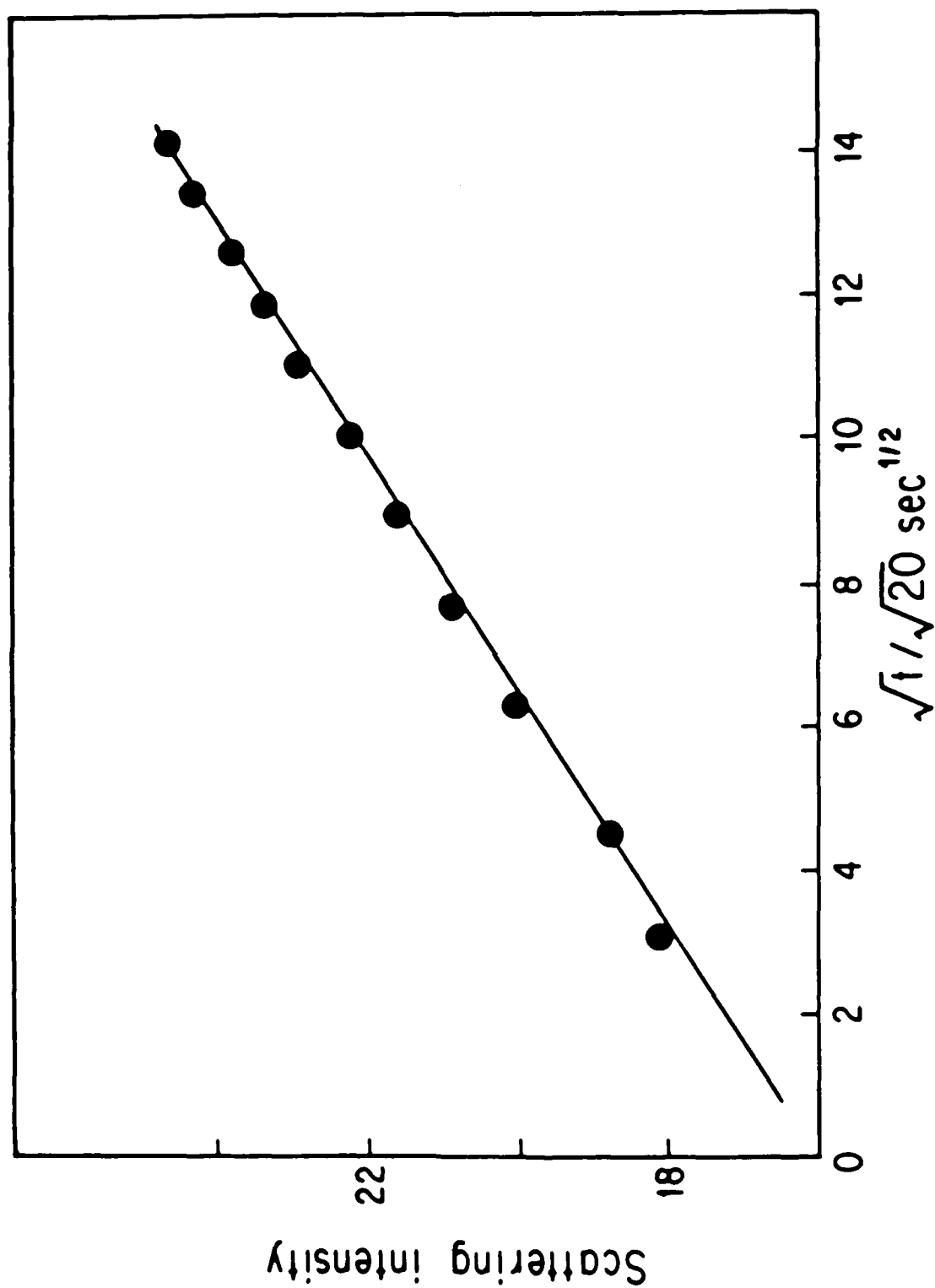
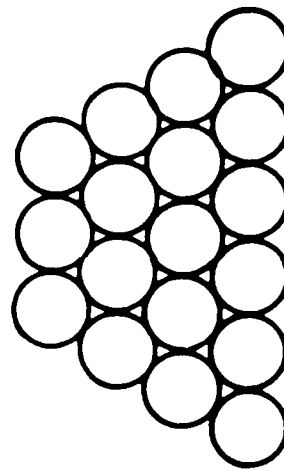


Figure 4

As Grain



As



As



Figure 5

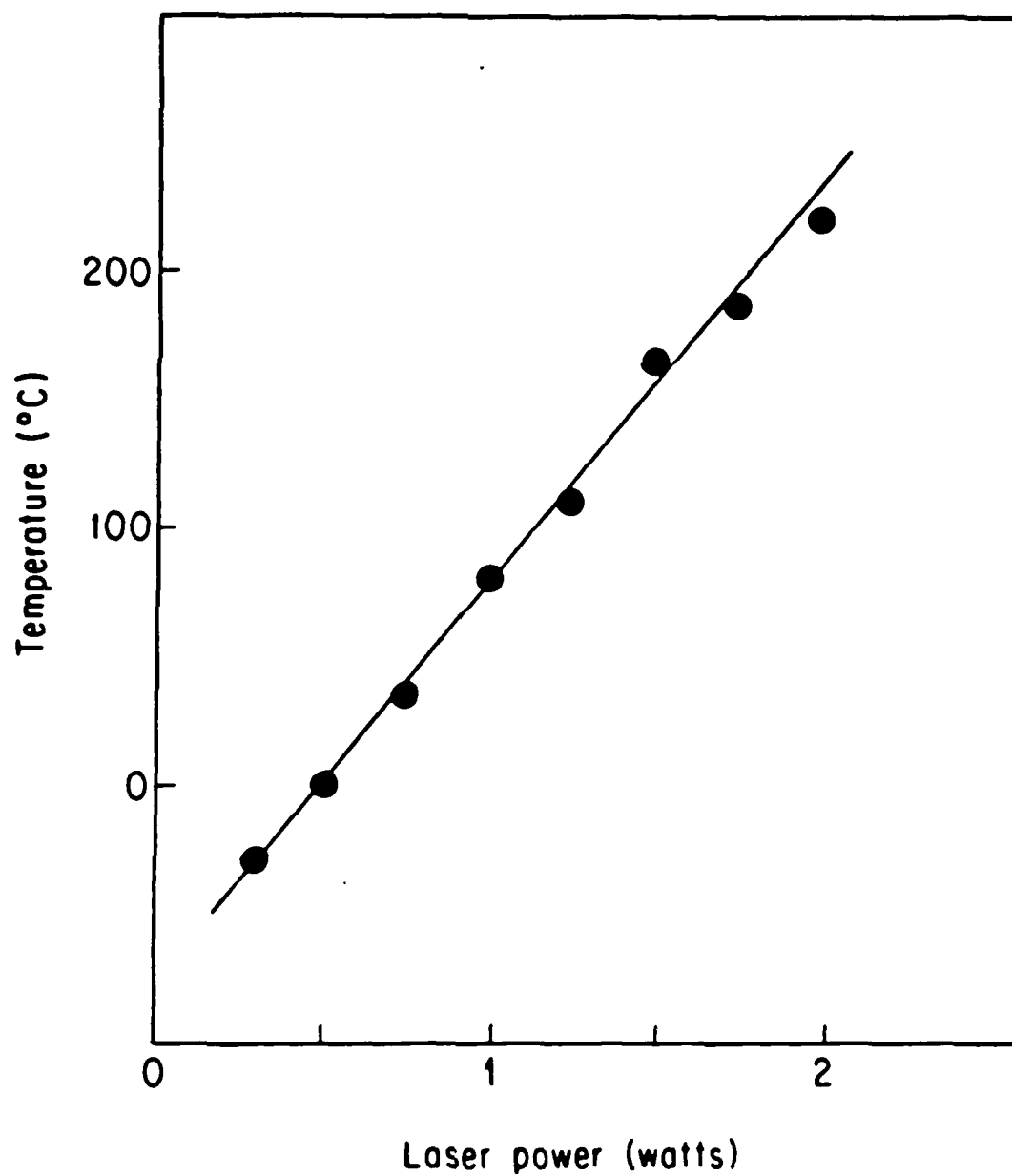


Figure 6

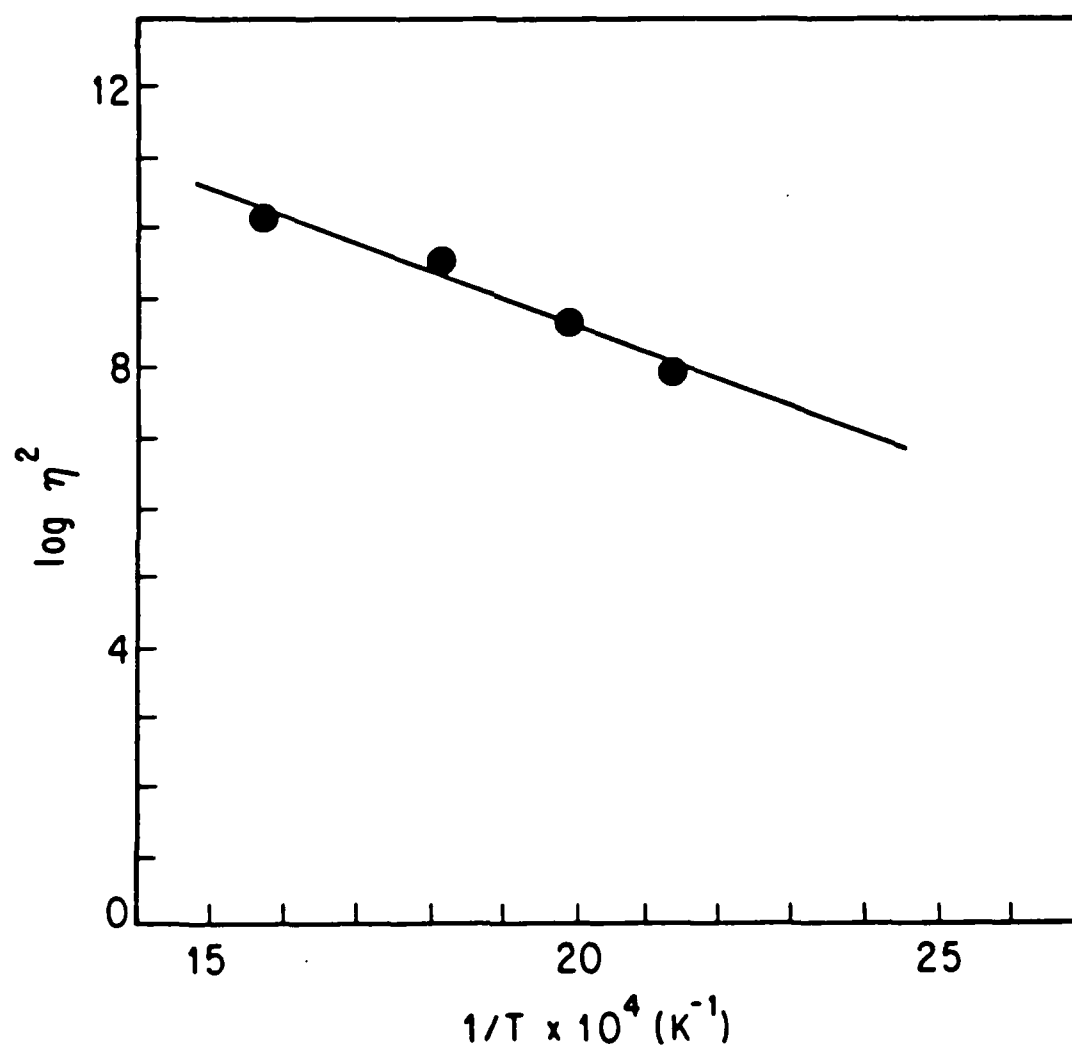


Figure 7

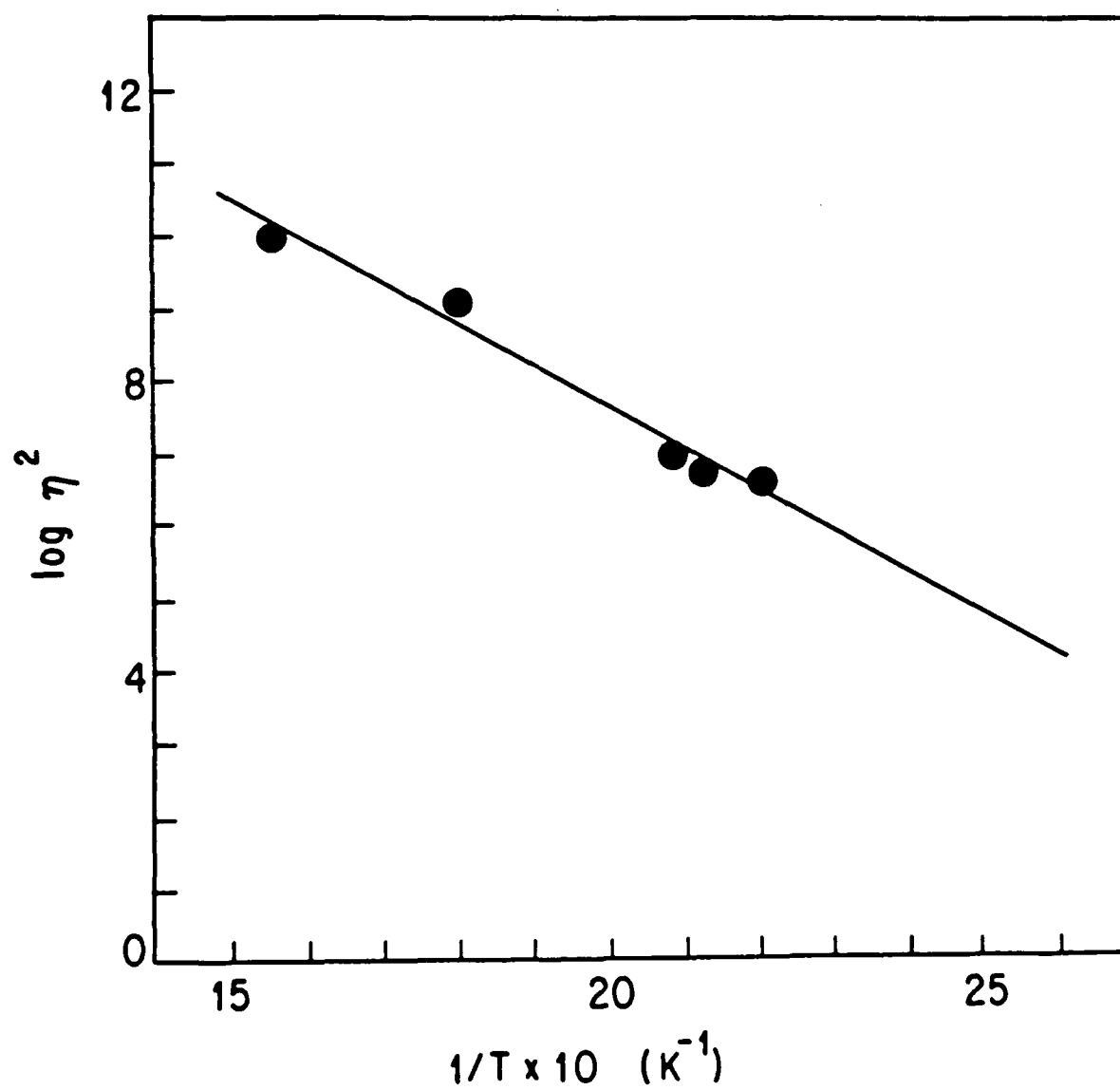


Figure 8



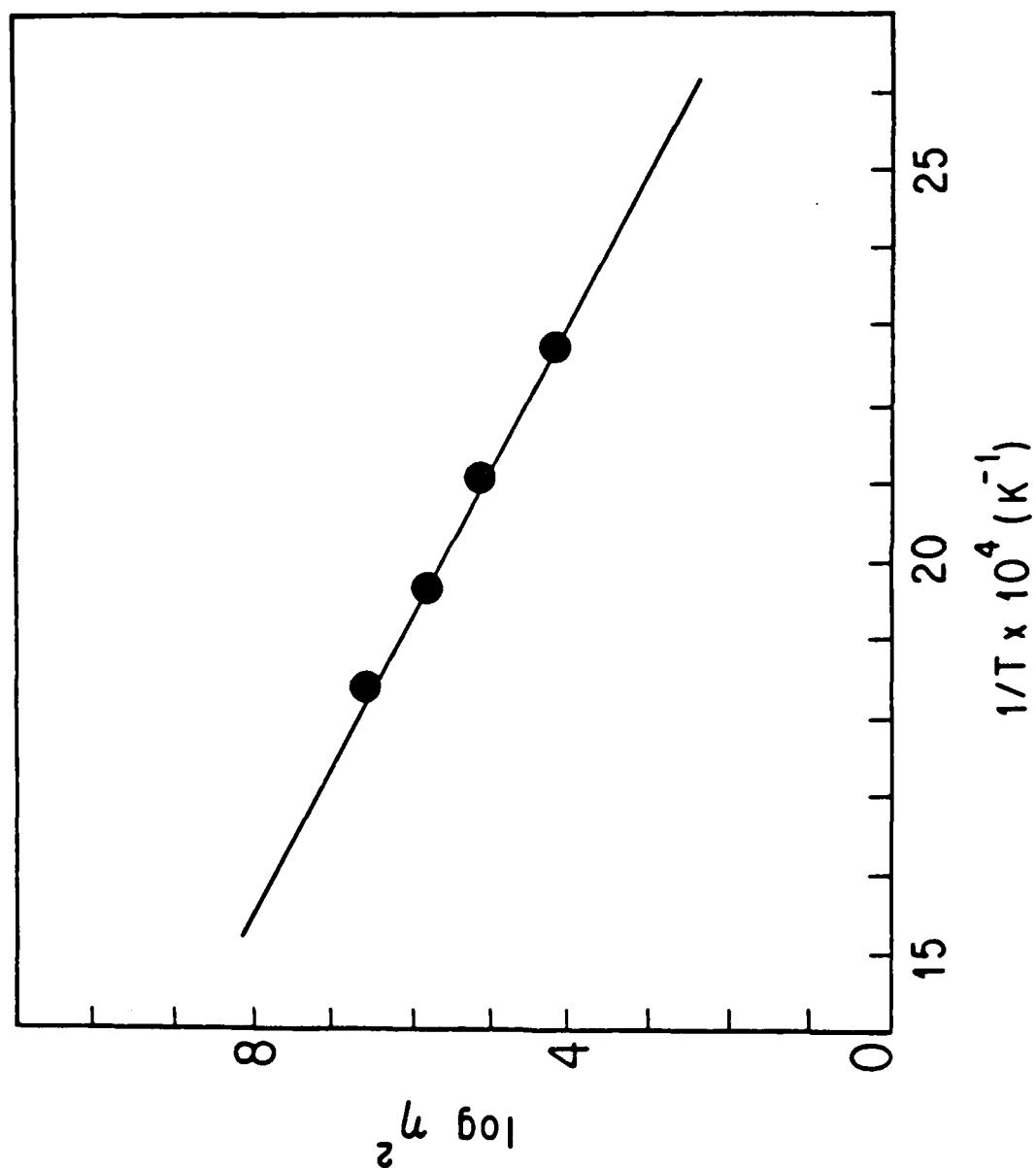


Figure 9

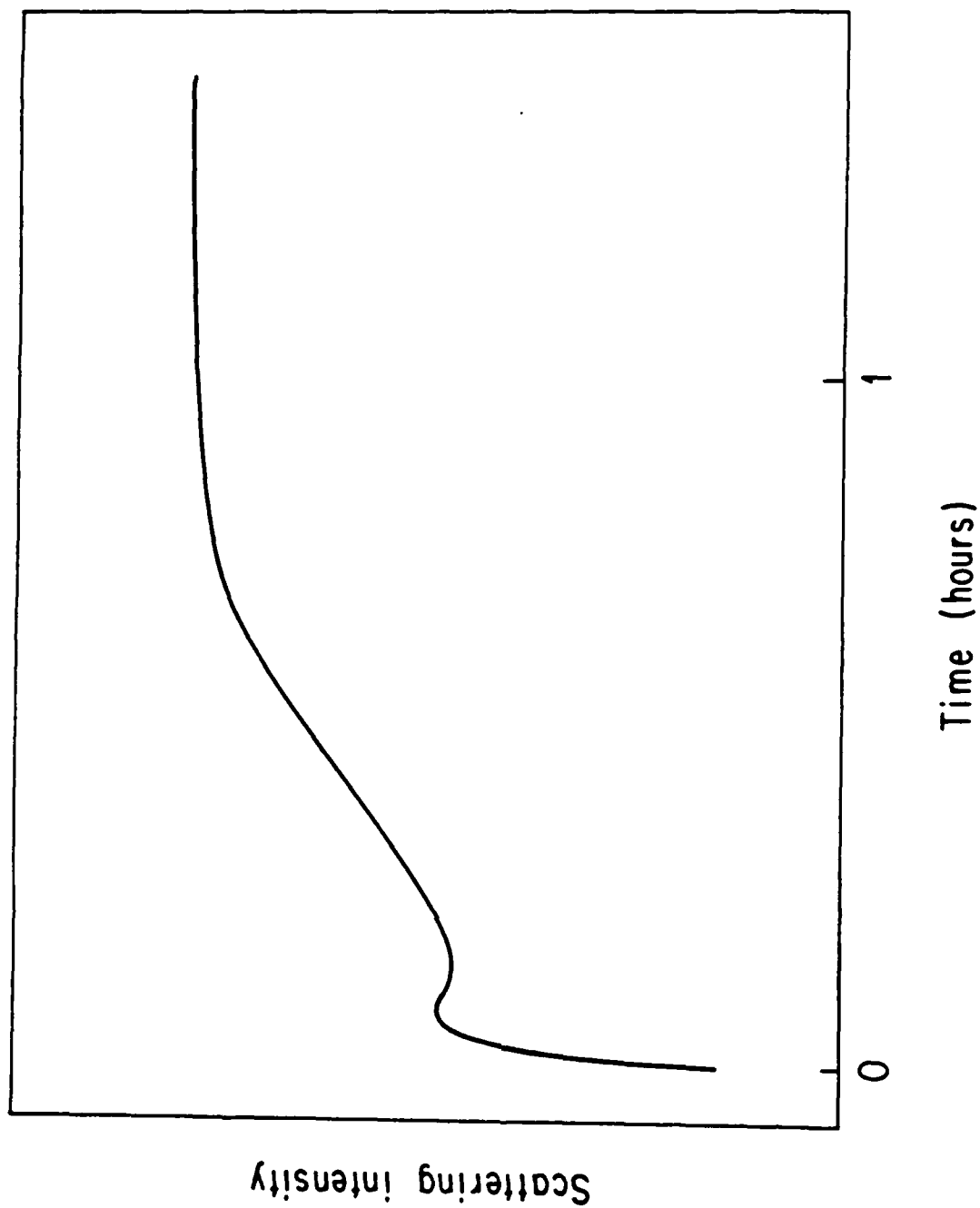


Figure 10

DEEP LEVELS IN SEMI-INSULATING,  
LIQUID-ENCAPSULATED-CZOCHELSKI GROWN GaAs \*

M.R. BURD AND R. BRAUNSTEIN

Department of Physics, University of California  
Los Angeles, CA 90024

**Abstract** - Photo-induced-transient-spectroscopy was performed on variously heat-treated samples of semi-insulating liquid-encapsulated-Czochralski grown GaAs. Seven deep levels at 0.57, 0.52, 0.42, 0.36, 0.27, 0.22, and 0.18 eV were observed. These levels can be identified with levels seen using other deep level techniques and a variety of crystal growth and sample preparation techniques. The levels at 0.52, 0.42, and 0.36 eV can be annealed out by heat treatment. These levels therefore seem to be associated with structural defects rather than impurities.

**Keywords:** Photo-induced-transient-spectroscopy, deep levels, semi-insulating, annealing.

## 1. INTRODUCTION

The deep levels present in GaAs which have been prepared by various growth techniques are of current technological and scientific interest. Unfortunately, in many of the studies done on samples produced by a particular growth method the measurement techniques used tended to obscure some of the deep levels which may have been present at the time of growth. For instance, the use of deep level transient spectroscopy [1] requires the construction of a diode structure from the sample to be studied causing the sample to be subjected to relatively high temperature annealing. Such temperature treatment can remove or add defects that give rise to certain deep levels, making them impossible to study in as grown material.

The purpose of this study was to investigate the deep levels present in samples of liquid encapsulated grown Czochralski (LEC) [2] semi-insulating GaAs. To accomplish this, photo-induced-transient spectroscopy was used as the measurement technique for detecting deep levels in the sample. This method was chosen for two reasons: First, it is a technique for detecting deep levels in semi-insulating material, and, second, the preparation of samples for this technique involves only a small amount of heat treatment allowing study of annealable deep levels which may have been introduced during the growth process.

Measurements were made on samples which had been subjected to a variety of heat treatments with the purpose of giving some evidence for possible defect structures which may be causing the deep levels. Using these methods seven deep levels were observed with most of them being readily identified with deep levels seen in other works involving other deep level techniques.

## 2. EXPERIMENTAL TECHNIQUES AND SAMPLE PREPARATION

The method used to detect the presence of the deep levels in the samples was photo-induced-transient spectroscopy [3]. This technique involves pulsing a monochromatic light source at a sample of GaAs which has a bias voltage applied across contacts on its surface. The transient current which follows the termination of the light pulse is then measured. If the trap being seen is an electron-like trap and the light intensity is sufficient so that a saturated condition is achieved for the photo-current, then the form of the transient current becomes:

$$(1) \quad \delta i(t) = CN_T e_n \exp(-e_n t)$$

where  $e_n$  is the emission rate,  $N_T$  is the trap concentration, and  $C$  is a constant. When this equation is differentiated with respect to temperature the following results:

$$(2) \quad \frac{d\delta i(t)}{dT} = C N_T (1-e_n) \exp(-e_n t) \frac{de_n}{dT}$$

It can be seen that an extremum occurs when  $t=1/e_n$ . Therefore, by choosing a time after the termination of the light pulse and plotting the magnitude of the transient current as a function of temperature, a series of peaks are obtained. Each peak corresponds to a different deep level with the position of the peak occurring at a temperature,  $T_m$ , where the level's emission rate is equal to the reciprocal of the time chosen. By graphing the transient current values at different times as a function of temperature, several values of  $T_m$  can be obtained for the different values of the time,  $t$ . Assuming the form for  $e_n$  [6] is:

$$(3) \quad e_n = \gamma_n T^2 [\sigma_{n\infty} g_n \exp(\alpha/k)] \exp(-E_A/kT).$$

where  $E_A$  is called the activation energy and  $\sigma_{na} = (\sigma_{n\infty} g_n \exp(\alpha/k))$  is the apparant cross-section. A plot of  $\log(T^2 t)$  versus  $1/T$  will yield a straight line graph. The value for  $\gamma_n$  has been determined to be  $(4\sqrt{6} \pi^{3/2} h^{-3} m_n^* k^2)$  [11]. For electrons this equals  $2.28 \times 10^{20} \text{ cm}^{-2}\text{s}^{-1}\text{k}^{-2}$  [6]. Putting in the effective mass term for holes yields a value of  $1.7 \times 10^{21} \text{ cm}^{-2}\text{s}^{-1}\text{k}^{-2}$  [5]. This straight line graph or the combination of  $E_A$  and  $\sigma_{na}$  ( $\sigma_{pa}$  for holes) is called the signature of the deep level and is a method for identifying a deep level.

The photo-induced-transient spectroscopy (P.I.T.S.) apparatus [4] consisted of a dewar in which the samples could be cooled to liquid nitrogen temperature. There were windows in the dewar to allow the light pulses from the two light sources used for this experiment to

strike the samples. The light sources used were a He-Ne laser and a GaAs light emitting diode which gave light at energies greater than and less than the band gap respectively. The temperature of the sample was monitored by a thermocouple. The current through the sample was measured as a voltage across a resistor which was placed in series with the sample and the DC power supply which provided the bias voltage to the sample. The apparatus was controlled and the temperature and transient current were read by a CAMAC data acquisition system under the control of an LSI-11/23 computer. A representation of the transient current was obtained at each temperature by having the computer read the voltage across the series resistor at several regularly spaced times following each pulse of light. This allowed a complete set of data to be obtained in only one temperature scan. Figure 1 shows a block diagram of the P.I.T.S. apparatus while Fig. 2 shows the flow diagram for the computer program which controls the system.

All of the samples used in this study were LEC grown GaAs and were semi-insulating because of the deep levels which were caused by the growth process as opposed to being deliberately introduced into the samples by doping with materials such as Cr. One sample, M177, however, did have a layer of GaAs grown on it by molecular beam epitaxy. A summary of the treatment samples is presented in Table 1.

Samples M039, M040, and M25-2 had no heat treatment performed on them until they had first been tested for deep levels; then the same samples were annealed and redesignated M039 ann, M043 ann, and M25-2 ann. The annealing process involved raising their temperature in a nitrogen atmosphere over a period of one hour from room temperature

to 700K. They were left at this temperature for four hours and then, over a period of one hour, their temperature was lowered back to room temperature. After being tested for deep levels sample M039 was given another heat treatment and redesignated M039 que. This particular heat treatment involved raising its temperature to 700K over a period of one hour. The sample was left at this temperature for a period of three hours and then was cooled back down to room temperature in approximately ten seconds.

Samples M25-2I, D9, M025 and M177 had ion-implanted electrical contacts. This process involves masking the samples and implanting Si ions into the surface at extremely high concentrations such that the conductivity becomes very large in the implanted regions. The samples are then given a high temperature anneal to drive in the Si and remove some of the damage caused by the implantation process. The electrical contacts on all of the other samples were made by soldering In to the surfaces of the samples with an ultrasonic soldering iron. The soldering process was performed as quickly as possible in order to minimize the amount of heating the samples were subjected to.

### 3. RESULTS AND DISCUSSIONS

The signatures of all the deep levels seen in all of the samples tested are compiled in Fig. 3, while a tabulation of which levels were present in a given sample is displayed in Table 2. As can be seen



there is a rich spectrum of deep levels in the samples which were not subjected to any heat treatment, these being M039, M043, and M25-2. For several of the deep levels definite patterns of behavior can be seen with regard to the heat treatment given the various samples. As can be seen by comparing Fig. 4 to Fig. 5, the difference between an as-grown sample and the same sample after being subjected to heat treatment is quite significant. Table 3 shows a listing of all the observed deep levels' activation energies and emission sections.

The level with an activation energy of 0.18 eV has a signature which matches that of the deep level designated as EL10 and observed in other studies [6]. As can be seen in Table 3 it has a  $\sigma_{na}$  equal to  $1.5 \times 10^{-15} \text{ cm}^2$ . The best identification of the level with the activation energy of 0.22 eV is EL17 [8]. The level being an electron level yields  $\sigma_{na}$  equal to  $1.5 \times 10^{-14} \text{ cm}^2$ . The best fit to the signature of 0.36 eV occurs for the deep level designated as HL7 [5]. The hole nature of the level yields  $\sigma_{pa}$  equal to  $5.6 \times 10^{-13} \text{ cm}^2$ .

The deep level listed in Table 3 with an activation energy of 0.56 eV has a signature which is an excellent fit to that of the level designated in other studies as HL3 [5] yielding a  $\sigma_{pa}$  equal to  $1.4 \times 10^{-15} \text{ cm}^2$ . This particular deep level has been found to correspond to the presence of iron in the samples tested in other works. This is supported here by the fact that the level appears in all of the samples used in this study which gives greater weight to the level being associated with a chemical impurity rather than just a crystal imperfection. Another feature which supports this identification is the presence of this level in the MBE sample M177. It is known that iron is a fast diffuser in GaAs [7] and tends to migrate toward the

surfaces of a sample. The presence of the 0.56 eV deep level in the MBE sample would imply that the iron-associated defect has migrated from the LEC substrate into the MBE layer during either the MBE process or the ion-implantation of the electrical contacts.

The deep level with a signature which most closely matches that of the level with the activation energy of 0.42 eV is HBS which is believed to be the same level as HLS [5]. This particular level is thought to be associated with a native defect in the crystal. This is supported in this study by the fact that it is readily annealed, as can be seen in Table 2 since it does not appear in any of the heat treated samples except M039 que. The fact that it reappears in the quenched sample means that it can be easily reintroduced by "freezing in" the high temperature concentration of these imperfections.

A multilevel defect complex with a resonant optical absorption peak near 0.40 eV with two side lobes was previously observed in the same samples of the present study using the sensitivity of wavelength modulation absorption [9]. The peak magnitude and the detailed shape as well as the side lobes of this structure varied from sample to sample indicating that the structure is probably due to a defect complex formed during growth and was not due to a multi-level impurity. Heat treatment similar to that performed in the present work showed that the spectra at 0.40 eV annealed out. These optical experiments indicated that the structure is due to a defect or defect complex with two main levels separated by 0.40 eV which may split into more levels or form complexes depending upon the nature of defects immediate environment resulting from a previous thermal history. The possible correlation of the 0.40 eV level observed in the previous

optical work and the present P.I.T.S. measurements is intriguing. However, an exact correlation between the levels observed by the wavelength modulation absorption and the level detected by P.I.T.S. must take into account the fact that the latter essentially yields information on the thermal emission from the level to the band, whereas the former gives information about the intra-center transitions.

There is some difficulty in assigning a designation to the 0.27 eV level in that its signature lies almost halfway between the signatures of EL8 and HL12 [5]. Assuming it is one of the two and not a newly seen level, the feature which lends more weight toward identifying it as HL12 is that the level appears in all of the samples except the MBE samples. HL12 has been seen in samples which contain zinc, a chemical impurity, and is, therefore, not as likely to be affected by annealing. As can be seen in Table 3 this identification results in  $\sigma_{pa}$  being equal to  $3.8 \times 10^{-15} \text{ cm}^2$ .

The best candidate for the identification of the deep level seen at an energy of 0.52 eV is a somewhat unconventional band seen in samples which have undergone ion-implantation using boron as the bombarding ions [10]. This boron-implantation produced defect structures which were annealable and the energy band associated with them has a peak at temperatures which agree with those seen for the level in this work. Since there is most likely boron present in the samples used in this study [11], and since the band is associated with boron the evidence for associating the level seen in this work with the so-called U-band reported in the literature [10] seems strong. The reason that this defect produced a clear level in the samples studied here while a band was seen in the samples which were boron-implanted would seem to be

due to the difference in the manner in which the boron was introduced into the samples. The associated damage produced in the boron-implantation process might be what caused this level to be broadened into a band. This damage may not be present in the samples where the boron was introduced during the growth process. Since it is not possible to determine whether the level is hole-like or electron-like with the P.I.T.S. both a  $\sigma_{pa}$  and a  $\sigma_{na}$  are reported for it in Table 3.

#### 4. CONCLUSIONS

Several deep levels were seen in samples of semi-insulating liquid encapsulated Czochralski grown GaAs by photo-induced-transient spectroscopy. Two of the levels one at 0.56 eV and the other at 0.27 eV appear in all of the LEC samples regardless of the heat treatment they received and seem to be related to the presence of iron and zinc impurities respectively. These are most probably due to accidental introduction during the growth process since there was no intentional doping of the GaAs used in this study. Most of the other deep levels seen were correlated with levels seen by other investigators. The levels at 0.52, 0.42, and 0.36 eV seem to be associated with structural defects since they can be annealed out by heat treatment.

## REFERENCES

- This work was supported by the Air Force Office of Scientific Research under AFOSR-84-01698, the Army Research Office - Durham under DAAG 29-K-1064 and the State of California - MICRO Program.
- 1. Sah C.T., Forbes L., Rosier L.L., and Tasch A.F. Jr., *Solid State Elect.* **13**, 759 (1970).
- 2. Thyagarajan R., Narula R.C., and Parashar T.R., *Ind. J. Pure and Appl. Phys.* **17**, 650 (1979).
- 3. Gurtes Ch., Boulou M., Mitonneau A., and Bois D., *Appl. Phys. Lett.* **32**, 821 (1978).
- 4. Burd M.R., doctoral thesis, University of California, Los Angeles (1984).
- 5. Mitonneau A., Martin G.M., and Mircea A., *Electron. Lett.* **13**, 666 (1977).
- 6. Martin G.M., Mitonneau A., Mircea A., *Electron. Lett.* **13**, 191 (1977).
- 7. Norquist P.E.R., Klein P.B., Bishop S.G., and Siebenmann P.G., *Inst Phys. Conf. Ser.* **56**, 569 (1981).

8. Mircea A., and Bois D., *Inst. Phys Conf. Ser.*, **46**, 82 (1979).
9. Eetemadi S.M., and Braunstein R., *J. Appl Phys.*, **58(10)**, 3856 (1985).
10. Martin G.M., Secordel P., and Venger C., *J. Appl. Phys.*, **53**, 8706 (1982).
11. Thomas R.N., Hobgood H.M., Barret D.L., and Eldridge G., *Proceedings of the Conference on Semi-Insulating III-IV Materials*, 76 (Shiva, Nottingham, 1980) p.76

TABLE 1 - DESCRIPTION OF SAMPLE PREPARATIONS

SAMPLE	DESCRIPTION OF SAMPLE PREPARATION
D9	LEC-grown GaAs with ion-implanted contacts
M025	(note: there is extensive annealing as part
M25-2I	of the ion-implantation process).
M177	LEC-grown with MBE layer, ion-implanted
	contacts (note: there is extensive heat
	treatment during both the MBE and ion-
	implantation processes).
M039	
M043	LEC-grown with In soldered contacts.
M25-2	
M039 ann	LEC-grown and annealed at 700K for four
M043 ann	hours with a one hour cool off, In-
M25-2 ann	soldered contacts.
M039 que	LEC-grown and heat treated at 700K for
	three hours with a fast cool off, in-
	soldered contacts.

TABLE 2 - ACTIVATION ENERGIES OF DEEP LEVELS DETECTED BY PHOTO-INDUCED  
TRANSIENT SPECTROSCOPY MEASUREMENTS

SAMPLE	ACTIVATION ENERGY OF THE LEVEL (eV)						
M2S-2I	0.57			0.36	0.27		0.18
D9	0.56			0.36	0.28	0.22	
M02S	0.55			0.36	0.27	0.22	
M177	0.56						
M2S-2	0.56	0.52	0.42	0.36	0.27		0.18
M039	0.56	0.52	0.42	0.36	0.27	0.22	0.18
M043	0.56	0.52	0.42	0.36	0.27		0.18
M2S-2 ann	0.56				0.27		0.18
M039 ann	0.56				0.27	0.22	
M043 ann	0.57				0.27		
M039 que	0.56		0.42		0.27	0.22	



TABLE 3 - ACTIVATION ENERGIES AND EMISSION CROSS SECTIONS  
FOR DEEP LEVELS SEEN IN THIS STUDY

LEVEL IDENTIFIED	ACTIVATION ENERGY (eV)	EMISSION SECTION (cm <sup>2</sup> )
HL3	0.56	$\sigma_{pa} = 1.4 \times 10^{-15}$
Boron defect	0.52	$\sigma_{pa} = 1.7 \times 10^{-14}$ $\sigma_{na} = 1.3 \times 10^{-13}$
HBS or HLS	0.42	$\sigma_{pa} = 2.2 \times 10^{-13}$
HL7	0.36	$\sigma_{pa} = 5.6 \times 10^{-13}$
HL12	0.27	$\sigma_{pa} = 3.8 \times 10^{-15}$
EL17	0.22	$\sigma_{na} = 1.5 \times 10^{-14}$
EL10	0.18	$\sigma_{na} = 1.5 \times 10^{-15}$

# FIGURE CAPTIONS

Fig. 1 Block diagram of the photo-induced transient spectroscopy apparatus.

Fig. 2 Flow diagram of the computer program which operates the photo-induced transient spectroscopy apparatus.

Fig. 3 Plots of  $\log(T_m^2 t)$  versus reciprocal temperature for all deep levels seen by photo-induced transient spectroscopy.

Fig. 4 Transient current vs. temperature for sample M039,  $t=40$  msec, Ne-Ne laser light source.

Fig. 5 Transient current vs. temperature for sample M039 ann  $t=40$  msec, Ne-Ne laser light source.

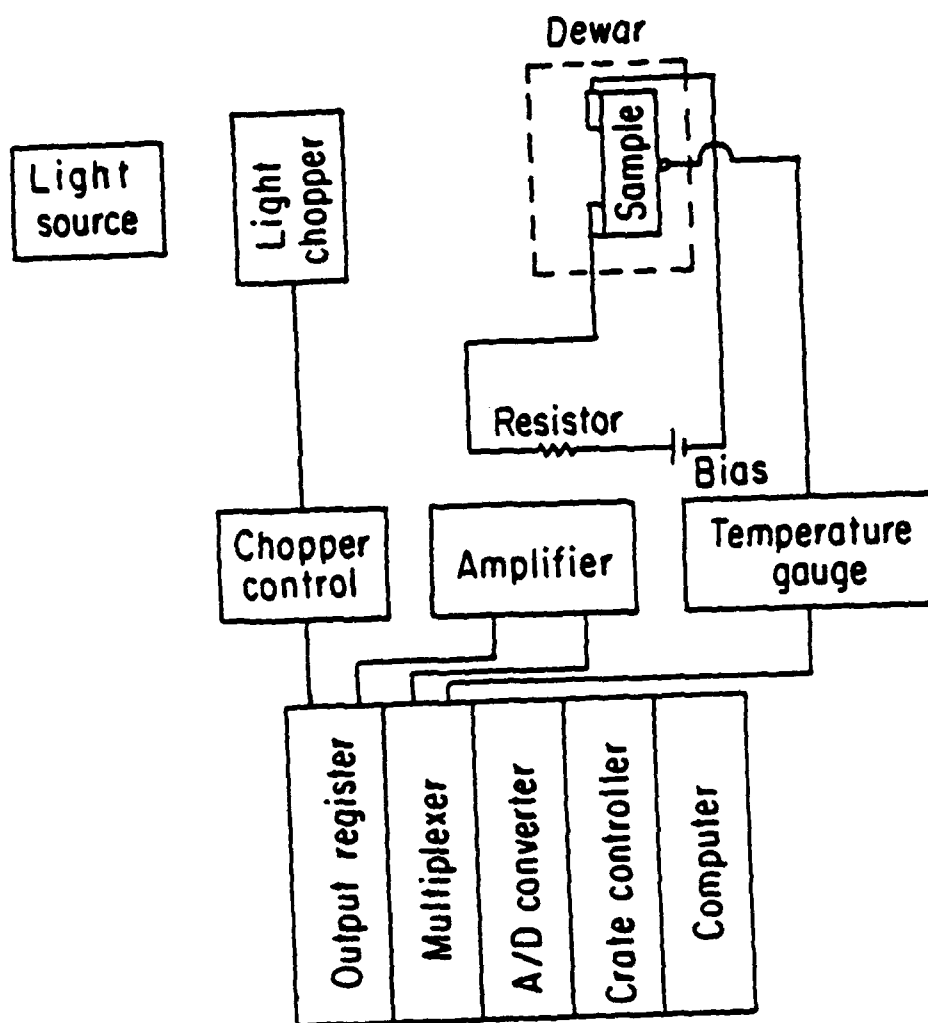


Fig. 1

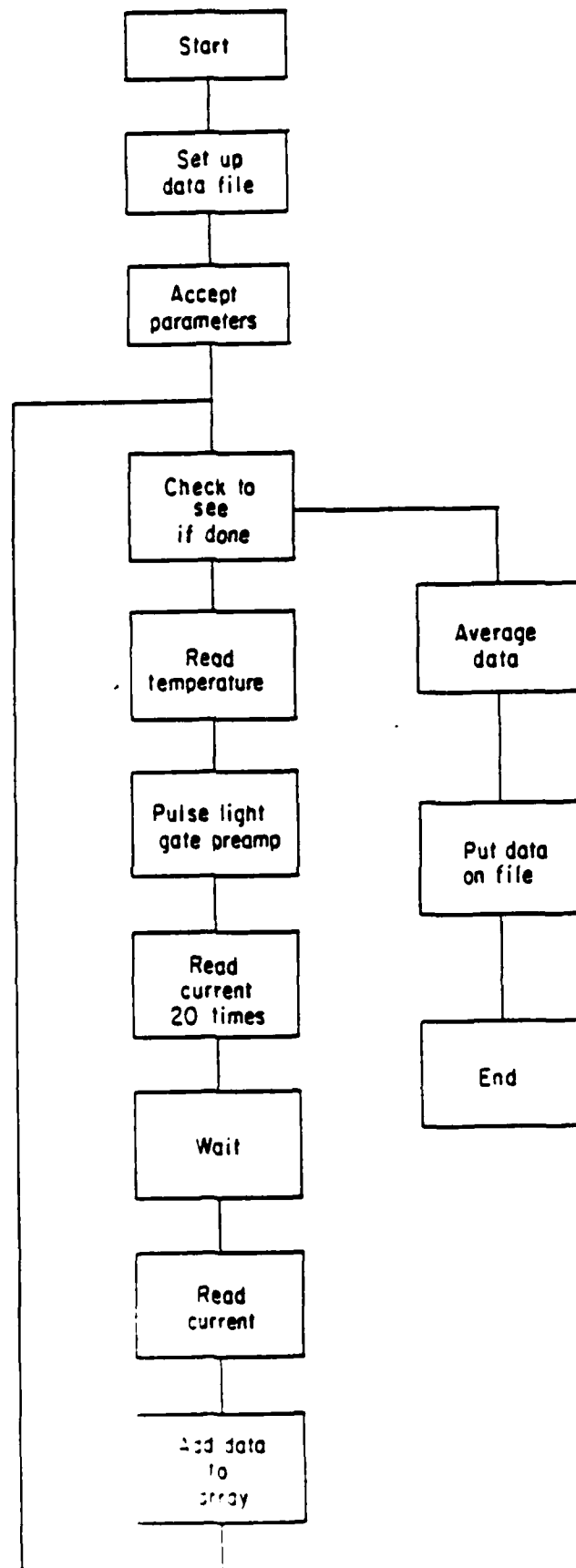


FIG. 2

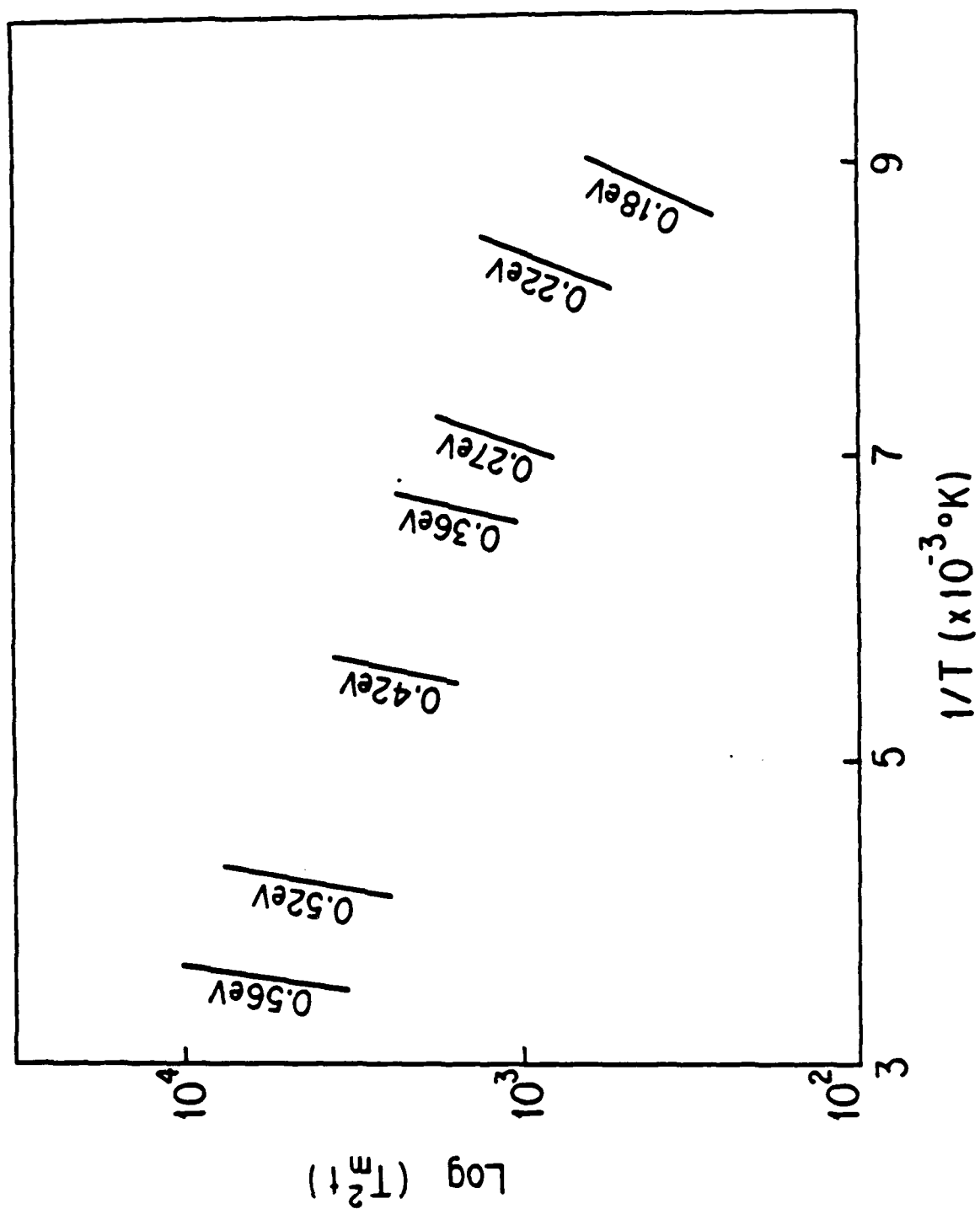


Fig. 3

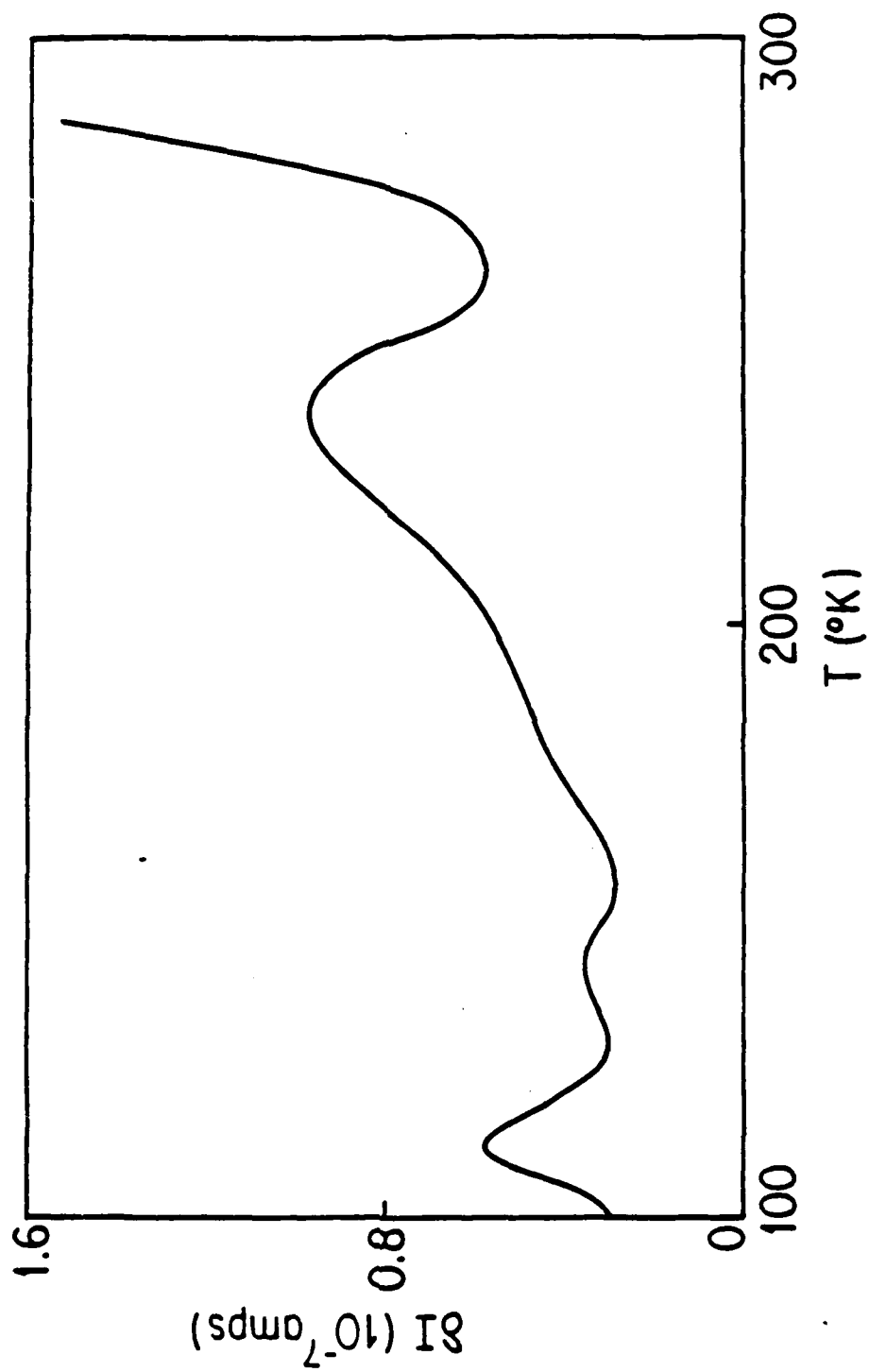


Fig. 4

END

7-87

DTIC